Performance Enhancement of Ultra Wideband Antennas for Communication and Microwave Imaging Applications

by

ABDELHALIM MOHAMED MAMDOUH MOHAMED

A Thesis submitted to the Faculty of Graduate Studies of
The University of Manitoba
in partial fulfillment of the requirements of the degree of

DOCTOR OF PHILOSOPHY

Department of Electrical and Computer Engineering
Faculty of Engineering
University of Manitoba
Winnipeg, Manitoba, Canada

Abstract

This thesis investigates omnidirectional and directional ultra wideband (UWB) antennas for communication and microwave imaging applications. To reduce interference with existing technologies, monopole antennas with efficient band-stop functions are introduced. Single and double slots acting as series resonators are used. Reduction in the antenna gain in the stop-band regions of about 19.5 dB is achieved. Central metal removal and ground plane size effects on the antenna performance are investigated.

To eliminate signal distortion caused by such monopole antennas, phase centre behaviour over the entire frequency band of operation is investigated at different principle planes, which have not been done before. This study will also show how these antennas act in different communication scenarios and where the radiation will be coming from at different frequencies. The effect of including different slots with different shapes on the performance of phase centre of these antennas is also investigated. Different methods to minimize the antenna phase centre movement are studied.

Novel microstrip antennas with UWB impedance and radiation pattern bandwidth and low cross polarization components are introduced to work over the frequency band from 3 to 20 GHz. The antennas introduced are double-layer structures in which the radiator is sandwiched between two identical partial ground planes or a partial ground plane is sandwiched between two radiators. Results show a significant reduction in the cross polarization components at all frequencies.

A novel high gain UWB Vee dipole antenna with a UWB coaxial balun feed is introduced to cover the existing and future UWB communication applications. Different type of loadings such as a reflecting ground below the antenna, a dielectric sleeve over the UWB balun and conical dielectrics between the Vee plates are also used and studied that show enhanced gains and lower sidelobes. A miniaturized-type UWB Vee dipole antenna is also investigated for microwave imaging applications. The antenna has a small radiation aperture which makes it a good candidate for array type applications. Full wave analysis of studied antennas are done using Ansoft HFSS, finite-element-methods based software. Experimental investigations are done to confirm the accuracy of simulated results.

Acknowledgement

First and foremost, I would like to thank my advisor, Prof. Lotfollah Shafai, for giving me the opportunity to work on this project, and also for his support and confidence in my work. Prof. Shafai's patience and encouragement were invaluable to me throughout the course of this PhD thesis. He is such a great advisor to have. He guided me to perform to the best of my abilities and gave me opportunities and exposure I would never have, if I had not joined his group. I would also like to thank my committee members Prof. H. Soliman and Prof. S. Noghanian for their valuable suggesions and discussions during this research.

I would like to thank The Mission Department, Ministry of Scientific Research, Egypt and NSERC, Canada, for financial supports. Many thanks go to all my friends and colleagues in the Applied Electromagnetic Group who were helpful to me tremendously, throughout this research with valuable discussions and suggestions. Special thanks go to Dr. AliReza Foroozesh, Dr. Saeed Latif, Ms. Zahra Allahgholi Pour, Mr. Ali Mehrbani and Ms. Krishna Kota. I also would like to thank Mr. Brad Tabachnick for providing help when needed in the antenna laboratory and regarding simulation software. Many thanks are due to Mr. Cory Smit at the machine shop for building the prototype antennas. Many thanks go to Shelly Girardin for invaluable assistance with administrative matter of my PhD program. Last but not least, I would like to thank my family who has always been a source of encouragement throughout my life. Thanks to Mona and my kids, Zeyad, Mazen, Basim and Sarah for understanding the type of research that took me away from them. All thanks goes to my loving mother for her sincere prayers for me.

DEDICATED TO THE MEMORY OF

My uncle……

My aunt……

My brother in law……

Table of Contents

List of Symbols

FCC Federal Communications Commission

GPS Global Positioning System

NTIA The National Telecommunications and Information Administration of America

RADAR: Radio detection and ranging

S/m: Conductivity units

SFF: System Fidelity Factor

SLL: Side Lobe Level

TEM: Transverse Electromagnetic

TSA: Tapered Slot Antenna

UWB Ultra Wide Band

List of Tables

List of Figures

CHAPTER 1

Introduction

1.1 Overview and Motivation

The proposed use of ultra wideband (UWB) technology in communication services, microwave imaging and as feeds for reflector antennas, especially in the last decade has increased the research interest for design and performance studies of novel UWB antennas. Unique characteristics of UWB communication technology include high data rate transmission and reception, low power consumption, secure communication link, high resolution and immunity to multipath environments. Areas of interest that need more research include interference of UWB antennas with the existing technologies, phase centre stability of UWB antennas, low cross-polarization UWB microstrip antennas, high gain directional UWB antennas with single or dual linear polarizations and miniaturized directional UWB antennas with small radiation aperture for microwave imaging applications.

In January and February 2001, The National Telecommunications and Information Administration of America (NTIA) conducted two important studies about the commercial use of UWB technology. One study was about the compatibility between UWB devices and some federal systems, while the second was about the compatibility between UWB systems and Global Positioning System (GPS) receivers [1, 2]. In February 2002 and based on these studies, The Federal Communications Commission

(FCC) issued a report containing part 15, subpart F, about operating UWB systems on an unlicensed basis [3]. The rules set by FCC opened a new window for the commercial use of UWB systems. Areas of application of UWB technology include vehicular radar systems, communications and measurements systems, and microwave imaging systems (GPR, medical systems, through wall imaging and surveillance systems).

A UWB antenna is a vital element in any UWB system. Designing a well-matched UWB antenna is the mile-stone in a successful UWB system. A UWB antenna should preserve all its characteristics over the entire frequency band of operation. UWB antenna characteristics include impedance bandwidth, radiation pattern, gain, directionality, and phase centre stability. In addition, a UWB antenna working within the communication band of 3.1 to 10.6 GHz should not exceed a certain spectral mask set by FCC, so that it can coexist with other communication systems with minimum interference levels. Achieving these characteristics are the main reasons for more research on UWB antennas for communication applications. Moreover, the growing demands for high gain directional UWB antennas for certain communication applications and miniaturized directional ones for microwave medical imaging, motivates researchers towards more research on these antennas.

1.2 Objective of the Research

This thesis explores different design concepts for UWB antennas and evaluates their potential for different applications including communications, microwave imaging

and as efficient feeds for reflector antennas. Novel UWB omnidirectional and directional antenna designs are being studied to improve their performance. To enhance the functionality of the stop band characteristics, different feature shapes and configurations are used to increase the impedance mismatch level in the stop-band, and to keep other antenna characteristics unchanged, over the operation-band. To eliminate the signal distortion when using UWB antennas, those with constant phase centre behaviour over the entire band of operation are designed and analyzed. Their phase centre is characterized at different principle planes. This is done to see how these antennas will act in different communications scenarios and where the radiation will be coming from at different frequencies. The effect of including slots of different shapes on the performance of phase centre is also studied. It is shown that some designs can adversely affect the phase of the radiated field, by displaying larger phase centre movements. For improved performance of the UWB antennas, such designs must be avoided. To decrease the antenna phase centre movement, interleaved monopole antennas with perpendicular elements in X-Z and Y-Z planes are studied.

Double-layers UWB microstrip antennas are studied. Two designs are proposed. One design consists of a partial ground plane sandwiched between two identical radiators, while the other design consists of one radiator sandwiched between two identical partial ground planes. The proposed antennas have low cross-polarization components. The results of the proposed double-layers antennas are compared to a single-layer microstrip one with the same parameters.

Novel high gain UWB directional antennas with constant phase centre to cover the existing and the future UWB applications are introduced. These designs include 3-D Vee dipole antennas with novel arm shapes and a modified coaxial cable feed. Several variations of this antenna including the ground planes and the dielectric loadings are investigated to improve the gain and sidelobe performance. Full wave analysis using HFSS, a finite-element-method, is used to design and analyze these antennas throughout this thesis. Measurements are done in the antenna laboratory at University of Manitoba to confirm simulation results discussed throughout the thesis

The contribution areas of this research can be summarized as follows:

- Introduced small size UWB square, circular and elliptical monopole antennas with UWB impedance bandwidth that covers the existing communication band of 3.1 to 10.6 GHz and extends up to 19.5 GHz with omnidirectional radiation pattern over the entire band. A reduction of 50% in the antenna metal area is achieved without affecting its performance. Ground plane size is optimized to decrease the lower frequency edge from 3.1 to 1.4 GHz.
- Introduced efficient band-stop functions that give maximum impedance mismatch level. By using double U-slots with optimum parameters, impedance mismatch of 16dB is achieved. While by using double spiral-slots with optimum parameters, impedance mismatch of 19.5 dB is achieved. The slot bandwidth is controlled by using different slot orientations.
- Determined the phase centre location of UWB square circular and elliptical monopole antennas over the entire frequency band and at different principle planes. The phase

centre location of UWB antennas with different slots is also determined at all frequencies and at different principle planes. Monopole antennas with perpendicular cuts are designed to reduce phase centre location movement over frequency.

- Introduce novel double-layer UWB microstrip antennas with low cross polarization and investigated the effect of all design parameters on impedance bandwidth and cross polarization levels.
- Introduced novel directional linear polarized UWB Vee dipole antennas. Antennas introduced have novel arm shape with UWB coaxial cable balun. Parametric studies on important parameters are done including Vee angle, arm size, dielectric loading, including directors and ground plane. A miniaturized version of this antenna with small radiation aperture is also introduced for medical imaging applications.

The potential applications of this research include:

- UWB Indoor Positioning System: Due to the mm resolution required by this system, constant phase centre antennas are needed.
- (3.1-10.6 GHz) UWB Communication Range: Due to the interference between existing technologies and UWB one, UWB antennas with efficient band-stop functions are needed.
- UWB applications that need polarization purity
- Microwave Medical Imaging Applications: Due to the limited space, directional UWB antennas with small radiation aperture are needed.
- UWB communication applications that need high gain directional UWB antennas

1.3 Structure of the Thesis

The structure of this thesis is as follows. Chapter 1 gives an overview of UWB technology and introduces the purpose and motivation of this work. Chapter 2 gives a literature review of UWB. It includes research work done so far, design concepts, interference issues, phase centre problems, omnidirectional and directional antennas, analysis methods, and measurements. Chapter 3 is devoted to performance studies of UWB omnidirectional antennas over ground planes. This study includes square, circular and elliptical monopole antennas with different configurations. Both impedance bandwidth and radiation pattern curves are studied and a physical interpretation for antenna operation is introduced. Results also include surface current distribution. Monopole antennas with efficient band-stop functions are introduced. The aim is to maximize the impedance mismatch losses within the stop-band region hence minimize antenna gain and reduce interference with existing technologies. The effect of the ground plane size on antennas performance is also studied. In chapter 4, the phase centre behavior of UWB antennas in the frequency domain is investigated. Antenna phase centre is calculated and measured at different principal planes. Different antenna designs are used in this study including circular and square type antennas. Ways to stabilize phase centre of such antennas include design modifications and using more than one radiator in the perpendicular plane over the ground plane. The effect of including resonant slots in the antenna structure on the phase centre location is also investigated. Chapter 5 introduces a UWB microstrip antenna with low cross-polarization components. Strip and microstrip line feedings are used along with a double-layer structure to reduce the cross-

polarization level. The effect of layers' misalignment on the antenna performance is also studied. Chapter 6 introduces a novel high gain UWB Vee dipole antenna with coaxial balun. The antenna is designed using a novel arm shape and both directors and reflectors are included to increase the directive gain. Finally, a scaled down version of this antenna, with small radiation aperture, is investigated for microwave imaging applications. Chapter 7 summarizes this work, discusses the contributions and states the future research plans.

Chapter 2

Literature Review

2.1 History of UWB Technology

Current UWB technology can be seen as a revisited research topic. That is because the concept of using baseband communication and pulse antennas has been around since the 1st half of the last century. Also, some of the UWB antennas used nowadays were known for more than 50 years. Examples of early antennas that are still in use, with different shapes and dimensions, are the square plate loaded dipole and spherical loaded dipole of Hertz. Oliver Lodge's preferred antennas of 1898 is the so called now bow tie antennas. Lodge was also the inventor of the biconical antenna in 1898. The link between UWB concept in the old days and with the revisited UWB antennas of today is discussed in references [4-9]. Due to the limited frequency spectrum and increasing demand for more bandwidths, UWB technology has witnessed increasing interest in the last two decades, especially after The Federal Communication Commission (FCC) issued its important report about operating UWB systems on an unlicensed basis. As per definition, the UWB technology needs to operate with other existing applications in the same frequency band. Also, the UWB technology uses its spectrum simultaneously. For this reason, FCC has specified a spectral mask for using UWB technology for the communication and measurement applications. When designing UWB systems, the maximum effective isotropic radiated power (EIRP) measured in a 1 MHz

bandwidth (dBm/MHz), radiated by the system, should not exceed certain limits for indoor and outdoor applications. For example, EIRP should not exceed -41.3 (dBm/MHz) for both indoor and outdoor applications in the frequency range from 3.1 to 10.6 GHz.

UWB applications have a diversity nature. Some applications need small omnidirectional antennas, while others need high gain directive ones. In all cases, the antenna designed has to preserve its characteristics simultaneously over the entire band of operation. Important characteristics of interest are impedance bandwidth, interference with other applications, phase centre stability, cross polarization and directive gain. The following sections will give brief definitions to some important antenna parameters and present some of the previous work done in UWB antennas with attention given to the previously mentioned parameters.

A UWB antenna is the one that keeps its wanted characteristics unchanged simultaneously over the entire bandwidth. These characteristics include impedance bandwidth, radiation pattern and phase centre stability. In [10], time domain characteristics of some UWB antennas were studied. Resonant monopole, double-ridged TEM horn, cavity backed Archimedean spiral, log-periodic pyramid, Vivaldi, and biconical antennas were studied. Frequency and time domain response were measured using Network Analyzer. It was found that Vivaldi offered good option over the slightly dispersive TEM horns, while Archimedean spiral suffered from dispersion. In [11], the size limitations of UWB antennas in terms of pulse width and 3dB cut-off frequency were developed. It was also shown that the 3dB cut-off frequency criterion can determine the

suitable antenna for a certain frequency range. In [12], the practical realization of Chu's minimum-sized antenna was investigated using self-complementary antennas. It was shown that, by using a more complicated matching circuit for broadband antennas instead of the single-stage inductor used in bandwidth estimation with the Q factor, the fabricated antenna was smaller than the minimum-sized one. In [13], fundamental physical limitations on UWB antennas regarding impedance matching, radiation-Q and directivity were reviewed using the concept of the minimum-Q antenna. It was also discussed how to approach these limits by means of antenna miniaturization. The method was applied to a spiral antenna.

As per IEEE definition of radiation efficiency, it is the ratio of the total power radiated by the antenna to the net power accepted by the antenna. In a Wheeler Cap technique, the reflection coefficient of an antenna in free space is compared to its reflection coefficient when placed in a Wheeler Cap. The disadvantage of this method is due to fact that, the size of the Wheeler Cap depends on the frequency of interest [14, 15]. A modified version of the Wheeler Cap method was applied to evaluate UWB antennas efficiency in [16]. In this method, the mismatch reflected power was explicitly included as a loss term. To overcome the problem of time consumed to measure efficiency using the frequency based techniques, a time domain based procedure was introduced in [17]. In this method, a reverberation chamber was used to measure the global efficiency of a UWB antenna using another UWB antenna with known efficiency. A waveform generator was used to transmit a pulse and a digital storage oscilloscope was used to receive it. After the signal was time reversed and amplified, it was then retransmitted and

the initial pulse could be refocused because of the high level of multipath propagation inside the reverberation chamber. At each transmission, the recorded power of the refocused pulse was related to the efficiencies of both transmitting and receiving antennas. Formulas were used to calculate the efficiency of the unknown antenna.

2.2 Analysis and Measurement Techniques for UWB Antennas

When applying voltage to an antenna, charge distributions get accelerated giving rise to currents. Then the time varying currents will generate radiation fields. The relation between the currents and their associated fields is given by Maxwell's equations. When looking at physical signals, one can use frequency domain or time domain approach. Aanalytic functions may be transformed between the time domain and frequency domain using integral relations. For example, the Fourier integral transformation:

$$F(\omega) = \int_{-\infty}^{+\infty} f(t) e^{-j\omega t} dt \tag{2.1}$$

gives the frequency domain spectral density, F(ω) of a time domain signal f(t), while the Inverse Fourier Integral Transformation:

$$f(t) = \int_{-\infty}^{+\infty} F(\omega) e^{-j\omega t} d\omega \tag{2.2}$$

gives the time domain signal corresponding to a frequency domain spectral density, [4].

In 1971, Garbacz described a method to determine characteristic mode current on thin wires of general shapes. It was shown that at each frequency, each conducting body

has a particular set of surface currents with their corresponding radiated fields. Those currents and their associated fields are characteristic of this body shape and independent of any specific excitation. By determining and controlling these modes, an optimum feeding arrangement can be found to obtain the desired radiating behavior. The problem was approached by diagonalizing the scattering matrix which led to a real mode current and that the tangential electric mode field is of constant phase over the surface of the body, [18]. Later, Harington approached the problem by diagonalizing the operator relating the current to the tangential electric field on the body. Simpler derivation of the theory and explicit formulas for determining the mode currents and fields were achieved in [19]. Since then, the theory of characteristic modes has been used to analyze the performance of different UWB antennas by studying resonance modes of each antenna and enhance the modes that support wider impedance bandwidth performance. A clear insight into the physical performance of these antennas along with the effect of using different geometries on their performance was obtained. This study led to modal solutions for arbitrarily shaped antennas and provided physical interpretation of the radiation phenomena taking place on them. The theory of characteristic modes was also applied to band-notched antennas to find current distributions around the notch area and study its effect on the radiation characteristics. Application of this theory on UWB antenna designs can be found in these references, [20-26]. Recently, circuit modeling methodology was introduced to model small UWB omnidirectional antennas [27].

UWB antenna characteristics include return loss curve over the entire frequency band, radiation patterns at certain frequency points, gain pattern represented in frequency

versus angle (θ or ϕ), and impulse response in time domain to illustrate pulse distortion. Characteristics also include the antenna group delay (or phase derivative) represented in time-frequency figures to show time needed by the signal to move from one antenna to the other. However, these important characteristics cannot be shown all together. System Fidelity Factor (SFF) uses S21 parameter to compare the received and transmitted signal between two antennas. It was used to compare the performance of different UWB antennas by first using simulation and measurement methods to calculate the system transfer function and then the time domain signals were calculated using post processing. Finally, the SFF was calculated from the transmitting and received signals, [5, 28 and 29].

UWB antennas are usually measured in an anechoic chamber to get impedance and radiation pattern parameters, [30-32]. In 2010, the theory of antenna measurements was presented using noise and compared to ultra wideband frequency domain method. This method provided a low cost alternative to the frequency domain method while experimentally proved to give the same results as Vector Network Analyzer (VNA) method. In this method, a complex formulation of Friis transmission equation was proposed from which the time-domain equation was obtained. It was proven that, the UWB noise-domain antenna measurement would yield the same result as the time-domain setup one. A system for gain measurement using noise was built. The system contained a noise source, a UWB amplifier, a splitter, a delay line, a low pass filter, a multiplier, a digital voltmeter, a transmitting antenna and a receiving one, [33].

In this thesis Ansfoft HFSS, a full wave 3-D electromagnetic simulator software, based on the Finite Element Method, is used to model and analyze all antennas studied, [34]. Then, the results are verified by measurements, done at the University of Manitoba Antenna Laboratory. Fig. 2.1 shows return loss and radiation pattern measurements done at the University of Manitoba Antenna Laboratory.

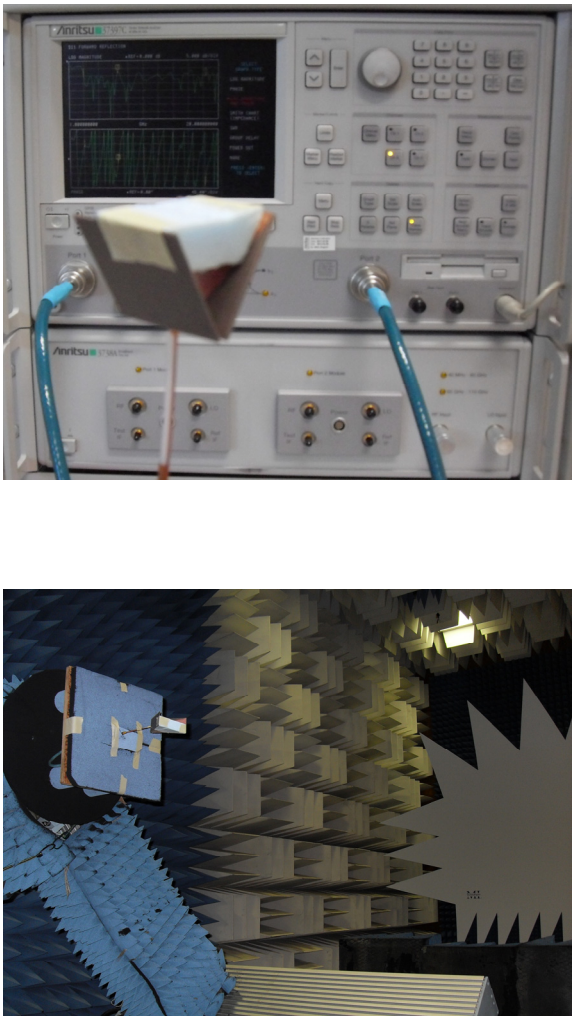

Fig. 2.1 Network Analyzer and Compact Antenna Range for return loss and radiation pattern measurements at the University of Manitoba Antenna Laboratory

2.3 Omnidirectional UWB Monopole Antennas

UWB monopole antennas are popular and easy to fabricate that are known for their omnidirectional radiation patterns. The bandwidth of a cylindrical monopole antenna increases with the increase of its diameter. This concept in UWB technology is known as "the fatter the better" [4]. That is why when designing square, circular or elliptical monopole antennas over a ground plane, the width of the radiator affects the higher frequency performance of the impedance bandwidth. One way to look at a planar monopole radiator is that its surface area can be equated with a cylindrical monopole one with a large effective diameter. The lower frequency of operation corresponding to VSWR=2 can be calculated using the monopole antenna concept described in [35, 36]. In [37], corrugations in the plate monopole were introduced to increase the total length of the antenna which reduced the lower frequency edge of the impedance bandwidth.

The parameters affecting the bandwidth of plate monopole antennas are the length of the probe, width of the plate and diameter of the feeding probe. Various geometries and perturbations were applied to design UWB monopole antennas with a coaxial type feed over a ground plane or by using planar structures with microstrip, strip or coplanar waveguide feed type. The main interest was driven to have a UWB impedance bandwidth and nearly omnidirectional pattern. Square, circular and elliptical radiator shapes with different modifications were used to design these antennas using different approaches including Genetic Algorithm and Transmission Line Modeling. However, the problem of phase centre stability of these antennas was not deeply studied, [38-55]. The effect of the

ground plane on the performance of a planar elliptical monopole antenna was studied. It was shown that by implementing slots in the partial ground plane, better impedance matching could be achieved, [56]. Ground plane shape effect on the performance of a circular monopole antenna mounted over a ground plane was also studied. It was shown that by using a trapezoidal ground instead of a rectangular one, a significant improvement in the radiation pattern performance could be achieved [57]. The theory of characteristic modes was applied to analyze several monopole antennas, [22]. It was shown that to have a broad impedance bandwidth, it is necessary to have a well matched traveling mode. For UWB monopole antennas mounted over a ground plane, currents need to be directed in the vertical direction to support the traveling modes. One way to do so was to use more than one feeding point. A UWB square monopole antenna with trident feeding strip to work over the communication band was introduced in [58]. However, this antenna needs further investigation regarding extending the bandwidth with smaller radiator sizes. Also the phase centre profile of this antenna and other different shapes need to be characterized. Finally, this antenna needs to be characterized with resonant feature to reduce interference.

2.4 Interference with Coexisting Technologies

UWB antennas need to coexist with other existing services. The antenna transmission and receiving capabilities need to be controlled in certain frequency bands, within the communication band from 3.1 to 10.6 GHz. By doing this, the antenna will act as a filter too, which will simplify the design of the communication system. In order to do

this, a slot of half wave length at the centre frequency of the stop-band can be implemented inside the radiator. Currents concentrate around the slot at the stop-band and cancel radiation. Also, the antenna becomes mismatched at the stop-band frequencies. VSWR curves and return loss curves can show this mismatch. Band-stop parameters include bandwidth, centre frequency, mismatch level and effects on other antenna parameters in the pass band including the phase centre profile. UWB antennas with band -stop functions have been widely studied. These studies included different slot shapes with different antenna designs. Some of the important parameters of the stop-band were fully investigated while others still need more investigation, including effect on the antenna phase centre and impedance mismatch level. Some of UWB antennas with stop-band function can be found in these references, [59-85]. They have shown that the mismatch level within the stop-band needs to be increased. Also the effect of including slots inside the radiator on the antenna phase centre needs to be studied.

2.5 Phase Centre of UWB Antennas

For some antenna applications, an accurate knowledge of the phase centre location is essential to the operation of the system such as Satellite and radio positioning systems. Moreover, other applications require the uniqueness of the phase centre over a large portion of the pattern such as feeds for reflector feeds antennas. In the case of UWB communication applications, system designer needs to know how well a UWB antenna will act and where the radiation will be coming from for different angles at different frequencies. This needs an accurate knowledge about the phase centre of the antenna over

the bandwidth. The phase centre at different principle planes needs to be characterized. It is also of importance to study the effect of including resonant features in the UWB antennas. That is, to fully characterize UWB monopole antennas working over the frequency range of 3.1 to 10.6 GHz. In 1956, David Carter studied the phase centre of microwave antennas and developed formulas for reflector antennas [86]. In 1982, L. Manila studied the role of the antenna phase centre in geodetic measurements based on satellite systems [87]. In 1984, K. Rao and L. Shafai used the feed efficiency to define uniquely a combined E- and H-plane phase centres of the feed pattern of a paraboloid reflector [88]. In 2003, J. Svigelj used measurements for the correction of antenna phase centre offsets in outdoor range measurements [89]. In 2006, K. Rambabu introduced a printed circuit UWB antenna based on stepped-patch with multiple resonating elements that had small phase centre variations [90]. In 2008, Shang used the least square method to compute antenna phase centre based on phase and amplitude pattern measurements [91]. In 2008, M. Mahfouz utilized Vivaldi phase centre calibration to solve the problem of reduced accuracy in a UWB indoor local positioning system [92]. Chapter 4 of this thesis investigates the phase centre profile of small UWB antennas with and without band-stop functions. This is done for the first time in the frequency domain and at different principle planes.

2.6 Directional UWB Antennas for Microwave Imaging Applications

Directional UWB antennas can be used in different applications including communications, microwave imaging, and RADARs. Important characteristics include

high gain, low side lobe and back lobe radiations, stable phase centre and suitability to be implemented in array configurations. Medical microwave imaging needs a small UWB directional antenna due to space limitation. UWB directional antennas have been studied including different antenna types and shapes. Also different feeding schemes were investigated along with dielectric loading and more than one polarization. Size reduction of these antennas was also investigated to be used in medical applications. In [93], a resistively loaded Vee dipole was designed for short-pulse ground penetrating radar (GPR) to detect buried antipersonnel land mines. The resistively loaded Vee antenna used to help in reducing clutter related to antenna, which in turn helped in distinguishing between land mines. In [94], a resistively loaded conical-cylindrical Vee dipole antenna was introduced to be used for UWB microwave radar applications, such as biological sensing and imaging. In this design, the conducting lower cylindrical part is attached to the upper conical part with finite conductivity. Vee angle was optimized for maximum bandwidth. The largest bandwidth was obtained with upper part conductivity of 140 S/m and Vee angle of 30^{o}. The drawback of using resistively loaded Vee dipole antennas was the reduction in antenna efficiency. In [95], a planar array consisting of 6x2 UWB antenna elements was designed for an UWB microwave imaging system, operating in 3.1 to 10.6 GHz band. Each antenna element was a compact (22mmx40mm) corrugated tapered slot antenna (TSA). Corrugations were used to reduce the antenna size, improve the matching of the antenna opening and suppress standing waves arising in the antenna. In [96], a compact UWB double-ridged horn antenna was introduced for biomedical diagnostics. The antenna had a radiation aperture size of $29x29mm^2$ and was loaded with ceramic dielectric for matching. Although this antenna gave promising results, it suffered

from ringing effects and needed more optimization. Different Planar Yagi and Log-Periodic Array antennas were designed for UWB applications. However, these antennas are dispersive by nature and suffer from inherent phase centre location movement over the frequency band of operation, and are not suitable for applications that need mm and sub mm accuracy [97-102]. A low-profile log-periodic UWB feed for the dual-reflector antenna to be used in a square kilometer array configuration was introduced in [103]. Antenna introduced could be enclosed in a volume of $0.5\lambda_L x 0.5\lambda_L x 0.5\lambda_L$ size, where λ_L is the wavelength at the lowest frequency. The dispersive nature of the log-periodic antenna was solved by constructing the antenna as two parallel dipoles, separated by 0.5 λ and located over a ground plane. This configuration gave equal E- and H-plane patterns and locked the phase centre to the ground plane. However, this antenna was not well matched over band of operation. Different modifications were introduced to this design to better match the antenna and to have dual polarization [104-107]. In [108], a balanced antipodal Vivaldi antenna with overall size of 80mmx44mmx9.2mm was introduced for microwave breast cancer detection system. The antenna had three copper layers; the central layer was the radiator and the two external ones were the ground planes. The copper layers were separated by supportive substrate with ε_r=2.94 and two additional dielectric layers were stacked on each side of the antenna. To improve antenna directivity, a piece of higher dielectric constant material with ε_r=6, with special shape was implemented. In [109], a unidirectional horn-shaped tapered bowtie slot antenna with a pyramidal reflector was designed for UWB high resolution radar imaging applications. The designed antenna showed a low return loss over 3 to 11.7 GHz band, with a high front-to-back ratio over the entire band. However, the overall size of the antenna with the

reflector is 60mmx44mmx20mm, which is not appropriate for medical imaging applications. Chapter 6 of this thesis introduces a novel high gain UWB Vee dipole antenna with a UWB coaxial balun for communications and microwave imaging applications.

2.7 Conclusion

In this chapter, a brief introduction to the history of UWB technology was discussed along with some of the open research problems associated with this technology that still need more investigations. Problems of interest include interference, phase centre, cross-polarization and directive UWB antennas. It has been shown that although there exist numerous publications on UWB antennas, more research is needed for characterizing these antennas with stop-band functions, the impedance mismatch level within the stop-band needs to be increased, and the phase centre of UWB antennas still needs to be characterized and stabilized. The cross polarization radiations of microstrip UWB antennas need more attention. Besides, more research needs to be done regarding directional UWB antennas for communications and microwave imaging applications.

Chapter 3

UWB Monopole Antennas and Incorporation of Band-Stop Functions

3.1. Introduction

Monopole antennas are good candidate for ultra wideband applications that require an omnidirectional pattern, such as ultra wideband wireless communications. Spheroidal, conical and teardrop monopole antennas are some of the traditional UWB antennas with excellent electrical characteristics. However, they are three-dimensional structures, and also difficult to fabricate. Monopole disc antennas, can also provide UWB impedance bandwidths, but have simpler two-dimensional geometries and are easier to fabricate. In 1992, Honda and others proposed a circular monopole TV antenna operating at 90-770 MHz [38]. These antennas can be designed to cover both existing and upcoming UWB communication applications, and have omnidirectional radiation patterns over the entire frequency of operation [39].

In this chapter, square, circular and elliptical monopole antennas over finite ground planes are investigated. The proposed designs cover the frequency band between 3 to 19 GHz. The effect of central metal removal from the interior structure of the radiator and implementing notch in the bottom end, on the impedance bandwidth and radiation pattern of these antennas, are also studied.

3.2 Impedance Bandwidth and Radiation Patterns

Impedance bandwidth is one of the characteristics that distinguish a UWB antenna from a narrow band one. The lower and upper frequencies are determined based on the 10 dB return loss bandwidth criterion. An antenna is considered well matched when its return loss is greater than or equal to 10 dB. This return loss represents the impedance mismatch level of this antenna. Techniques to increase the bandwidth and control the lowest frequency of operation have been used including geometry changes, loading effects, using shorting post or feeding the antenna with different feeding schemes. A physical interpretation of the bandwidth increase of these antennas using the theory of characteristic modes was given in [22]. The idea is to enhance the modes that give the current distributions that support the radiation. In the case of monopole antennas, it is found that the first three modes J1, J2 and J3 are enough to characterize the antenna behaviour. J1 mode supports the radiation in the lower frequency band while J3 supports radiation in the upper band. When the monopole antenna is placed vertically over a horizontal ground plane, modes J1 and J3 give vertical current distributions on the antenna surface, while mode J2 gives horizontal currents parallel to the ground plane. In this case, it will be useful to suppress mode J2 to reduce cross polarization component. Monopole antennas have an omnidirectional radiation pattern in the H-Plane which makes them good candidates for communication applications. There are some shortcomings with existing UWB antenna designs which include high cross polarization components especially at higher frequencies, angular dependence of the E-plane patterns and deterioration in the H-plane patterns.

One of the general principles of small-element antenna design is the equivalent outline design one. It states that an outline of a planar antenna element performs approximately like the original planar one [4]. A study is made to remove central metal gradually from the interior of all investigated antennas, while keeping the impedance and radiation characteristics unchanged. The minimum metal depth that could be achieved is about 50% from the total radiator area. The effect of implementing a notch close to the feeding structure on impedance bandwidth is also studied. The ground plane size reduction is also investigated. The study started with a ground plane size of 120x120mm^2 and end up with a size 20x20mm^2, that maintains the required antenna characteristics.

#

3.3 Square Monopole Antennas

Square monopole antennas are simple antennas to fabricate and have radiation characteristics that are suitable for certain UWB applications. They are omnidirectional antennas with impedance bandwidth that depends on the antenna design parameters. These design parameters include height, width and distance from the ground plane. To increase the bandwidth of this square monopole antenna, Wong introduced the trident-shaped feeding strip to feed the square monopole [58]. Wong's optimum design parameters for the trident-shaped feeding strip gave a 10 dB bandwidth of 10 GHz with the lower frequency of 1.376 GHz. Wong used a 40x40 mm^2 square monopole over a 150x150 mm^2 ground plane, all strip widths used were 2mm. Based on this idea, a square monopole antenna with trident-shaped feeding strip is designed to work over the

frequency band starting from 3GHz. Fig. 3.1 shows different configurations for the square monopole antenna along with the return loss curves. The square monopole side is scaled down to 16 mm over a 120x120 mm^2 ground plane, Fig. 3.1a. The optimum strip dimensions for this antenna are t = 7 mm, d = 1 mm, h = 3 mm, and all strip widths are 1.5 mm. Simulation results of this antenna show an omnidirectional radiation pattern over the frequency band from 3GHz to 19.5 GHz. To study the effect of implementing a notch close to the feeding structure, a rectangular notch, appears shaded in Fig. 3.1b, of height 2mm and width 3.75mm is implemented at each lower side of the square monopole, Fig. 3.1b. As can be seen from Fig. 3.1d, the 10dB higher frequency edge of the impedance bandwidth was decreased from 19.5 GHz to 15 GHz because of implementing this notch. Radiation patterns at different frequencies show no significant effect of implementing such a notch.

In an earlier work, it was proven by the author that by removing metal from the centre of the radiator, and using a single feeding strip, a loop ultra wideband monopole antenna was achieved keeping its radiation characteristics unchanged [110]. To further study the performance of the square monopole antenna with trident-feeding structure, gradual metal removal was done from the centre of the monopole. With this square monopole design, 8x8 mm^2 metal area was removed from the radiator, as shown in Fig. 3.1c. The impedance bandwidth of the resulting antenna gives the same impedance bandwidth from 3 to 19.5 GHz with omnidirectional radiation patterns over the entire frequency bandwidth. Fig. 3.2 shows its E-plane and H-plane radiation patterns at

different frequencies and different planes. It is clear that this antenna maintains its radiation characteristics at higher frequencies.

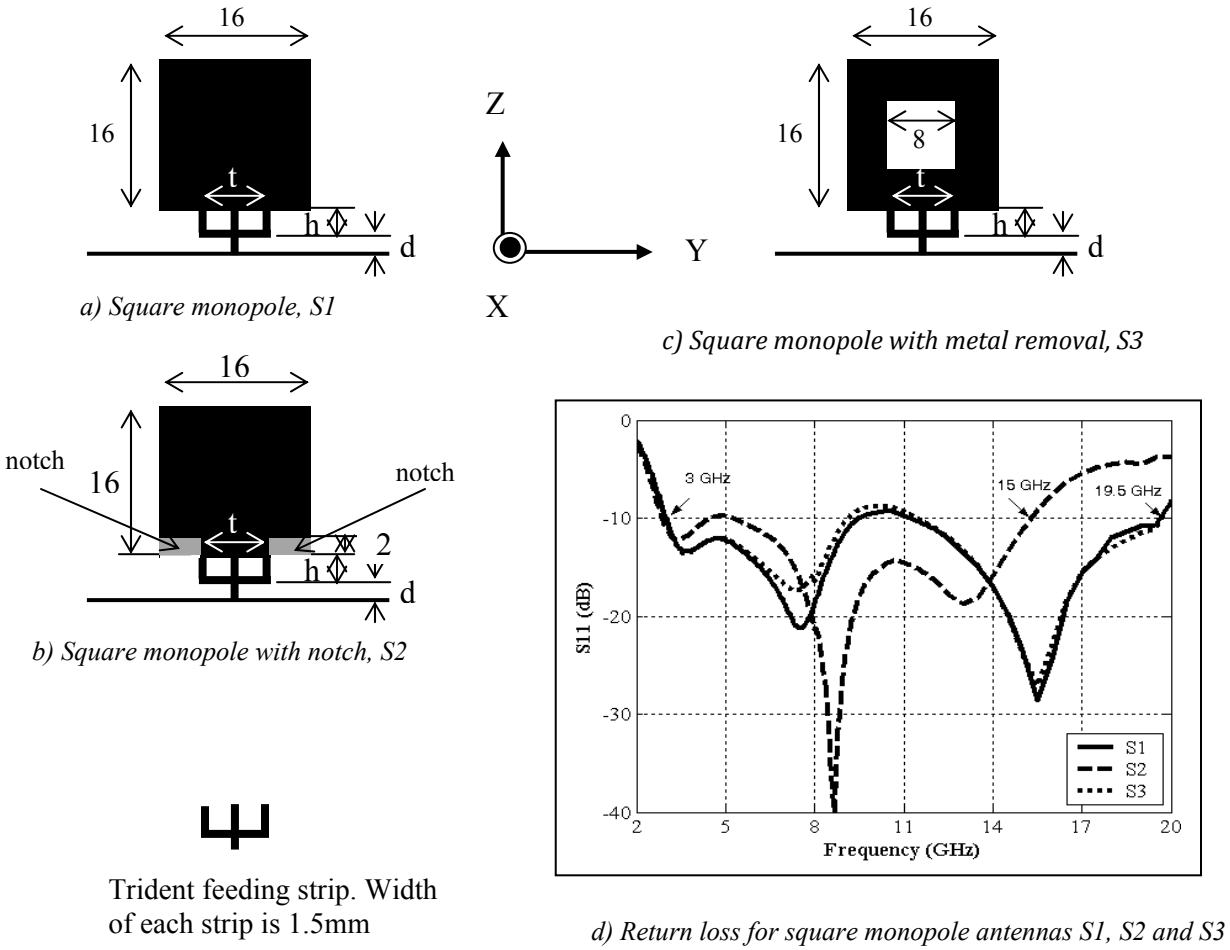

a) Square monopole, S1

b) Square monopole with notch, S2

c) Square monopole with metal removal, S3

d) Return loss for square monopole antennas S1, S2 and S3

Fig. 3.1 Square monopole antenna with 120x120 mm^2 ground plane and different configurations. t = 7, d = 1, h = 3, and all strip widths are 1.5. Notch height =2, width=3.75. All dimensions in mm

Fig. 3.2 Shows radiation patterns of different square monopole antennas, with trident-feeding strip at different frequencies for different planes. As can be seen, all square monopole antennas have omnidirectional radiation patterns.

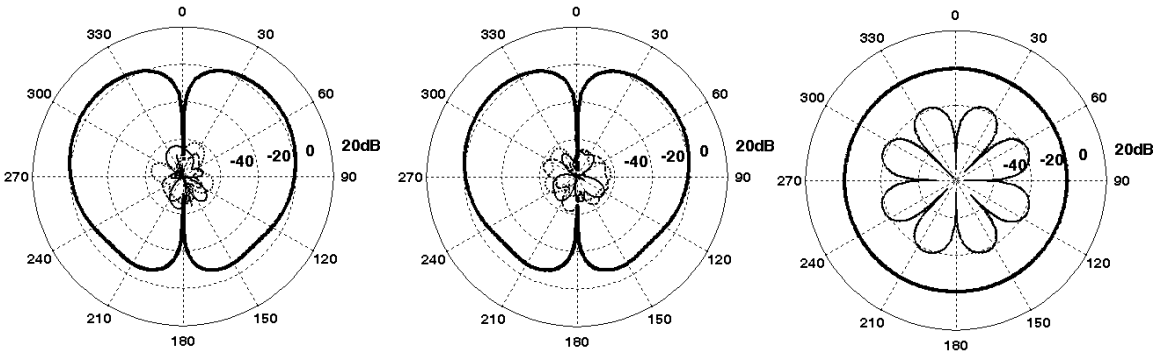

X-Z plane, F = 3 GHz *Y-Z plane, F = 3 GHz* *X-Y plane, F = 3 GHz*

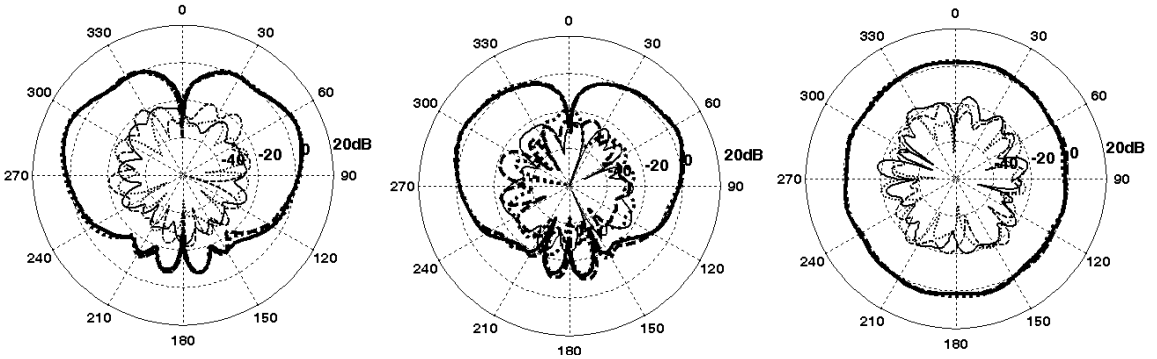

X-Z plane, F = 8 GHz *Y-Z plane, F = 8 GHz* *X-Y plane, F = 8 GHz*

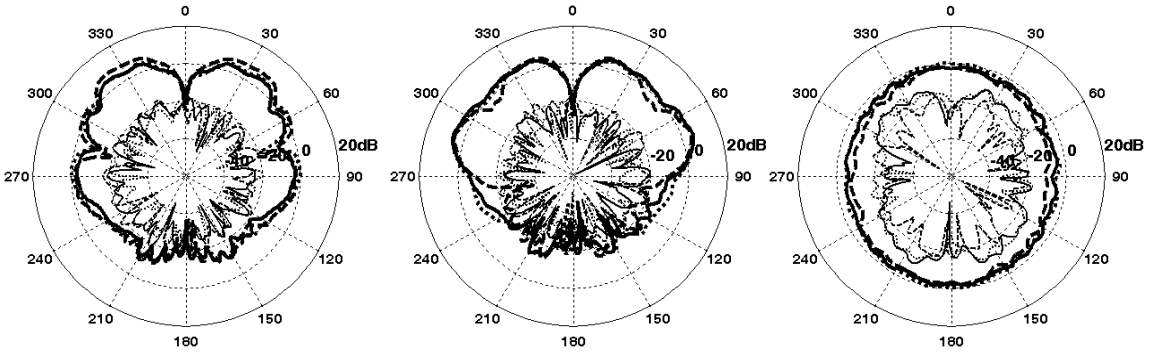

X-Z plane, F = 18 GHz *Y-Z plane, F = 18 GHz* *X-Y plane, F = 18 GHz*

Fig. 3.2, Radiation patterns for square monopole antennas S1, S2 and S3 of Fig. 3.1 at different frequencies

$E_{\theta, S1}$ —— $E_{\theta, S2}$ – – $E_{\theta, S3}$ ····· $E_{\phi, S1}$ —— $E_{\phi, S2}$ - - - $E_{\phi, S3}$ ·····

Fig. 3.3 shows pictures of the mesh adapted by FEM while solving at different frequencies. Note that the mesh gets denser at higher frequencies. This means when the solution frequency increases, the time consumed in solving the problem of UWB antennas will increase. Solution time will also increase as the problem size increase. For

example, the time needed to solve the structure at f=3GHz is 27 sec, while it is 95 sec at f=8GHz and 462 sec at f=12GHz.

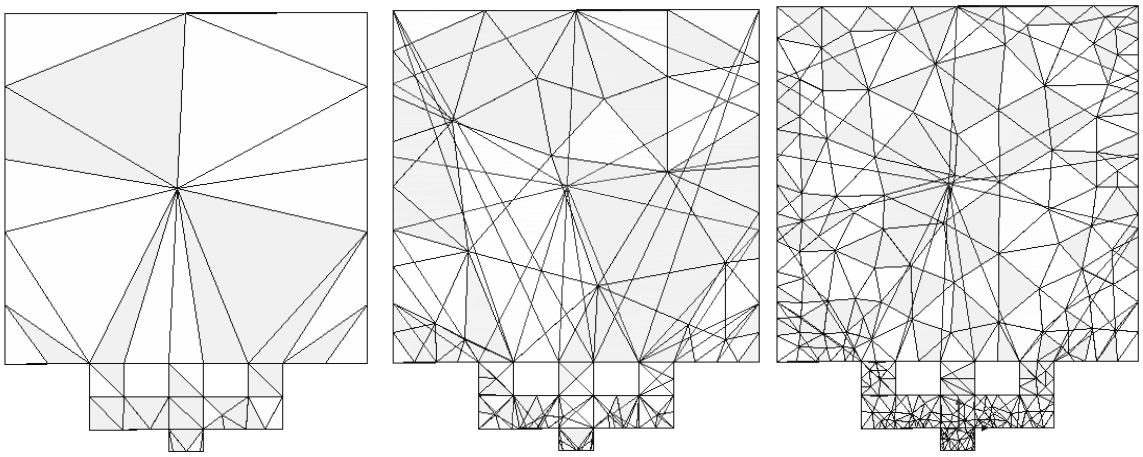

Mesh at 3 GHz Mesh at 8 GHz Mesh at 12 GHz

Fig. 3.3 FEM mesh at different solution frequencies, for geometry of Fig.3.1a

Fig. 3.4 shows surface current distributions at different frequencies for the square monopole antenna S1 at Fig. 3.1a. The size of the arrows represents current values. As can be seen from current distributions, strong currents exist at different locations for different frequencies. These current distributions represent different characteristic modes for each geometrical shape. While Fig. 3.5 shows the surface current distributions for the square monopole antenna with central metal removal shown at Fig. 3.1c. The 3-D radiation patterns of the square monopole antenna with central metal removal of Fig. 3.1c are shown in Fig. 3.6.

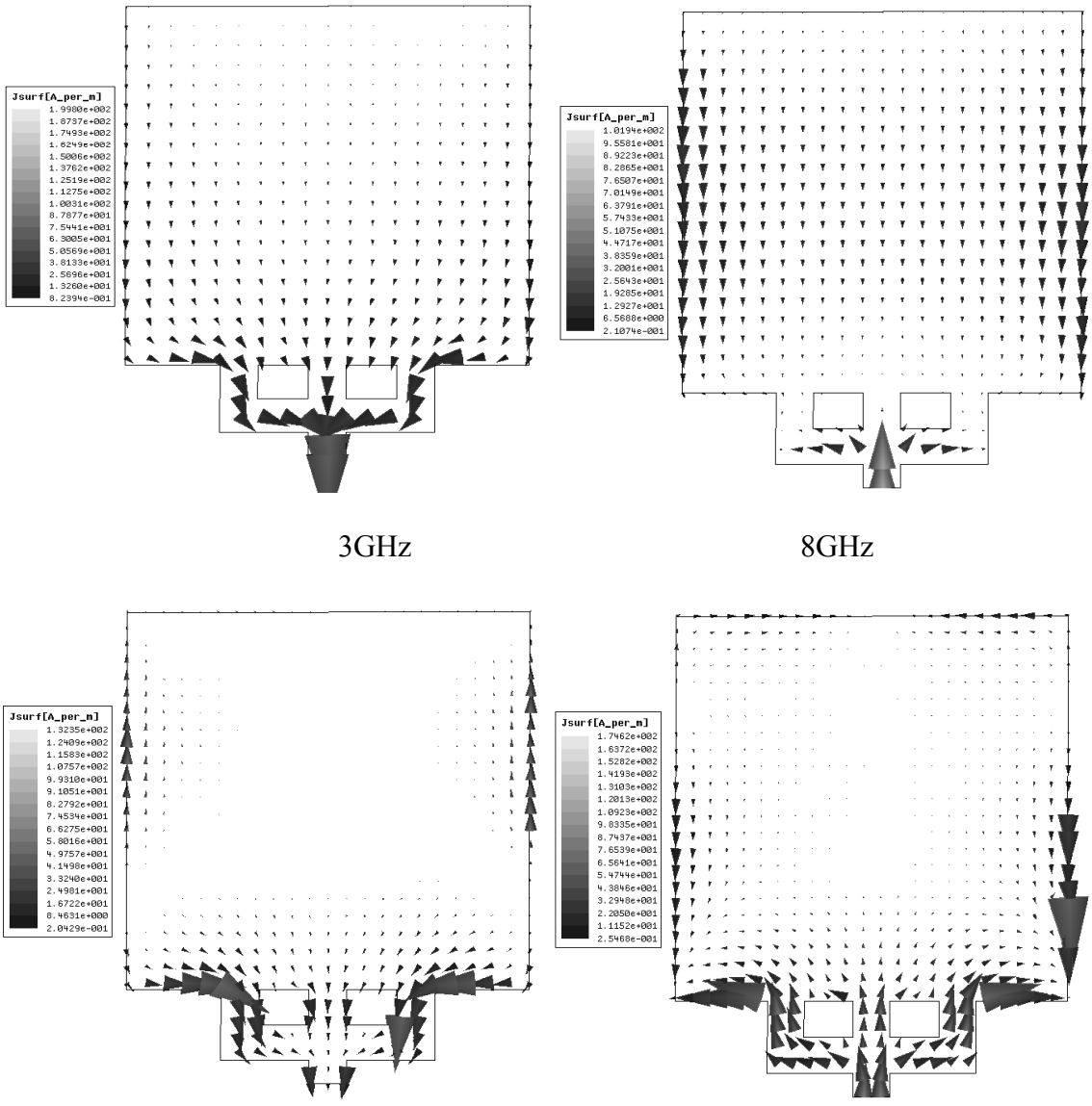

Fig. 3.4 Simulated surface current distributions of the square monopole S1 shown in Fig.3.1.a

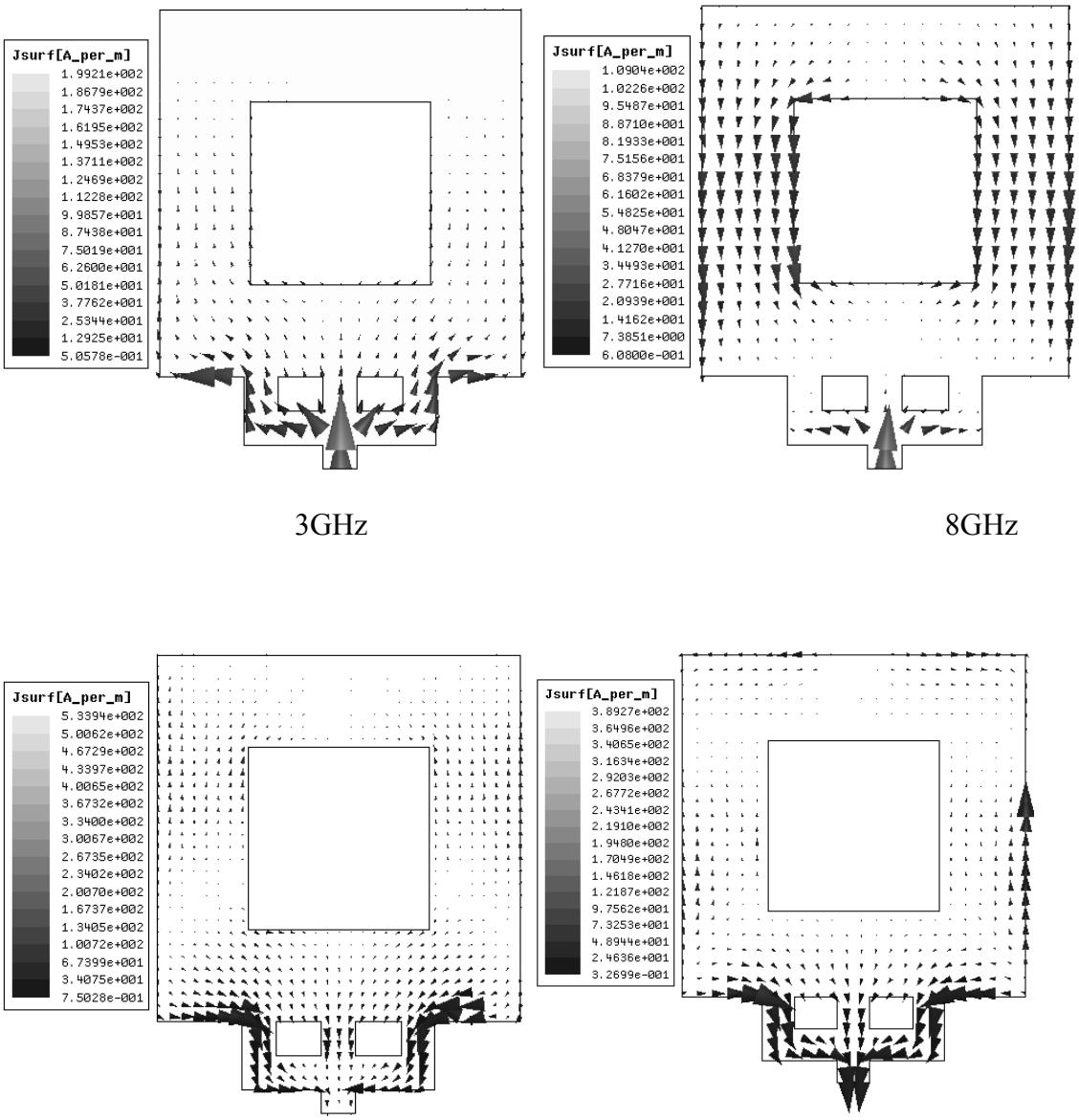

Fig. 3.5 Simulated surface current distributions of the square monopole with central metal removal, S3 shown in Fig. 3.1c at different frequencies

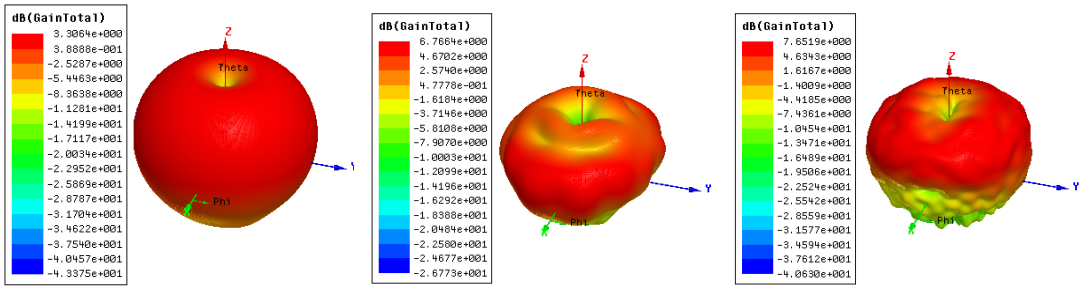

S3, F=3GHz S3, F=8GHz S3, F=13GHz

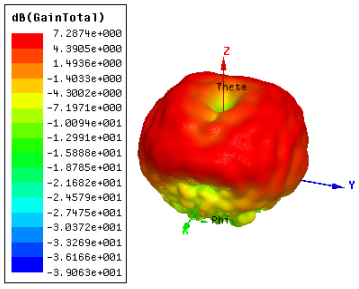

S3, F=15GHz

Fig. 3.6 3-D radiation patterns at different frequencies for the square monopole with central metal removal, S3 shown in Fig. 3.1c at different frequencies

3.4 Circular Monopole Antennas

The second antenna to be studied is the circular monopole antenna. For the sake of comparison between this antenna and the square one, the height of the antenna, the trident-feeding strip configuration and the ground plane dimensions are kept the same. Antenna dimensions are given in Fig.3.7a where t, h, and d are the same as in the square monopole of Fig. 3.1a. Fig.3.7a, b and c show different circular monopole configurations. In Fig.3.7b and Fig.3.7c, the same notch and central metal removal used with the square monopole are implemented. The removed metal here is a circle of radius 4 mm. It is noted from the return loss curves shown in Fig.3.7d that the notch has a minor effect on

the return loss of the circular antenna. On the other hand, the metal removal effect, which made a circular loop monopole, gives almost the same impedance bandwidth of 130.58%, [111].

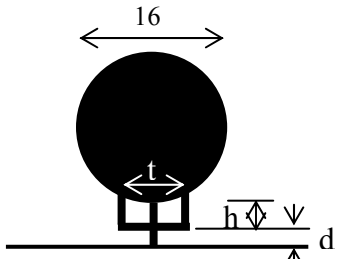

a) Circular monopole, C1

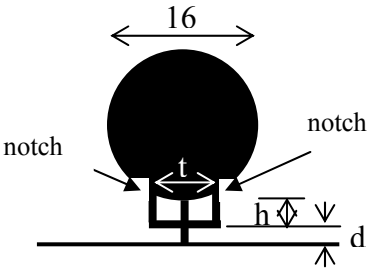

b) Circular monopole with notch, C2

Trident feeding strip. Width of each strip is 1.5mm

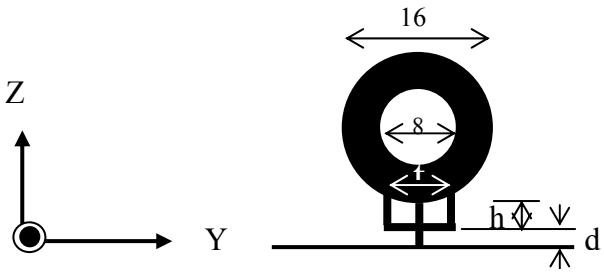

c) Circular monopole with metal removal, C3

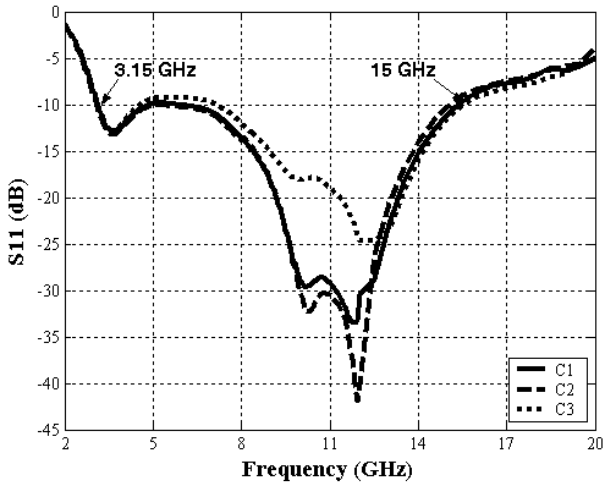

d) Return loss for circular monopole antennas C1, C2 and C3

Fig. 3.7 Circular monopole antenna with trident-feeding strip and different configurations. t = 7, d = 1, h = 3, and all strip widths are 1.5. Notch height =2, width=3.75. All dimensions in mm

The co and cross polarization radiation patterns are shown in Fig.3.8. The circular monopole antenna with different configurations shows an omnidirectional radiation pattern over the frequency band of operation. The circular loop monopole antenna shows a better omnidirectional behaviour at higher frequencies. While implementing notches

near the feeding region does not have a significant effect on the radiation patterns curves of these antennas. The surface current distributions are shown in Fig. 3.9, while the 3-D simulated radiation patterns are shown in Fig. 3.10.

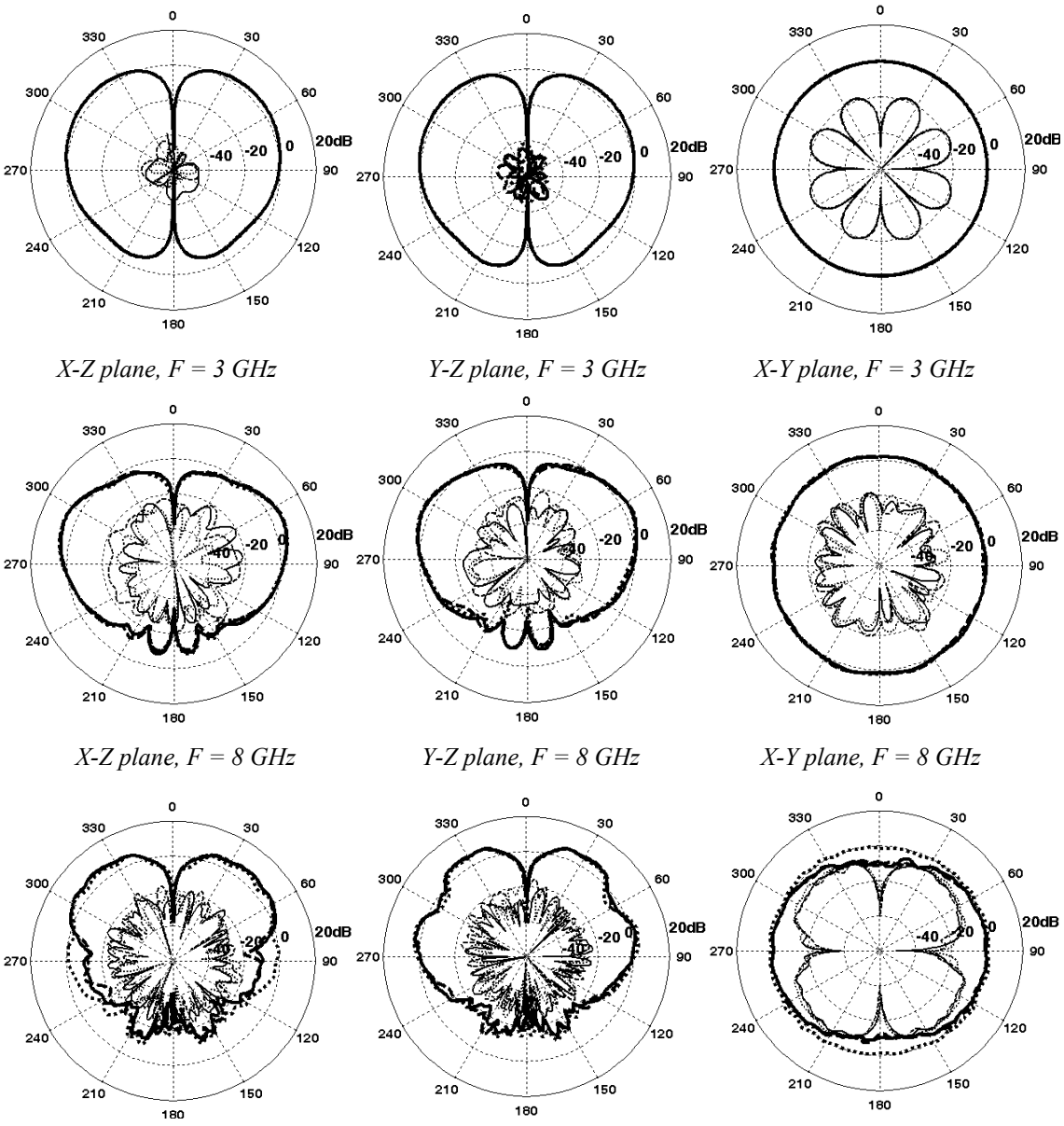

Fig. 3.8, Radiation patterns for circular monopole antennas C1, C2 and C3 of Fig. 3.7at different frequencies

$E_{\theta, C1}$ —— $E_{\theta, C2}$ – – $E_{\theta, C3}$ ····· $E_{\phi, C1}$ —— $E_{\phi, C2}$ - - - $E_{\phi, C3}$ ·····

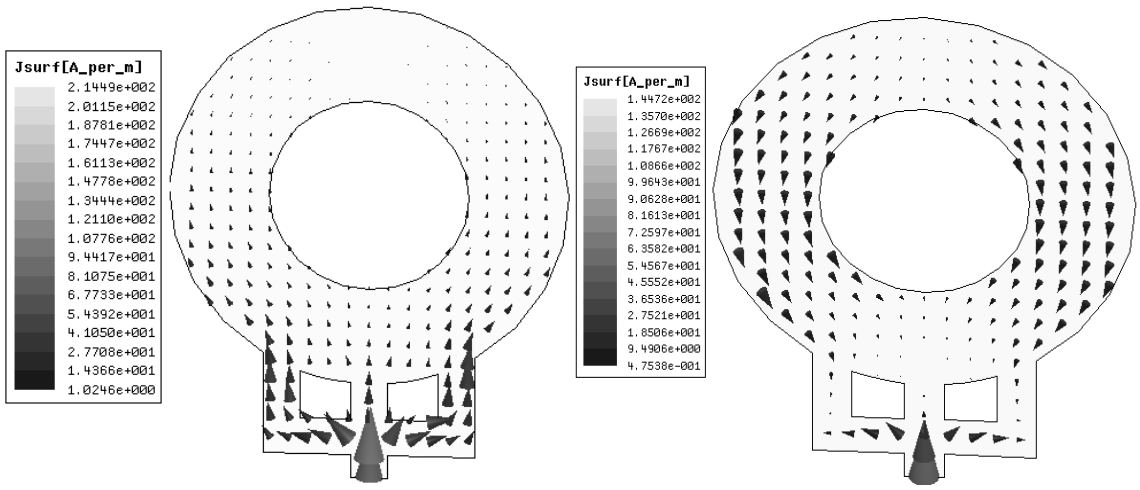

3GHz 8GHz

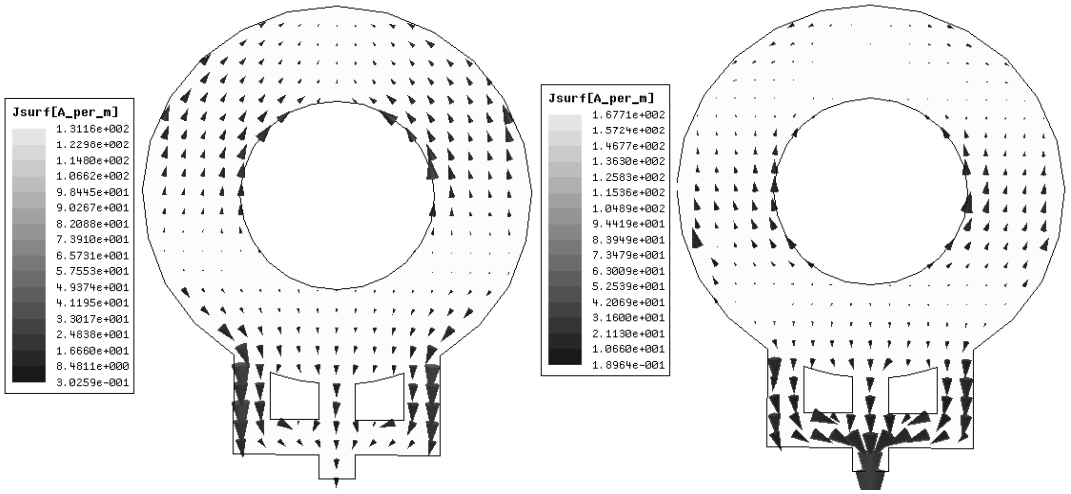

13GHz 15GHz

Fig. 3.9 Simulation surface current distributions of the circular monopole with central metal removal, C3 shown in Fig. 3.7c at different frequencies

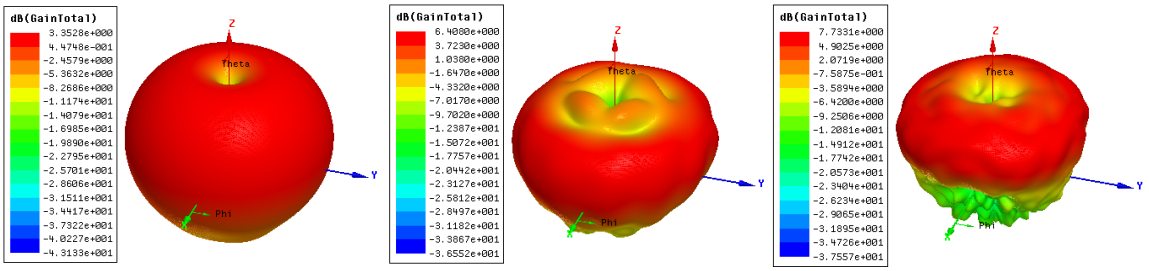

C3, F=3GHz C3, F=8GHz C3, F=13GHz

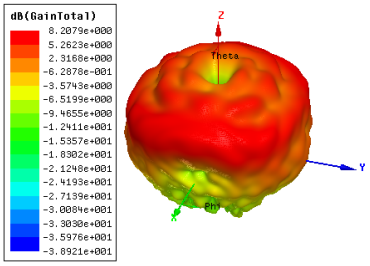

C3, F=15 GHz

Fig. 3.10 3-D radiation patterns of circular monopole with central metal removal, C3 shown in Fig. 3.7c at different frequencies

3.5 Elliptical Monopole Antennas

The third antenna to be studied is the elliptical monopole antenna with trident-feeding strip. The same feeding structure and ground plane used for square and circular monopole are used here. The height of the elliptical monopole, which is the minor diameter, is 16 mm and the major diameter is 20 mm as seen in Fig. 3.11. The notch implemented in the lower edge reduced the upper frequency limit from 16.5 to 15.5 GHz. On the other hand, removing elliptical metal, having minor and major axes of 8x10mm^2 from the centre of elliptical monopole, has increased the upper frequency limit to 17 GHz.

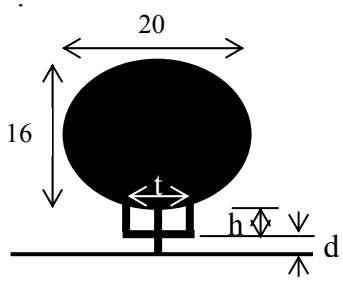

a) Elliptical monopole, E1

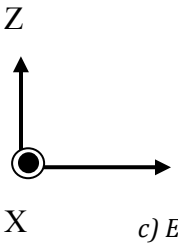

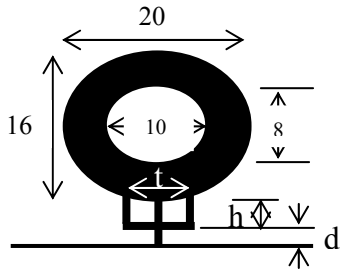

c) Elliptical monopole with metal removal, E3

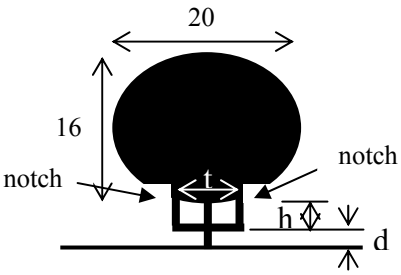

b) Elliptical monopole with notch, E2

Trident feeding strip. Width of each strip is 1.5mm

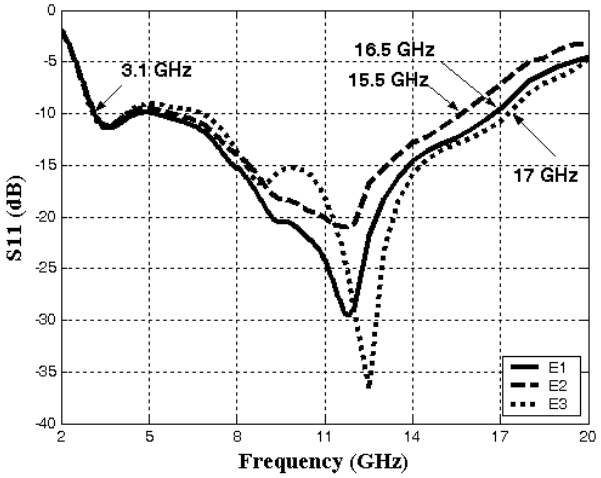

d) Return loss for elliptical monopole antennas E1, E2 and E3

Fig. 3.11 Elliptical monopole antenna with trident-feeding strip and different configurations. t = 7, d = 1, h = 3, and all strip widths are 1.5. Notch height =2, width=3.75. All dimensions in mm

Radiation patterns of the elliptical monopole antenna with different configurations at different frequencies are shown in Fig.3.12. All elliptical antenna configurations show omnidirectional patterns with low cross polarization. There is no significant effect of the notches or the metal removal on the radiation patterns at lower frequencies. While at higher frequencies, the elliptical monopole with metal removal has better omnidirectional

behaviour. The surface current distributions are shown in Fig. 3.13, while the 3-D simulated radiation patterns are shown in Fig. 3.14.

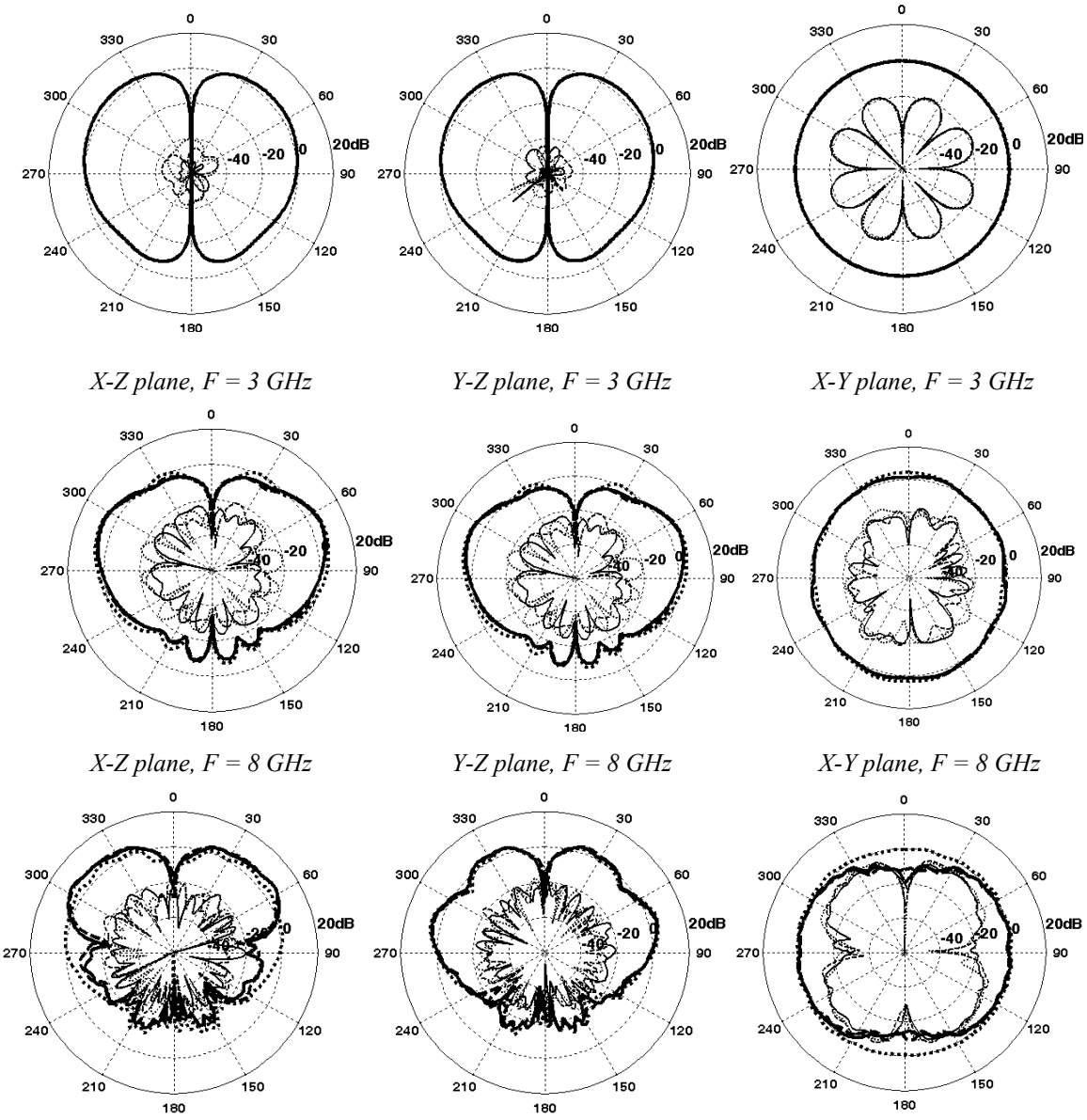

Fig. 3.12, Radiation patterns for elliptical monopole antennas E1, E2 and E3 of Fig. 3.11 at different frequencies

$E_{\theta,\,E1}$ —— $E_{\theta,\,E2}$ – – $E_{\theta,\,E3}$ ····· $E_{\phi,\,E1}$ —— $E_{\phi,\,E2}$ - - - $E_{\phi,\,E3}$ ·····

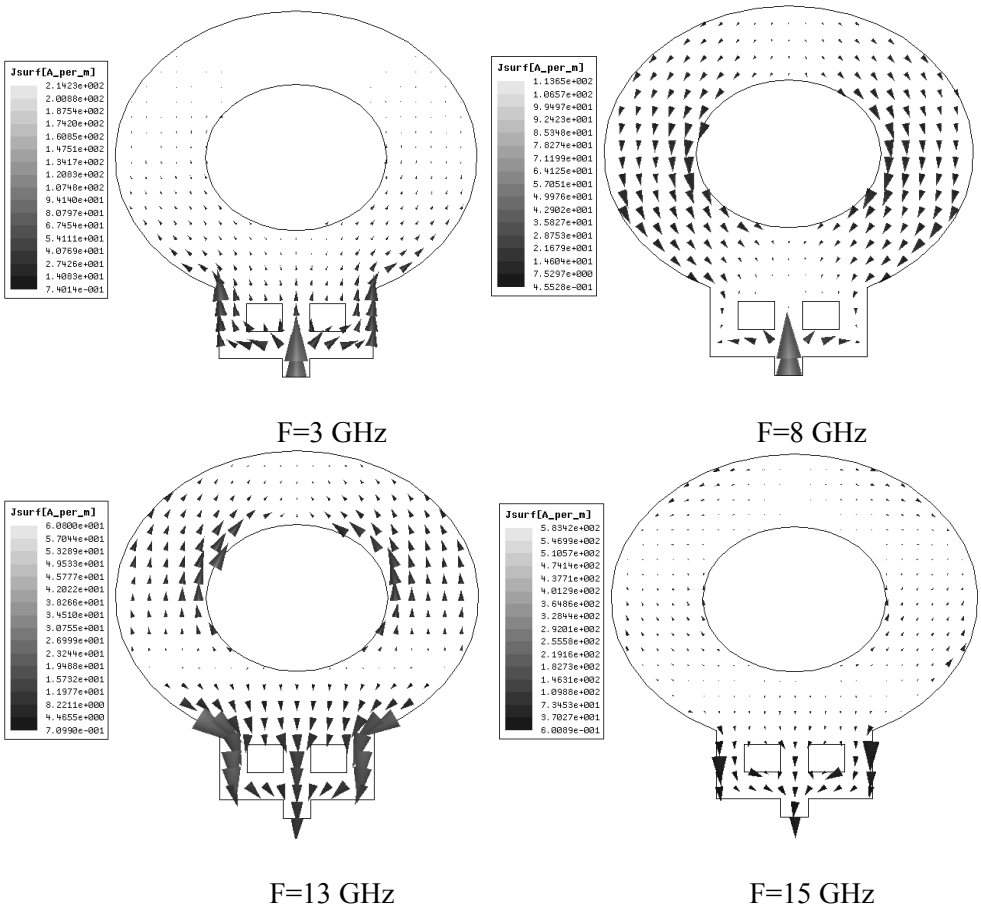

Fig. 3.13 Simulated surface current distribution of the elliptical monopole with central metal removal, E3 shown in Fig. 3.11c at different frequencies

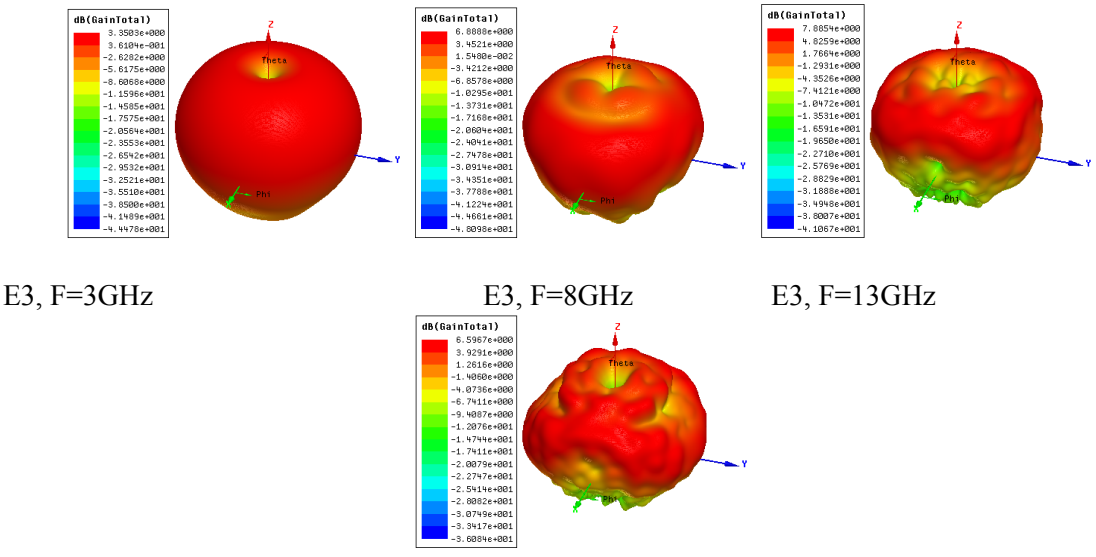

Fig. 3.14 3-D radiation patterns of elliptical monopole with central metal removal, E3 shown in Fig. 3.11c at different frequencies

3.6 UWB Monopoles with Resonant Features

Since, other services already operate within the UWB band. To eliminate the interference, a common approach is to implement certain resonant features in the antenna structure, like half wavelength slots at the centre frequency of the stop-band, to cause resonances and current concentration around the features. This will eliminate radiation at the required frequencies. It is worth mentioning that the main function of the resonant feature is to prevent radiation within the stop band without affecting the antenna characteristics in the pass band. This effect can be seen in the return loss or VSWR curves of the antenna by increasing the impedance mismatch level and also can be seen in the radiation pattern by affecting the omnidirectional behaviour of the antenna. The current distribution plots can also show this effect by having current concentration around the slot at the stop-band. Another important and herein observed characteristic of the antenna that might be affected, is the phase centre profile of the antenna. The effect of including such features on the antenna phase centre will be discussed in chapter 4 of this thesis. The relation between antenna VSWR and its impedance mismatch is shown in Fig. 3.15. This impedance mismatch is proportional to the reduction in gain of this antenna. The required impedance mismatch level will depend on the application area. However, the more the impedance mismatch in the stop-band, the less interference this antenna will have with other existing technologies in this band.

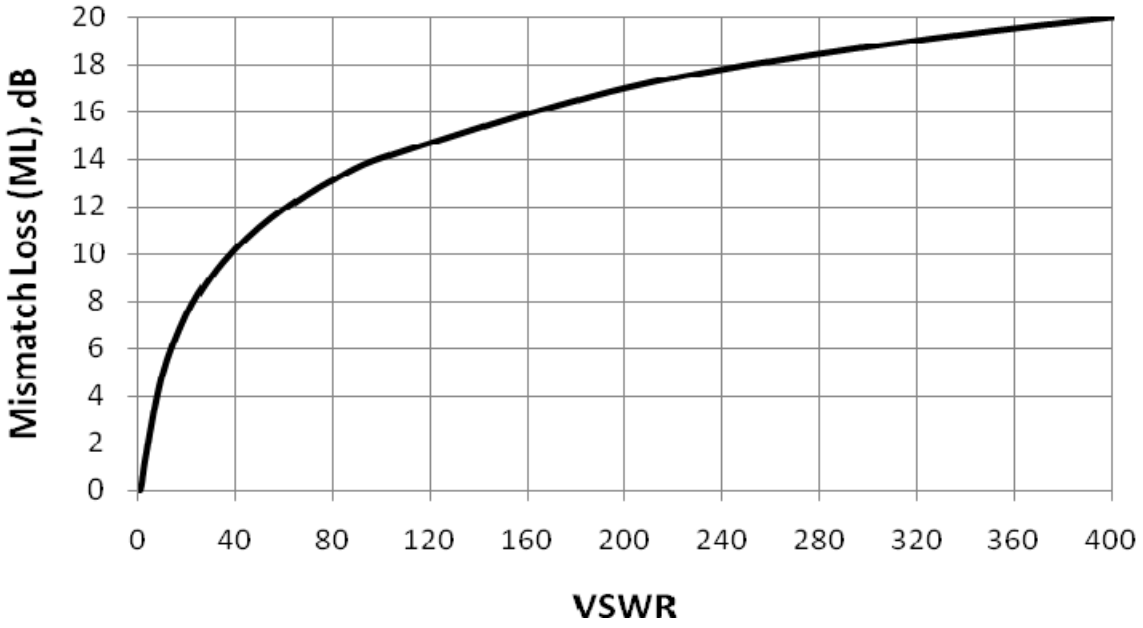

Fig. 3.15 Impedance mismatch of an antenna as a function of its VSWR

3.6.1 Band-stop Feature Parameters

Three important control parameters are involved when designing a band-stop feature, Fig. 3.16. The first parameter is the length of the slot which should be half wave length at the centre frequency of the stop-band. The second parameter is the width of the slot which determines the bandwidth of the stop-band. The third parameter is the position of the slot inside the radiator which contributes for determining the stop-band bandwidth and its centre frequency. The effectiveness of the stop-band feature is defined by how this feature will block the antenna radiation or receiving capability. In this section, UWB antennas with different stop-band features are studied to increase the mismatch level in the stop-band [112].

3.6.2 Position and Width of the Slot

Current distributions on the radiator surface control its radiation patterns. When implementing a slot inside a radiator, the current distribution is affected. One way to look at the problem is to consider three frequency regions. The first one is the stop-band one where no radiation is required. The second one the region right close to the first one where the effect of including slot on this region needs to be minimized. The third region is the pass band one where the slot should have no effect on the radiation in this region. To have preliminary results that will help in modeling this type of antennas, different slots with the same length and width, but at different positions in the radiator, are implemented. The goal is to see whether a new control parameter can be determined. Different antenna designs are used for this study to generalize this concept. Fig. 3.16 shows the same antenna design of section 3.3, Fig. 3.1a after including a 27mm U-slot shape (≅λ/2 @ f=5.5 GHz) inside the radiator. The width of the slot is kept constant at 1mm. The parameter of study here is the position of the slot along the Z-axis.

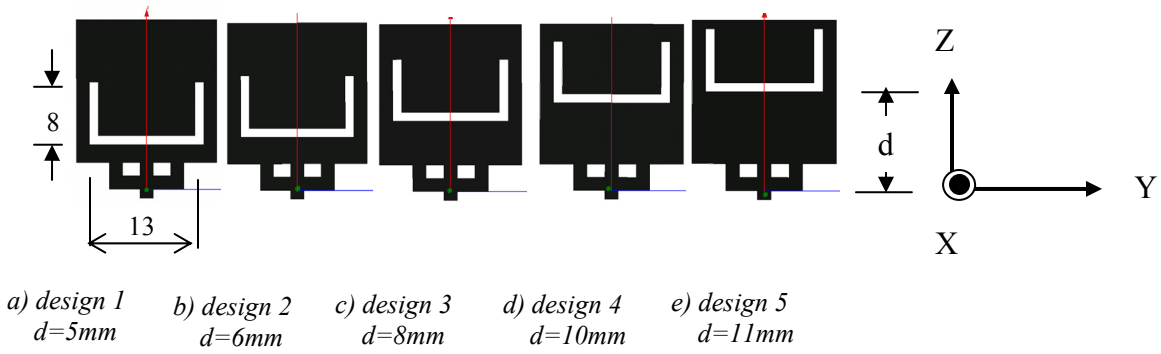

Fig. 3.16 UWB monopole with U-shape slot at different positions (d). Antenna has the same parameters as Fig. 3.1a. The length of the U-slot is 27 mm, width =1mm

The VSWR curves are shown in Fig. 3.17. As can be seen, the bandwidth of the stop-band is not affected by the change of the slot position. However the centre frequency of the stop-band decreases with the movement of the slot away from the feeding structure. It is worth noting that there should be a minimum distance between the slot and the feeding structure, in order not to affect the pass band region of the UWB antenna. Regarding the mismatch level within the stop-band, it increases with the movement of the slot toward the feeding structure. By increasing the slot length to 29mm, in design1 at Fig. 3.16a, a considerable mismatch increase in the stop-band is achieved while maintaining the centre frequency of the stop-band at 5.5 GHz. Fig. 3.18 shows the VSWR curve of such a design.

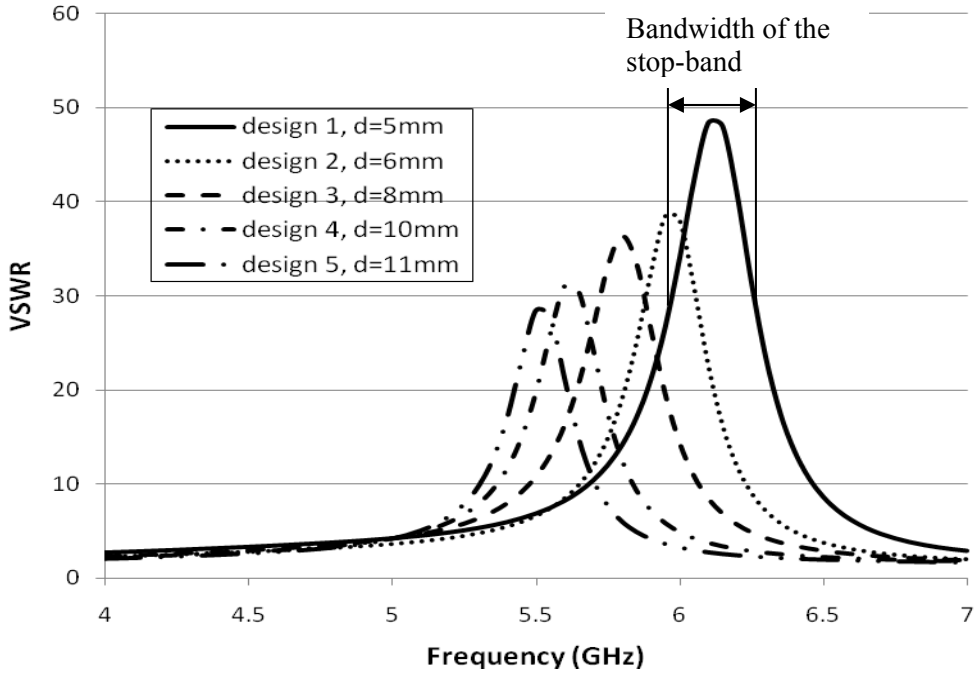

Fig. 3.17 VSWR for the antenna designs of Fig. 3.16 as a function of d, where d is the distance from Z=0 to the bottom of the slot. Slot length is 27mm in all designs

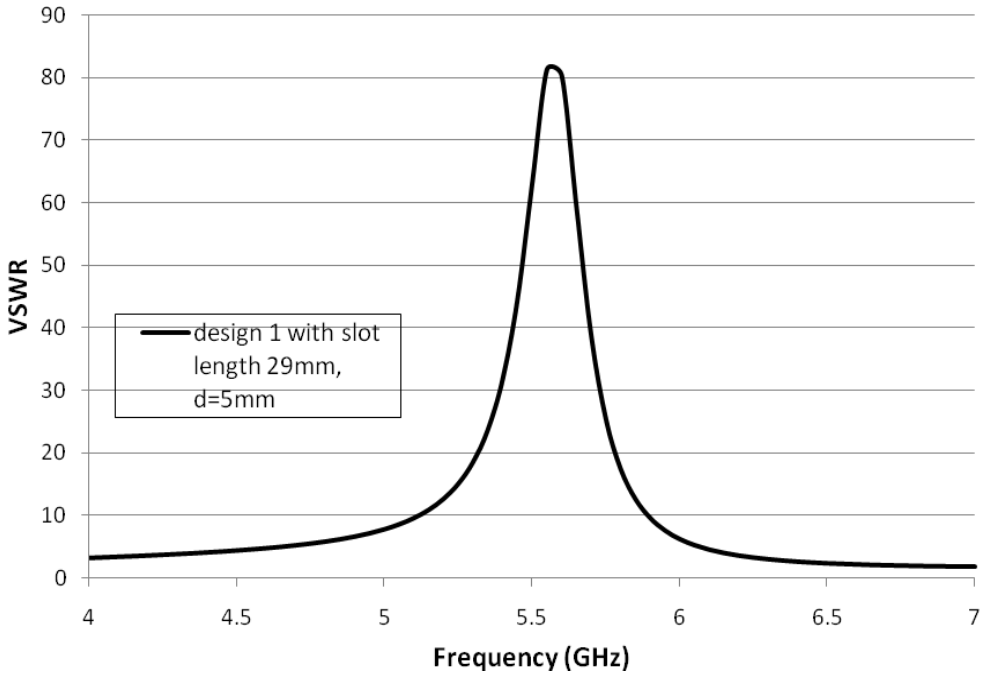

Fig. 3.18 VSWR for the antenna design of Fig. 3.16a with slot length =29mm and d=5mm.

As can be seen from Fig. 3.18, the VSWR at the band-stop centre frequency is about 80 which give an impedance mismatch loss of 13dB. This in turn means that the reduction in gain for this antenna in the stop-band will be about 13 dB.

To further increase the impedance mismatch in the stop-band, a double slot with the same length is used. The novel antenna design with double slot is shown in Fig. 3.19. The optimum length of each is 27 mm. The optimum width of each slot is 1mm. The lower slot is the same as that of Fig. 3.16a, with distance d=5mm from plane Z=0. The optimum separation between the horizontal part of the upper slot and lower one is 1mm. The optimum separation between the adjacent vertical sides of the slots is 0.5mm. Fig.3.20 shows the VSWR curves for both antennas with single and double slots. As can

be seen, the antenna with double slot configuration has a VSWR of about 158 at the stop-band centre frequency. This means the impedance mismatch of this antenna is about 16 dB with 3 dB more than that of a single slot configuration.

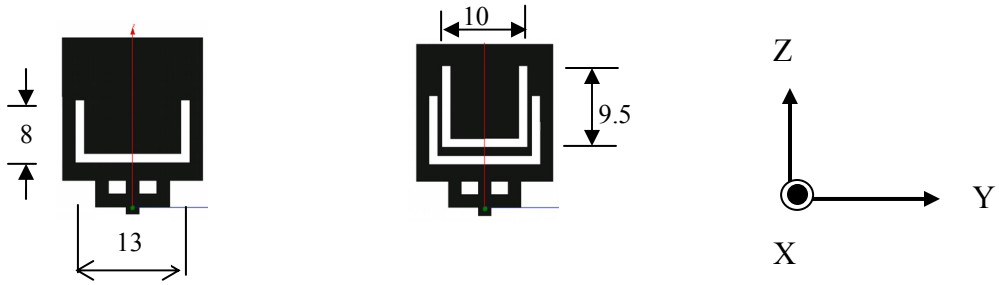

a) single slot *a) double slot*

Fig. 3.19 UWB monopole antenna with single and double slots. Length of slot is 27 mm. Width of each slot is 1mm. Lower slot is the same as that of Fig. 3.16a with distance, d=5mm from plane Z=0. Separation between horizontal part of the upper slot and lower one is 1mm. Separation between the adjacent vertical sides of the slots is 0.5mm

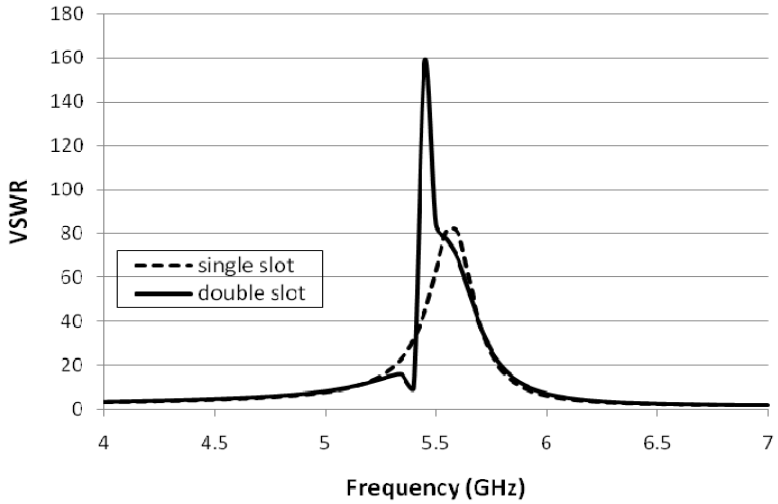

Fig. 3.20 VSWR curves for UWB antenna with single and double slots of Fig. 3.19 along with current distributions at the stop-band centre frequency

Fig. 3.21a shows current distributions at the band-stop centre frequency, while Fig. 3.21b shows the maximum measured radiation pattern of the antenna at the same notch frequency at different principle planes. As can be seen, the loss in gain at the notch

frequency is about 20dB at the three planes $\phi=0^o$, 45^o and 90^o for all values of θ from -180 to 180^o.

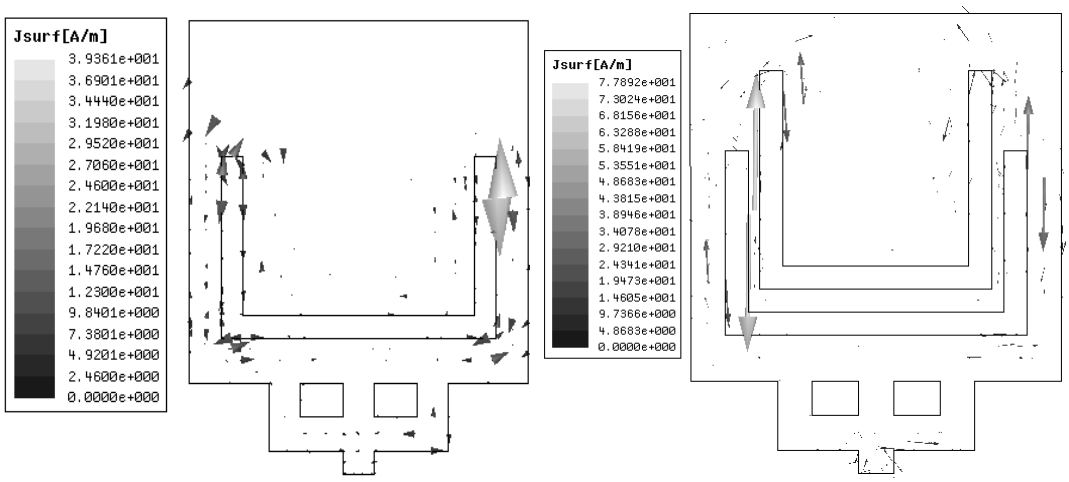

Fig. 3.21a Simulated current distributions at notch frequency of Fig. 3.19

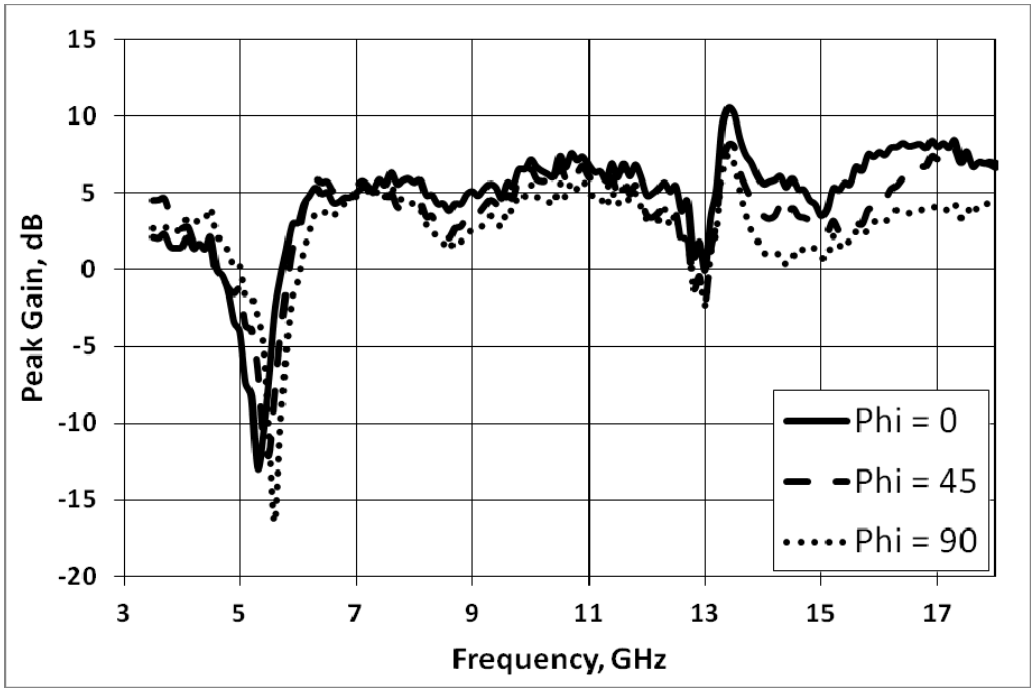

Fig. 3.21b Measured peak gain of the square monopole with 2-U slots shown in Fig. 3.19 at different principle planes

3.6.3 Different Slot Shapes

In this section, the effect of using different slot shapes is studied. One reason is to have a new degree of freedom when designing these antennas over the bandwidth of the stop-band. The other important reason is to study the effect of using different slot shapes on the phase centre behaviour of these antennas. The first reason will be discussed here, while the other one will be discussed in details in chapter 4 of this thesis. The coming figures show both antenna designs and effects of having different slot shapes on the stop-band parameters. Fig. 3.22 shows antenna design with different slot shapes. The antenna design is the same as Fig. 3.1a. All slots have the same lengths of 12mm and widths of 0.5 mm.

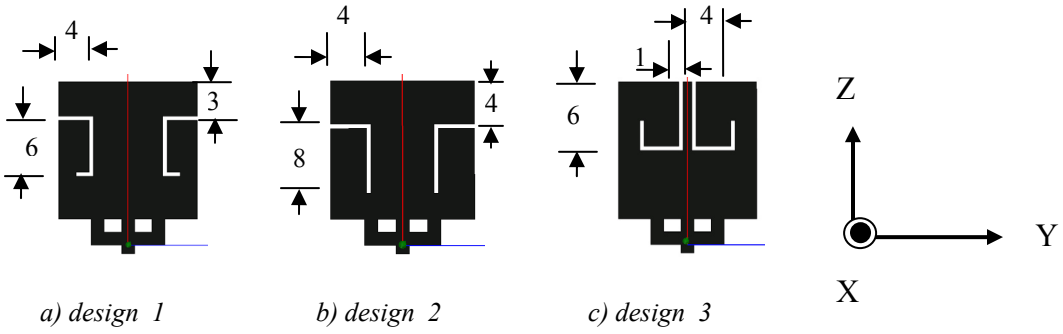

a) design 1 *b) design 2* *c) design 3*

Fig. 3.22 UWB monopole with different slot shapes. Antenna has same parameters of Fig. 3.1a. The length of the all slots is 12 mm, width =0.5mm

As can be seen from Fig. 3.23, the change of slot shape controls the bandwidth of the stop band and also the mismatch level.

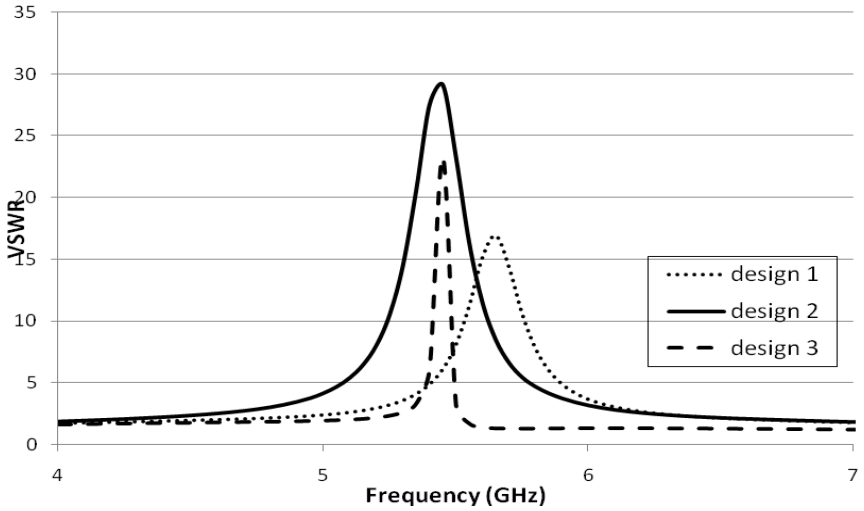

Fig. 3.23 VSWR for the antenna designs of Fig. 3. 22

3.6.4 Control of the Mismatch by Two Spiral Slots with Different Orientations

Another new parameter discussed in this section is the coupling effect between the two slots on creating and controlling the stop-band behaviour of UWB monopole antennas. Antenna designs with two slots coupled at different orientations and distances are studied. The goal is to have a new control parameter and degree of freedom when designing such antennas. The square monopole antenna with trident-feeding introduced in section 3.3, is used to illustrate this concept.

Spiral-slots are introduced in the structure of the square monopole antenna to have a stop band at different frequencies. The spiral-slot is used because the structure of the spiral allows minimizing the physical size of the slot, to act effectively at the desired frequencies. Also, the combination of more than one spiral with different orientations can add another degree of freedom to the notches design process. Initially, a rectangular-

spiral slot is implemented at the center of the square monopole antenna as shown in Fig. 3.24. The spiral length is 27mm and the width of each tern is 0.5mm. The spacing between the turns is kept constant at 0.5mm, and the widths of the spiral elements are uniform.

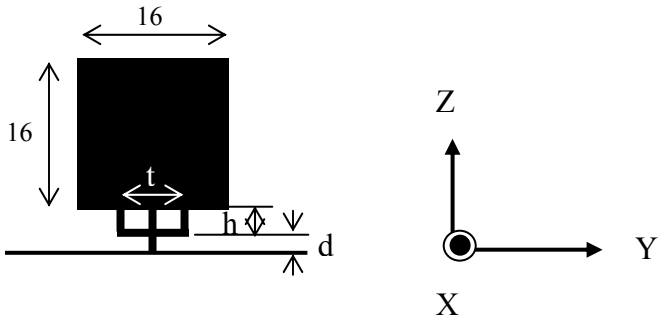

a) Square monopole antenna with trident-feeding and dimensions given in Fig. 3.1

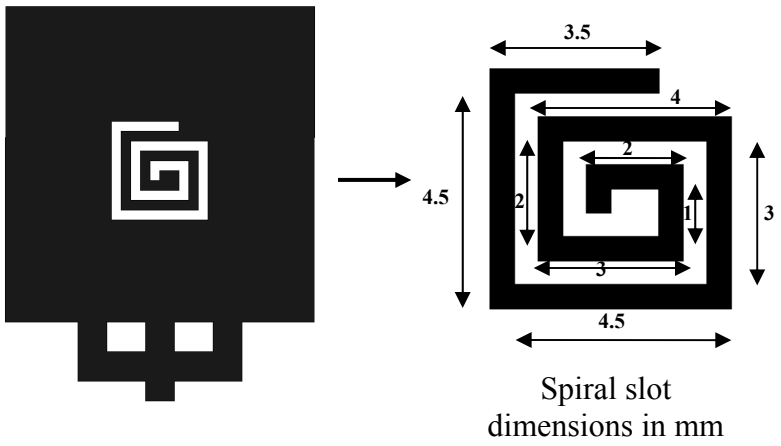

b) A spiral slot implemented at square centre

Fig. 3.24 Square monopole antenna with dimensions given in Fig. 3.1

Fig. 3.25 shows the effect of moving the spiral-slot along the Z-axis on the impedance mismatch level within the stop-band. The more the spiral is closer to the feeding point, the better the stop-band efficiency. By moving the spiral slot 7.8mm from the square centre towards the feeding, we can have impedance mismatch of 15.5 dB.

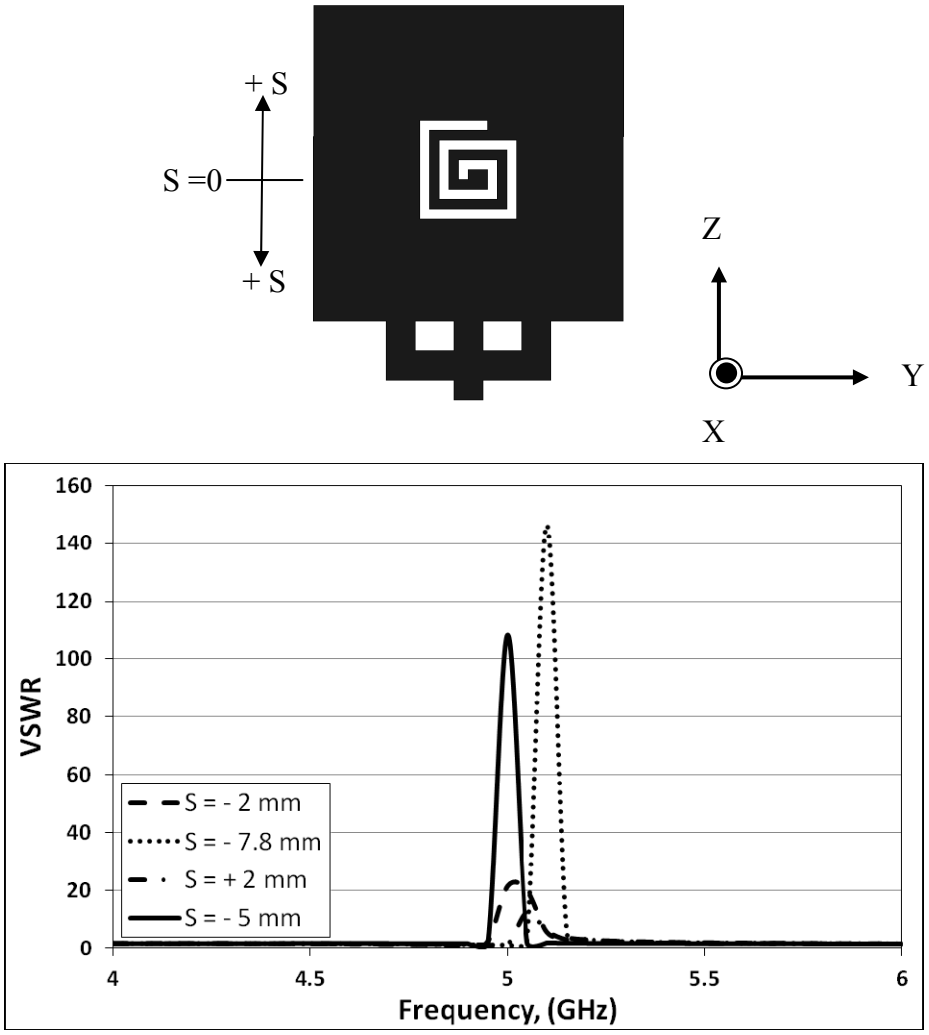

Fig. 3.25 VSWR curves of antenna in Fig. 3.24 with the movement of the spiral-slot Positive distance means upward movement while negative distance means downward movement. Antenna dimensions are given in Fig. 3.1. The spiral length is 27mm

The effect of using two identical spiral-slots on the VSWR of this antenna is also studied. Two spiral-slot orientations are studied, one with the two spirals are on top of each other, and the other when they are side by side. To show this concept, two identical spiral-slots with parameters given in Fig. 3.24, are implemented on top of each other, inside the square monopole radiator, given that the two spirals have different direction of rotation. This new design gives rise to a new parameter in antenna design. The coupling between the two spiral-slots controls both the centre frequency of the stop-band and the impedance mismatch level. Fig. 3.26 shows the effect of using two spiral-slots, on the impedance mismatch levels. It is found that an impedance mismatch level of 18 dB can be achieved when the lower slot is at distance of 4.2mm from the bottom of the square radiator and the vertical separation between the two slots S1= 0.9 mm. The bandwidth of the stop-band of this antenna can be increased by increasing the width of the spiral slot.

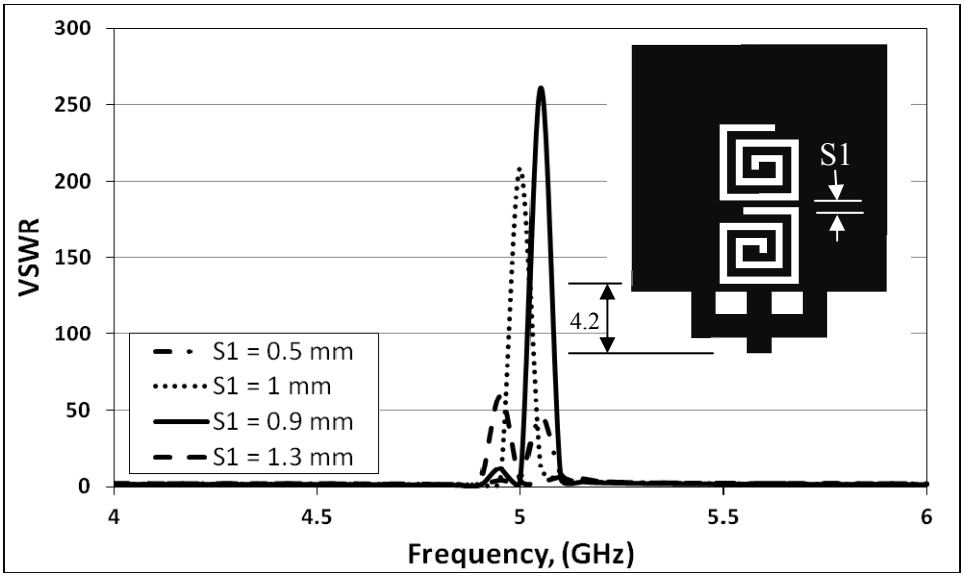

Fig. 3.26 VSWR curves of antenna with spiral dimensions given in Fig. 3.24 with different separation distance, S1 between the two spiral-slots

Two side by side spiral slots can also be used to control both the impedance bandwidth and the centre frequency of the stop-band. The horizontal separation between the two slots S2, affects both the bandwidth and centre frequency of the stop-band. The two spiral slots are placed around the Z-axis, and at a distance of 4.5 mm from the bottom of the square radiator. The design parameters of each spiral-slot are the same as that appears in Fig. 3.24. The VSWR curves for the antenna with the two side by side spiral-slots with different separation distance S2 between them are shown in Fig. 3.27. The distance between both spiral-lots and the bottom of the square radiator is fixed at 4.5mm. The maximum impedance mismatch achieved in this case is about 14dB when the separation between slots S2 = 0.4 mm.

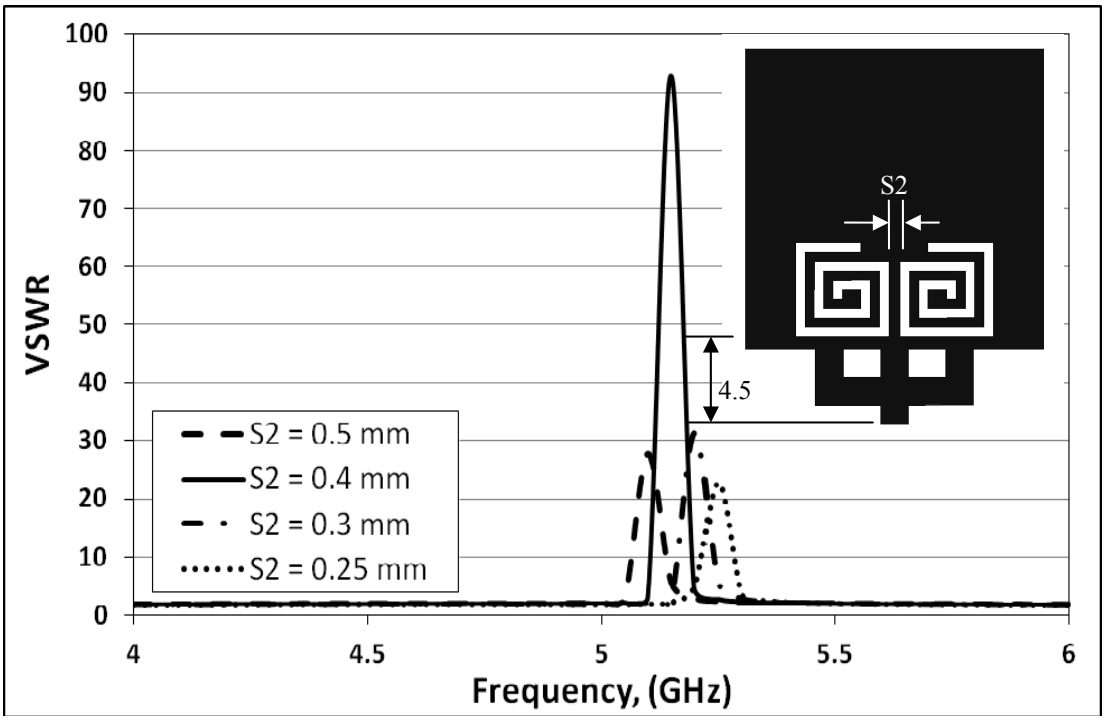

Fig. 3.27 VSWR curves of antenna with spiral dimensions given in Fig. 3.24 with different separation distance, S2 between the two spiral-slots

As can be seen from Fig. 3.27, the maximum VSWR of 91 is achieved when the separation distance between the two-spirals, S2 is 0.4mm. This VSWR value corrosponds to a 13.5 dB impedance mismatch loss. To further increase the mismatch loss of this design, the separation distanse between the two spiral-slots, S2, is kept constant at 0.4 mm, and the distance between the two spiral-slots and the bottom of the monopole, S3 is optimized. Fig. 3.28 shows the VSWR curves of the square monopole with different distance, S3 between the two spiral-slots and the bottom of the monopole. The maximum VSWR obtained is 350 which corrosponds to an impedance mismatch loss of 19.5 dB. This mismatch loss value is acheived when the distance between the two spiral-slots and the bottom of the monopole, S3 =4.2 mm and separation distance between the two spiral-slots, S2 = 0.4 mm.

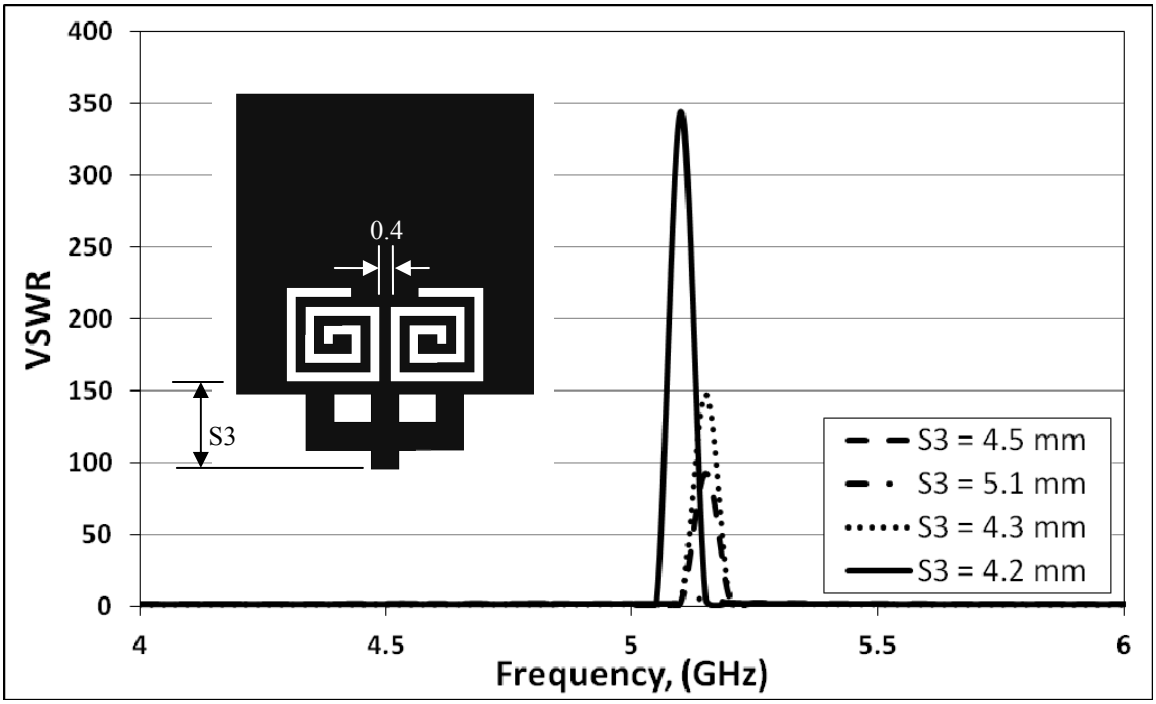

Fig. 3.28 VSWR curves of antenna with spiral dimensions given in Fig. 3.24 with different separation distance, S2 between the two spiral-slots

3.7 Ground Plane Effect on the Performance of UWB Monopole Antennas

Throughout the study done in this chapter, the ground plane chosen for all monopole antennas was a 120x120 mm^2 square metal plate (1.2λ @ lower frequency edge of 3 GHz). The effect of a ground plane with this size appears in the results of the square, circular and elliptical monopole antennas discussed before. It was shown that by using a 16mm monopole antenna, an impedance bandwidth of 3 GHz to 15 and 19.5 GHz can be obtained. The radiation patterns of these antennas are monopole-like patterns with the maximum radiation in the E-plane around $\theta=60^o$, and an omnidirectional radiation pattern in the H-plane. Although the studied antennas so far satisfied the UWB communication applications, regarding the impedance bandwidth and radiation patterns, the small height of the antenna over the ground plane affects the lower frequency band of operation. Also, the size of the ground plane was fixed throughout the study, with a total area of 120x120 mm^2 (Ground side length = 1.2λ @ lower frequency edge of 3 GHz). To further investigate the performance of such monopole antennas, the size of the ground plane was modified and different slots were implemented to study their effects on the antennas performance. The square monopole antenna with a trident feeding strip designed in section 3, is used to illustrate the effect of the ground plane size on its performance. Simulation results indicate that by optimizing the ground plane size of UWB monopole antennas, the lower frequency edge of operation can be reduced from 3 GHz to 2.1 GHz. But this reduction in the ground plane size will have an effect on the radiation patterns of the antenna. It is found that, by implementing a square slot in the original ground plane, the frequency reduction in the lower edge of the impedance bandwidth can be maintained as well as the wanted radiation patterns. The radiation patterns are monopole-like

patterns, with the peak gain shifted to around θ = 60° above the horizon, because of the existence of the finite ground plane. Fig. 3.29 shows the square monopole antenna used in this study, while Fig. 3.30 shows the return loss curves for this antenna with different ground plane sizes.

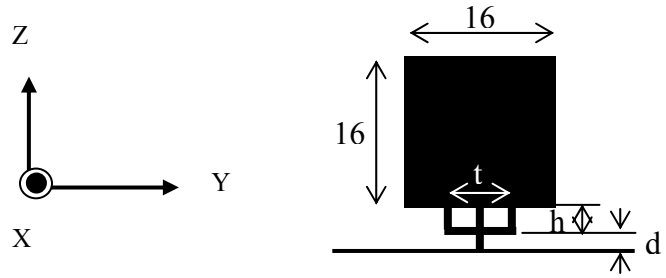

Fig. 3.29 Square monopole antenna with trident-feeding strip and different ground plane sizes. Optimized parameter values are: t=7mm, h=3mm, d=1mm, and all strip widths = 1.5mm

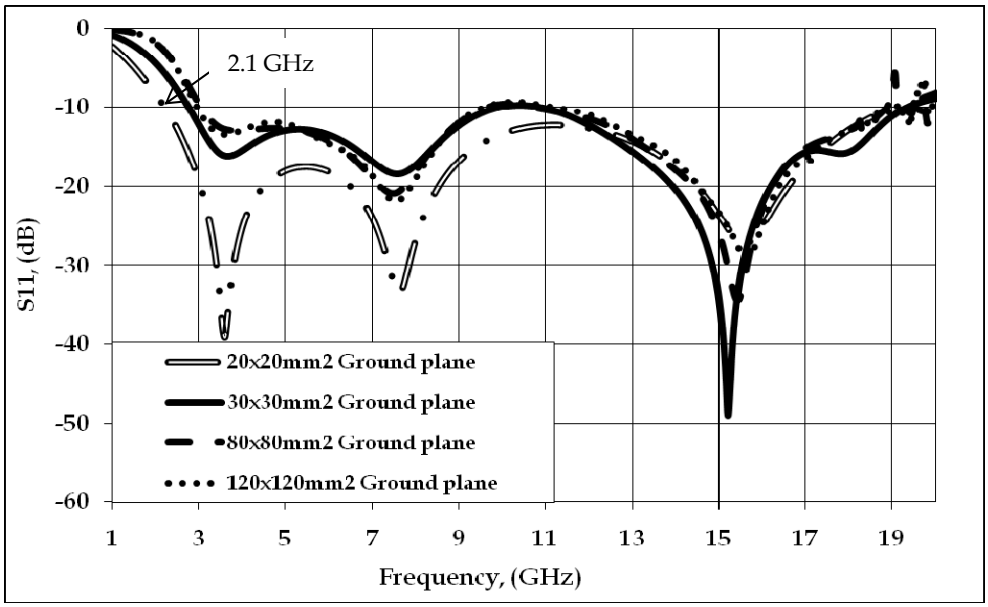

Fig. 3.30 Return loss curves for the square monopole antenna in Fig. 3.29 with different ground plane sizes

As can be seen from Fig. 3.30, the square monopole antenna with 20x20mm^2 square ground plane (Ground side length = 1.2λ @ lower frequency edge of 3 GHz) has a UWB impedance bandwidth that starts at 2.1 GHz. This reduction of the lower edge of the bandwidth from 3 to 2.1 GHz is acheived without increasing the monopole height. In all cases, the higher edge of the impedance bandwidth extends to almost 20 GHz. To show the effect of the ground plane size on the radiation patterns, they are presented in Fig. 3.31, in E and H-planes at different frequencies of 3, 8 and 13 GHz, with a 20x20mm^2 ground plane. While in section 3, Fig. 3.2 shows E and H-plane curves for the same antenna and same planes, but with a 120x120mm^2 ground plane. As can be seen from Fig. 3.31, Fig. 3.2 and other simulated results, the effect of the small ground plane size is realized at lower frequencies. But, the gain is reduced at the maximum angle of radiation. Another attempt is made to further decrease the ground plane size and compensate for the effect of its small size on the radiation patterns. Square slots of different widths and at different distances from the origin are introduced within the ground plane. The study showed no significant effect on the radiation patterns of the antenna. However, by having a 20x20mm^2 small ground plane and increasing the height of the antenna to only 30 mm, the lower frequency edge was reduced from 2.1 to 1.4 GHz, and the gain was increased in the direction of maximum radiation. Fig. 3.32 shows the return loss curve for the antenna of Fig. 3.29, but with a height of 30 mm, while Fig. 3.33 shows its E and H-plane patterns at different frequencies and different planes.

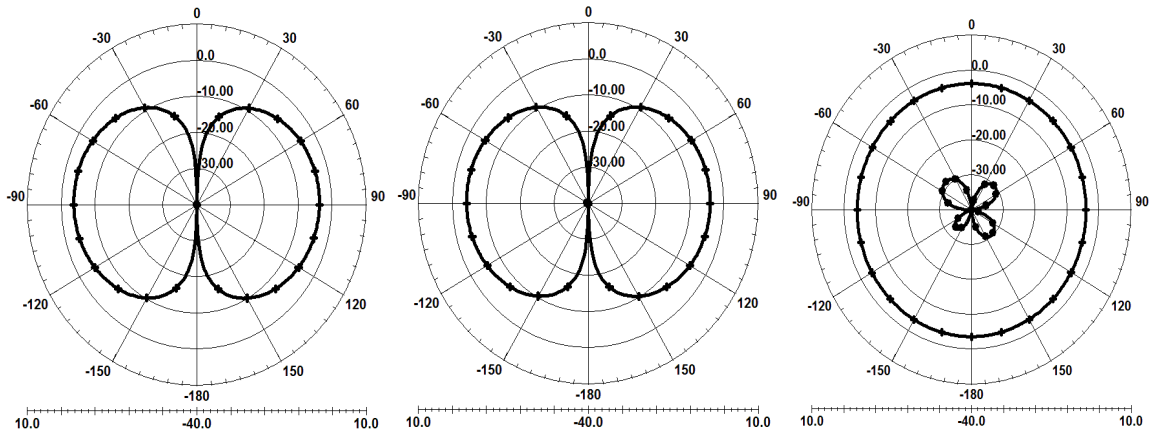

f=3GHz: *X-Z* *Y-Z* *X-Y*

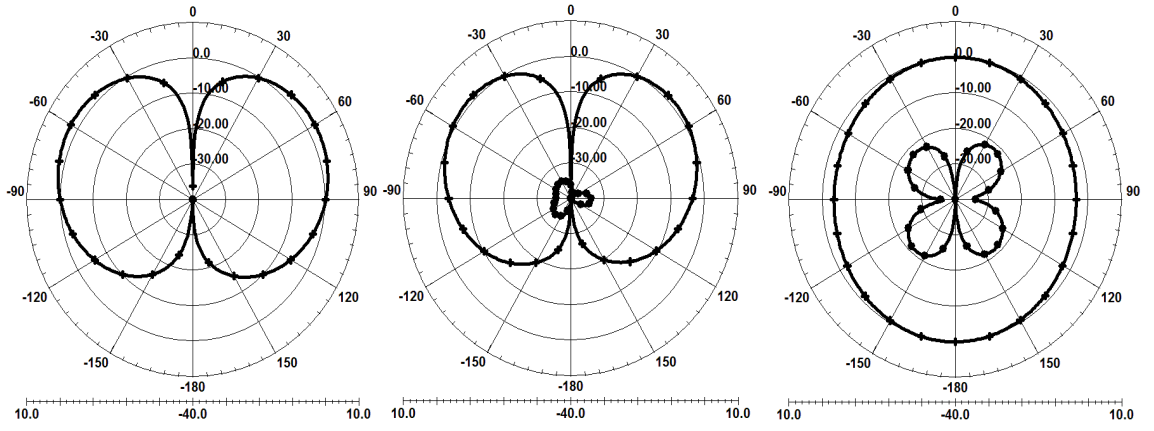

f=8GHz: *X-Z* *Y-Z* *X-Y*

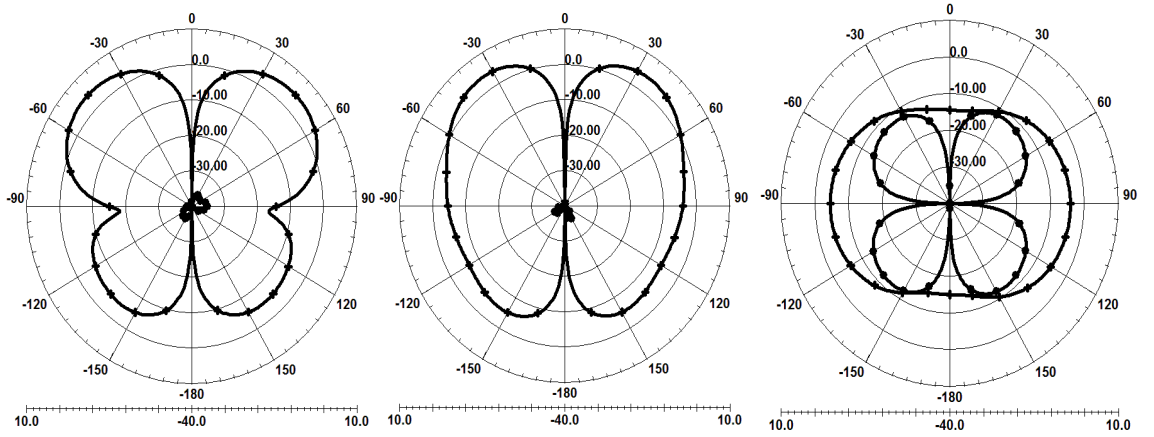

f=13GHz: *X-Z* *Y-Z* *X-Y*

Fig. 3.31 Radiation patterns for the antenna shown in Fig. 3.29 with 20x20 mm^2 ground plane

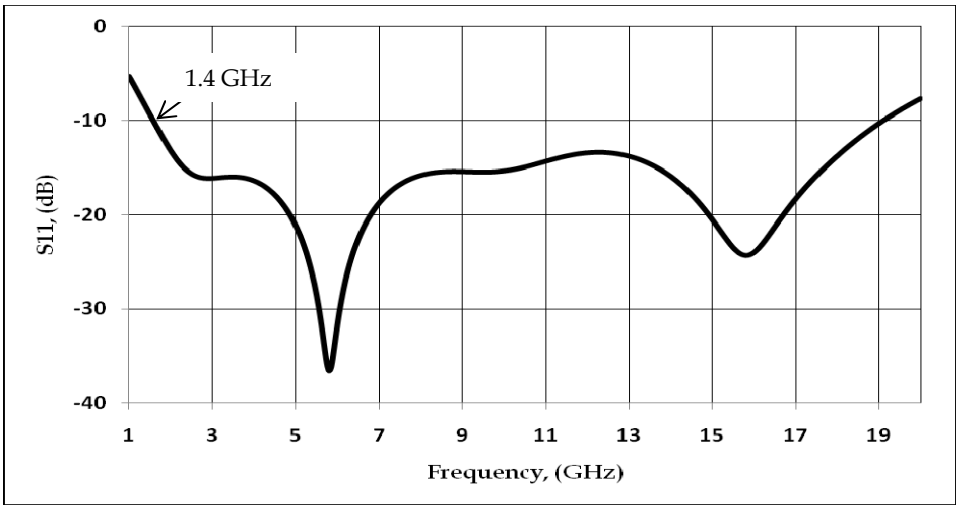

Fig. 3.32 Return loss curve for antenna in Fig. 3.29 with total height of 30mm

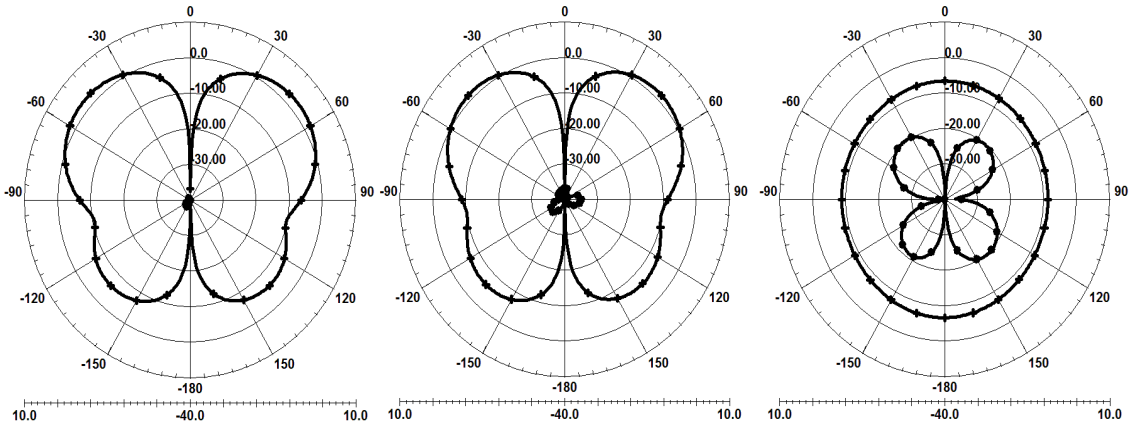

f=8GHz: *X-Z* *Y-Z* *X-Y*

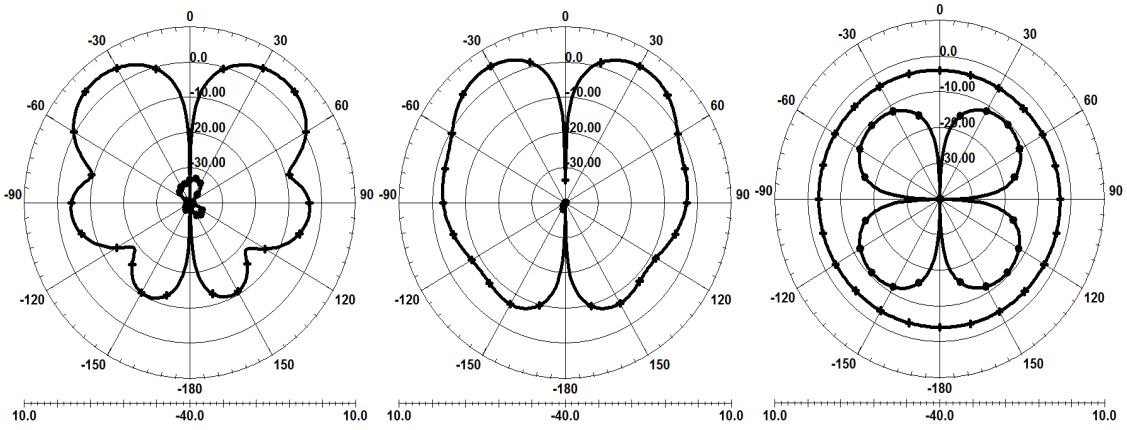

f=13GHz: *X-Z* *Y-Z* *X-Y*

Fig. 3.33 Radiation Patterns for the antenna with return loss curve shown in Fig. 3.30, with 20x20 mm^2 ground plane and 3mm antenna height

This study showed that, the ground plane size can be reduced to 20x20 mm^2 to reduce the lower frequency limit to 2.1 GHz, with some deterioration in its radiation patterns. Also the total height of the antenna can be increased from 20mm to 30 mm, to compensate for the change in the radiation patterns and to further reduce the lower frequency edge to 1.4 GHz.

3.8. Experimental Verifications

To verify the performance of the antennas studied in section 3.3 through section 3.7, some of them were built and tested at the University of Manitoba Antenna Laboratory. All antennas studied were made of metal plates, mounted vertically over a horizontal ground plane. Metal was considered a perfect conductor during simulation processes using Ansoft-HFSS software, [34]. However, to overcome the problem of deformation in the planar shape of the metal plates, when mounted on the ground plane, the fabricated antennas were etched on a 22 x 22 mm^2 hard substrate, with 0.8mm thickness and permittivity of $\varepsilon_r = 2.5$. This configuration also solved the problem of soldering the metal plate to the SMA connector without damaging it. Ground planes used in the measurements were Aluminium sheets to maintain its flatness. Fig. 3.34 shows one of the designed antennas after being mounted on the Aluminium ground plane for return loss and radiation pattern measurements.

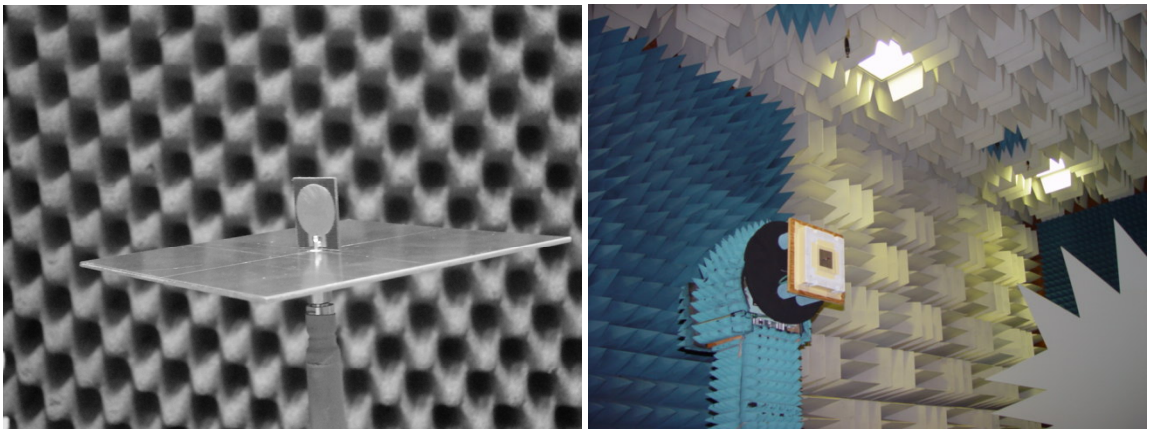

Fig. 3.34 Circular monopole antenna mounted on a 120x120mm^2 Aluminium ground plane and ready to be tested at University of Manitoba Antenna Lab using Anritsu 37397C Vector Network Analyzer and Compact Range radiation pattern setup.

Fig. 3.35 shows the square monopole antenna with trident feeding strip, with and without central metal removal, studied in Section 3.3. Metal plates are etched on a 22x22mm^2 single sided substrate. Fig. 3.36 shows the return loss curves of both antennas after being mounted on a 120x120mm^2 Aluminium ground plane. Measured results are compared to simulated ones. As can be seen, there is a good agreement between measured and simulated return loss curves, regarding the lower frequency limit and resonance frequencies. There are shifts in some resonance frequencies and the upper frequency limit. Similar results can also be seen for the circular monopole antenna, with and without central metal removal, as shown in Fig. 3.37 and their return loss curves shown in Fig. 3.38. Elliptical monopole antennas with and without central metal removal are shown in Fig. 3.39 and compared to the Canadian Dollar Coin to show their sizes. The Return loss curves of the two elliptical monopole antennas are shown in Fig. 3.40.

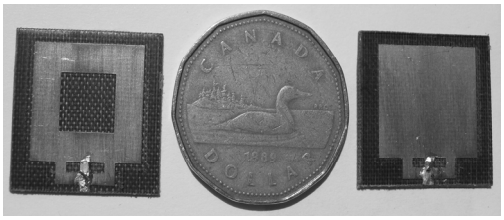

Fig. 3.35 Square monopole antennas of Fig. 3.1a and Fig. 3.1c etched each on a 22x22mm^2 substrate with ε_r=2.5, height=0.8mm. Antennas are compared to the Canadian Dollar Coin before being mounted on the Aluminium ground plane

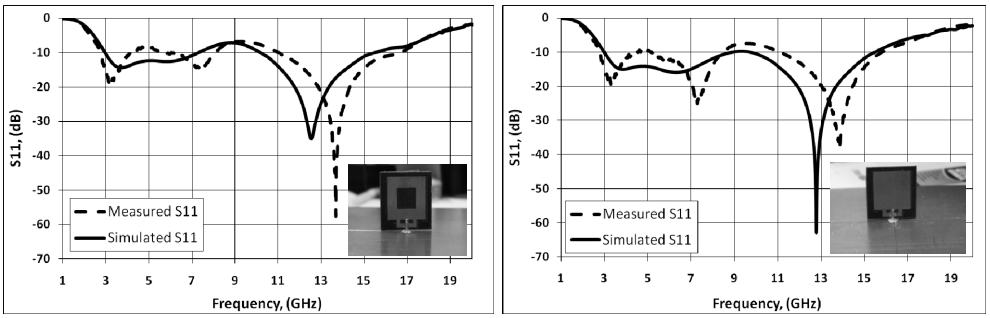

Fig. 3.36 Return loss curves for the square monopole antennas shown in Fig. 3.35

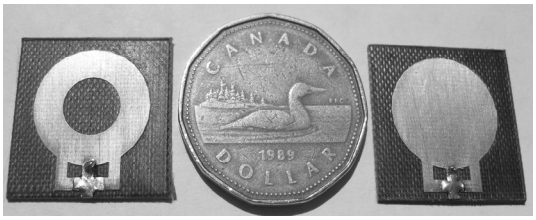

Fig. 3.37 Circular monopole antennas of Fig. 3.8a and Fig. 3.8c etched each on a 22x22mm^2 substrate with ε_r=2.5, height=0.8mm. Antennas are compared to the Canadian Dollar Coin before being mounted on the Aluminium ground plane

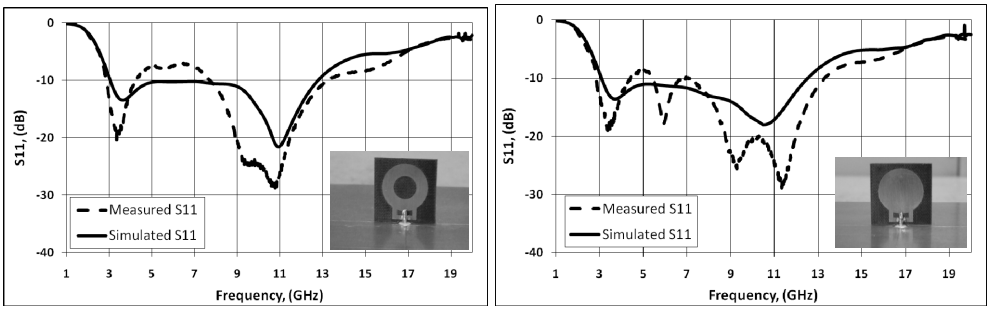

Fig. 3.38 Return loss curves for the circular monopole antennas shown in Fig. 3.37

Fig. 3.39 Elliptical monopole antennas of Fig. 3.12a and Fig. 3.12c etched each on a $22x22mm^2$ substrate with ε_r=2.5, height=0.8mm. Antennas are compared to the Canadian Dollar Coin before being mounted on the Aluminium ground plane

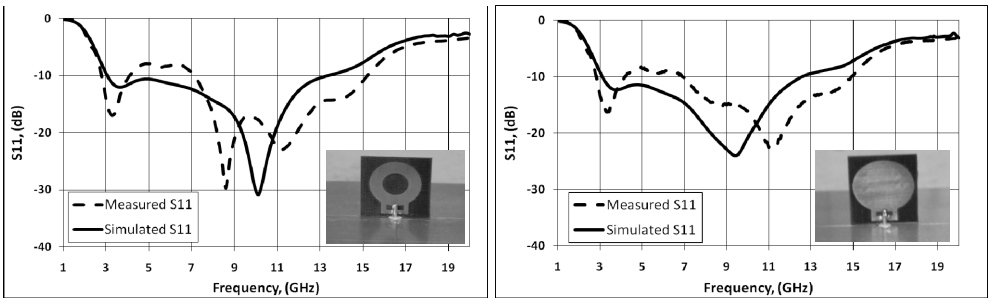

Fig. 3.40 Return loss curves for the elliptical monopole antennas shown in Fig. 3.39

The radiation pattern curves of some of the studied antennas are measured at different principle planes over the entire frequencies band of operation. Studied antennas showed omnidirectional radiation patterns in the H-plane (theta=90^o and theta=60^o) and dipole-like patterns in the E-planes, (phi=0^o, 45^o, and 90^o). Fig. 3.41 shows radiation pattern curves for the circular monopole antenna at 4, 7 and 10 GHz. The antenna has high cross-polarization components at 10 GHz in phi=45^o plane. Fig. 3.42 shows radiation patterns for the elliptical monopole without central metal removal at 4, 7 and 10 GHz. This antenna also has high cross-polarization components at 10 GHz in phi=45^o plane. Finally, Fig. 3.43 shows radiation patterns for the elliptical monopole with the central metal removal at 4, 7 and 10 GHz. Although this antenna has high cross-polarization components at 10 GHz in phi=45^o plane same as that of the other two

antennas, its patterns show better omnidirectionality at all frequencies in theta=90^{o} plane than that of the other antennas..

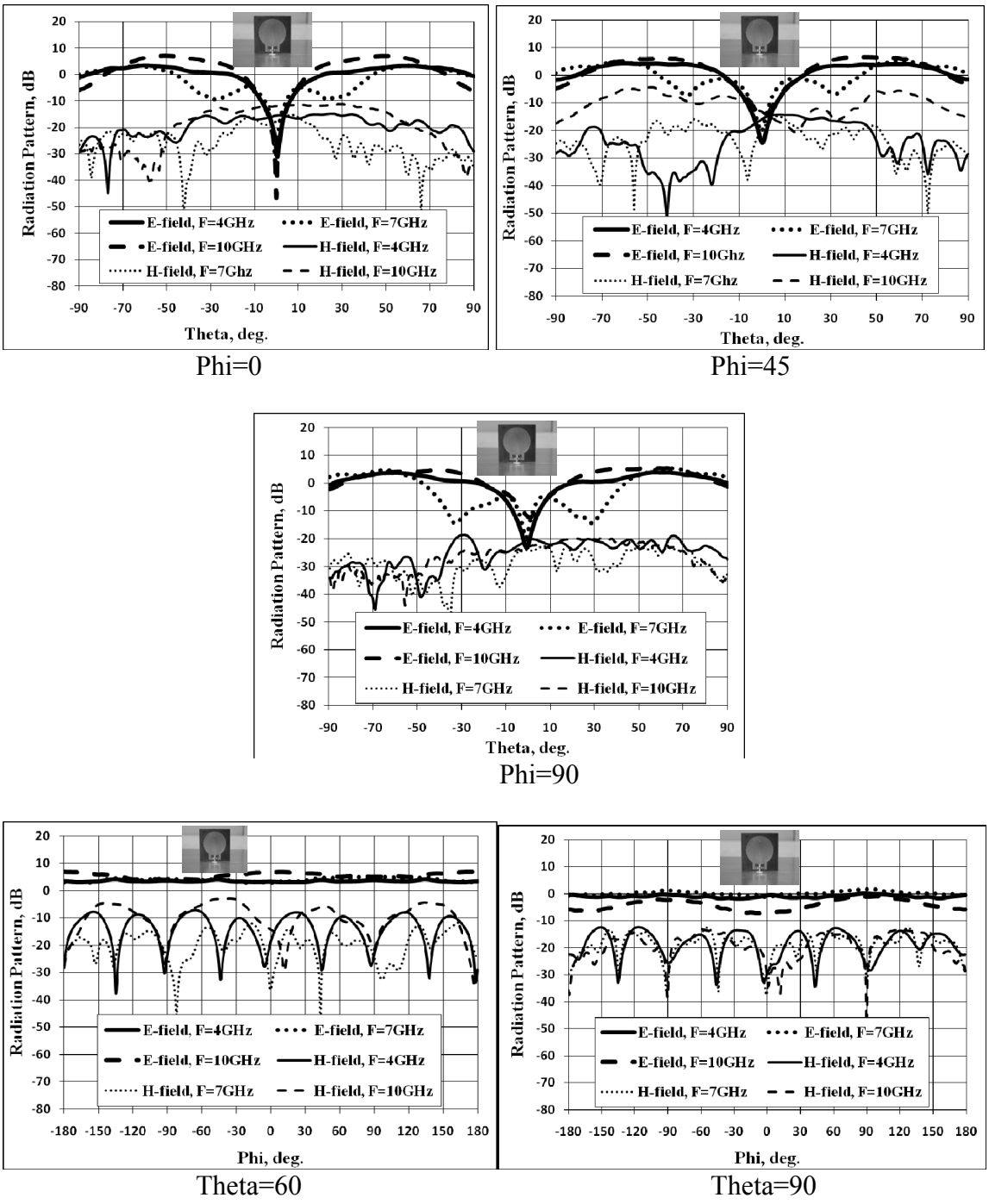

Fig. 3.41 Measured radiation patterns for the circular monopole antenna of Fig. 3.37 at different principle planes and at different frequencies

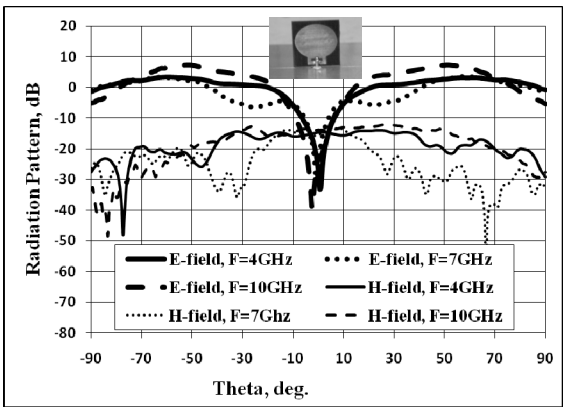

Phi=0

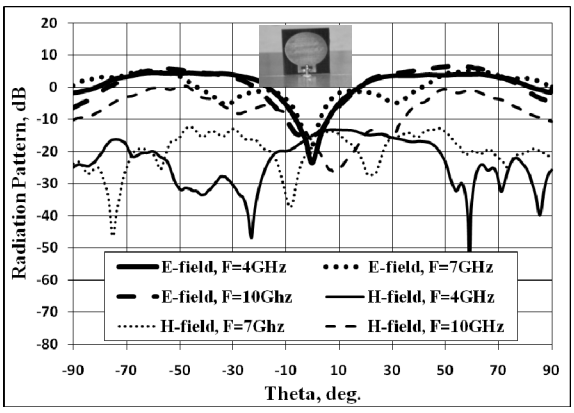

Phi=45

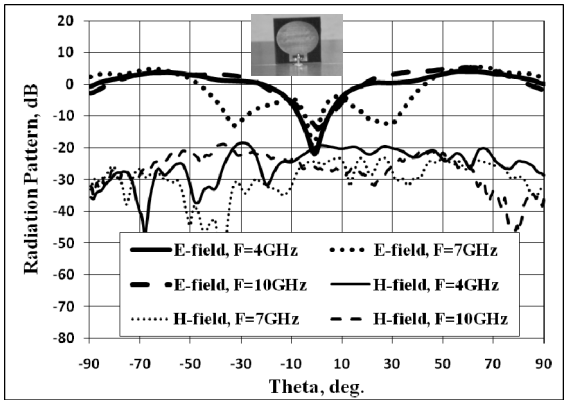

Phi=90

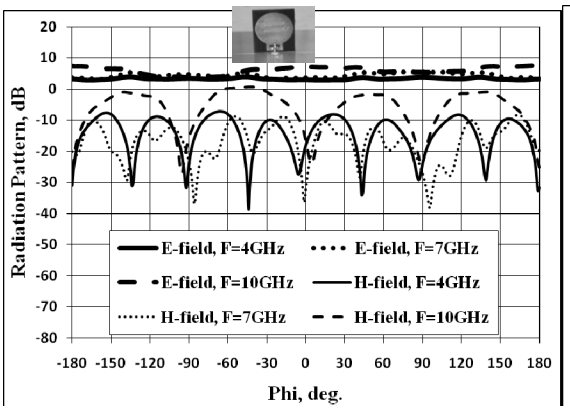

Theta=60

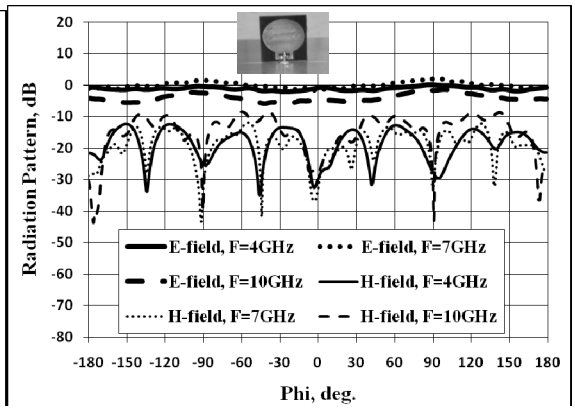

Theta=90

Fig. 3.42 Measured radiation pattern curves for the elliptical monopole antenna of Fig. 3.39 at different principle planes and at different frequencies

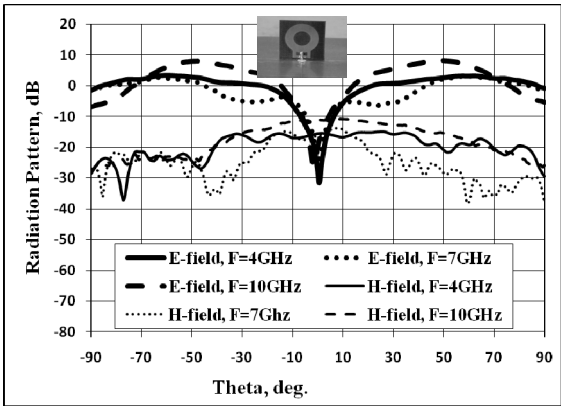

Phi=0

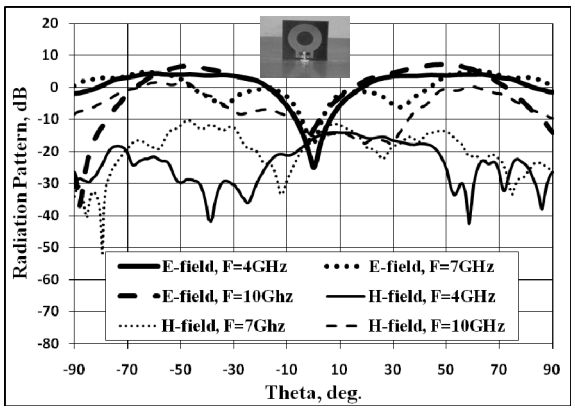

Phi=45

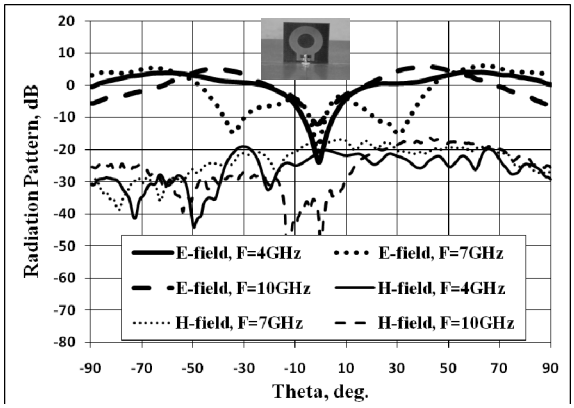

Phi=90

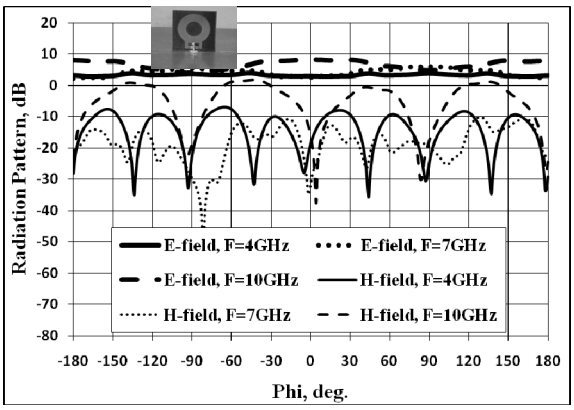

Theta=60

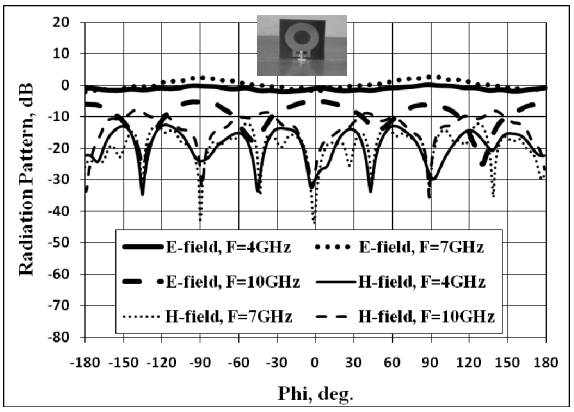

Theta=90

Fig. 3.43 Measured radiation pattern curves for the elliptical monopole antenna of Fig. 3.39 with central metal removal at different principle planes and at different frequencies

To further understand how the signal transmitted or received from these antennas will be distorted; the group delay curves of the tested antennas were measured. Table 3.1 shows the maximum group delay of each antenna over the entire frequency band of operation, from 3 to 20 GHz. As can be seen from Table 3.1, all monopole antennas tested have group delays less than 0.5 ns, which is less than that of the circular disc monopole with single strip feed, [46].

Maximum group delay (ns) measured over the entire frequency band, 3 to 20 GHz	
Square monopole antenna 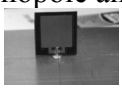	0.2325 ns
Square monopole with central metal removal 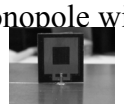	0.2406 ns
Circular monopole antenna 	0.3154 ns
Circular monopole with central metal removal 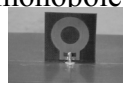	0.2811 ns
Elliptical monopole antenna 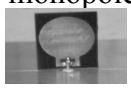	0.2377 ns
Elliptical monopole with central metal removal 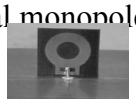	0.2703 ns

Table 3.1 Maximum group delays measured over the frequency band, 3-20 GHz

3.9 Conclusion

In this chapter, different UWB monopole antennas were studied. Square, circular and elliptical monopole antennas showed UWB impedance bandwidth that covered the existing defined ultra wideband communication band of 3.1 to 10.6 GHz, and extended behind up to 19.5 GHz for future applications. It was found that implementing slots close to the trident-feeding strip structure did not increase the impedance bandwidth of circular and elliptical antennas. Further, incorporating the slot decreased the impedance bandwidth of the square monopole antenna. On the other hand, removing metal from the centre of the square, circular and elliptical monopoles gave the same impedance bandwidth for square and circular monopole and increased the bandwidth of the elliptical one. The circular and elliptical monopole antennas, with metal removed, showed better omnidirectional behaviour at higher frequencies. UWB antennas with different slot configurations were studied to have new control parameters over the bandwidth, centre frequency and impedance mismatch level of the stop-band. UWB antennas with novel slots were introduced and simulated. The size of the ground plane was optimized to decrease the lower frequency of the impedance bandwidth. Slots were incorporated to isolate the effect of this small ground plane on the radiation pattern of the antenna. These antennas have important uses in UWB communications. The finding of this chapter can be summarized as follows:

- The effect of using different slot shapes on the bandwidth of the stop-band was studied.

- A UWB antenna with an optimized U-shape slot was studied for the slot position and length. This antenna gave an impedance mismatch of 13 dB within the stop-band
- A novel UWB antenna design with 2-U-shape slots of the same length was also introduced. The impedance mismatch of this antenna was 16 dB, i.e. 3 dB more than that of a single slot
- A novel UWB square monopole antenna with a spiral-slot was introduced. The impedance mismatch loss achieved was 15.5 dB. Two spiral-slots of the same length were also implemented with two configurations. The first one, with the two spiral-slots on top of each other, gave an impedance mismatch loss of 18 dB. While the second one, with the two spiral-slots beside each other, gave an impedance mismatch loss of 19.5 dB.
- The effect of the ground plane size on the performance of the monopole antennas was investigated.

Chapter 4

Phase Centre Characterization of UWB Antennas

4.1 Introduction

In this chapter, a method for determining the phase centre location of ultra wideband monopole antennas is presented and used to investigate its movement within the frequency band of operation. The method is applied first to a simple circular monopole antenna with a single feed over a ground plane and then used to calculate the phase centre of the trident feeding monopole antennas studied in chapter 3. The method is also used to study the effects of different band-stop designs on the degree of the phase centre movements. It is shown that some designs can adversely affect the phase of the radiated field, by displaying larger phase centre movements. For improved performance of the UWB antennas, such designs must be avoided.

4.2 Phase Centre Determination

The phase centre of a monopole antenna is defined as the origin of a sphere, over which the phase of the radiated field is nearly (≤ 7 degrees phase variation) constant over the frequency band of operation from 3 to 11 GHz, for θ from 60 to 70 degrees, at the three principle ϕ =0°, 45° and 90° planes. HFSS (High Frequency Structure Simulator Based on the Finite Element Method) [34] is used for simulation of the antenna configurations, and computation of the radiated E_θ field, and its phase for different θ

ranges at ϕ = 0°, 45° and 90° planes. Fig. 4.1 shows the geometry for calculating the phase centre, where O (0, 0, 0) is the origin of the coordinates, and O′ (0, 0, Z_0) is the phase centre location.

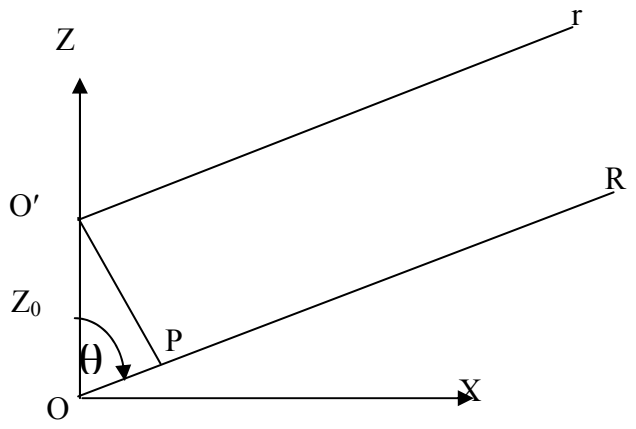

Fig. 4.1 Geometry for phase centre calculation of UWB monopole antennas

Here it is assumed that for small UWB monopole antennas, the phase centre will be moving on Z-axis. This assumption can be generalized to investigate movement in all directions when the antenna dimension is large compared to the wavelength. So for now and because of the symmetry, it is assumed that the phase centre will move on the Z-axis. R is the distance from the origin to the far field point and r is the distance from the phase centre location to the same observation point. Both R and r are much larger than Z_0 and can be considered parallel. The radiated far field can be expressed as [113 and 114],

$$\overline{E}(R,\theta,\phi) = f(\theta,\phi)\frac{e^{-jK_0R}}{R}e^{j\psi(\theta,\phi)} \tag{4.1}$$

where $f(\theta,\phi)$ is the amplitude pattern, K_0 is the free space propagation constant and $\psi(\theta,\phi)$ is the phase distribution of the radiated field. From Fig. 4.1, R and r are related as:

$$R = r + Z_0 \cos\theta \tag{4.2}$$

Then the phase of the radiated field can be expressed as,

$$\psi(\theta,\phi) - K_0 Z_0 \cos\theta - K_0 r \tag{4.3}$$

At the phase centre point O′(0, 0, Z_0) the phase term in (4.3) becomes independent (or nearly independent) of θ and ϕ. Using the HFSS simulation results, for the phase distribution of the E_θ far field, in (4.3) the antenna phase centers, with and without the stop-band slots are determined for the three principle ϕ =0°, 45° and 90° planes.

4.3 Phase Centre of Circular Monopole Antennas with Single Feeding Point

4.3.1 Antenna Design

A circular monopole with radius 10 mm over a 120x120 mm^2 ground plane is investigated. The optimum distance between the antenna and the ground plane, d, is 1mm and its width is 1.5 mm. The antenna is fed through a SMA connecter from underneath the ground plane at its center. This configuration gives a 10 dB impedance bandwidth of more than 10 GHz, which is in excess of the requirements of UWB communications from 3.1 to 10.6 GHz. Fig. 4.2 shows the antenna parameters and the return loss curve, [115-116].

4.3.2 Phase Centre Determination Process

Due to the symmetric nature of the studied structure, the phase centre of this antenna is expected to move on the Z-axis. Then, the phase data of the far field, E_θ component, is used to calculate the displacement needed on the Z-axis to minimize the discrepancies in the radiated far field phase over certain θ ranges for different ϕ values. As this is an omnidirectional antenna, attention is given to the θ ranges between 40 and 90 degrees. The displacement needed is calculated and recorded in λ units at different frequencies over the band of operation from 3 to 15 GHz.

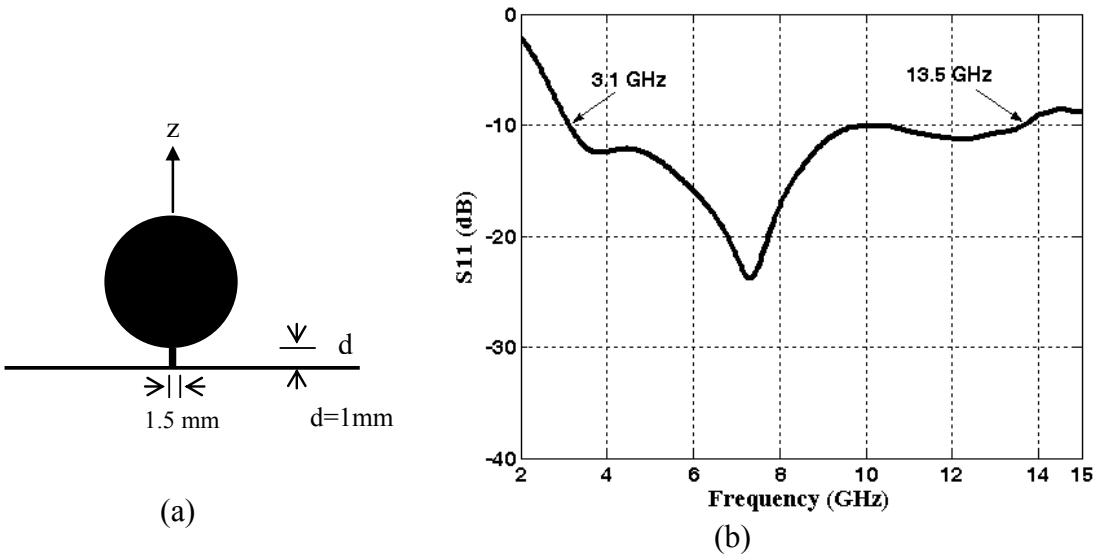

Fig. 4.2 The circular monopole antenna with radius 10 mm on a 120x120 mm^2 square ground plane, (a) Antenna parameters, (b) Return loss curve of the antenna

As the phase of the radiated E_θ component can not be completely constant over θ ranges, the aim is to find the point on the Z-axis that leads to a minimum change in the phase of E_θ at different frequencies for ϕ =0, 45 and 90 degrees. Due to the fact that this

antenna is an omnidirectional one and has its main radiation close to θ = 90 degree, the study will consider the θ ranges of 80-90, 70-80, 60-70, 50-60 and 40-50. This study is done over the frequency range from 3 to 15 GHz.

4.3.3 Phase Centre Location of the circular Monopole Antenna with Single Feed

The antenna studied has a 10 dB impedance bandwidth of 125.5% and works from 3.1 to 13.5 GHz. It also has an omnidirectional radiation pattern throughout this band. It is found that the phase centre of this antenna moves on the Z-axis over the frequency band of operation. The phase centre changes within 0.2λ over the frequency band 3 to 9 GHz for θ from 70^o to 90^o degrees, within 0.6λ for θ from 50^o to 90^o, within 1λ for θ from 40^o to 90^o degrees. These ranges of phase centre movement are for $\phi = 0^o$, 45^o and 90^o. Fig. 4.3 shows the required movement on the Z-axis to have a minimum change in the phase of the radiated E_θ field over a specified range of theta. Table 4.1 summarizes the phase centre range movement of this circular monopole antenna. It is also noted that the phase centre curves have noticeable differences with respect to the three principle planes $\phi = 0^o$, 45^o and 90^o. This is due to the fact that the circular radiator is setting in one plane (Y-Z plane). It is found that we can stabilize the phase centre movement over the frequency band of operation for the three principle planes $\phi = 0^o$, 45^o and 90^o, by using circular monopole with perpendicular planar cuts in X-Z and Y-Z planes. This finding is discussed in the following section.

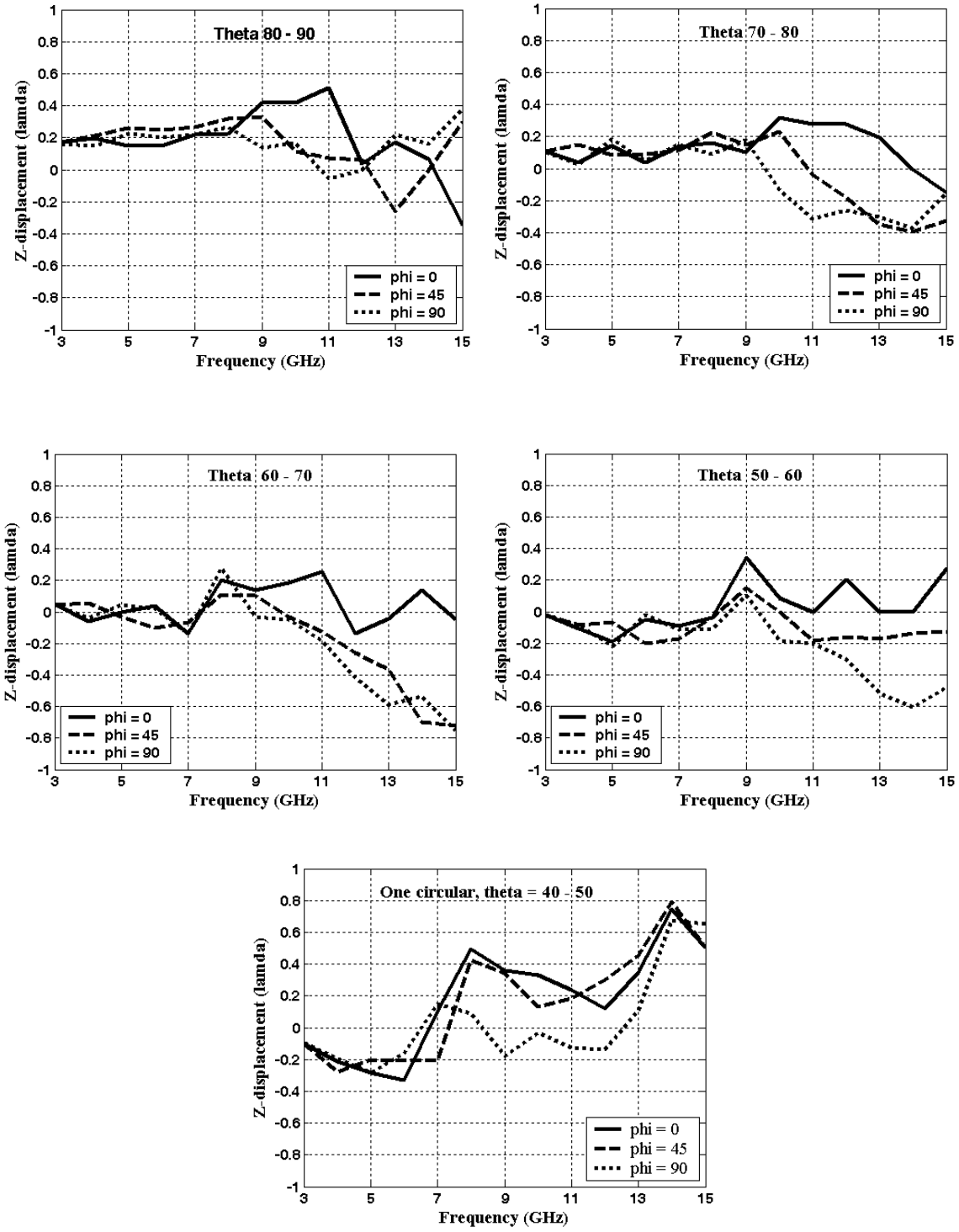

Fig. 4.3 Displacement on Z-axis in λ units to have the minimum change in the phase of the radiated E_θ of the circular monopole antenna at different θ ranges for $\phi = 0^o$, 45^o and 90^o

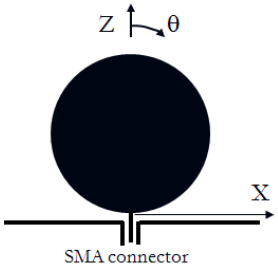

θ Ranges in Degrees	Phase Centre Movement Range in the Three Principle Planes ϕ =0°, 45° and 90°
70° to 90°	0.6 λ
50° to 90°	0.6 λ
40° to 90°	0.8 λ

Table 4.1 Maximum range phase centre movement over the frequency band 3 to 15 GHz, for the three principle planes ϕ =0, 45 and 90 at different θ ranges

4.4 Phase Centre of Double Circular UWB Monopole Antennas with Two Interleaved Perpendicular Planar Cuts

To solve the problem of unstable phase centre behaviour of UWB monopole antennas with respect to the three principle planes ϕ =0°, 45° and 90°, more radiators are added to the monopole and fed from the same feeding point. It is found that, by having a double monopole configuration with one radiator in the X-Z plane and the other in Y-Z

plane, does not have deterioration effect on the impedance bandwidth nor the radiation patterns of the antenna. However, using this double configuration helps in having symmetrical antenna behaviour. Fig. 4.4 shows the circular monopole antenna introduced in section 4.2 after adding another replica of the circle in the perpendicular plane as shown. The double circular antenna has even more impedance bandwidth than the circular one starts at 3.1 GHz and extends up to 14.25 GHz instead of 13.5 GHz. It also has an omnidirectional radiation pattern in the X-Y plane throughout this band.

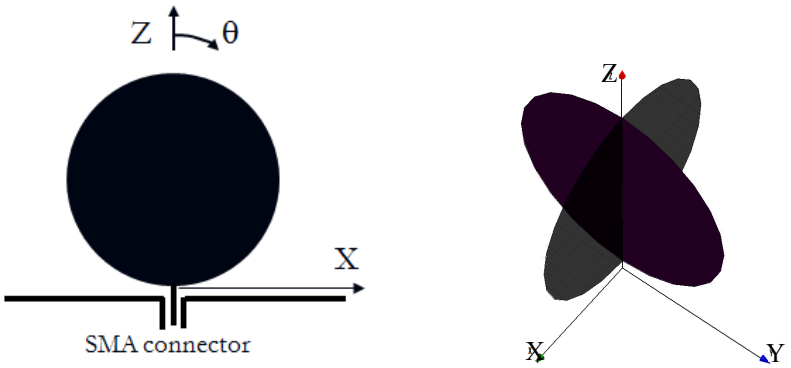

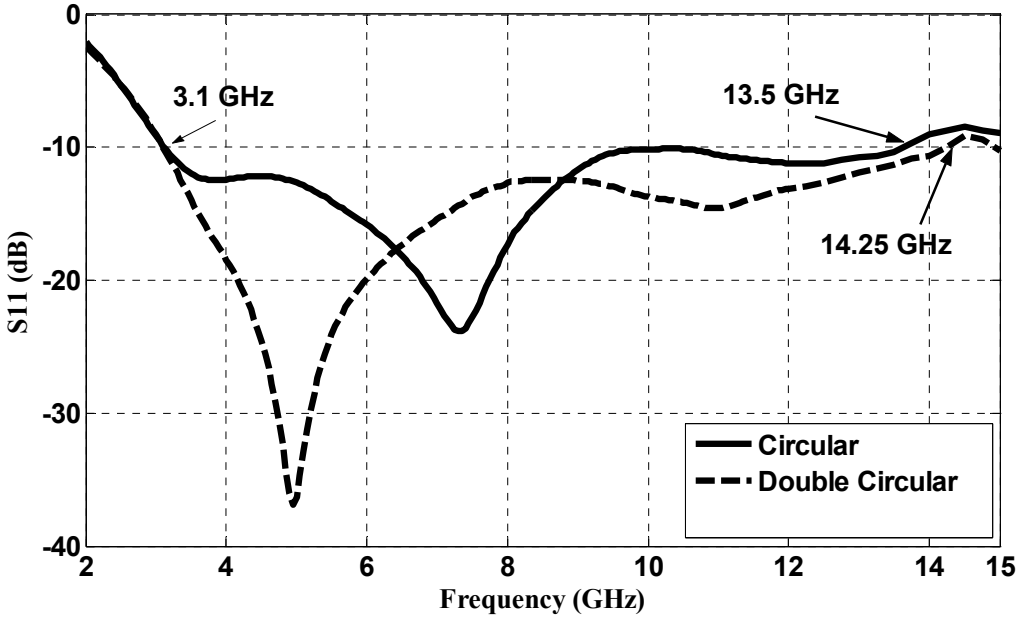

Fig. 4.4 Return loss of the circular monopole antenna versus interleaved double circular monopole one

Fig. 4.5a and Fig. 4.5b show the effect of using double circular monopole configuration on the phase centre behaviour of this antenna. Two benefits are achieved because of using this configuration. One is the decrease in the phase centre movement range over the frequency as can be seen from Table 4.2. The other is the stabilization of the phase centre over the three principle planes $\phi = 0^o$, 45^o and 90^o for all θ ranges used as shown in Fig. 4.5a,b.

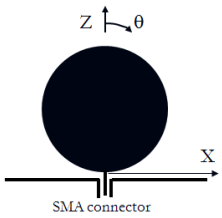

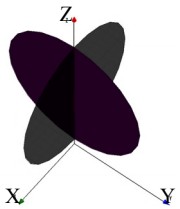

θ Ranges in Degrees	**Phase Centre Movement Range in the Three Principle Planes $\phi = 0^o$, 45^o and 90^o**	
70^o to 90^o	0.6 λ	0.4 λ
50^o to 90^o	0.6 λ	0.5 λ
40^o to 90^o	0.8 λ	0.5 λ

Table 4.2 Comparison of maximum range phase centre movement over the frequency band 3 to 15 GHz for the three principle planes $\phi = 0^o$, 45^o and 90^o at different θ ranges, for a single and double interleaved circular monopole antennas

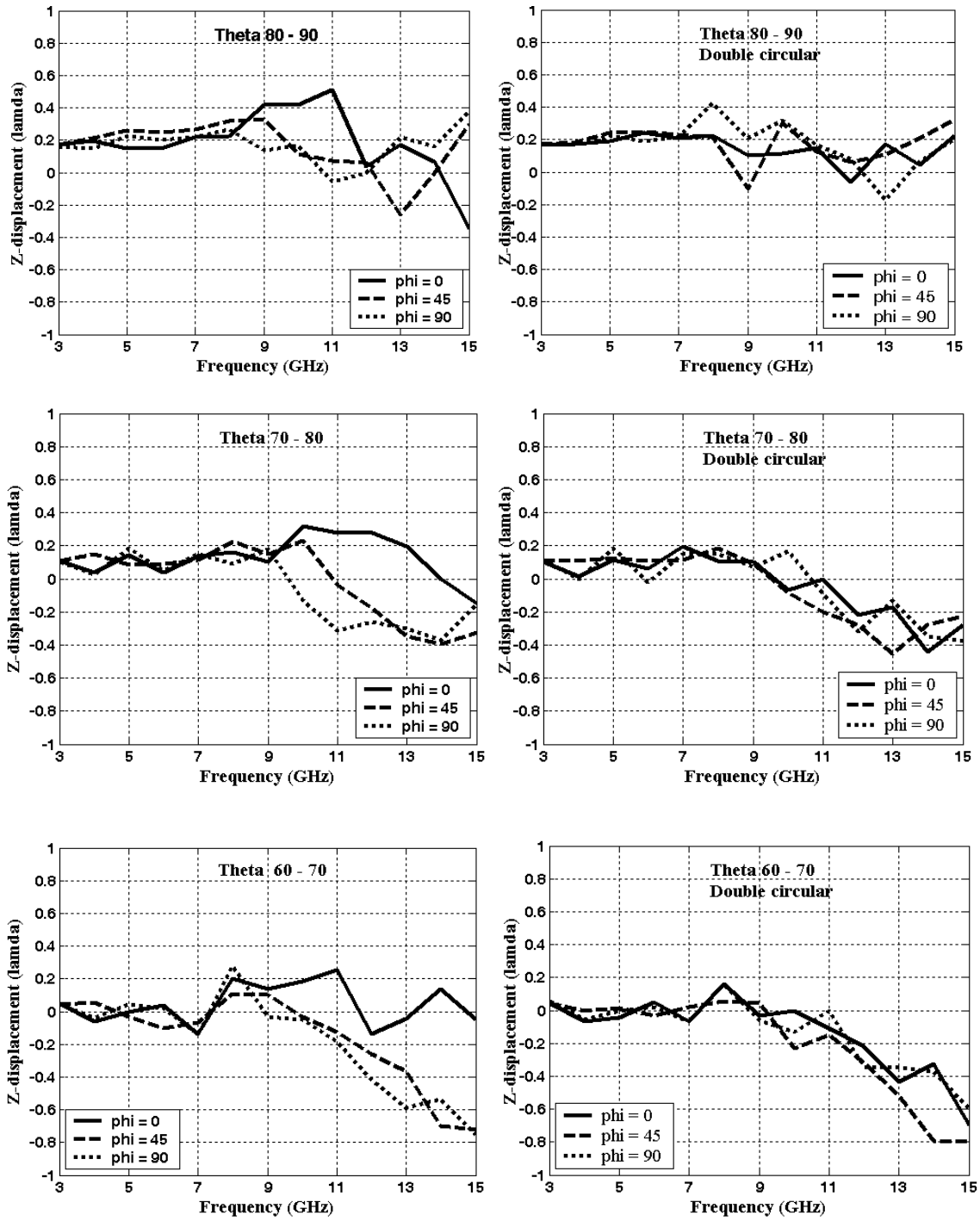

Fig. 4.5a Comparison between the phase centre behaviour of the circular monopole and the double circular one for the three principle planes $\phi = 0^o$, 45^o and 90^o at different θ ranges

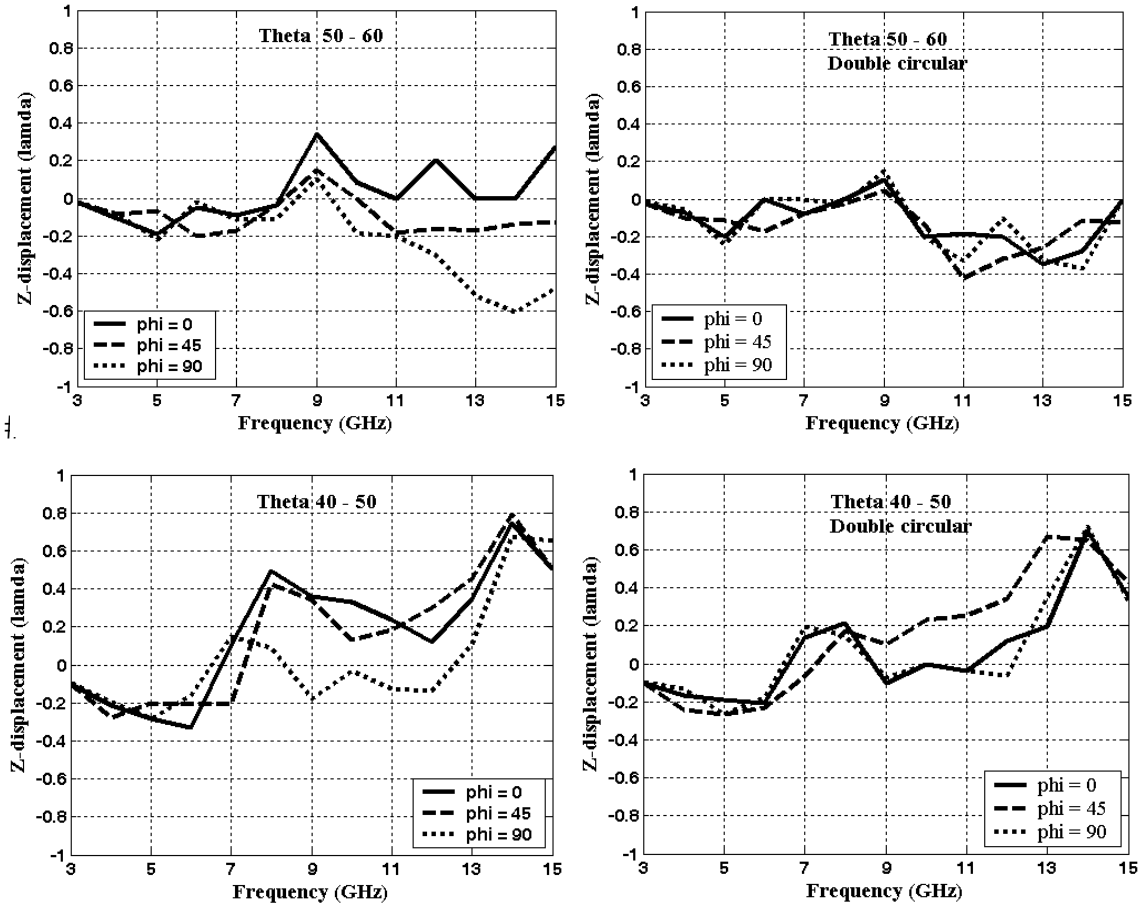

Fig. 4.5b Comparison between the phase centre behaviour of the circular monopole and the double circular one for the three principle planes $\phi = 0^o$, 45^o and 90^o at different θ ranges

4.5 Phase Centre of UWB Monopole Antennas with Trident-Feeding

4.5.1 Phase Centre Movement with Frequency

It was shown in chapter 3 that square, circular and elliptical monopole antennas with trident-feeding strip are proven to have UWB impedance bandwidth and omnidirectional radiation pattern over the frequency band of operation. The studied cases have a 10 dB impedance bandwidth that starts with 130.58% and can reach up to

146.67%. The lower frequency band edge of these antennas is around 3 GHz and the upper band edge reached 19.5 GHz in the square case. The antennas studied also have omnidirectional radiation patterns with better performance at higher frequencies, for the antennas with central metal removal. These antennas can be used in the ultra wideband communication range of 3.1 to 10.6 GHz and are also good candidates for the extended frequency band behind 10.6 GHz for the future applications. Fig. 4.6 shows the square, circular and elliptical monopole antennas with trident-feeding, introduced earlier in chapter 3.

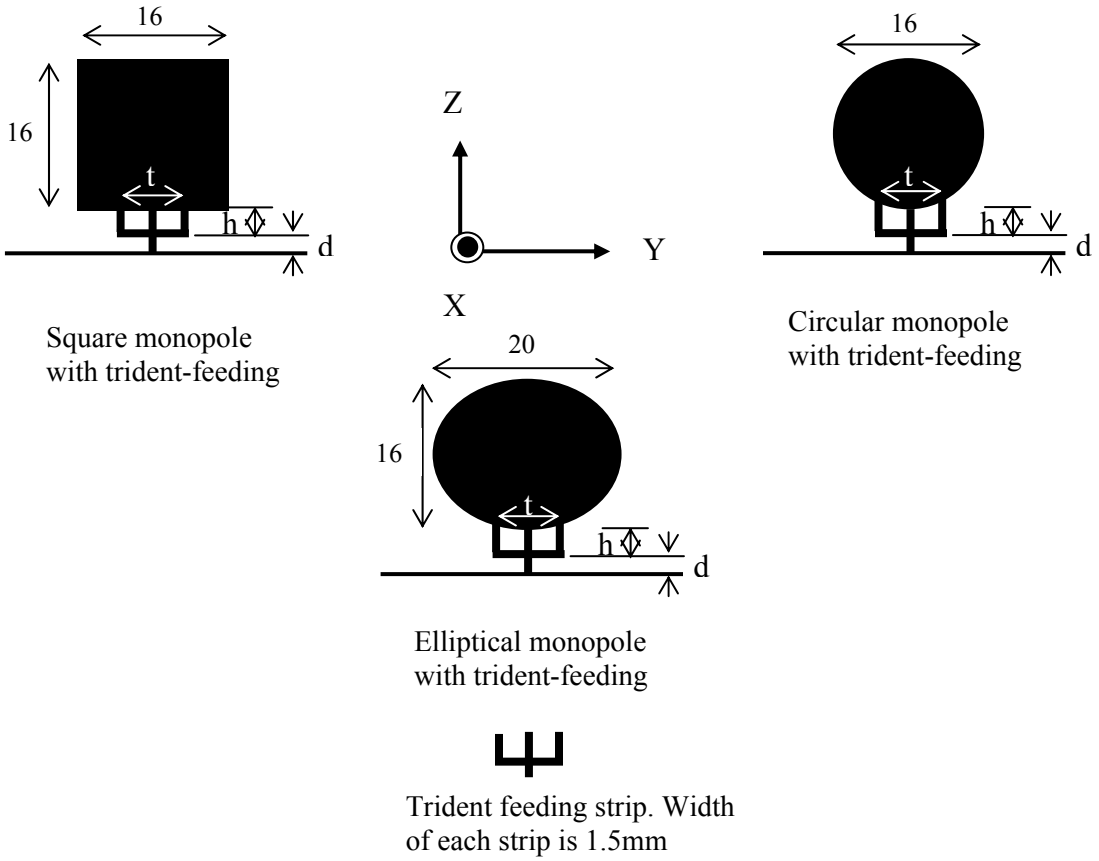

Fig. 4.6 Square, circular and elliptical monopole antennas with trident-feeding on a 120x120 mm^2 ground plane. t = 7, d = 1, h = 3, and all strip widths are 1.5. All dimensions in mm

Since these antennas can transmit/receive high data rates, are compatible with the new generations of wireless communication systems and have potential applications in areas like microwave imaging. And according to the fact that these antennas work over large frequency bands, it is important to determine their phase centre locations within the same band and over a part or entire angular range of the space. Studying the phase centre location of such antennas is also important when using them for pulse transmission/reception, as the movement of the phase centre will distort the signal. As mentioned before, the phase centre is the origin of a sphere over which the phase of the radiated field has minimum change, for certain θ and ϕ ranges. Using this definition, the phase centre locations of square, circular and elliptical UWB monopole antennas with trident-feeding strip are determined over the frequency band of operation. The study includes the frequency band starting at 3 GHz and extends to 20 GHz. This is done based on the simulated radiation patterns of the studied antennas using the HFSS software (high frequency structure simulator based on Finite Element Method).

4.5.2 Phase Centre determination process of the Square, Circular and Elliptical Monopoles with Trident-Feeding

Due to the symmetric nature of the studied antennas with respect to the Z-axis, the phase centre of these antennas is expected to move on the Z-axis. Then, the phase data of the far field for E_θ component, is used to calculate the displacement needed on the Z-axis to minimize the discrepancies in the radiated far field phase over certain θ ranges for different ϕ values. As these antennas are omnidirectional, attention in this study is given

to the θ ranges between 40^o and 90^o. The displacement needed is calculated and recorded in λ units at different frequencies over the band of operation from 3 to 20 GHz.

As the phase of the radiated E_θ component can not be completely constant over θ ranges, the point on the Z-axis that leads to a minimum change in the phase of E_θ at different frequencies for $\phi = 0^o$, 45^o and 90^o is determined. The phase centre calculation method used here is based on the same approach used in [113, 114]. In this example, the study considers θ ranges of 80^o-90^o, 70^o-80^o, 60^o-70^o, 50^o-60^o and 40^o-50^o and is done over the frequency range from 3 to 20 GHz.

It is found that the locus of the phase centre on Z-axis is not the same for different studied square, circular and elliptical monopole antennas. The phase centre location curves, on the Z-axis and at different θ ranges, over the frequency band of operation are plotted in Fig.4.7 to Fig. 4.9. These phase centre studies are done for the planes $\phi = 0^o$, 45^o and 90^o. This information is useful to better understand how will these antennas act, and where the radiation will be coming from, for different θ angles at different frequencies. Also, this information is useful to determine, which antenna can be used for certain application at a specific θ range. In Table 4.3, the range of λ over which the phase centre locations of these three antennas change are shown. It is clear from this table that square, circular and elliptical monopole antennas with trident-feeding have different phase centre movement ranges over frequencies for different θ ranges.

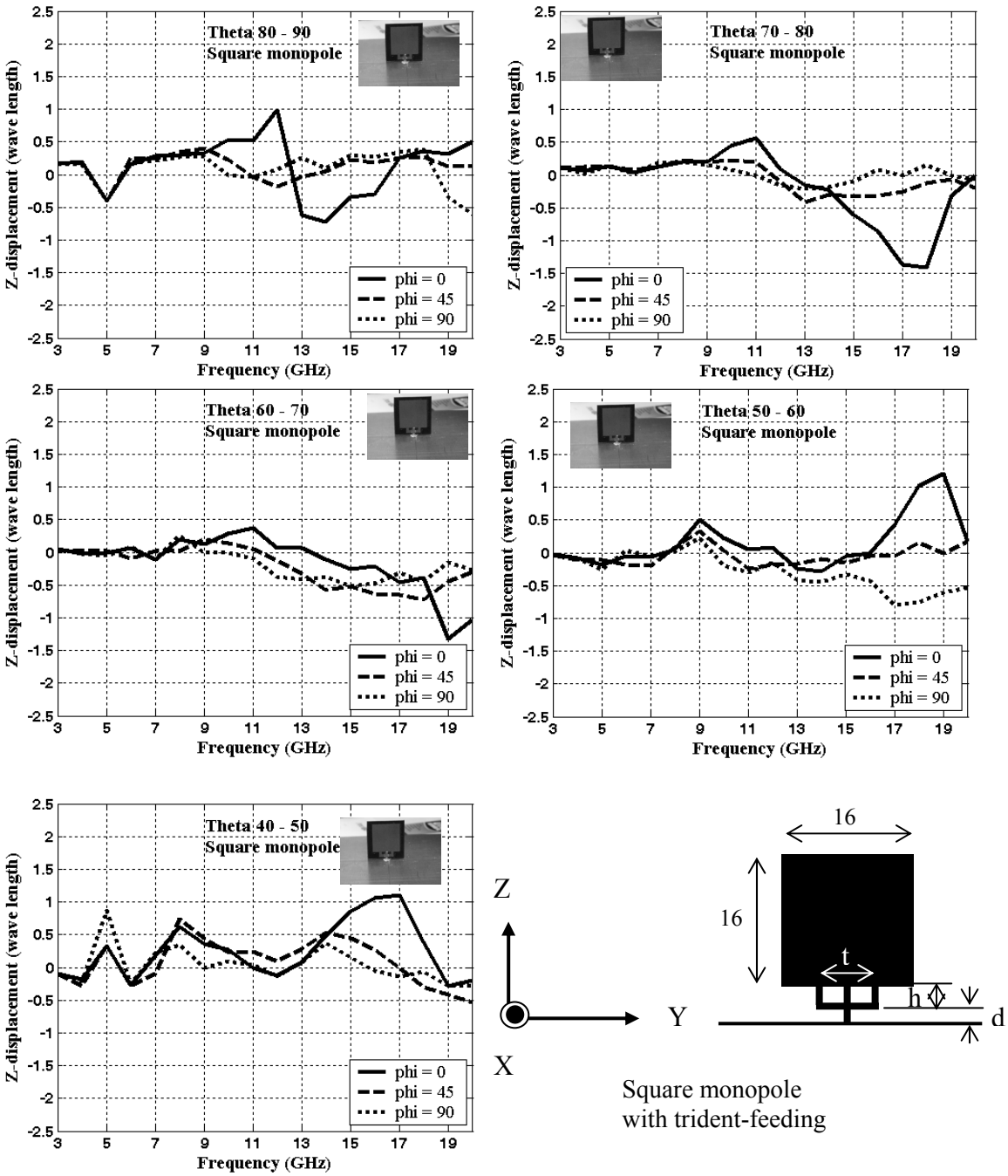

Fig. 4.7 The movement of phase centre location in wavelength units over the Z-axis with frequency, for different principle planes $\phi = 0^o$, 45^o and 90^o at different θ ranges for the square monopole antenna with dimensions given in Fig.4.6. The vertical axis gives the location on the Z-axis of the phase centre

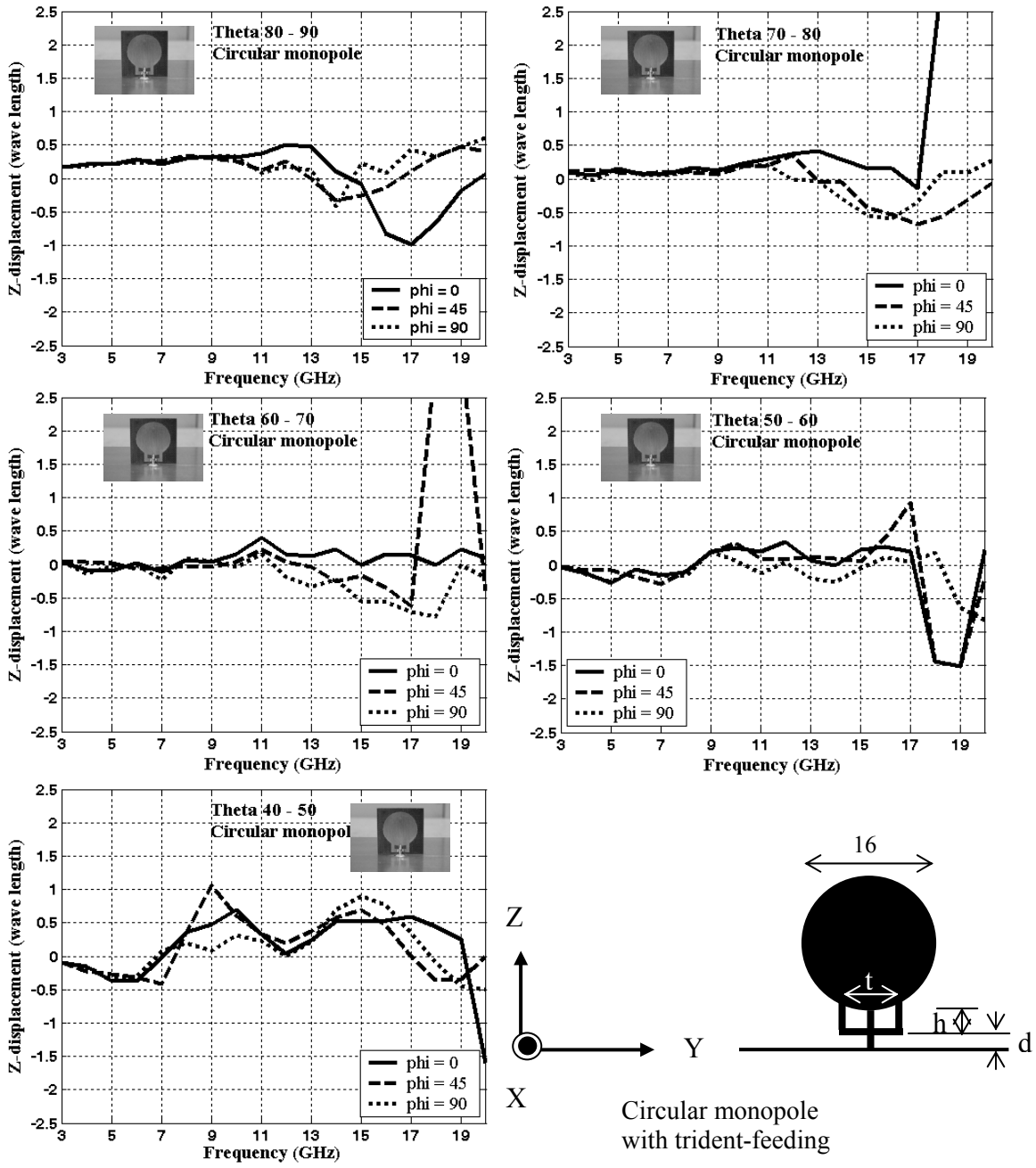

Fig. 4.8 The movement of phase centre location in wavelength units over the Z-axis with frequency, for different principle planes $\phi = 0^o$, 45^o and 90^o at different θ ranges for the circular monopole antenna with dimensions given in Fig.4.6. The vertical axis gives the location on the Z-axis of the phase centre

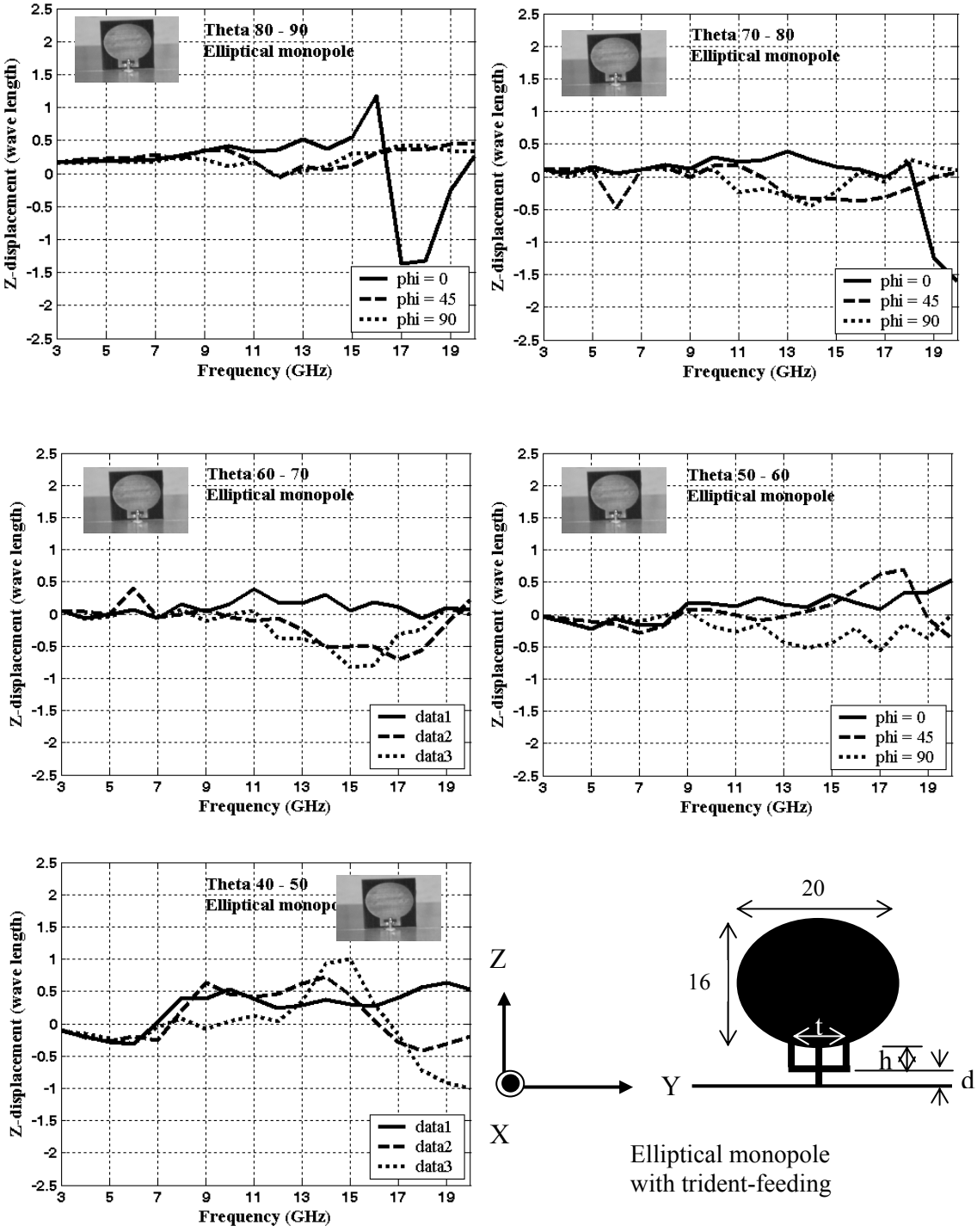

Fig. 4.9 The movement of phase centre location in wavelength units over the Z-axis with frequency, for different principle planes $\phi = 0^o$, 45^o and 90^o at different θ ranges for the elliptical monopole antenna with dimensions given in Fig.4.6. The vertical axis gives the location on the Z-axis of the phase centre

Frequency range		F = 3 to 11 GHz	F = 3 to 20 GHz
θ = 80 - 90	Square, S1 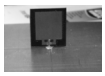	0.9	1.7
	Circular, C1 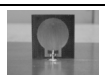	0.4	1.6
	Elliptical, E1 	0.5	2.4
θ = 70 - 80	Square, S1 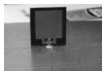	0.6	2
	Circular, C1 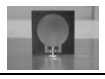	0.3	3.2
	Elliptical, E1 	0.7	1.9
θ = 60 - 70	Square, S1 	0.5	1.7
	Circular, C1 	0.6	3.3
	Elliptical, E1 	0.5	1.2
θ = 50 - 60	Square, S1 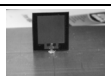	0.8	1.9
	Circular, C1 	0.6	2.5
	Elliptical, E1 	0.5	1.2
θ = 40 - 50	Square, S1 	1.2	1.6
	Circular, C1 	1.4	2.6
	Elliptical, E1 	0.8	2

Table 4.3 Phase centre movement range (λ) on the Z-axis for square, circular and elliptical monopole antennas with trident-feeding of Fig. 4.6

From above results in Figs 4.7 to 4.9 and Table 4.3, it was found that, although the studied antennas satisfy the desired impedance and radiation bandwidth

characteristics, their phase centres move with frequency. This movement is not the same for all these three antennas. It is found that for the frequency range 3 to 11 GHz, the circular monopole has the least phase centre movement for $\theta = 70^o$ to 90^o range. While the elliptical monopole has the least phase centre movement for $\theta = 40^o$ to 70^o range, and for the same frequency range. For the frequency range from 3 to 20 GHz, the circular monopole has the least phase centre movement range for $\theta = 80^o$ to 90^o, the elliptical monopole has the least phase centre movement range for $\theta = 50^o$ to 80^o, while the square monopole has the least phase centre movement range only for $\theta = 40^o$ to 50^o. This information is useful to determine the appropriate antenna for different θ ranges and for specific applications.

4.6 Effect of Resonance Features on Antenna Phase Centre

The proposed use of UWB communication services, over the bandwidth of 3.1-10.6 GHz, has increased the research interest on design and performance studies of UWB antennas, especially monopole types with omnidirectional radiation patterns. However, other services already operate within this band. Thus, to eliminate the interference between the existing and upcoming ultra wideband communication services, UWB Antennas with band-stop functions are being investigated. As was explained in chapter 3, a common approach to reduce the interference is to implement certain features in the antenna structure, like half wavelength slots at the centre frequency of the stop-band, to cause resonances and current concentrations around the features to eliminate radiation at the required frequencies. These additional design features naturally affect the antenna

performance, especially the phase of the far field patterns over its wide frequency band. This is due to the fact that the new antenna becomes effectively two separate antennas, the original UWB antenna and the added feature, whose radiation cancels that of the original antenna within the desired band. For this reason, the phase performance of the new antenna can become more complex, as the two antennas have their own separate phase centers, with subsequent interactions. Since, the location and intensity of the current distribution on the original UWB antenna changes within its wide frequency band, the resulting phase centre location of the composite antenna will change within the band. This means, different frequency components of a wideband pulse will radiate from different regions of the antenna, with subsequent deteriorating effect on the radiated pulse at the far fields. Thus, it is important that in designing a band-stop feature a configuration be selected such that it does not have a detrimental effect on the phase centre location of the resulting composite antenna. To demonstrate this phenomenon, the problem of phase centre location and its movement within the required band are investigated for a few common designs. It is shown that indeed some designs are inferior and must be avoided.

The circular monopole antenna designed in section 4.3 of this chapter is used as a host for different slot features. Since the radiation of these antennas is mostly near the horizontal plane, between $\theta = 60°$ to $90°$, the phase centre locations in this section are determined for this angular range. However, the antenna configurations is angular dependent and creates angular dependent phases in the frequency domain, which in turn causes distortion in the time domain signal that are not symmetric along the azimuth angle ϕ. To understand this phenomenon, the computations are made in the principal and

diagonal planes $\phi = 0^o$, 45^o and 90^o. The features studies are the spiral slot, circular arc slot, and two different fork type structures, [117, 118].

4.6.1 Antenna Configurations

A circular monopole of radius 10 mm at 1mm distance from a 120x120 mm^2 square ground plane is studied. The width of the feeding strip is 1.5 mm, Fig. 4.10a. It is designed to work over the frequency band of 3.1 to 10.6 GHz. Then, different slot features are included inside the circular antenna to create a stop-band, centered at 5.5 GHz, to eliminate interference with the IEEE 802.11a, working in the frequency band of 5.15-5.825GHz. Four different slot shapes are used for this study including the spiral, circular arc, fork and ring shape slots. The total length of each slot is half wavelength at the center frequency of the stop-band, at 5.5 GHz. The slot widths are 2 mm and create a stop-band from 5 to 6 GHz. The spiral slot is an Archimedean one with 0.5 mm separation between the arms, [115]. The circular arc slot has an outer radius of 8mm and its centre is at Z=10mm. The fork is a circular metal arc of width 2mm, an outer radius of 4.5mm, centre at Z=10mm and attached to the feed region through a strip 1.5mm high and 2mm wide. The ring slot is a circular arc of outer radius 4.5mm and centre at Z=10mm, attached to the feed region through two strips 1.5mm high and 2mm wide. They are shown in Figs. 4.10b, 4.10c, 4.10d and 4.10e, respectively.

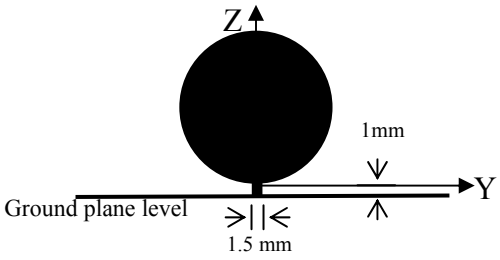

a) Circular monopole

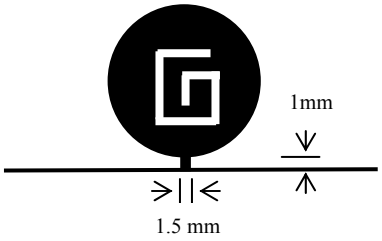

b) slot 1

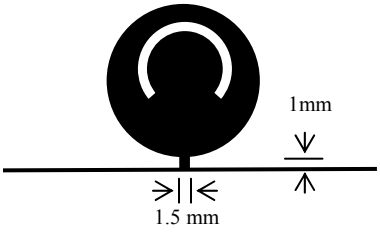

c) slot 2

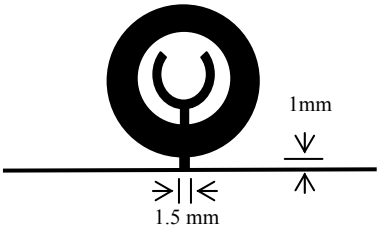

d) slot 3

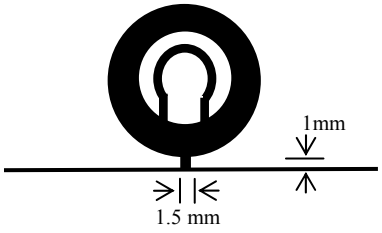

e) slot 4

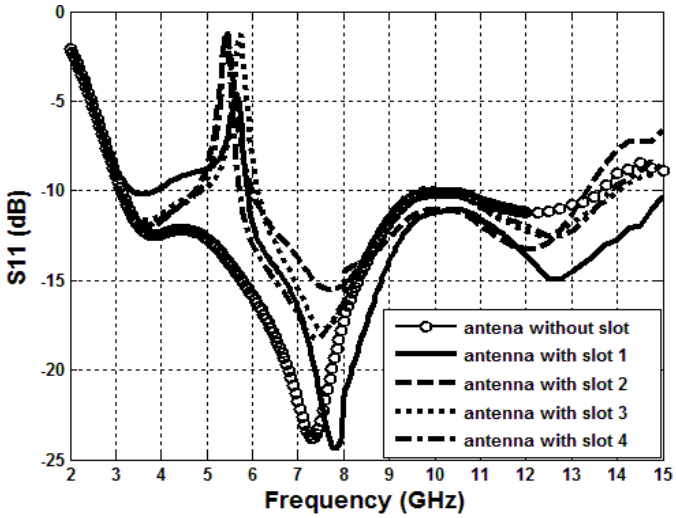

f) return loss curves

Fig. 4.10 Circular monopole antenna with different slots, a) antenna without slot, b) antenna with slot 1, c) antenna with slot 2, d) antenna with slot 3, e) antenna with slot 4, f) return loss curves of the antennas.

4.6.2 Phase Centre of Circular Monopole Antenna with Resonant Slots

The simulation results using HFSS software are used to obtain the phase of the E_θ radiated field with respect to origin O (0, 0, 0). Then this information is used to calculate

the phase centre of each antenna using the procedures described in section 4.2. Fig. 4.11a and 4.12a show the phase centre locations of the circular monopole antenna without slot, for two different θ ranges of 80°-90° and 70°-80°, where the radiated field is strong. From these figures it can be seen that the phase centre movement increases at higher frequencies, where there is also a big difference in the three ϕ =0°, 45° and 90° planes. Fig. 4.11b and Fig. 4.12b show the same results for the antenna with slot 1(spiral slot), in which the phase centre movements in all three ϕ planes are similar up to 9 GHz, with no detrimental effect on the overall performance of the phase centre curves. Fig. 4.11c and Fig. 4.12.c show the results for the antenna with slot 2 (circular arc), where the phase centre movements are similar in all three ϕ planes, with better performance at high frequencies. Thus, this band-stop slot design improves the overall performance of the phase centre carves in all three principle ϕ =0°, 45° and 90° planes. This is due to the fact that this circular arc slot was placed away from the feed region and is symmetric around the Z-axis. Fig. 4.11d and Fig. 4.12d show the results for the antenna with slot 3 (fork). It can be seen that the double effect of metal removal and the inclusion of a circular arc in the bottom of the radiator, attached to the centre of the feed region, did not disturb the performance of the phase centre curves. However this configuration did not improve the phase centre performance. Fig. 4.11e and Fig. 4.12e show the phase centre movement curves for the antenna with slot 4 (ring slot), where it can be seen that the effect of metal removal along with the inclusion of a ring attached to the feed region of the antenna has a noticeable deteriorating effect on the overall performance of the phase centre curves.

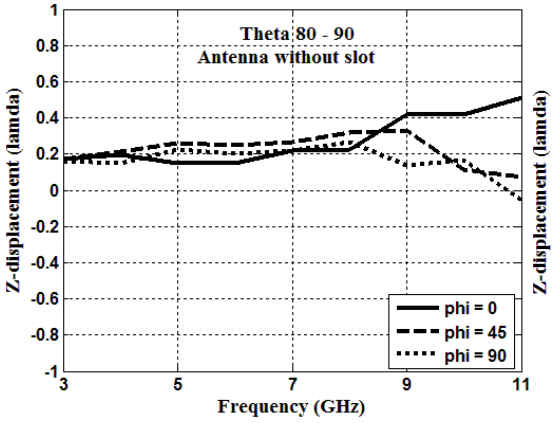

a) Antenna without slot

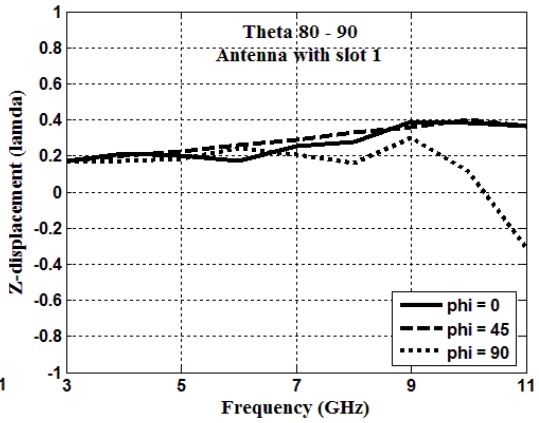

b) Antenna with slot 1

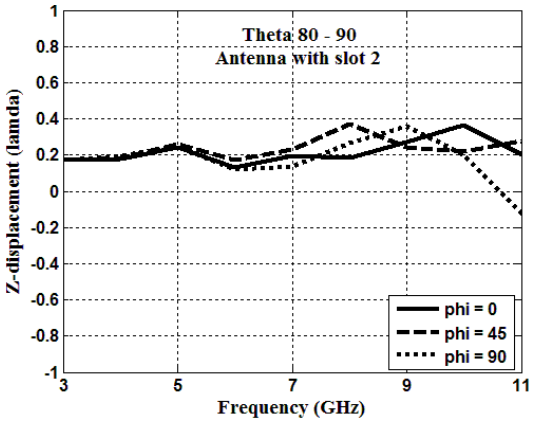

c) Antenna with slot 2

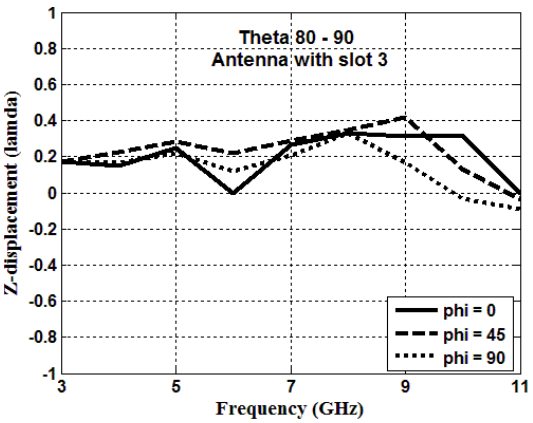

d) Antenna with slot 3

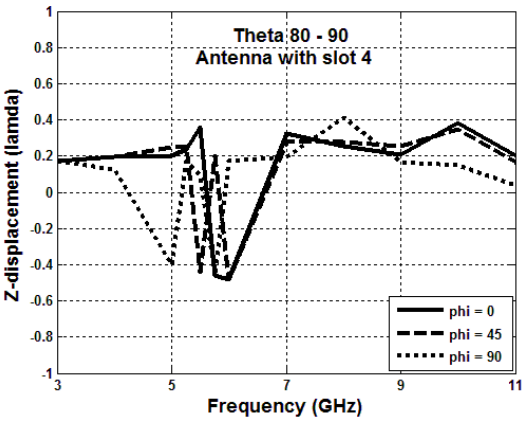

e) antenna with slot 4

Fig. 4.11 Phase centre displacements on Z-axis (in λ units at f=6.5GHz) correspond to the minimum change in the radiated E_θ phase for the θ range from 80° to 90°, at ϕ=0°, 45° and 90°

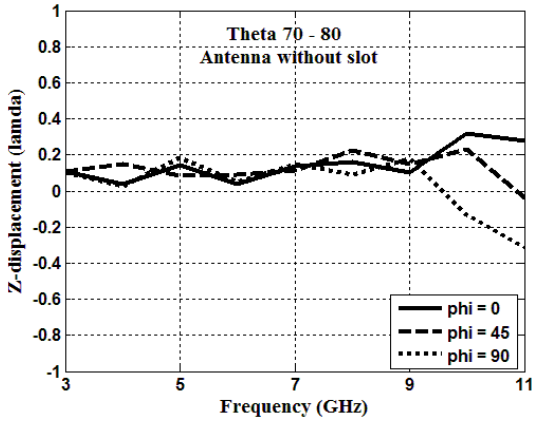

a) Antenna without slot

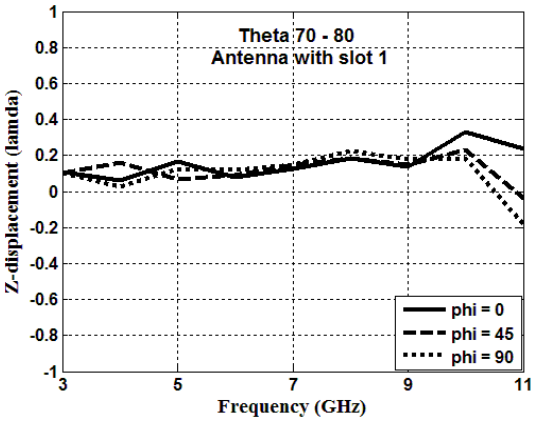

b) Antenna with slot 1 (spiral)

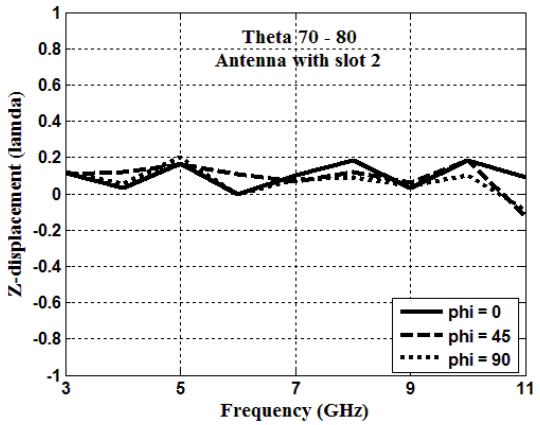

c) Antenna with slot 2 (circular arc)

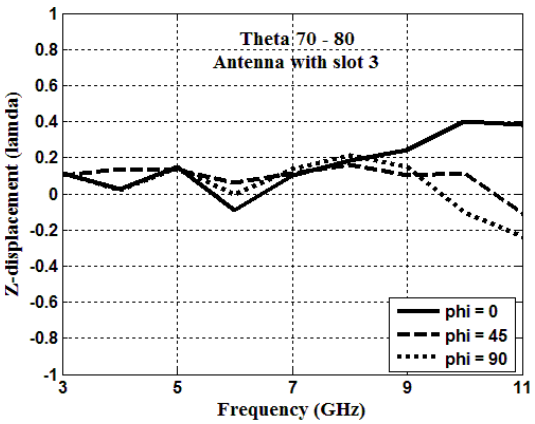

d) Antenna with slot 3 (fork)

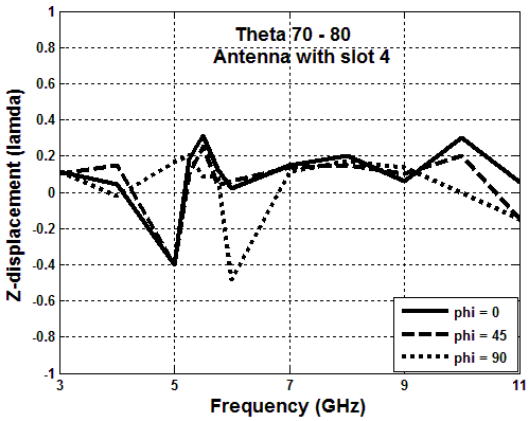

e) Antenna with slot 4 (ring)

Fig. 4.12 Phase centre displacements on Z-axis (in λ units at f=6.5GHz) correspond to the minimum change in the radiated E_θ phase for θ range from 70° to 80°, at ϕ=0°, 45° and 90°.

Table 4.4 summarizes the maximum range of the phase centre movement on the Z-axis for each antenna, over the entire frequency band and at the three principle ϕ = 0°, 45° and 90° planes. It should be noted that this range can be smaller if one is interested in the phase centre movement in one or two planes only. Based on the phase centre movement curves with frequency, the phase centre for each antenna could be determined over the entire frequency band at the three principle planes of ϕ = 0°, 45° and 90°, for θ range from 60° to 90°. However, some variation in the far field phase will be present and must be tolerated, in order to easily find the phase centre location over the entire band, and all principal planes.

	Antenna without slot	Antenna with slot 1 "spiral"	Antenna with slot 2 "Circular"	Antenna with slot 3 "fork"	Antenna with slot 4 "ring"
θ Range, deg.	Maximum phase centre movement range for the three principle planes ϕ=0°, 45° and 90°				
70^o to 90^o	0.6 λ	0.7 λ	0.5 λ	0.6 λ	0.9 λ
50^o to 90^o	0.6 λ	0.7 λ	0.6 λ	0.7 λ	0.9 λ

Table 4.4 Maximum phase centre movement ranges at ϕ =0°, 45° and 90° planes for the studied antennas, over 3 to 11 GHz. λ is the wave length at 6.5 GHz

4.7 Conclusion

In this chapter, the phase centre behavior of UWB monopole antennas was investigated. First the loci of the phase centre of the antenna was determined over the frequency band of operation at the three principle planes ϕ=0°, 45° and 90° for different θ ranges. It was found that the phase centre moves on the Z-axis with different behavior at the three principle planes ϕ=0°, 45° and 90°. To overcome this problem, a circular monopole antenna with two perpendicular planar cuts in X-Z and Y-Z over a ground plane was introduced which stabilized the phase centre behavior.

Also the phase centre locations of the square, circular and elliptical monopole antennas with trident-feeding structure studied in chapter 3 were investigated. A detailed phase centre movement loci of those antennas were determined. The phase centre loci were calculated at different principle planes ϕ=0°, 45° and 90° and for different θ ranges, over the frequency band of operation.

Finally, the phase centre loci of antennas with different band-stop functions were investigated. It was found that the current distribution and the active regions of UWB monopole antennas at different frequencies can be affected by inclusion of resonant features in the antenna structure, near or connected to the feed point. However by carefully selecting the feature shape and position, the phase centre curves of such antennas can be stabilized in all three principal ϕ =0°, 45° and 90° planes at a θ range from 60 to 90 degrees. In this study, the E-plane phase centre of a UWB circular

monopole antenna with different features for the band-stop function was calculated at each frequency and determined for the entire band. It was found that certain feature shapes have small, or even beneficial, effects on the antenna phase centre behavior, while others deteriorate the performance. Examples of Phase centre location behaviors, for different θ ranges were illustrated.

Chapter 5

Low cross-Polarization UWB Microstrip Antennas

5.1Introduction

Microstrip antennas are widely used due to their known characteristics including light weight, low price, ease of fabrication and integration with other UWB system components. However, they suffer from low gain and high cross polarization components.

In this chapter, novel microstrip antennas with UWB impedance and radiation pattern bandwidth and low cross polarization components are introduced to work over the communication frequency band. These antennas are designed over a 30 x30mm^2 substrate with ε_r = 2.5 and height h = 1.0 mm or 1.6 mm. A 30 x 7.95 mm^2 partial ground plane is used, which ensures a UWB impedance bandwidth. Furthermore, a notch is implemented in this ground plane to enhance the impedance bandwidth. Antennas are fed through microstrip or strip line feed with appropriate widths according to the height h of the substrate and its relative permittivity ε_r. Parametric studies are conducted to determine optimum critical dimensions including the ground plane, notch and distance between the radiator and ground plane. Fig. 5.1 shows the geometry of the three antenna configurations used in this study.

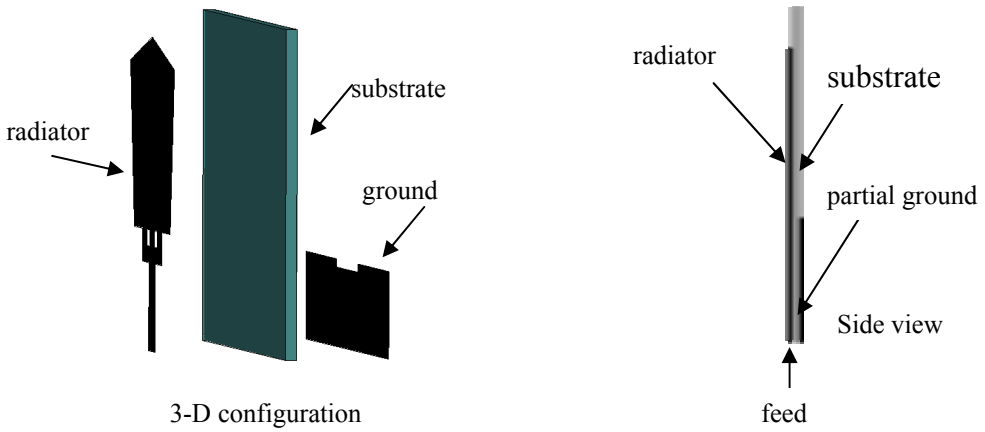

Fig. 5.1a Single layer UWB microstrip antenna

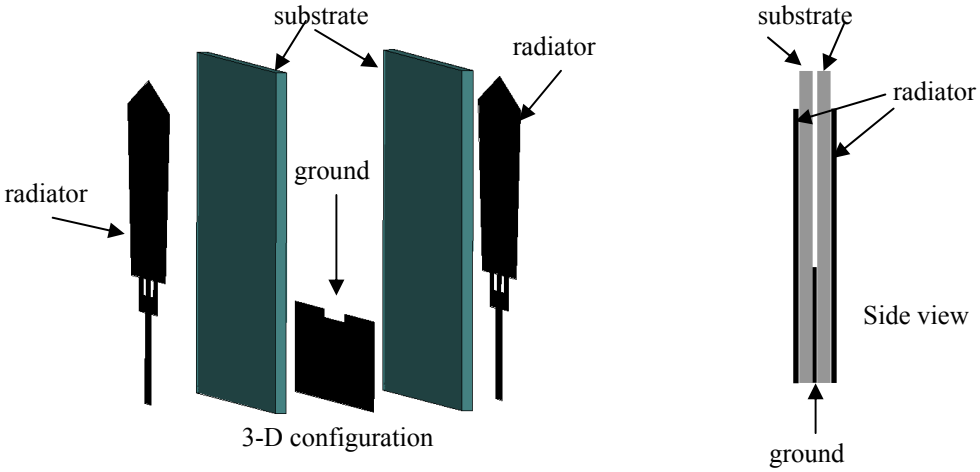

Fig. 5.1b Double layer UWB microstrip antenna with two identical radiators

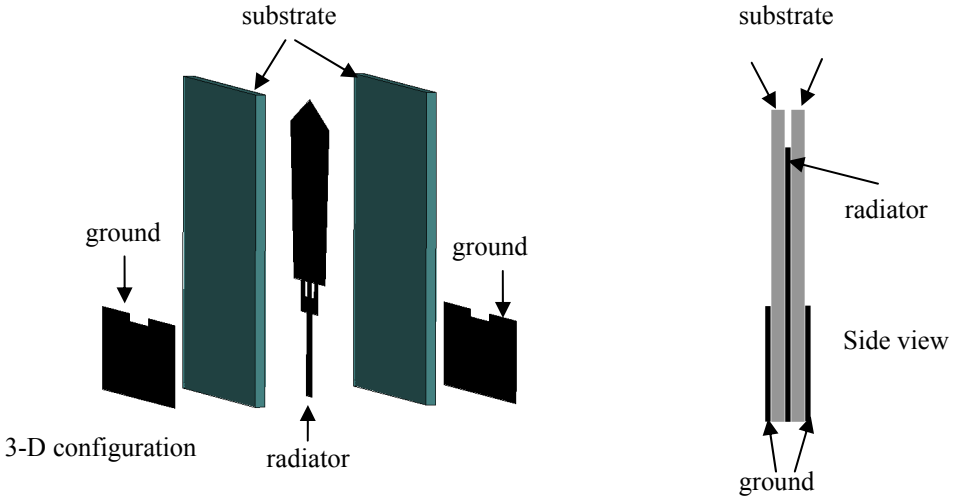

Fig. 5.1c Double layer UWB microstrip antenna with two identical grounds

5.2 Antenna Geometry

A novel trapezoidal shape radiator introduced in chapter 3 is used with some modifications including the tapering of the rectangle and adding three strips between the radiator and the microstrip line feed. The single layer microstrip antenna, shown in Fig. 5.1a, showed a UWB impedance bandwidth with a lower frequency edge of 3 GHz and upper one extending beyond 10.6 GHz. It also had omnidirectional radiation patterns. However the cross-polarization components were high especially at higher frequencies. To overcome this problem, in this chapter, double layer microstrip antennas with different configurations are investigated. In the first configuration, the partial ground plane is sandwiched between two identical radiators. In the second one, a strip-line feeding is used to feed one radiator sandwiched between two identical ground planes with the same previous parameters. Fig. 5.1b and Fig. 5.1c show these configurations. Parameters for the feed line are calculated using microstrip line and strip line formulas. Both new designs showed a significant reduction in the cross polarization components at all frequencies. More than 20 dB reduction is achieved at certain principle planes. Fig. 5.2 shows the novel arm shape introduced in this chapter with optimum parameters and partial ground plane with a notch.

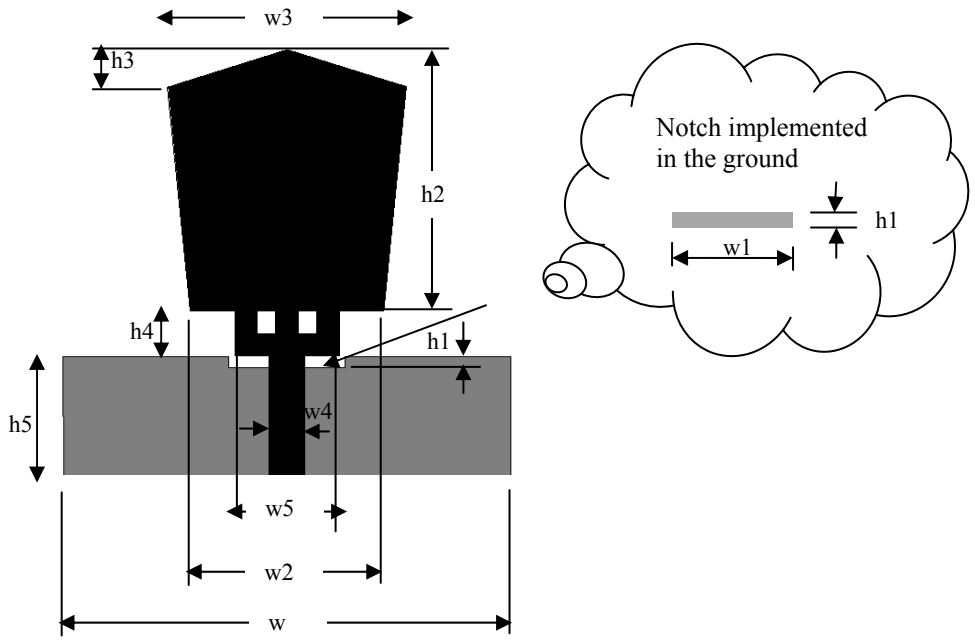

Fig. 5.2 UWB antenna and ground plane parameters

5.3 Polarization

As per IEEE definition, polarization of a radiated wave is that property of an electromagnetic wave describing the time-varying direction and relative magnitude of the electric field victor. In other words it is the curve traced by the end point of the arrow representing the instantaneous electric field. Polarization of a wave can be linear, circular or elliptical. At each point on the radiation sphere around the antenna, polarization is resolved into a pair of orthogonal polarization, co-polarization and cross-polarization. When designing a linear polarized antenna, it is then important to minimize the cross polarization components of the radiated field coming out from this antenna. The study in this chapter includes single and double layers antennas with microstrip and strip line

feedings. Simulations are conducted using Ansoft HFSS, a Finite Element Method software, and measurements are done at the University of Manitoba Antenna Laboratory to verify simulation results, [34].

5.4 Single Layer UWB Microstrip Antenna

Fig. 5.2 shows the single layer microstrip antenna investigated in this section. As can be seen, the antenna consists of a radiator with trapezoidal shape radiator with specific parameters on one side of a substrate. On the other side of the substrate, their exists a partial ground plane to support UWB impedance bandwidth. The feeding of this antenna is through a microstrip line feeding with width calculated using microstrip line impedance formulas based on the height, h and the permittivity, ε_r of the substrate.

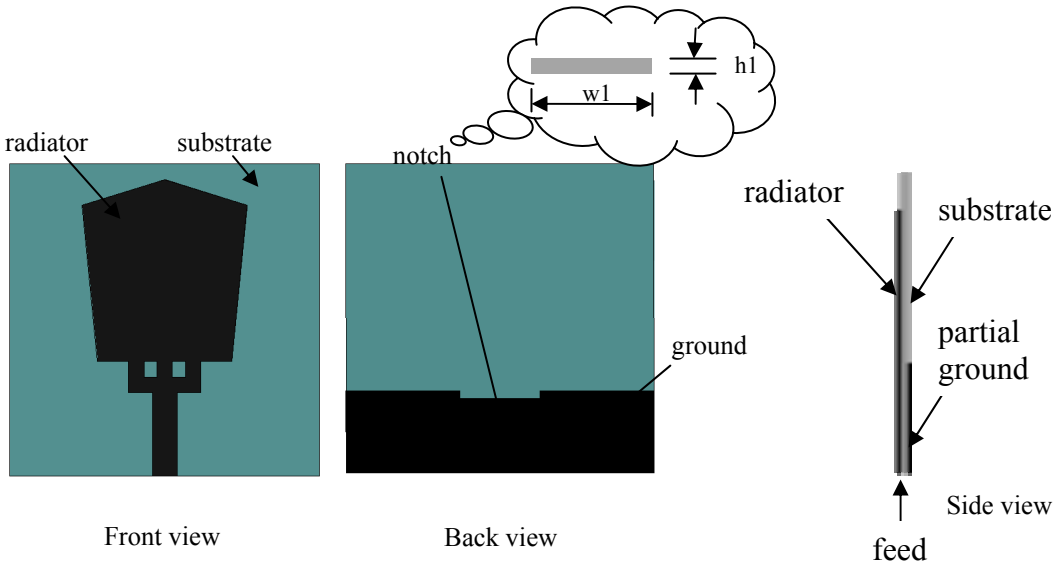

Fig. 5.3 Single layer UWB microstrip antenna with partial ground plane and trapezoidal radiator

Parametric studies are done to investigate the effect of important design parameters on the performance of this antenna. The first parameter is the trapezoidal length which was chosen to support impedance bandwidth starting at 3 GHz. Other important parameters include the ground plane size, notch dimensions, and distance of the radiator from the notch. In this study a 30x30 mm^2 substrate with a permittivity of ε_r=2.5 and height h=1mm is selected. Fig. 5.4a shows both the trapezoidal radiator and partial ground plane optimum parameter values. While Fig. 5.4b shows how this antenna is modeled using Ansoft HFSS software.

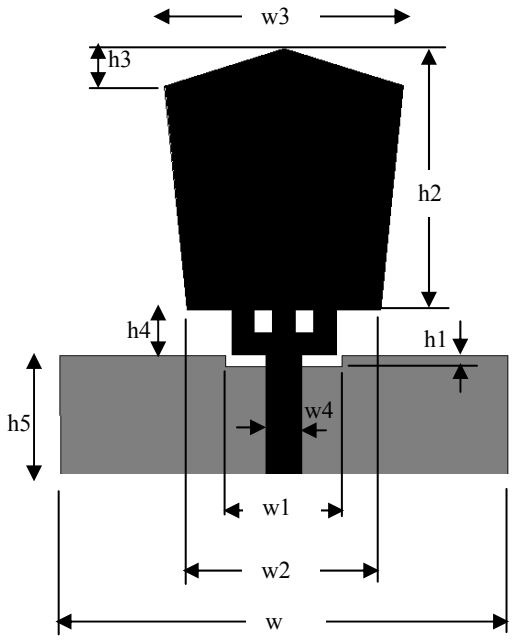

Fig. 5.4a UWB antenna parameters with optimum values as follows: w=30mm, h5=7.95mm, w1=7.8mm, h1=0.75mm, w4=2.4mm, h4=3mm, w2=13mm, w3=16mm, h2=17.5mm, h3=2.5mm

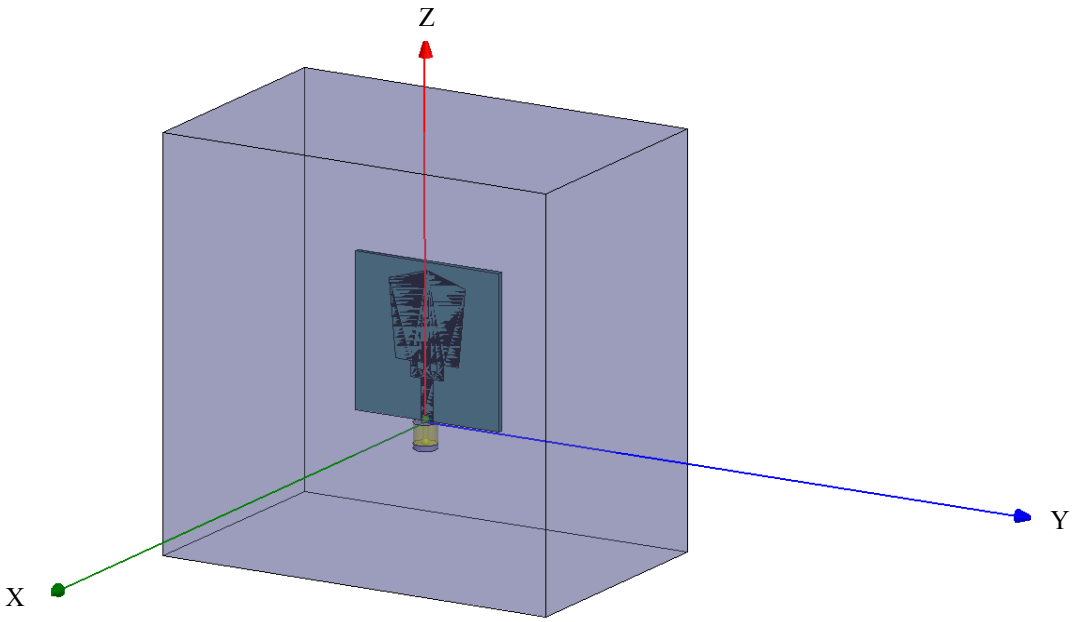

Fig. 5.4b Single layer UWB microstrip antenna including coaxial feed and radiation box, modelled in HFSS software

Parametric study results are shown in Fig. 5.5, Fig. 5.6 and Fig. 5.7. The return loss curves are plotted against frequency for different parameters. Important parameters include dimension of the notch, included in the partial ground plane, and the distance between the notch and the radiator. As can be seen from Fig. 5.5, the distance between the radiator and the notch D, affects both the low and high frequency edges. While the height of notch h1, affects both the mid and upper frequencies, Fig. 5.6. The width of the notch, w1, only affects the middle band frequencies, Fig. 5.7. The return loss curve of the single layer microstrip antenna with optimum parameters is shown in Fig. 5.8. While the return loss curves of the same antenna with different substrate parameters are shown in Fig. 5.9.

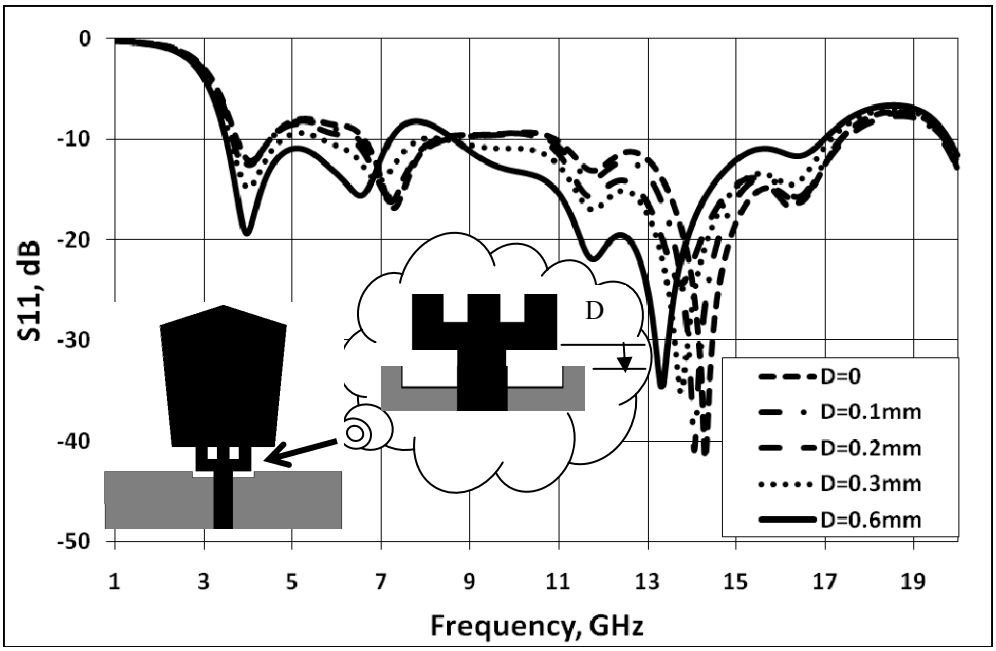

Fig. 5.5 Return loss curves of the single layer UWB microstrip antenna with different distance D from the notch. Other parameters shown in Fig. 5.4a are: w=30mm, h5=7.95mm, w1=7.8mm, h1=0.75mm, w4=2.4mm, h4=3mm, w2=13mm, w3=16mm, h2=17.5mm, h3=2.5mm

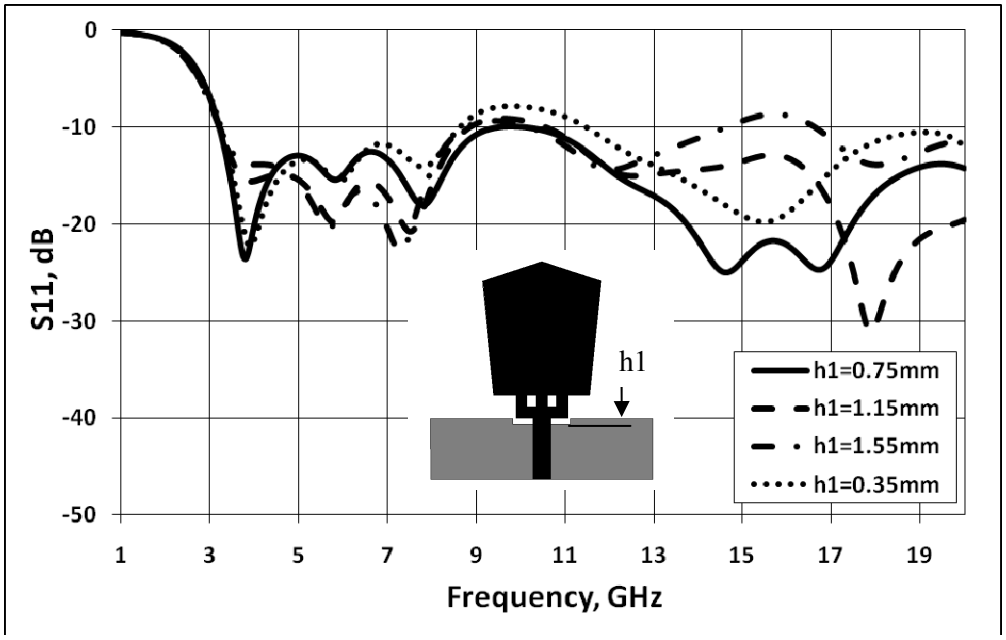

Fig. 5.6 Return loss curves of the single layer UWB microstrip antenna with different notch height h1. Other parameters shown in Fig. 5.4a are: w=30mm, h5=7.95mm, w1=7.8mm, D=0.6mm, w4=2.4mm, h4=3mm, w2=13mm, w3=16mm, h2=17.5mm, h3=2.5mm

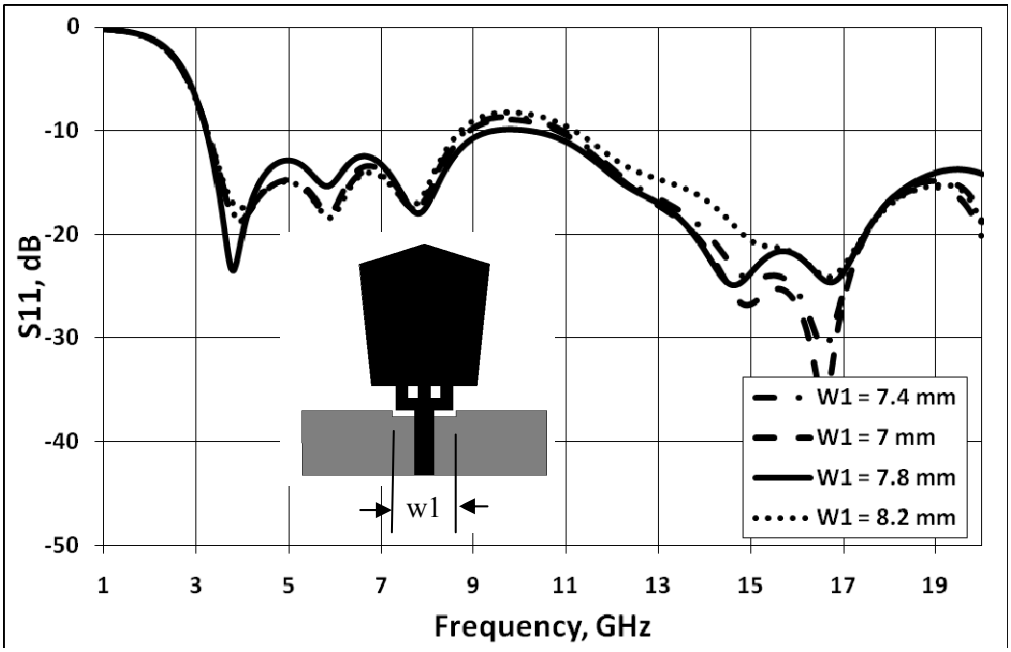

Fig. 5.7 Return loss curves of the single layer UWB microstrip antenna with different notch width w1. Other parameters shown in Fig. 5.4a are: w=30mm, h5=7.95mm, D=0.6mm, h1=0.75mm, w4=2.4mm, h4=3mm, w2=13mm, w3=16mm, h2=17.5mm, h3=2.5mm

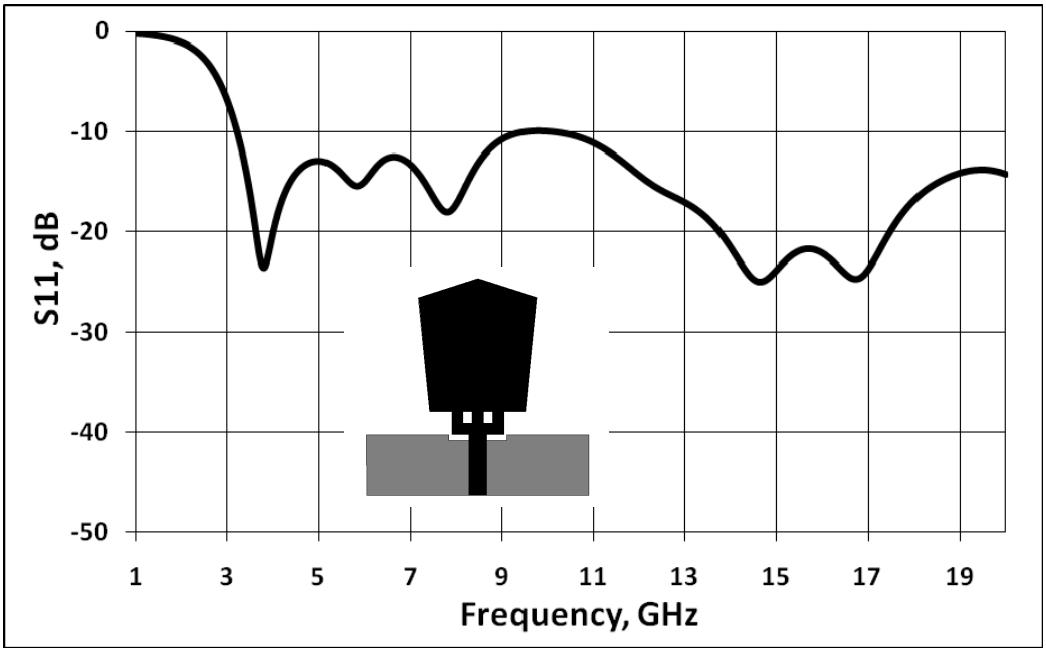

Fig. 5.8 Return loss curve for the UWB microstrip antenna with optimum parameters on a substrate with ε_r=2.5, h=1mm, w=30mm, h5=7.95mm, w1=7.8mm, h1=0.75mm, w4=2.4mm, h4=3mm, w2=13mm, w3=16mm, h2=17.5mm, h3=2.5mm, D=0.6mm

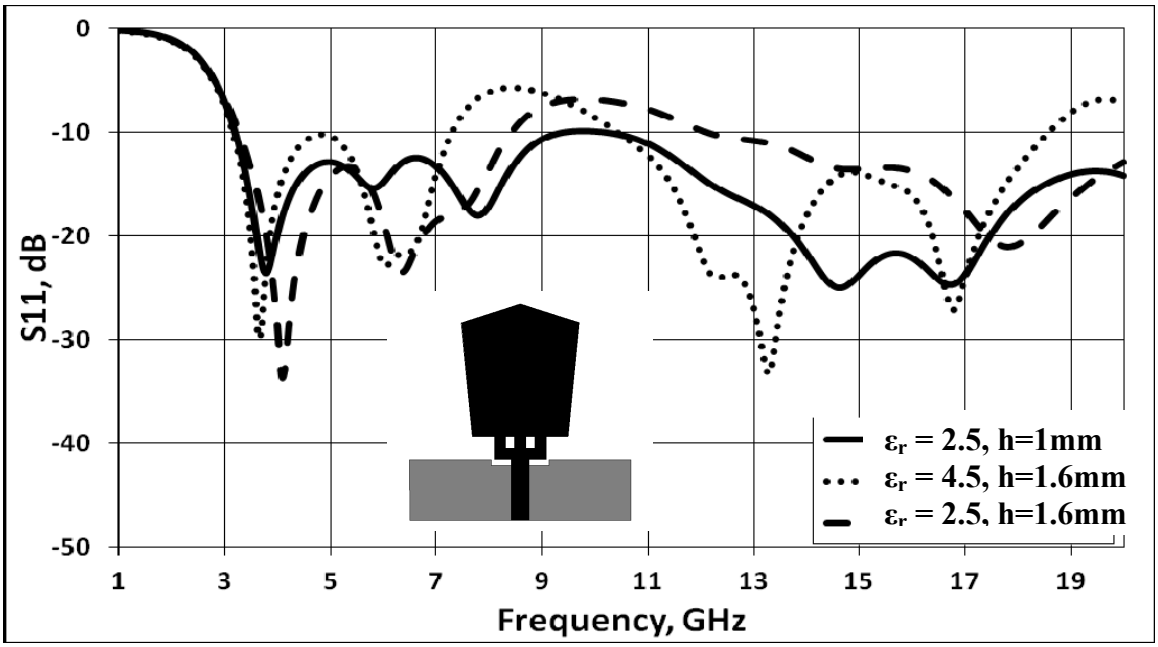

Fig. 5.9 Return loss curves of the single layer UWB microstrip antenna of Fig. 5.8 with different substrate parameters

The microstrip antenna with the trapezoidal radiator shape and single layer substrate showed UWB impedance bandwidth that can be controled by the design parameters of the antenna. In Fig. 5.10, the simulated efficiency at the direction of maximum radiation and at different frequencies are shown. The radiation pattern curves of this antenna at the three princible planes are shown in Fig. 5.11. As can be seen, the antenna has an omnidirectional pattern at the H- plane and dipole-like pattern at the E-plane. However, the cross polarization components are high especiaaly at higher frequencies.

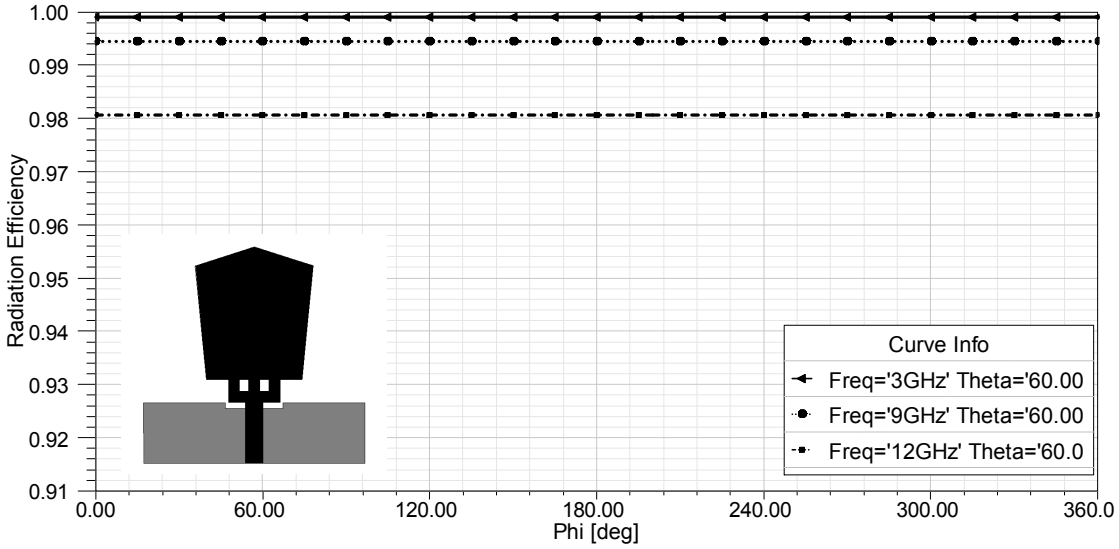

Fig. 5.10 Radiation efficiencies of the single layer UWB microstrip antenna with parameters shown in Fig. 5.8 at different frequencies and in the direction of maximum radiation angle

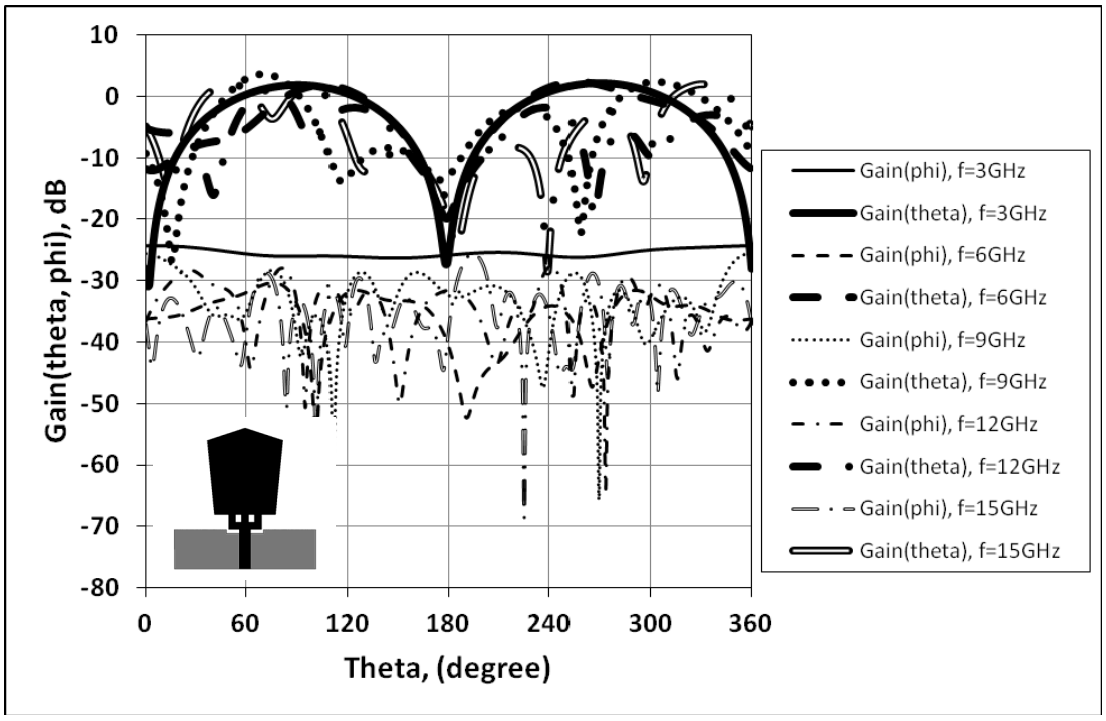

Fig. 5.11a Radiation patterns of the single layer UWB microstrip antenna with parameters shown in Fig. 5.8 at X-Z plane, $\phi = 0^{o}$

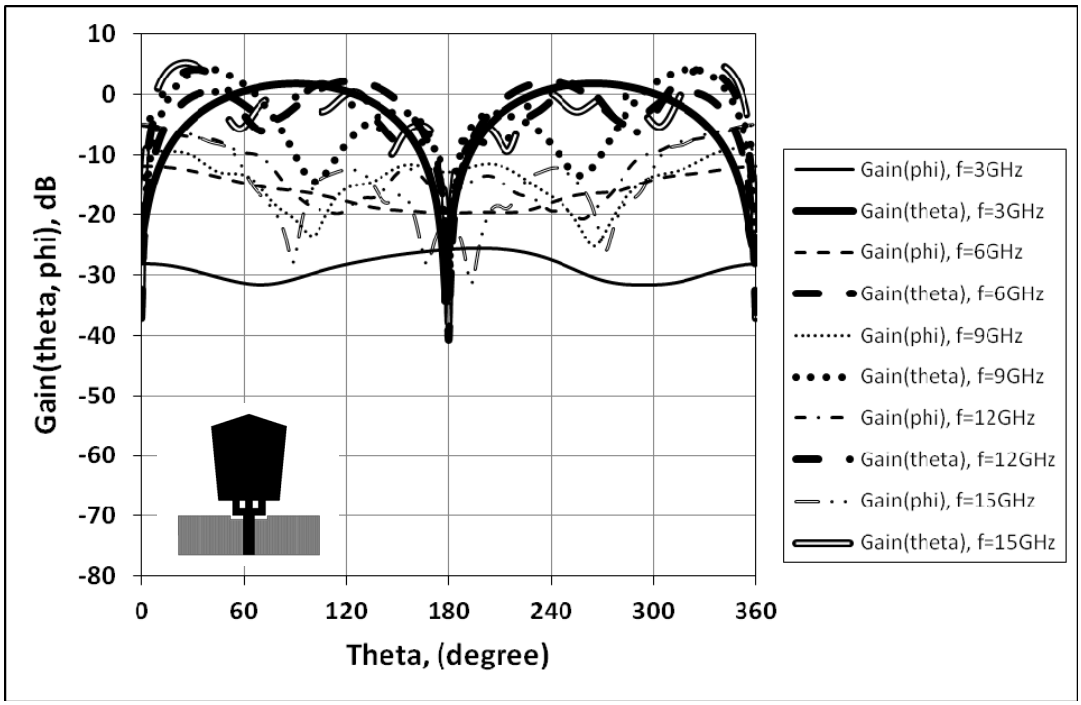

Fig. 5.11b Radiation patterns of the single layer UWB microstrip antenna with parameters shown in Fig. 5.8 at Y-Z plane, $\phi = 90^{o}$

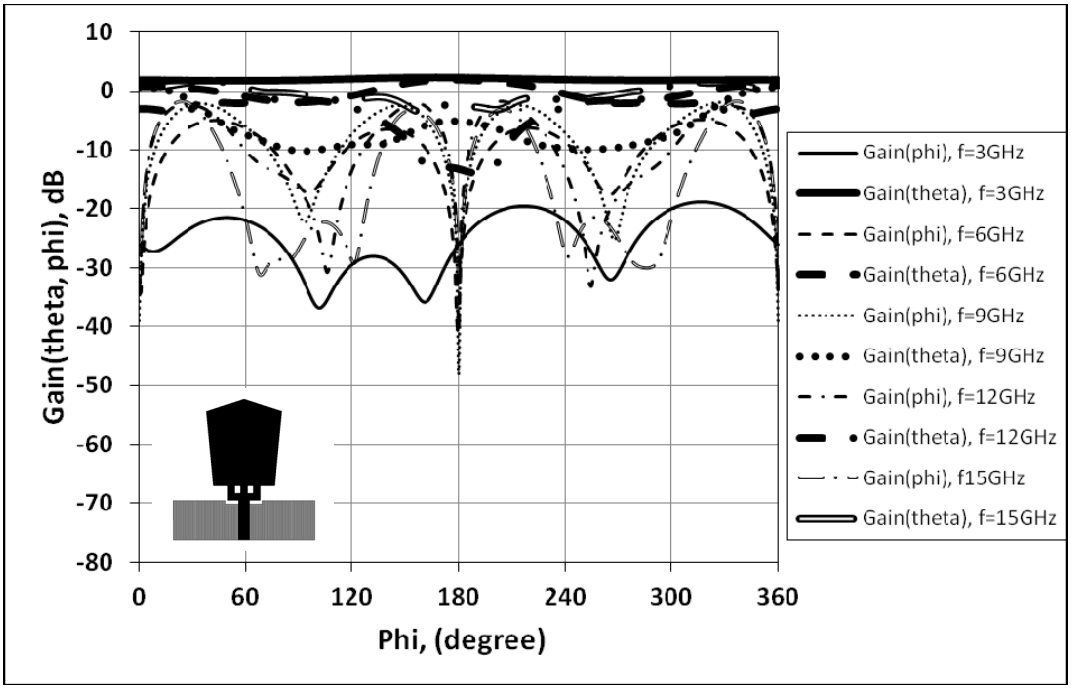

Fig. 5.11c Radiation patterns of the single layer UWB microstrip antenna with parameters shown in Fig. 5.8 at X-Y plane, $\theta = 90^{o}$

5.5 Double Layer Embedded-Ground Plane UWB Microstrip Antenna

The first attempt to reduce the cross polarization components of the single layer microstrip antenna introduced in section 5.3 is by implementing double layer design with the same parameters of the trapezoidal radiator and the partial ground plane. The two substrates used are of ε_r=2.5 and height h=1mm. The only parameter that will be changing here is the width of the microstrip line w4, from 2.4 to 1.5mm, using the strip line design formulas. Fig. 5.1b shows the side view and the 3-D configuration of the double layer microstrip antenna having the same partial ground plane, before being sandwiched between two identical substrates. Then, two identical trapezoidal radiators the same as designed before are etched on both outer sides of the substrates. Their parameters are shown in Fig. 5.12.

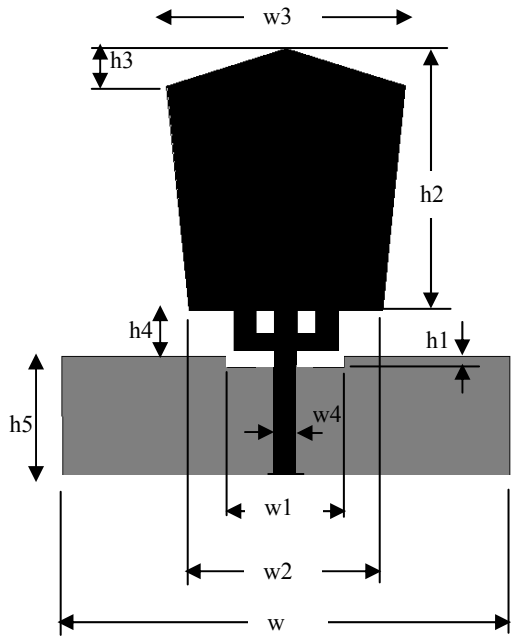

Fig. 5.12 Radiator and partial ground plane parameters for the double layer UWB microstrip antenna with configuration shown in Fig. 5.12. w=30mm, h5=7.95mm, w1=7.8mm, h1=0.75mm, w4=1.5mm, h4=3mm, w2=13mm, w3=16mm, h2=17.5mm, h3=2.5mm

The return loss curve of this antenna is shown in Fig. 5.13. The parameters used to design this antenna are shown in Fig. 5.12. As can be seen from the return loss curve, this antenna has a UWB impedance bandwidth. The radiation efficiency curves of the antenna at different frequencies at the maximum radiation direction are shown in Fig. 5.14.

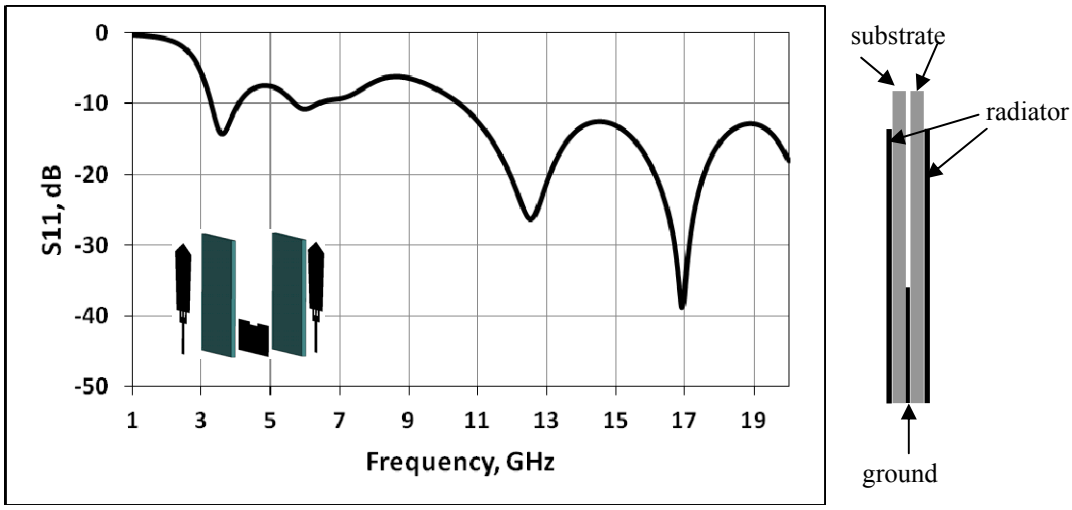

Fig. 5.13 Return loss of the double layer UWB microstrip antenna with embedded ground plane with configuration shown in Fig. 5.12 and parameters shown in Fig. 5.13

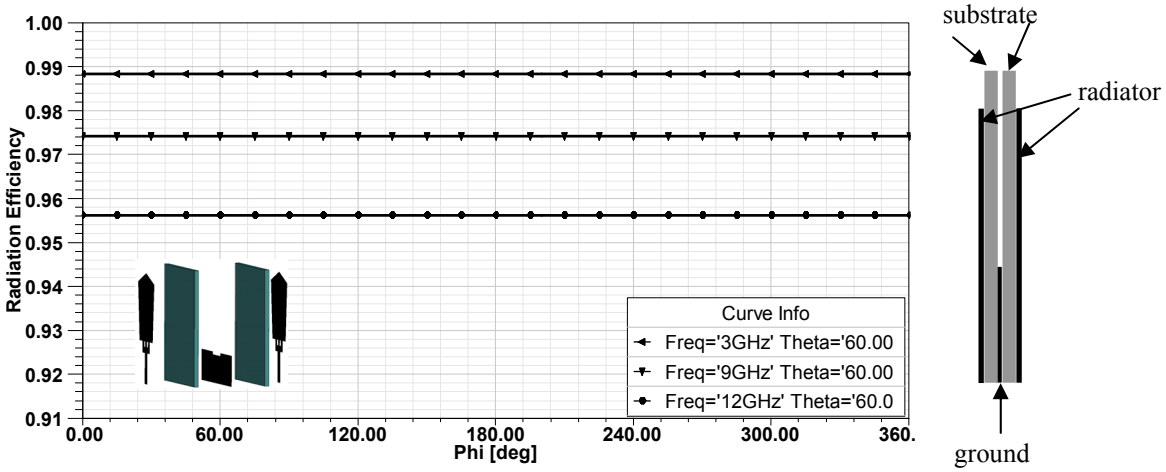

Fig. 5.14 Radiation efficiencies of the double layer UWB microstrip antenna with embedded ground plane, with configuration shown in Fig. 5.1b and parameters shown in Fig. 5.12, at different frequencies and maximum radiation angle

The radiation patterns of this antenna at the three principle planes and at different frequencies are shown in Fig. 5.15. The antenna shows low cross polarization components at different frequencies, especially at Y-Z plane.

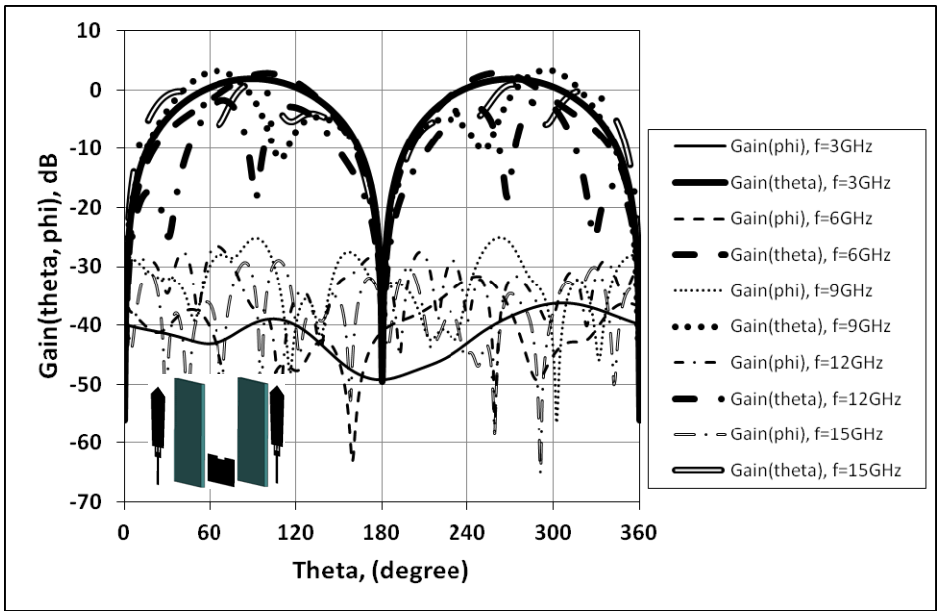

Fig. 5.15a Radiation patterns of the double layer UWB microstrip antenna shown in Fig. 5.12 with parameters shown in Fig. 5.13 at X-Z plane, $\phi = 0^{o}$

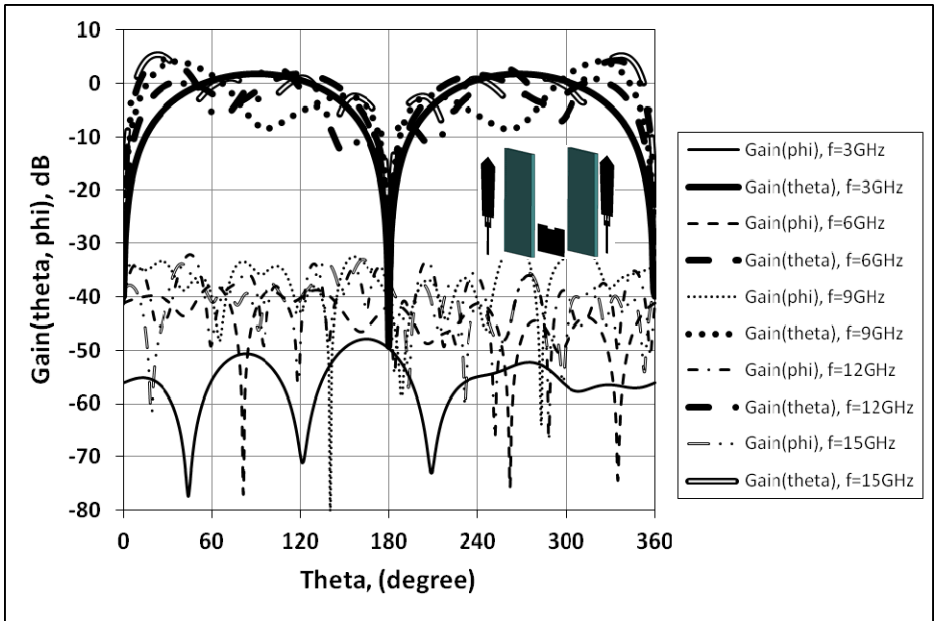

Fig. 5.15b Radiation patterns of the double layer UWB microstrip antenna shown in Fig. 5.1b with parameters shown in Fig. 5.12 at Y-Z plane, $\phi = 90^{o}$

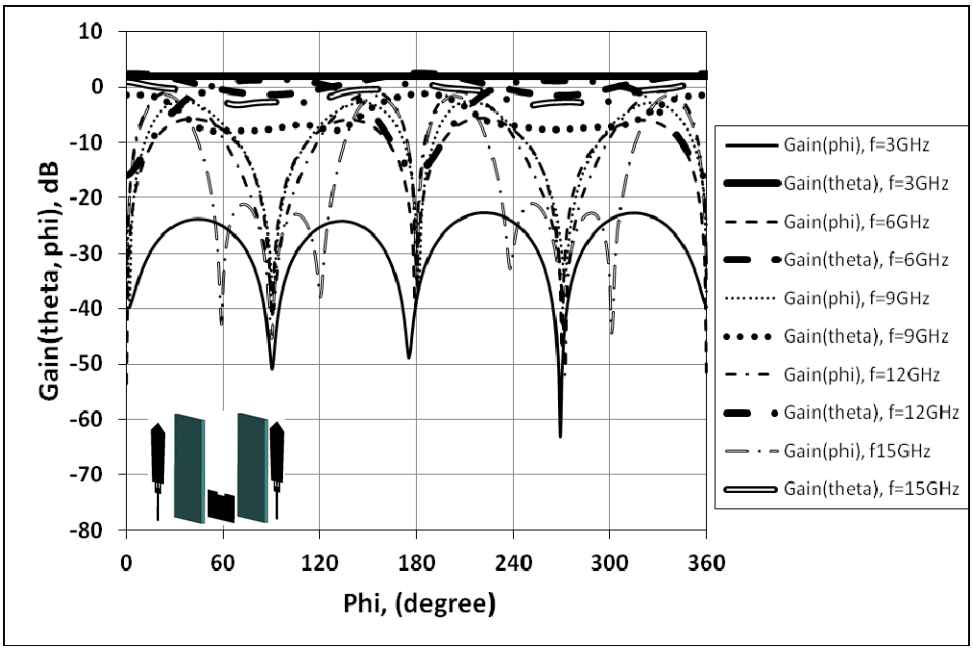

Fig. 5.15c Radiation patterns of the double layer UWB microstrip antenna shown in Fig. 5.1b with parameters shown in Fig. 5.12 at X-Y plane, $\theta = 90^{o}$

5.6 Double Layer Strip-Line Fed UWB Antenna

The second attempt to reduce the cross polarization components of the single layer microstrip antenna introduced in section 5.4 is by implementing another double layer design with the same parameters of the trapezoidal radiator and the partial ground plane. The two substrates used are of ε_r=2.5 and height h=1mm. The only parameter that will be changing here is the width of the microstrip line w4 from 2.4 to 1.5mm, using the strip line design formulas. Fig. 5.1c shows the side view and the 3-D configuration of the double layer microstrip antenna having the same trapezoidal radiator used as before being sandwiched between two identical substrates. Then, two identical partial ground planes same as designed before are etched on both outer sides of the substrates. Their parameters are shown in Fig. 5.12.

The return loss curve of this antenna is shown in Fig. 5.16. The parameters used to design this antenna are shown in Fig. 5.12. As can be seen from the return loss curve, this antenna has a UWB impedance bandwidth. The radiation efficiency curves of the antenna at different frequencies at the maximum radiation direction are shown in Fig. 5.17.

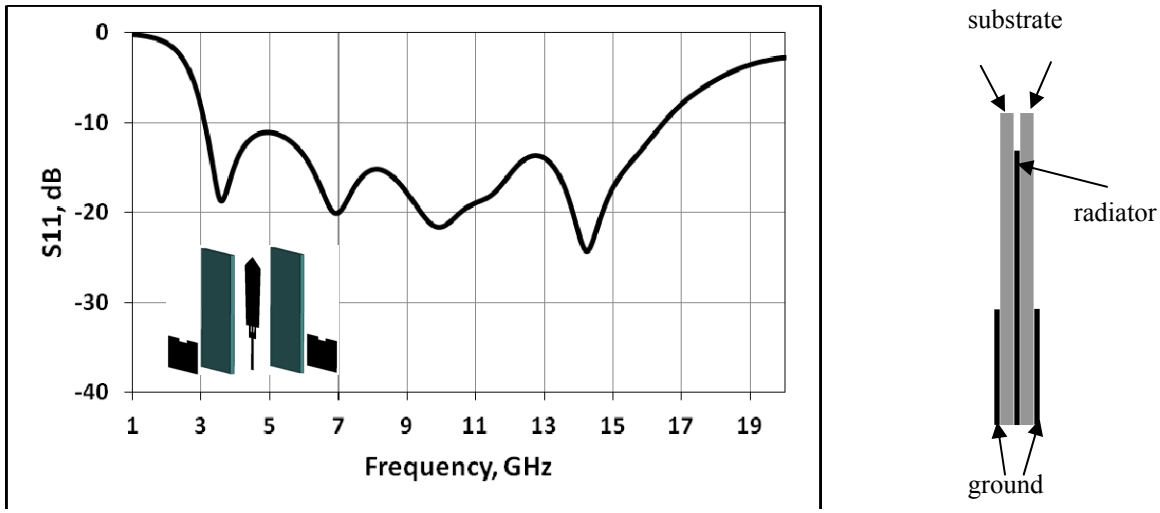

Fig. 5.16 Return loss of the double layer UWB microstrip antenna with strip-line feed with configuration shown in Fig. 5.1c and parameters shown in Fig. 5.12

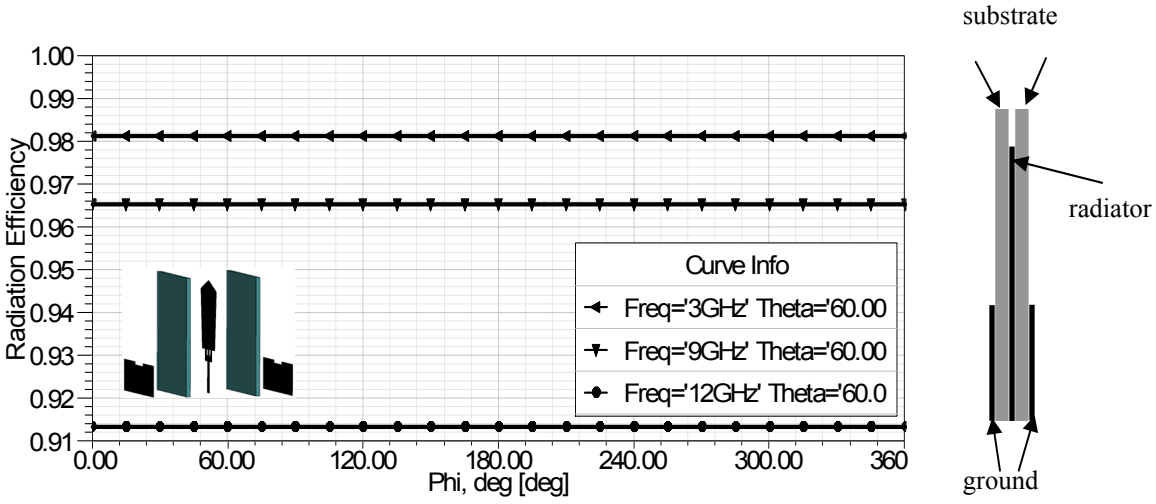

Fig. 5.17 Radiation efficiencies of the double layer microstrip antenna with strip-line feed with configuration shown in Fig. 5.1c and parameters shown in Fig. 5.12, at different frequencies and maximum radiation angle

The radiation patterns of this antenna at the three principle planes and at different frequencies are shown in Fig. 5.18. The antenna shows low cross polarization components at different frequencies especially at Y-Z plane.

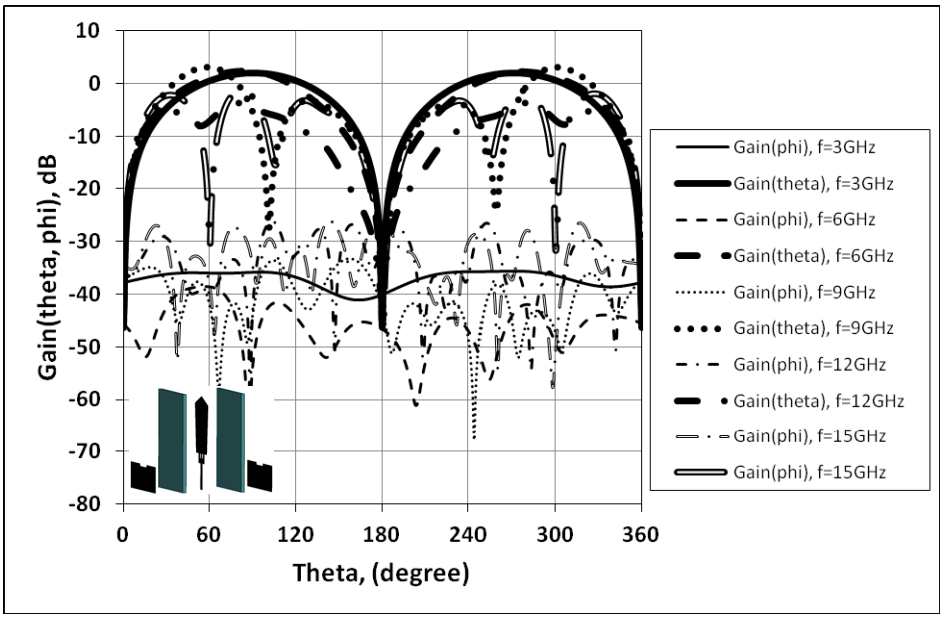

Fig. 5.18a Radiation patterns of the double layer UWB microstrip antenna shown in Fig. 5.1c with parameters shown in Fig. 5.12 at X-Z plane, $\phi = 0^o$

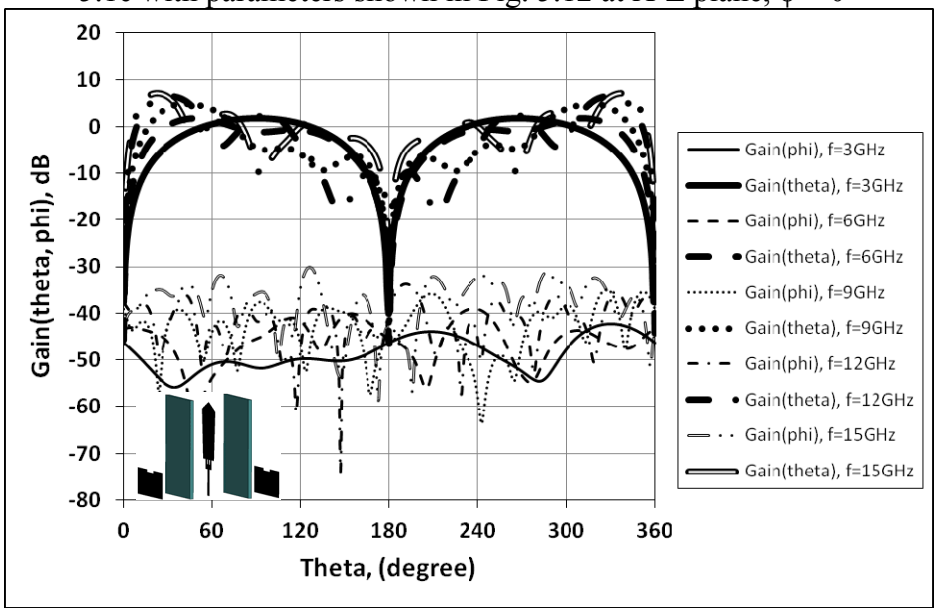

Fig. 5.18b Radiation patterns of the double layer microstrip antenna shown in Fig. 5.1c with parameters shown in Fig. 5.12 at Y-Z plane, $\phi = 90^o$

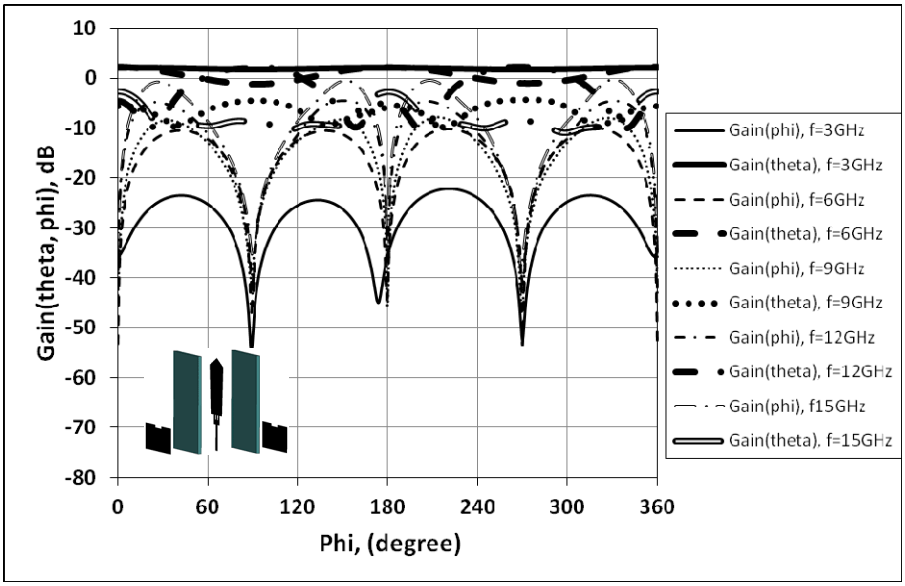

Fig. 5.18c Radiation patterns of the double layer UWB microstrip antenna shown in Fig. 5.1c with parameters shown in Fig. 5.12 at X-Y plane, $\theta = 90^{o}$

5.7 Performance Comparison for the Studied Microstrip Antennas

In this section, comparison will be made between the microstrip antennas with single and double layer configurations, studied in Section 5.4, 5.5 and 5.6. This comparison will include return loss curves and radiation patterns at different frequencies and different principal planes.

5.7. 1 Antennas of Figs. 5.1a and 5.1b

The Return loss curves of these antennas are given in Fig. 5.19, the single layer showing more superior results. Their radiation patterns are shown in Fig. 5.20 at Y-Z plane, $\phi=90^{o}$, and at different frequencies. Their copolar patterns are about the same, but the double layer antenna with two radiator gives much lower cross polarization.

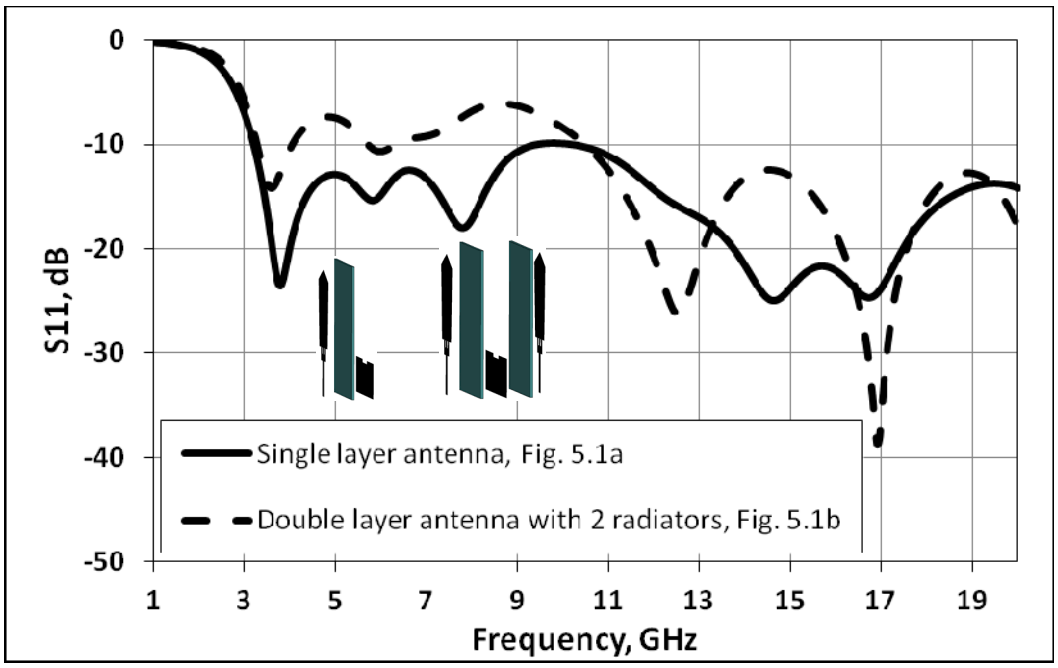

Fig. 5.19 Return loss curves for the single layer UWB microstrip antenna shown in Fig. 5.1a with parameters shown in Fig. 5.4a and and the double layer antenna shown in Fig. 5.1b with parameters shown in Fig. 5.12

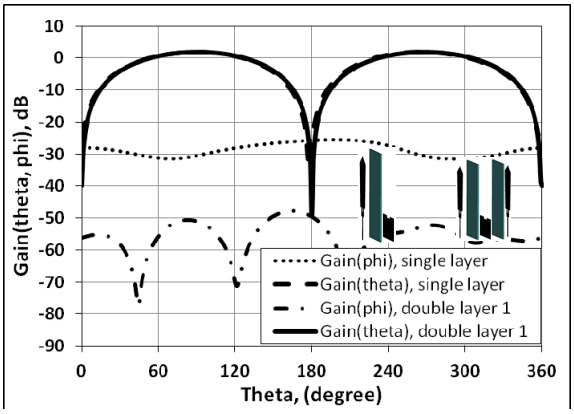

f = 3GHz, ϕ=90^o

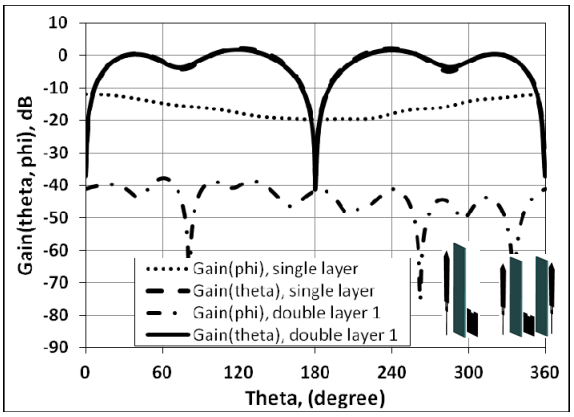

f=6GHz, ϕ=90^o

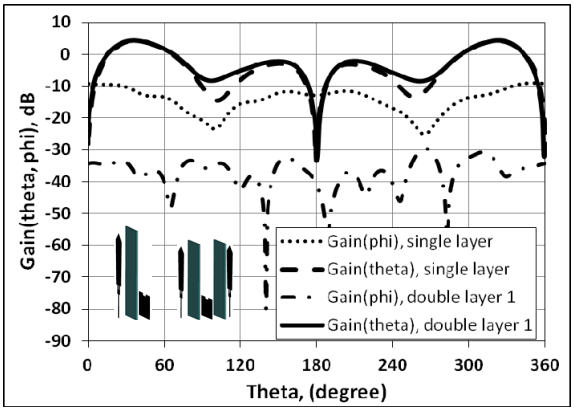

f = 9GHz, ϕ=90^o

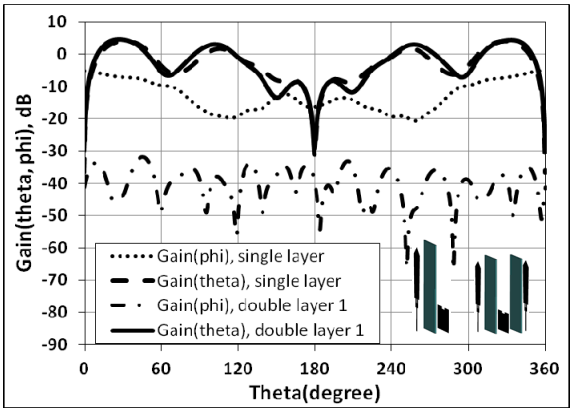

f=12GHz, ϕ=90^o

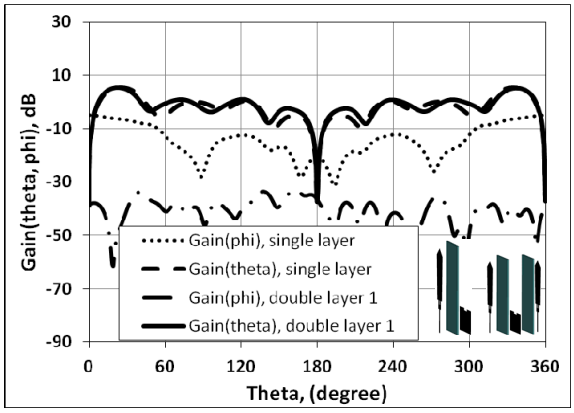

f = 15GHz, ϕ=90^o

Fig. 5.20 Radiation patterns at Y-Z plane, ϕ=90^o, of the single layer UWB microstrip antenna of Fig. 51a with parameters shown in Fig. 5.4a and the double layer UWB microstrip antenna with two radiators of Fig. 5.1b with parameters shown in Fig. 5.12

5.7. 2 Antennas of Figs. 5.1a and 5.1c

The Return loss curves of these antennas are given in Fig. 5.21, and both are satisfactory. Their radiation patterns are shown in Fig. 5.22 at Y-Z plane, $\phi=90^{o}$, and at different frequencies. The double layer antenna again gives lower cross polarization.

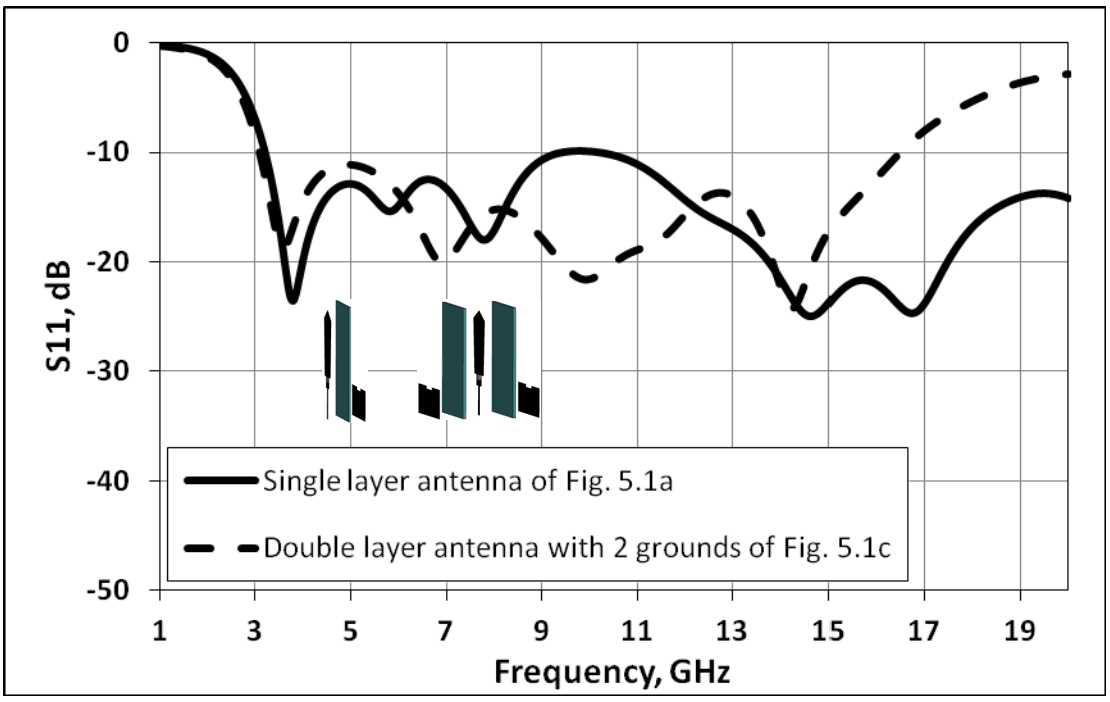

Fig. 5.21 Return loss curves for the single layer UWB microstrip antenna shown in Fig. 5.1a with parameters shown in Fig. 5.4a and the double layer UWB microstrip antenna shown in Fig. 5.1c with parameters shown in Fig. 5.12

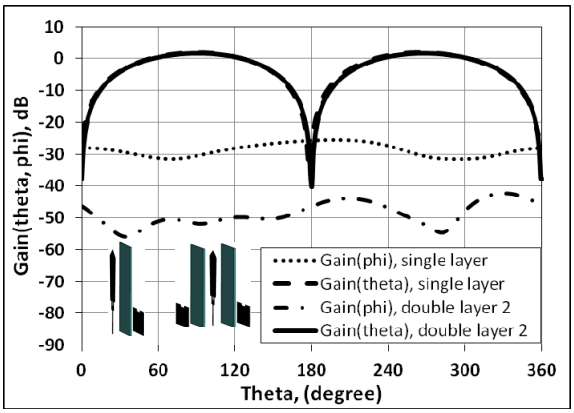

f = 3GHz, ϕ=90^o

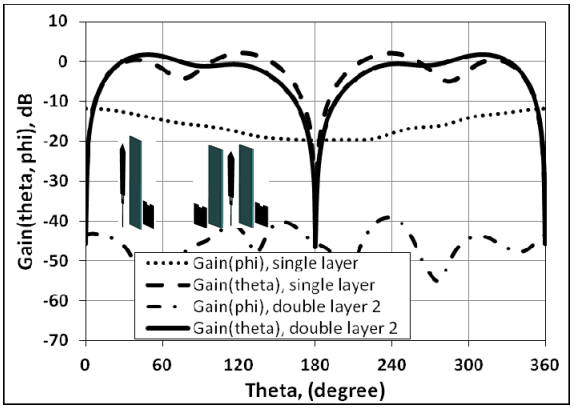

f=6GHz, ϕ=90^o

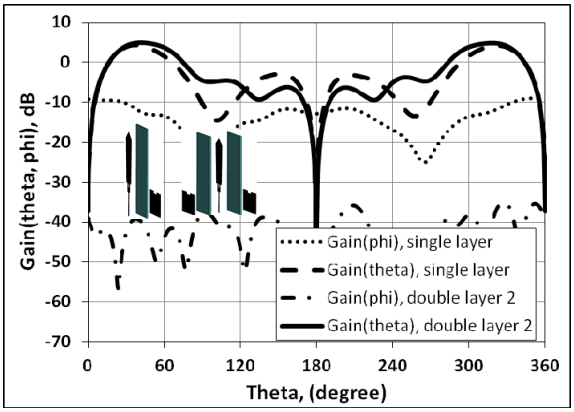

f = 9GHz, ϕ=90^o

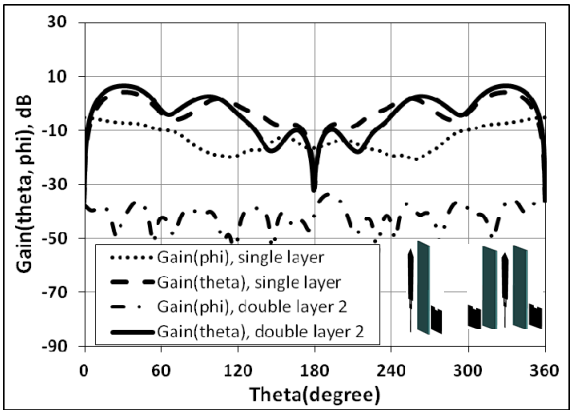

f=12GHz, ϕ=90^o

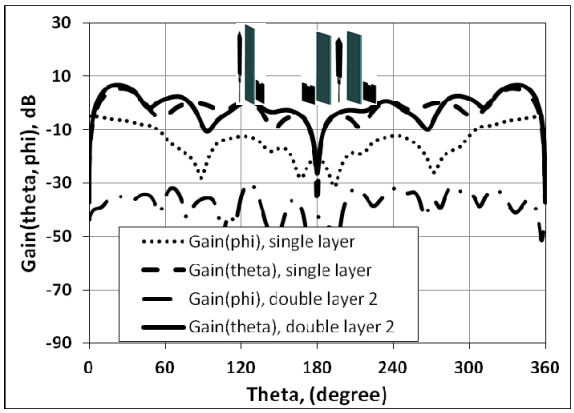

f = 15GHz, ϕ=90^o

Fig. 5.22 Radiation patterns at Y-Z plane, ϕ=90^o, of the single layer UWB microstrip antenna of Fig. 51a and the double layer microstrip antenna with two grounds of Fig. 5.1c.

5.8 Effect of Layer Misalignment on the Cross Polarization

In this section, the effect of misalignment between layers of the double layer antennas is studied. The study is done for the double layer microstrip antenna of Fig. 5.1c, with strip-line feed. The antenna is shown in Fig. 5.1c with optimum parameters given in Fig. 5.4a. The antenna has two identical substrates. The radiator and one ground plane are etched on both sides of one of them. The other substrate only has one ground plane on one side and no metal on the other side. In this study, displacements on Y- and Z-axis are implemented on the substrate, which has only the ground plane, as shown to the right of Fig. 5.23. The maximum cross polarization levels at $\phi=90^{o}$ plane, are shown in Figs 5.24 and 5.25 at different frequencies, for different displacements along the Y- and Z-axes. As can be seen, the cross polarization levels are more sensitive to the layers misalignments, along the Z-axis than along the Y-axis.

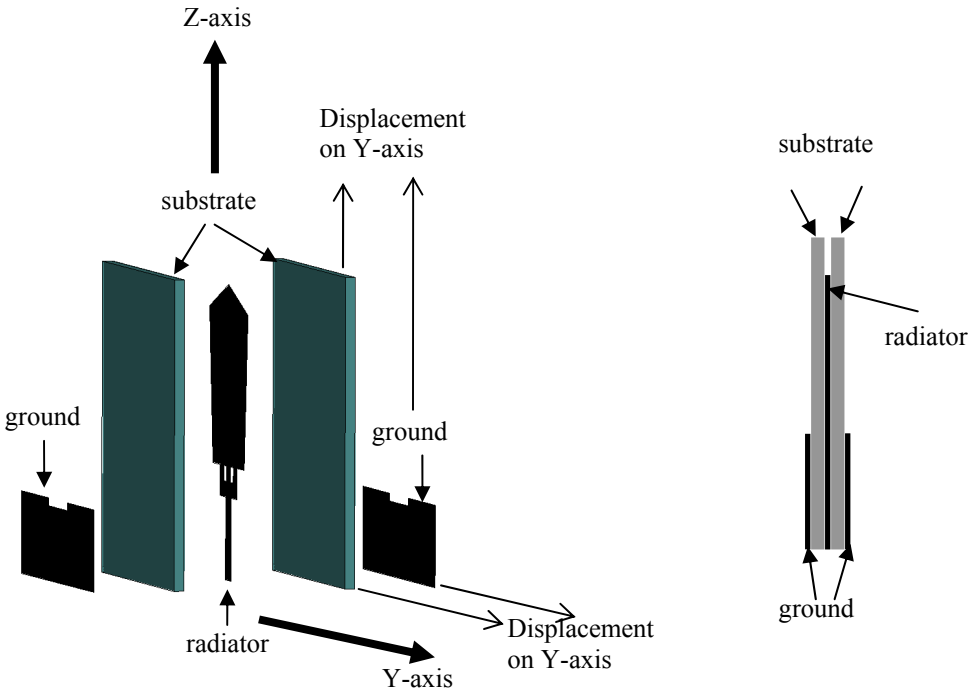

Fig. 5.23 Double layer UWB microstrip antenna of Fig. 5.1c, studied in Section 5.6. Parameters are given in Fig. 5.12

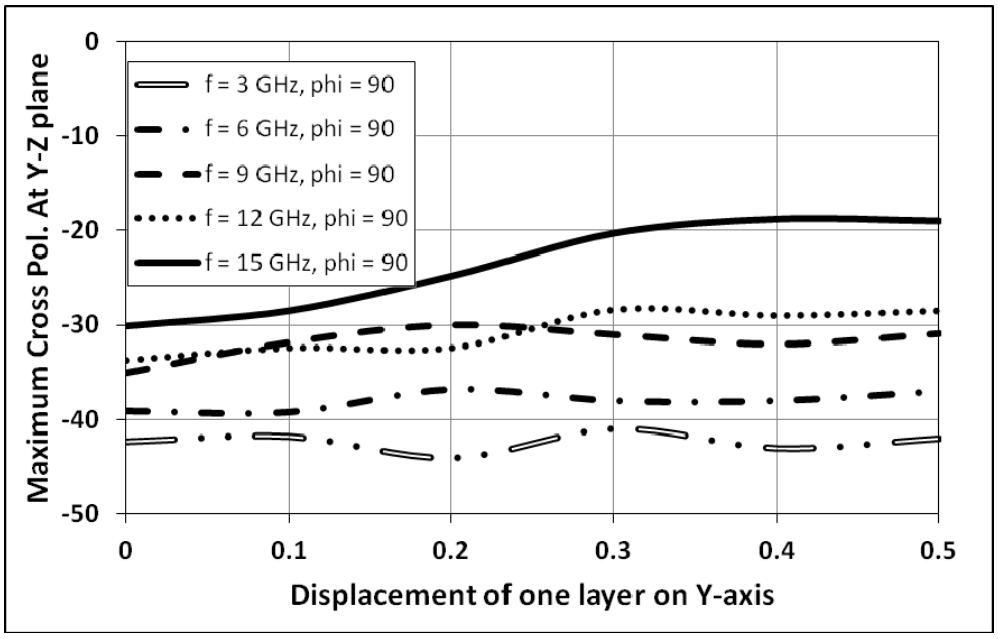

Fig. 5.24 Maximum Cross polarization levels (dB) at $\phi=90^{o}$ plane, of the antenna shown in Fig. 5.1c, with the displacement of the ground plane along the Y-axis (mm)

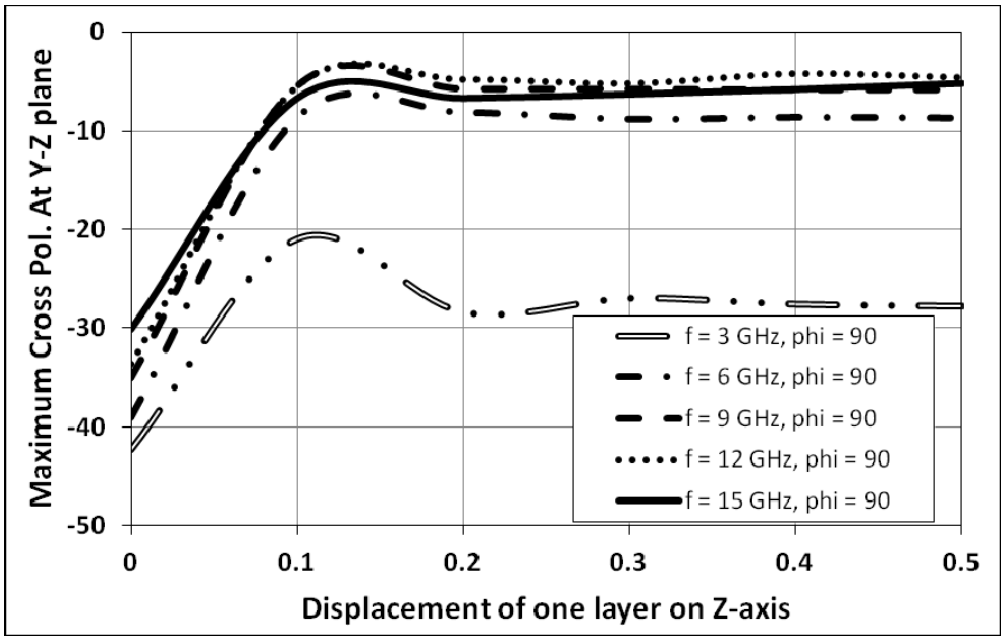

Fig. 5.25 Maximum Cross polarization levels (dB) at $\phi=90^{o}$ plane, of the antenna shown in Fig. 5.1c, with the displacement of one of the ground planes along the Z-axis (mm)

5.9 Fabricating and Testing UWB Microstrip Antennas

To verify the simulated results presented in section 5.4 through section 5.6, two microstrip antennas are fabricated and tested at the University of Manitoba Antenna Laboratory. Both the single layer microstrip antenna introduced in section 5.4 and the double layers microstrip antenna with strip line feeding and two ground planes, introduced in section 5.6 are built and tested. A 30 x 30 mm^2 substrate with $\varepsilon_r = 2.5$ and height, h = 1.6 mm is used for both antennas. Fig. 5.26 shows the picture of the fabricated single and double layers microstrip antennas. Fig. 5.27 and Fig. 5.28 show the measured and simulated return loss curves for both antennas. As can be seen both antennas have UWB impedance bandwidth and there is a good agreement between simulated and measured curves.

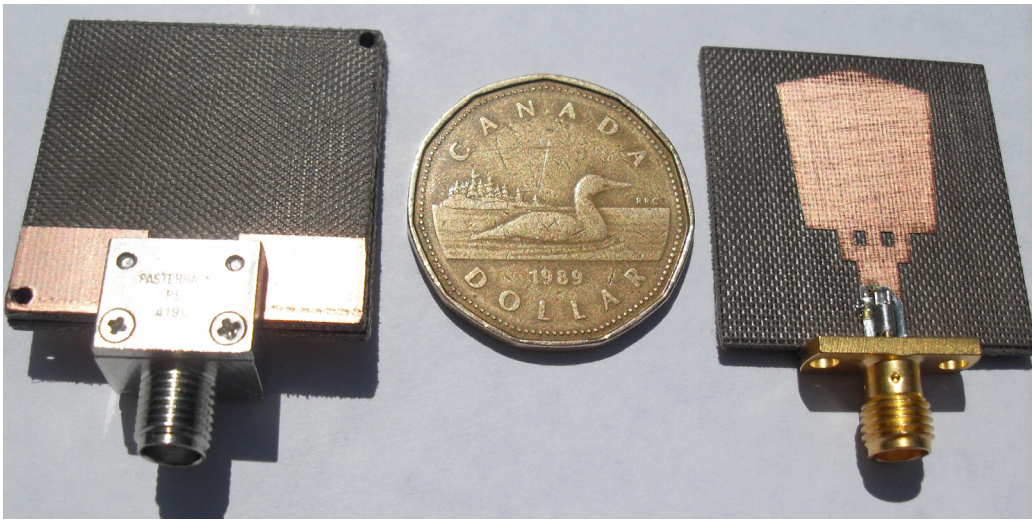

Fig. 5.26 Single layer UWB microstrip antenna of Fig. 4.1a with parameters given in Fig. 5.4a and double layer UWB microstrip antenna of Fig. 5.1c with parameters given in Fig. 5.12.

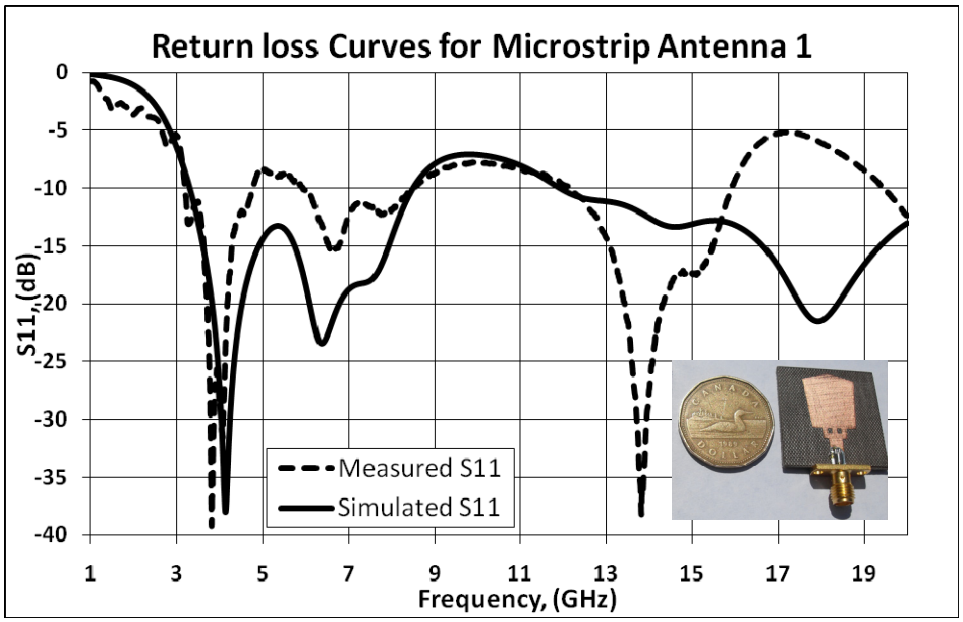

Fig. 5.27 Measured and simulated return loss curves for the single layer UWB microstrip antenna of Fig. 5.1a with parameters shown in Figs. 5.4a

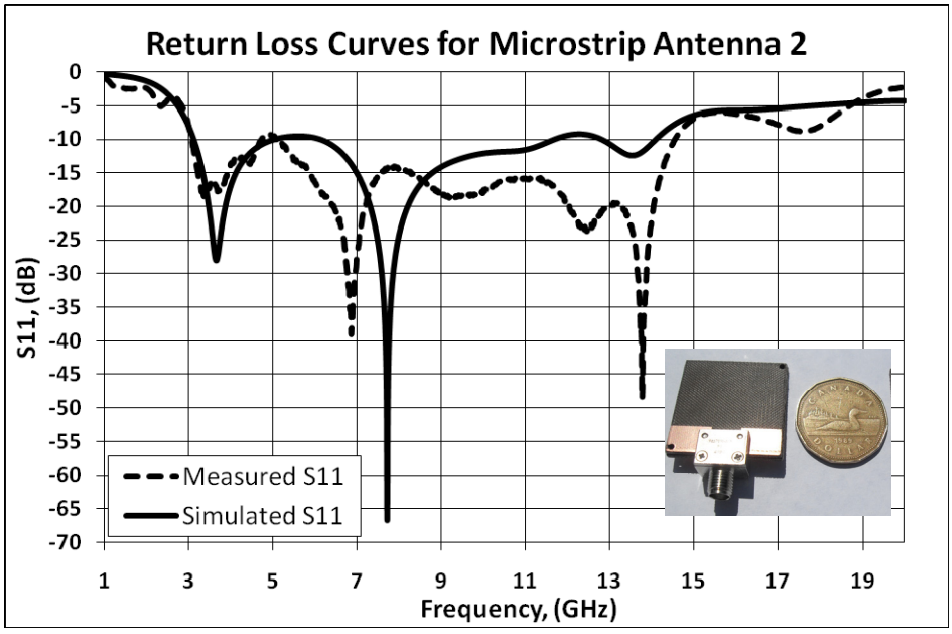

Fig. 5.28 Measured and simulated return loss curves for the double layer UWB microstrip antenna of Fig. 5.1c with with parameters shown in Figs. 5.12

Radiation patterns for both antennas are measured at different planes and at different frequencies. Radiation patterns are measured at both E and H planes. Fig. 5.29 shows picture of both antennas, ready for radiation pattern measurements. The measured radiation patterns of both antennas are compared in Fig. 5.30 and 5.31. As can be seen, the double layer microstrip antenna with strip line feeding gives lower cross polarization comonents than the single layer one.

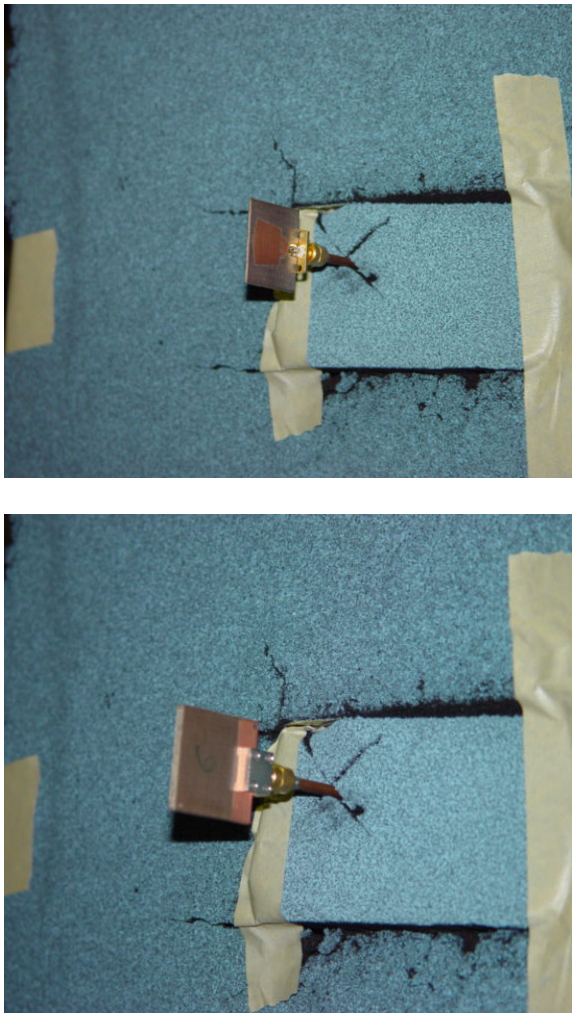

Fig. 5.29 Single and double layer UWB microstrip antennas mounted and ready for radiation pattern measurements at the University of Manitoba Antenna Laboratory

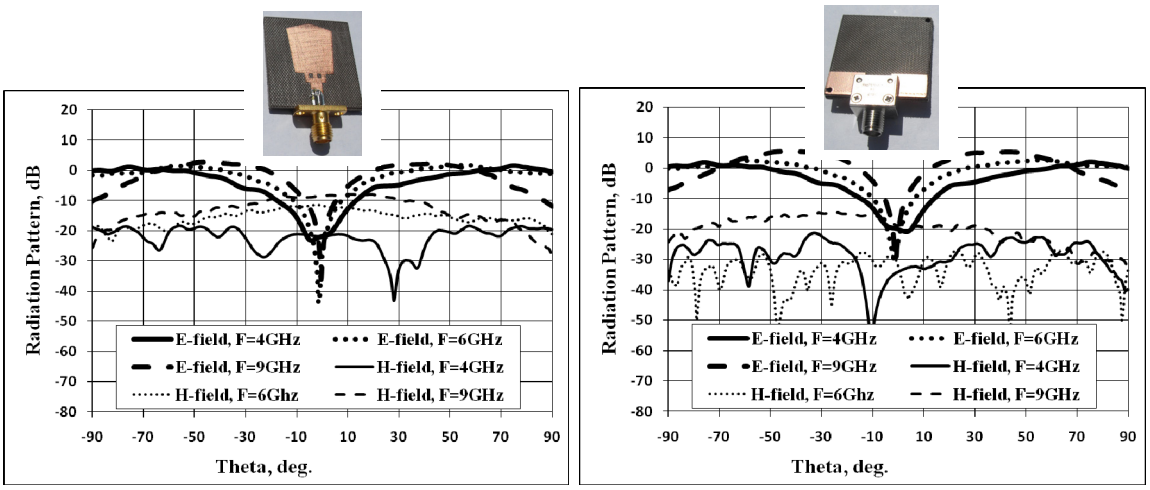

X-Z plane, $\phi = 0^o$

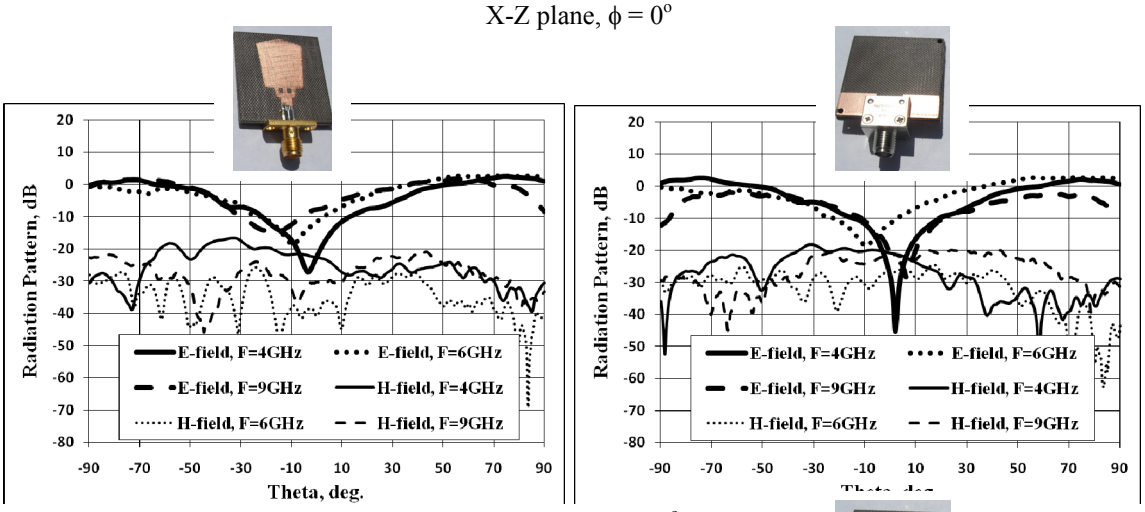

Y-Z plane, $\phi = 90^o$

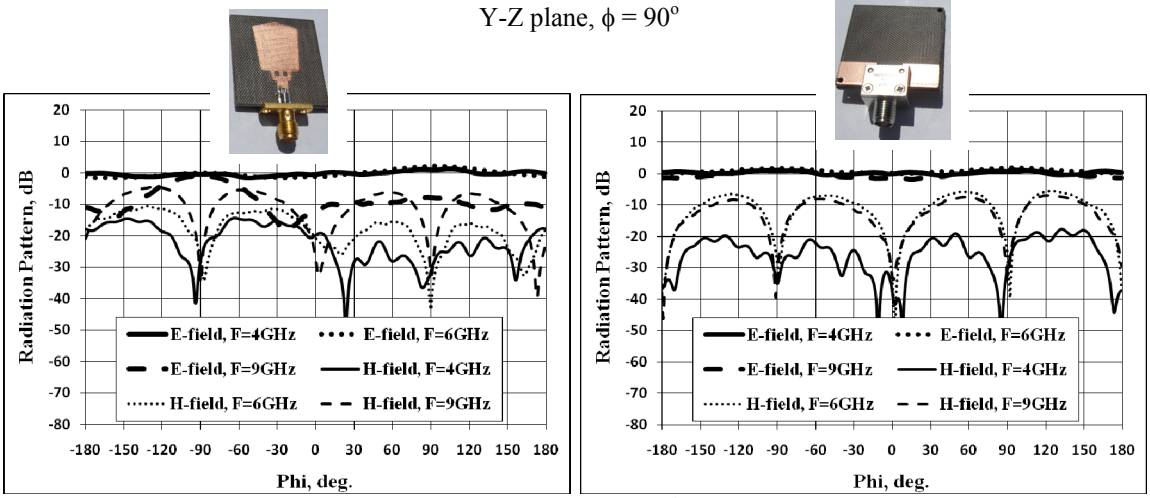

X-Y plane, $\theta = 90^o$

Fig. 5.30 Measured radiation patterns of single and double layer UWB microstrip antennas shown in Fig.5.26 at different frequencies, (f = 4, 6 and 9 GHz)

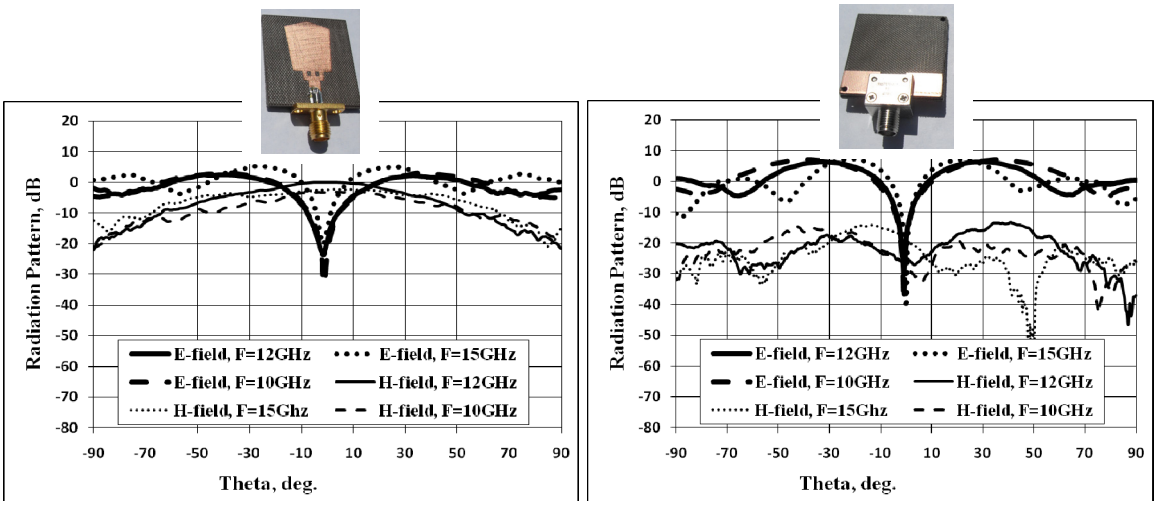

X-Z plane, $\phi = 0^o$

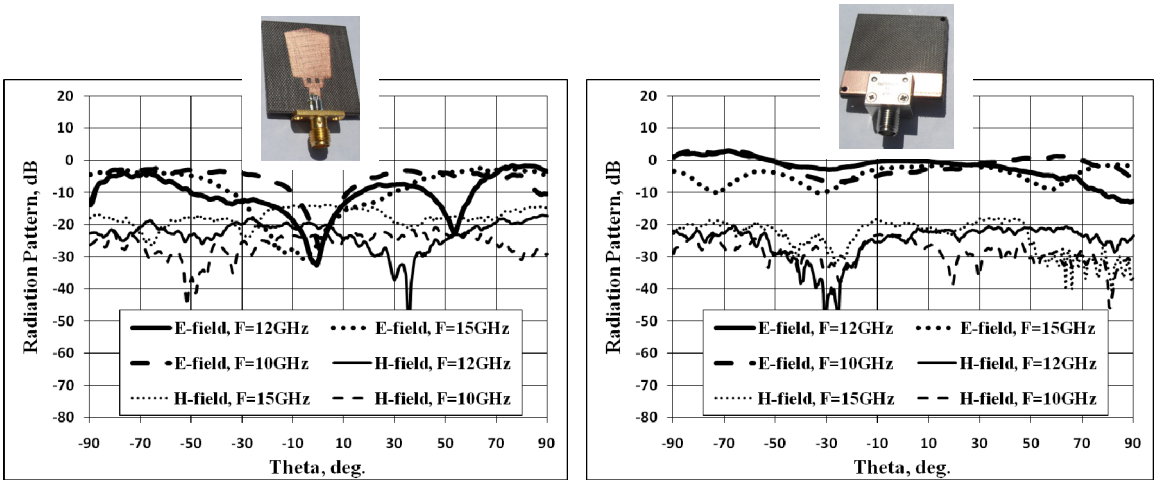

X-Y plane, $\theta = 90^o$

Fig. 5.31 Measured radiation patterns of single and double layer UWB microstrip antennas shown in Fig. 5.26 at different frequencies, (f = 10, 12 and 15 GHz)

5.10 Conclusion

In this chapter, a novel microstrip antenna with UWB impedance and radiation pattern bandwidth and low cross polarization components was investigated to work over the UWB communication frequency band. Both single and double layer antennas were

designed over a 30 x 30mm^2 substrate, with ε_r= 2.5 and different heights. A partial ground plane with width 30mm and length 7.95mm was used to increase the impedance bandwidth. Furthermore, a notch was implemented in the ground plane to enhance the impedance bandwidth. The antenna was fed through a microstrip line of width=2.4mm. Parametric studies were done to determine its optimum critical dimensions including the ground plane, notch and distance between the radiator and ground plane. A novel trapezoidal shape radiator was used with some modifications, including tapering of the rectangle and adding three strips between the radiator and the microstrip line feed. The antenna showed a UWB impedance bandwidth, starting at 3 GHz and extending beyond 10.6 GHz, with omnidirectional patterns in the H-plane. However the cross-polarization components were high, especially at high frequencies. To overcome this problem, two modifications were implemented to reduce the cross polarization components of this antenna. First, a double layer microstrip antenna was introduced in which the partial ground plane was sandwiched between the two identical radiators separated by two identical substrates. Second, a double layer microstrip antenna with a strip-line feed was investigated. In this design the radiator was sandwiched between two identical ground planes separated by two identical substrates with the same previous parameters. Parameters for the feed lines were calculated using the microstrip and strip line design formulas. Both new designs showed significant reductions in the cross polarization components at all frequencies. More than 20 dB reduction was achieved at ϕ=90^o plane, at different frequencies. The effect of misalignment between the two layers on the cross polarization levels was also investigated. It was shown that the maximum cross polarization levels were increased when one of the layers was displaced along the Y- or

Z-axis. Two antennas with single and double layer were built and tested at the University of Manitoba Antenna Laboratory. The return loss curves and radiation patterns were measured for both antennas. Simulated and measured return loss curves were in good agreement, while the measured cross polarizations curves were higher than the simulated ones because of the misalignment between the two layers, during the layer assembly.

Chapter 6

High Gain Directional UWB Antennas

6.1 Introduction

This chapter investigates the performance of Vee dipole antennas with novel arm configurations for ultra wideband applications. The Vee dipole antennas will be designed originally to work over the frequency band from 3 to 11 GHz and then to be extended to wider bandwidths. Impedance bandwidths and radiation pattern characteristics for different antenna designs will be compared and discussed to investigate the effects of Vee angle, arm length and arm shape on the antenna characteristics. Finally methods to increase the directivity and reduce the back radiation will be investigated, where scaled shaped arms will be used as the directors. Loading effects using a ground plane, a dielectric ring over the UWB balun, and a conical dielectric between the Vee arms will also be considered and studied.

6.2 Directional UWB Antennas

UWB technology's important characteristics include sending and receiving high data rate and immunity to interference with other existing technologies. The antenna is an essential part in the UWB systems. This makes the development of UWB antennas a priority task for researchers in this area. Recently, UWB antennas are being used in UWB radar systems, high speed wireless communication systems including LAN and WAN applications, microwave imaging applications, such as medical and military applications and satellite communications systems. Therefore, analysis, design and manufacture of

appropriate UWB antenna for each specific application are a corner stone of designing an efficient ultra wideband system. Some of the aforementioned applications require directional UWB antennas with high gain, directive patterns, compact design and stable phase behaviour. This chapter investigate one such antenna.

6.3 Vee Dipole Antennas

Vee dipoles are traveling wave antennas that direct the wave to a desired direction. As a traveling wave antenna, it should be designed to match its characteristic impedance to free space impedance of $120\pi\ \Omega$ over the entire frequency band of operation when used in an open environment, or to be matched to a specific impedance when designed to work in microwave imaging applications. Also, the characteristic impedance of the antenna should be matched to the input impedance of the coaxial cable used to feed the antenna. Vee dipole antennas are good candidates for applications that require less interference and high quality information signals. Their simple configurations have inspired researchers for further developments to meet recent ultra wideband application requirements. The geometry of a Vee dipole antenna is shown in Fig. 6.1.

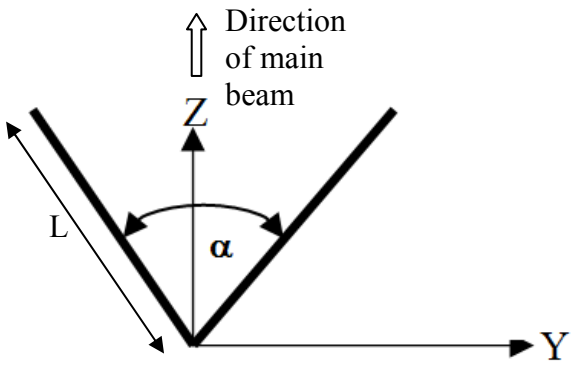

Fig. 6.1 Vee dipole antenna configuration

In 1972, a parametric study was done on the arm length, Vee angle and wire radius of a narrow-band Vee dipole antenna [119]. Later in 1980, narrow-band Vee dipole design formulas were introduced [120]. The formulas were used to estimate the Vee angle α for certain Vee arm length L.

$$\alpha = -149.3(L/\lambda)^3 + 603.4(L/\lambda)^2 - 809.5(L/\lambda) + 443.6, \quad 0.5 \le L/\lambda \le 1.5 \qquad (6.1)$$

$$\alpha = 13.39(L/\lambda)^2 - 78.27(L/\lambda) + 169.77, \qquad 1.5 \le L/\lambda \le 3.5 \qquad (6.2)$$

$$D = 2.94(L/\lambda) + 1.15 \qquad (6.3)$$

where α is the Vee dipole angle, L is the arm length and D is the maximum directivity that can be achieved, Fig. 6.1.

It is worth noticing that these formulas were to be used for narrow-band antennas. In this study, they will be used as a first estimation for the optimum angle α of the UWB Vee dipole antennas at the centre frequency of operation. It was shown that by selecting the proper Vee angle with the specified arm length, the directivity in the normal direction increases over the linear dipole with lower side lobe levels. Method of Moments was used to search for the optimum Vee angle for certain arm lengths [121]. For applications that require a modest bandwidth, higher gain and lower side lobe and back lobe levels, a double Vee dipole antenna was introduced in [122]. Another Vee dipole antenna with directors was also introduced to improve the gain and reduced back radiation [123]. The designed antenna had a gain improvement of 1.4 dB, and 12 dB reduction in the back radiation over the conventional Vee dipole at the frequency of interest.

6.4 UWB Vee Dipole Antennas

UWB Vee dipole antenna is one with an impedance bandwidth and radiation characteristics that extend over the entire frequency band of operation. Arm shape, length and feed are important parameters along with the Vee angle that affect the impedance bandwidth and radiation characteristics of the antenna. Vee antennas feeding include coaxial cable, microstrip line or coplanar waveguide (CPW). A Marchand balun along with microstrip line-to-coplanar strip line transition was used to feed a tapered planar Vee-dipole antenna in [124]. In this chapter, a novel UWB Vee dipole antenna is introduced. A coaxial cable is used to feed the Vee dipole antenna with novel arm configurations. The study starts with a conventional triangular arm shape Vee dipole antenna of length less than 0.5λ at the lowest frequency of operation. Then a novel arm shape is introduced which contains a trident matching strip along with tapering the rest of the arm length. To increase the gain of these antennas a set of directors of scaled dimensions are used.

6.4.1 Antenna design

6.4.1.1 Vee Arm Shape

Ansoft HFSS is used to design and simulate the UWB Vee dipole antenna. For the sake of comparison, a Vee dipole with triangular arm of width W=40 mm and length

L=44 mm is designed. Fig. 6.2a shows the coordinate system of the Vee antenna, where the radiation is in the Z-direction and Fig. 6.2b shows a triangular arm shape. Then a novel arm is designed with rectangular shape of the same length and width, with trident strip shape at the bottom and tapering to the rest of the arm. Fig. 6.2c shows the shape of the arm and Fig. 6.2d shows the details of the feeding area. The optimum parameters used to design this arm are W1=1.5mm, W2=9mm, W3=20mm, L1=1mm and L2=3mm. In this design, the length L of the Vee arm is chosen to be ≅ 0.5λ at the lowest frequency of operation, which is 3.1 GHz.

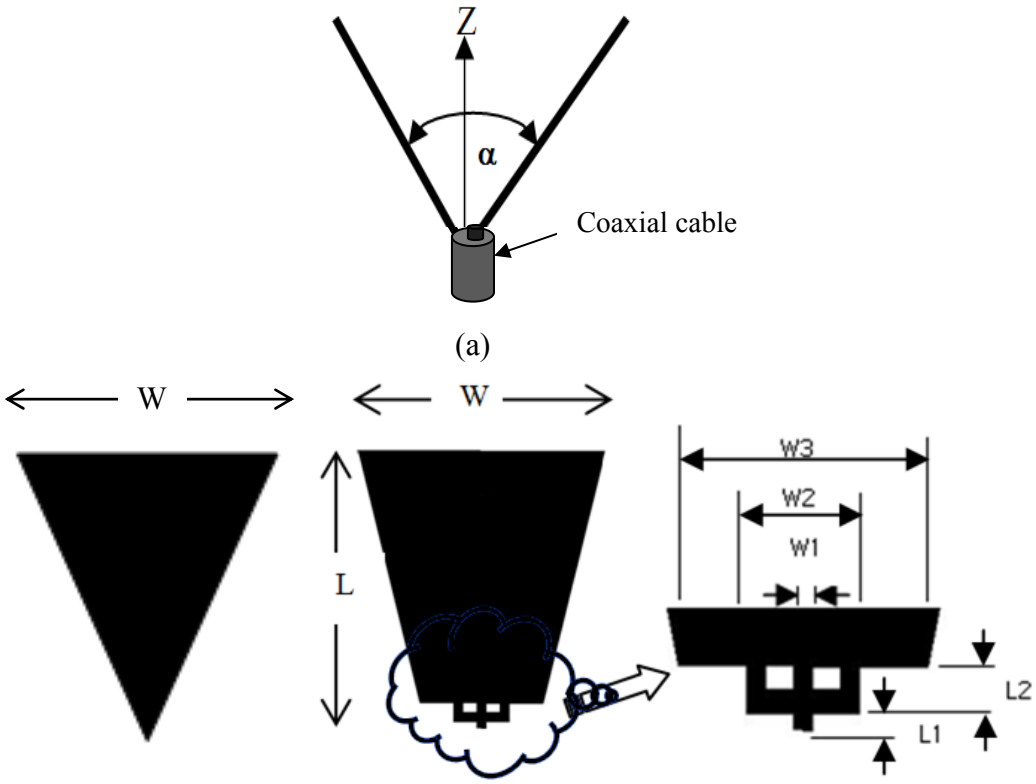

Fig.6.2 Vee dipole antenna fed by a coaxial cable (a) Dipole configuration (b) Triangular arm (c) Novel UWB arm (d) Feeding area details of (c), W = 40, L=44, W1=1.5, W2=9, W3=20, L1=1 and L2=3, all in mm

Equations (6.1), (6.2) and (6.3) are used to first estimate the optimum Vee angle that corresponds to an arm length at different frequencies over the band of operation. The angle used for this antenna is $\alpha=45^{o}$.

Fig. 6.3 shows the difference between using the novel arm and the triangular arm with coaxial cable feed, i.e. without the UWB balun. It can be seen that, the return loss curve improved, but does not fully satisfy needs. Further studies are conducted to determine the effect of arm length and Vee angle. Fig. 6.4 and Fig. 6.5 show the optimum Vee dipole angle α with different arm lengths, without using the balun. It is expected that the optimum angle value decreases as the arm length increases.

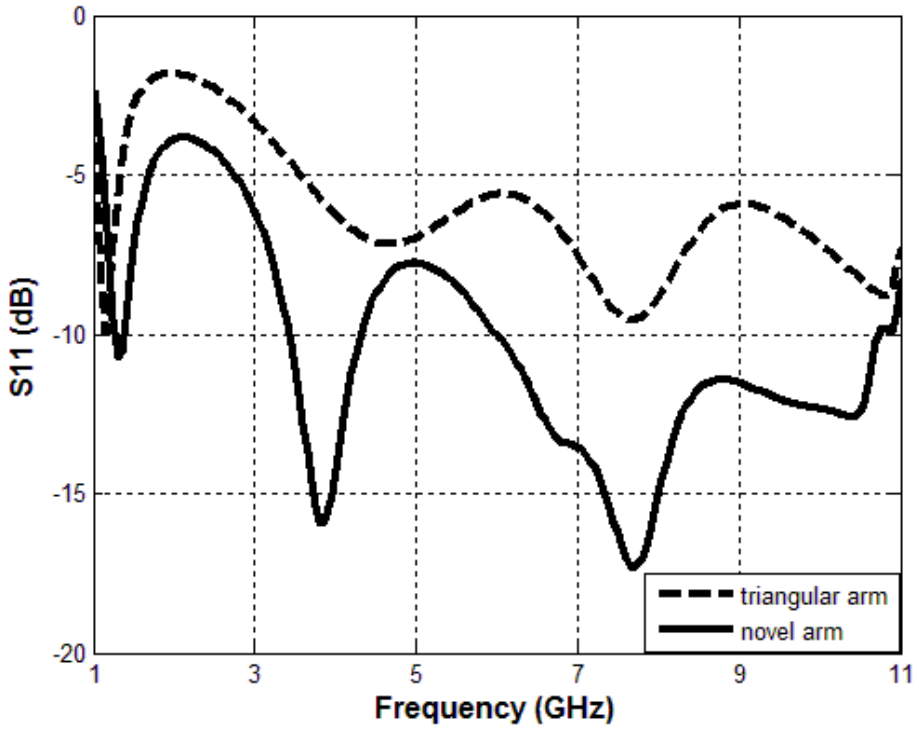

Fig. 6.3 Return losses of the Vee dipole antennas of Fig. 6.2b (triangular arm) and Fig.6.2c (novel UWB arm), without the new UWB coaxial balun, fed by a coaxial cable

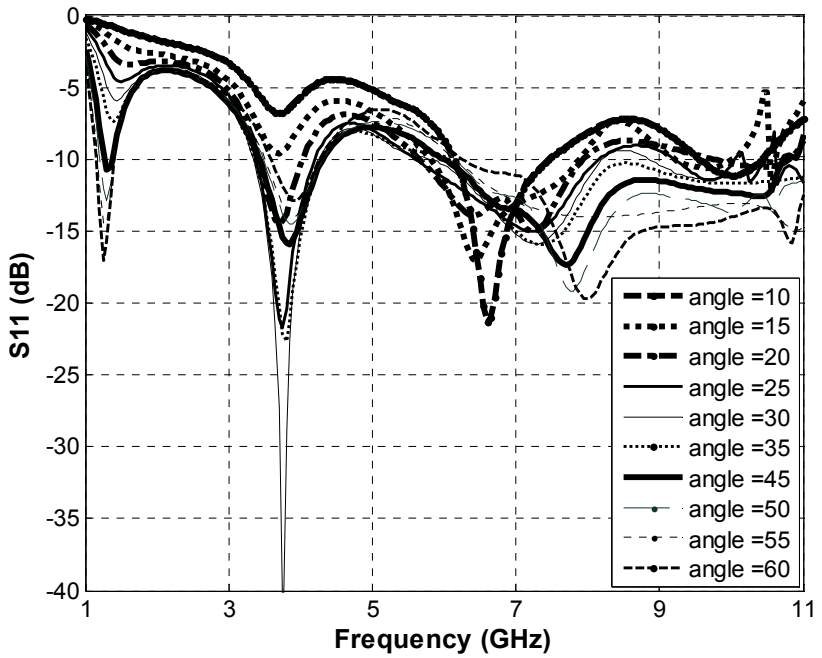

Fig. 6.4 The impedance bandwidth of the Vee dipole antenna without the new UWB coaxial balun, fed by a coaxial cable as in Fig. 6.2a, parameters are shown in Fig. 6.2c with an arm length =44 mm, optimum angle=45^{o}

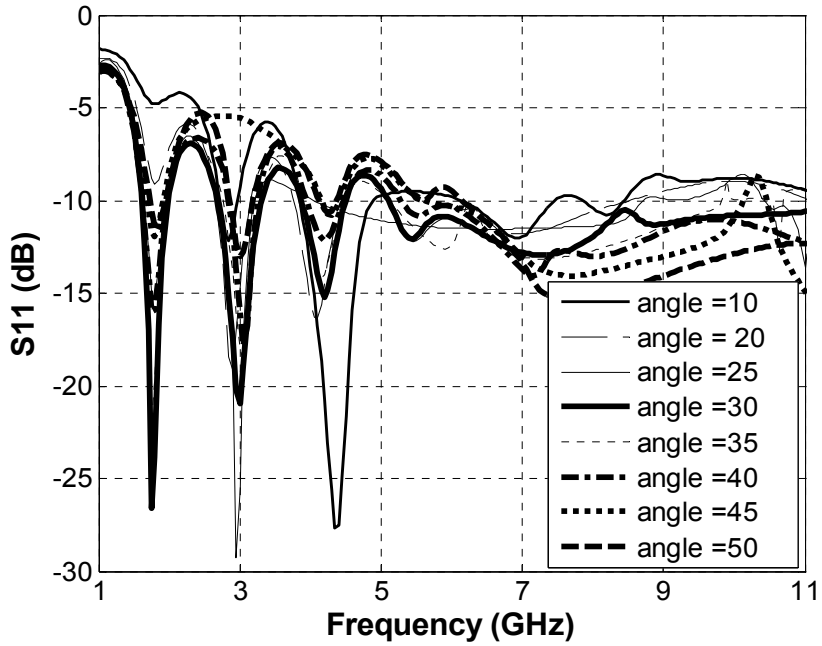

Fig. 6.5 The impedance bandwidth of the Vee dipole antenna without the new UWB coaxial balun, fed by a coaxial cable as in Fig. 6.2a, parameters are shown in Fig. 6.2c, with an arm length =104 mm, optimum angle=30^{o}

6.4.1.2 UWB Coaxial Balun

The coaxial cable is modified to better match its 50 Ω input impedance to the characteristic impedance of the antenna [125]. The dimensions of the coaxial cable used in the simulation are as follow. The radius of the inner cylinder is r_1=0.6mm. The radius of the outer cylinder is r_2=2.175mm. The material between the two cylinders has a relative permittivity of 2.2 and dielectric loss tangent of 0.0009. The Balun used here is made by cutting the outer cylinder starting at the top, leaving a width of w4=0.675mm, and cutting diagonally a length of L3=47.8mm from the cylinder. The rest of the cylinder length L4=4mm is attached to the 50 Ω wave port. This Balun is shown in Fig. 6.6.

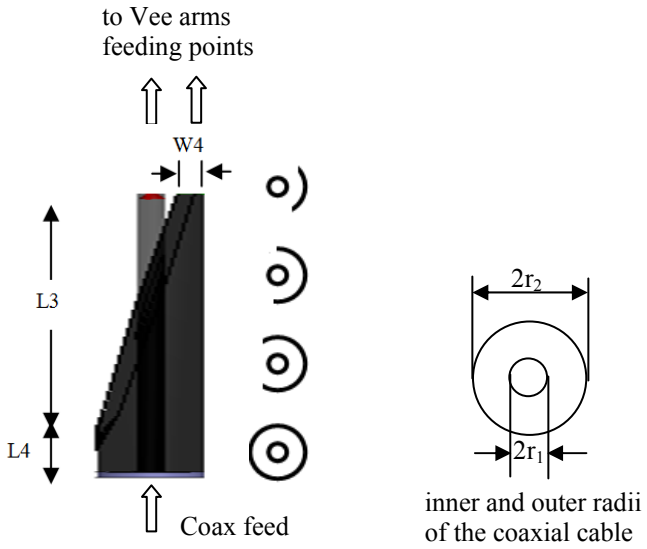

Fig.6.6 Balun used to match the coaxial cable to the Vee dipole input impedance, radius of inner cylinder r_1=0.6, radius of outer cylinder r_2= 2.175, L3 = 47.8, L4 = 4, W4 = 0.675, all in mm

Fig. 6.7 shows the optimum angle α that gives the maximum impedance bandwidth for the Vee dipole antenna of Fig. 6.2c, by using the new balun. It can be seen that using the new balun, changes the optimum Vee angle α from 45^{o} to 40^{o}. The impedance bandwidth of this Vee dipole antenna of Fig. 6.2c, fed by a coaxial cable, extends from 3.4 to 11 GHz with a directional pattern in the Z-direction. While the impedance bandwidth of the same antenna with the new balun increases and covers from 2.5 to 19 GHz.

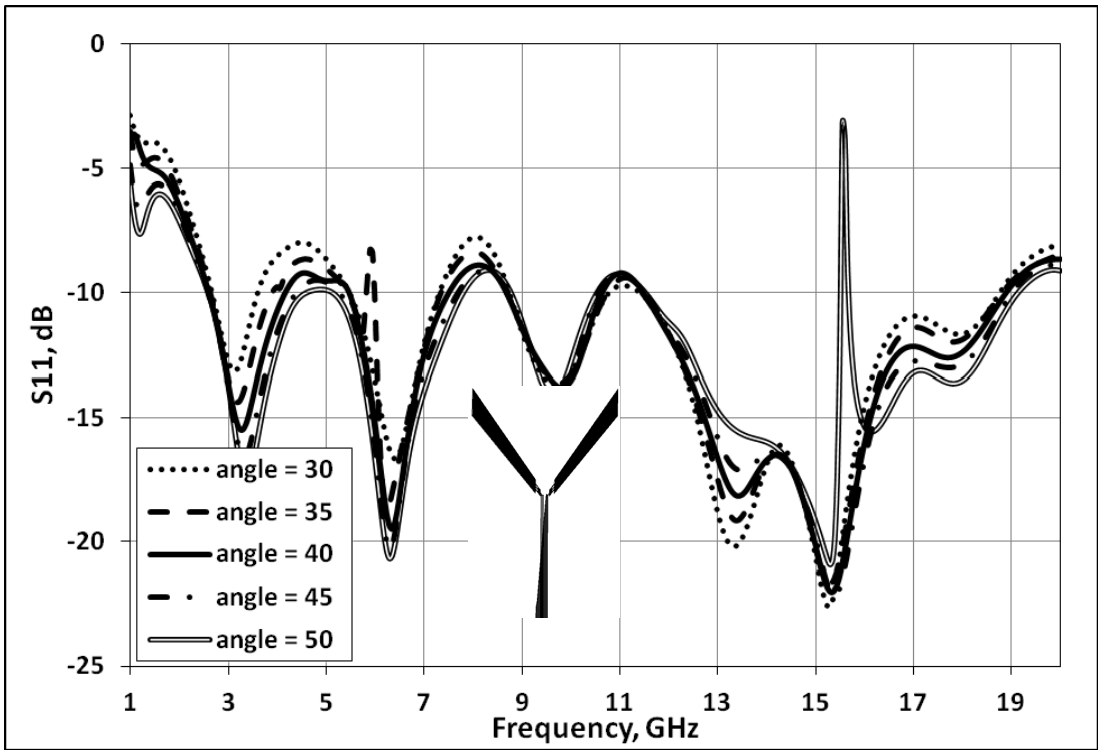

Fig. 6.7 The impedance bandwidth curves for the antenna with parameters shown in Fig. 6.2c with the new UWB balun, having parameters shown in Fig. 6.6

6.4.1.3 Radiation Characteristics

Fig. 6.8 and Fig. 6.9 show radiation patterns of the Vee dipole antenna of Fig.6.2c, with an arm length of 44mm and Vee angle of 40^{o}. The new UWB balun of Fig. 6.6 is used for impedance matching and the antenna is located in the Y-Z plane. Table 6.1 summarizes some of the important characteristics of this antenna including, gain, 3-dB beamwidth, sidelobe level (SLL), and front-to-back radiation ratio. The antenna has directive gain patterns over the frequency band of operation with low cross polarization components at all frequencies. The differences between the directive Gain at 12 GHz and 4 GHz are 4.24 and 5.42 dB in the X-Z and Y-Z planes, respectively.

As can be seen from Figs. 6.8 and 6.9, the 3-dB beamwidths at different frequencies of the antenna are wider in the X-Z plane than those in Y-Z plane. It is noted also that, the side lobe levels are high especially in the Y-Z plane because of the phase error introduced by the Vee angle as will be explained latter. The SLL values shown in Table 6.1 are measured from the maximum value of the main beam at different frequencies. The following sections will discuss different ways to enhance the directive gain of this antenna, reduce SLL and back radiations.

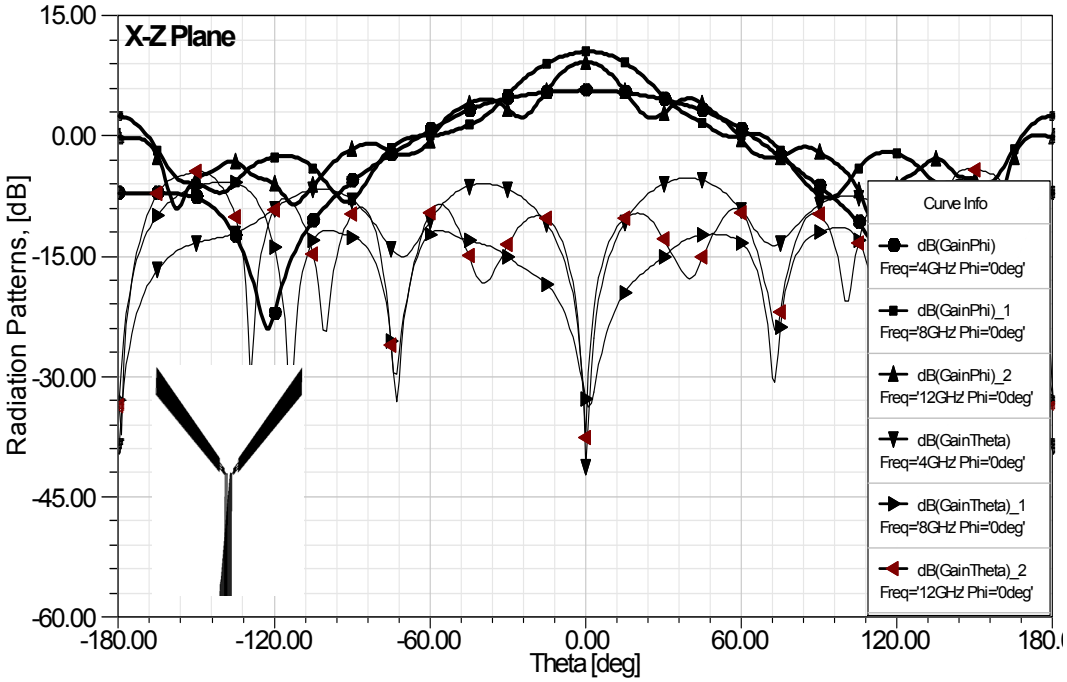

Fig. 6.8 Radiation patterns at X-Z plane of the novel arm Vee dipole with parameters shown in Fig. 2c and the new UWB balun with parameters shown in Fig. 6.6, Vee angle is 40^{o}

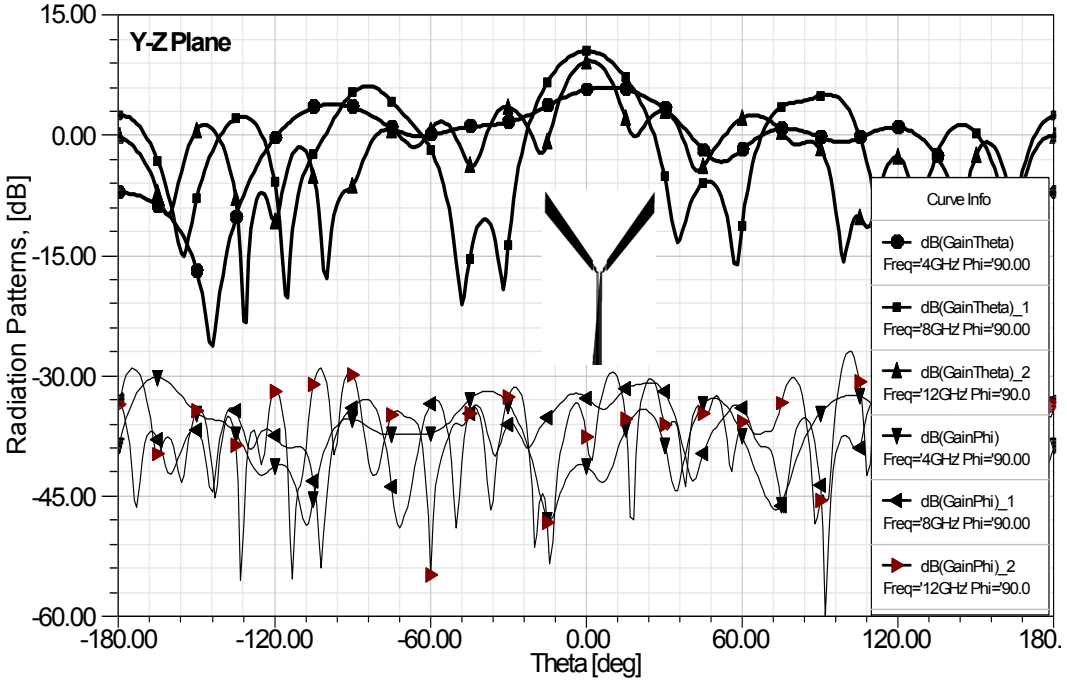

Fig. 6.9 Radiation patterns at Y-Z plane of the novel arm Vee dipole with parameters shown in Fig. 2c and the new UWB balun with parameters shown in Fig. 6.6, Vee angle is 40^{o}

UWB Vee Dipole Antenna of Fig. 6.2c with the new balun of Fig. 6.6, Vee angle =40^o 			
Boresight Gain, dB$_i$		f =4GHz	5.96 dB$_i$
		f =8GHz	10.91 dB$_i$
		f =10GHz	11.55 dB$_i$
		f =12GHz	9.57 dB$_i$
3-dB Beamwidth, degree	X-Z plane	f =4GHz	96.60^o
		f =8GHz	42.88^o
		f =10GHz	32.20^o
		f =12GHz	26.80^o
	Y-Z plane	f =4GHz	62.00^o
		f =8GHz	24.00^o
		f =10GHz	22.60^o
		f =12GHz	14.60^o
SLL, dB down from the main beam	X-Z plane	f =4GHz	12.74 dB
		f =8GHz	10.40 dB
		f =10GHz	8.83 dB
		f =12GHz	4.57 dB
	Y-Z plane	f =4GHz	1.75 dB
		f =8GHz	4.42 dB
		f =10GHz	6.42 dB
		f =12GHz	5.77 dB
Front-to-Back Ratio, dB		f =4GHz	12.86 dB
		f =8GHz	8.4 dB
		f =10GHz	14.66 dB
		f =12GHz	9.57 dB

Table 6.1 Radiation characteristics of the Vee dipole antenna of Fig. 6.2c, with the new UWB balun of Fig. 6.6 and Vee angle of 40^o

6.4.1.4 Effect of Vee Angle on Side Lobe Levels

The radiation patterns of the Vee dipole antennas show high SLL in the Y-Z plane, especially at higher frequencies. This is because of the fact that the Y-Z plane is the one that has the Vee angle. At higher frequencies, the aperture phase errors increase, which results in higher sidelobes. This phenomenon appears clearly at frequencies greater than 10 GHz. It is found that by decreasing the Vee angle, the first side lobe level is reduced because of the reduction of the aperture phase error. This finding is also confirmed from the measured and simulated radiation pattern curves, shown later in this chapter at 18 GHz. Fig. 6.10 shows the aperture phase error introduced because of the Vee angle, at higher frequencies. While Fig. 6.11 shows the effect of decreasing Vee angle on the SLL at Y-Z plane at different frequencies.

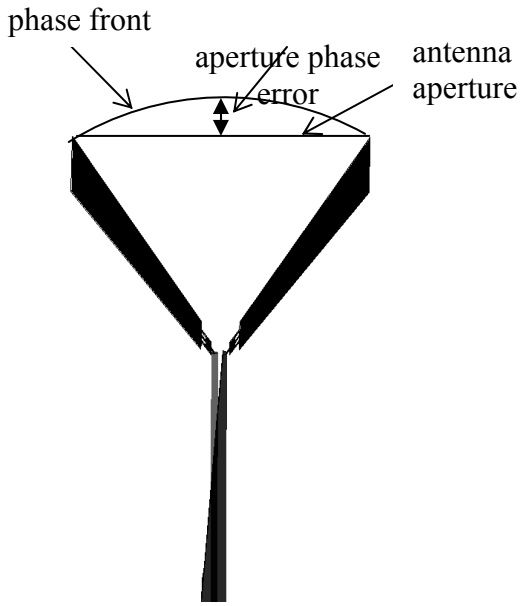

Fig. 6.10 Aperture phase error of the radiated field from a Vee dipole antenna, affects its sidelobe levels (SLL)

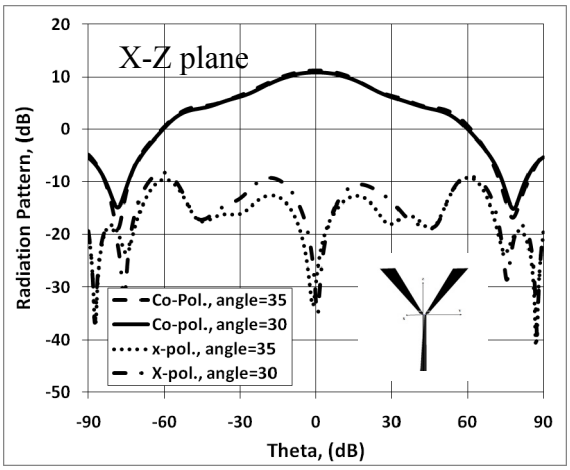

X-Z plane, f = 10 GHz

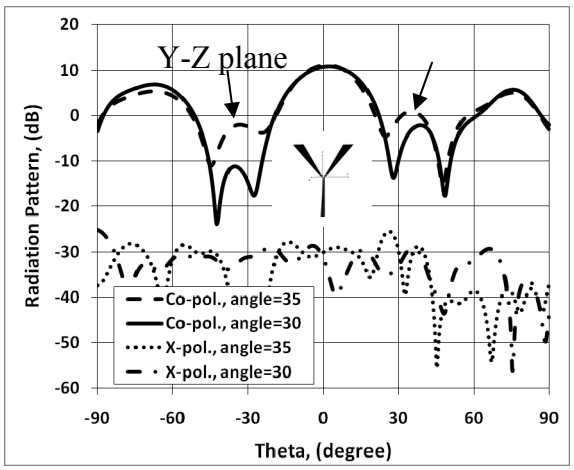

Y-Z plane, f = 10 GHz

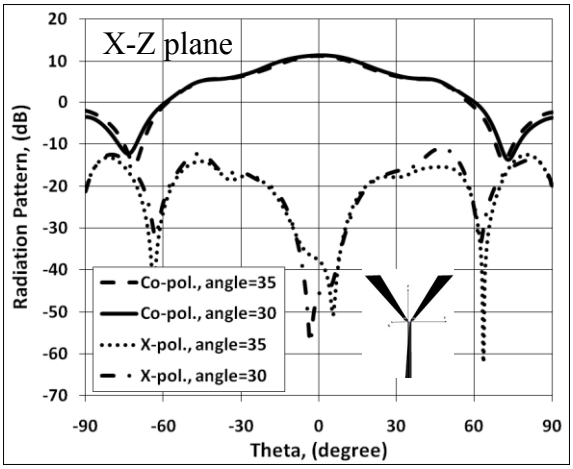

X-Z plane, f = 11 GHz

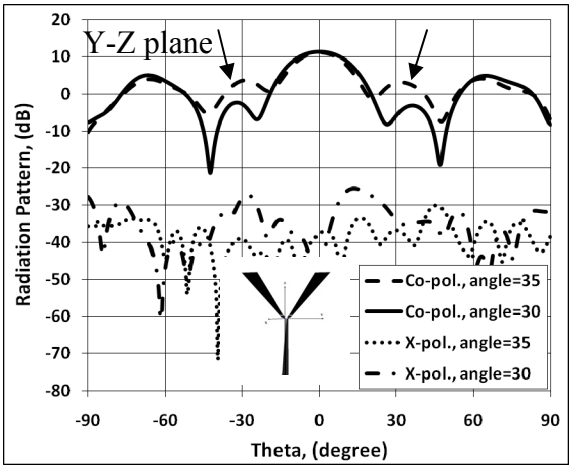

Y-Z plane, f = 11 GHz

Fig. 6.11 The effect of decreasing Vee angle on the side lobe level of the Vee dipole antenna of Fig. 6.2c with the new UWB balun of Fig. 6.6 and different Vee angles

6.5 Performance Enhancement over the UWB Vee Dipole Antenna

6.5.1 Directors of Same Shape as the Vee Dipole Arm

To increase the gain of the antenna in Fig. 6.2c, a set of directors of the same novel arm shape with different scaling factors and at different distance from the radiating arm are designed. A parametric study is done to find the appropriate scaling factor and the distance from the main radiating arm. An antenna with a Vee-director is shown in Fig. 6.12.

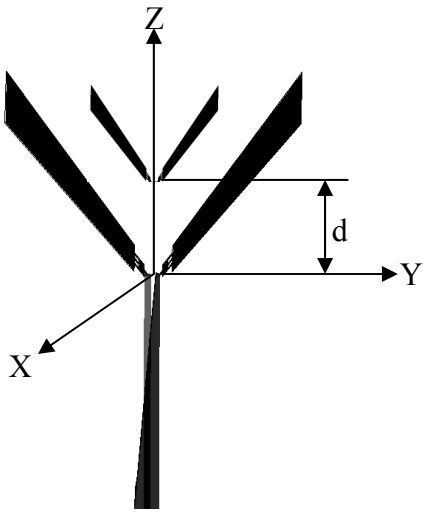

Fig. 6.12 UWB Vee dipole antenna with a Vee-director, the parameters of the Vee dipole are the same as those shown in Fig. 6.2c, balun parameters are shown in Fig. 6.6, directors with the same arm shape, and with 0.5 scaling factor, at a vertical distance d from the radiator arm feeding point

By using directors of the same shape as the Vee arms and parallel to them, and at a vertical distance of d=20 mm, from the feeding point of the Vee arms, as shown in Fig. 6.12, with antenna parameters shown in Fig. 6.2c and balun parameters shown in Fig. 6.6, gain increases at different frequencies. The directors are scaled down with a factor of 0.5 from the Vee arms. The gain is increased by 1, 1.7 and 1.4 dB at 3, 4 and 5 GHz, respectively. The effect of including such directors at different distances d from the origin on the return loss curves of the Vee dipole antenna is investigated. Fig. 6.13 shows the return loss curves of the Vee dipole antenna of Fig. 6.12 with the directors at different distances d from the Vee arm feeding point. As can be seen, the optimum distance d is 20 mm from the Vee arm feeding point to have a better impedance matching. It can be seen also that this Vee dipole antenna can have a band-notch function between 5 and 6 GHz when the directors are at a small distance d from the Vee arm feeding point.

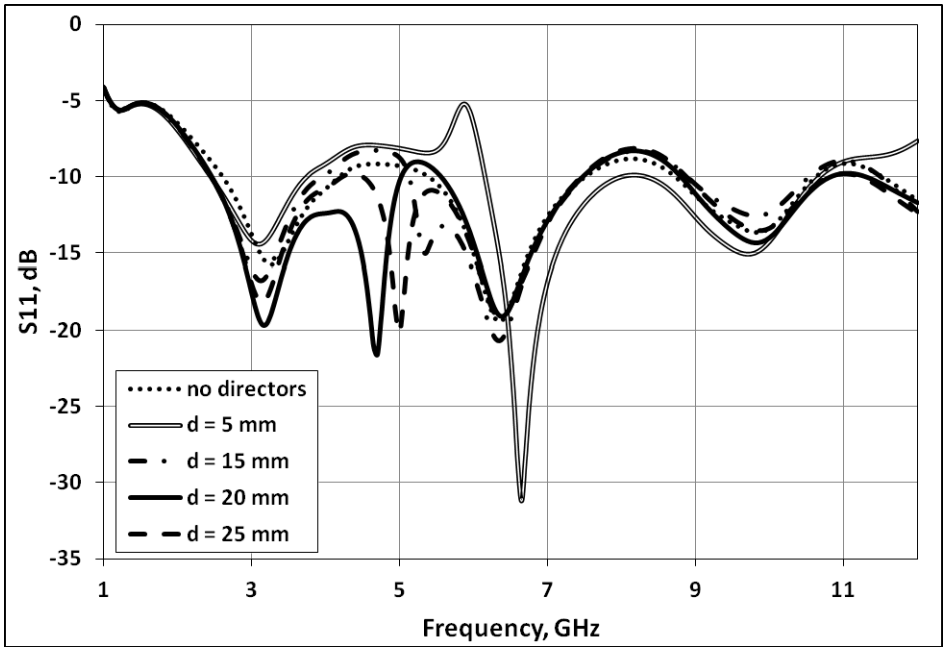

Fig. 6.13 Return loss curves of the Vee dipole antenna of Fig. 6.2c with the directors having the same shape as the driven elements, with a 0.5 scaling factor and at different distances d from the Vee arm feeding point

6.5.2 Improving the Radiation Characteristics by Using a Ground Plane

The radiation characteristics of the Vee dipole antenna discussed so far showed that, this antenna suffers from high side lobe levels especially at Y-Z planes along with high back radiation at some frequencies. In this section, a ground plane is implemented to enhance the radiation characteristics of this antenna by increasing the forward gain and decreasing the back radiation and sidelobe levels. In this study, a 120x170mm^2 rectangular plane is introduced at different distances from feeding points of the Vee dipole to have an optimum impedance matching and a better forward gain. Fig. 6.14 shows the Vee dipole antenna with the ground plane. Fig. 6.15 shows the return loss curves of this antenna with the ground plane at different distances S from the feeding point of the Vee arms. Although, S= 10mm gave a better return loss performance, it did not give a better forward gain, and front to back ratio. It was found that with S= 30mm, the return loss curve was compared to that without the ground, and the forward gain was increased along with a reduction in the backlobe radiation, at different frequencies. Figs. 6.16 and 6.17 show the Vee dipole antenna radiation patterns for S= 30 mm. Table 6.2 summarizes the forward gains, 3-dB beamwidths, sidelobe levels and front to back ratios at different frequencies, for the antenna alone and with the ground plane and S=30mm. As can be seen from Figs.6.16 and 6.17, the antenna gains increased at all frequencies with values shown in Table 6.2. Sidelobe levels were decreased at all frequencies along with an increase in the front to back ratios. The 3-dB beamwidths were narrower both at X-Z and Y-Z planes.

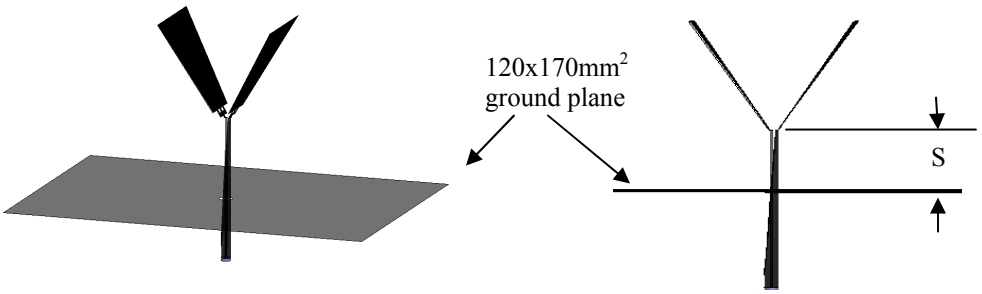

Fig. 6.14 Vee dipole antenna of Figure 6.2c with a 120x170mm^2 ground plane at different distance, S from the feeding points30mm distance from the origin

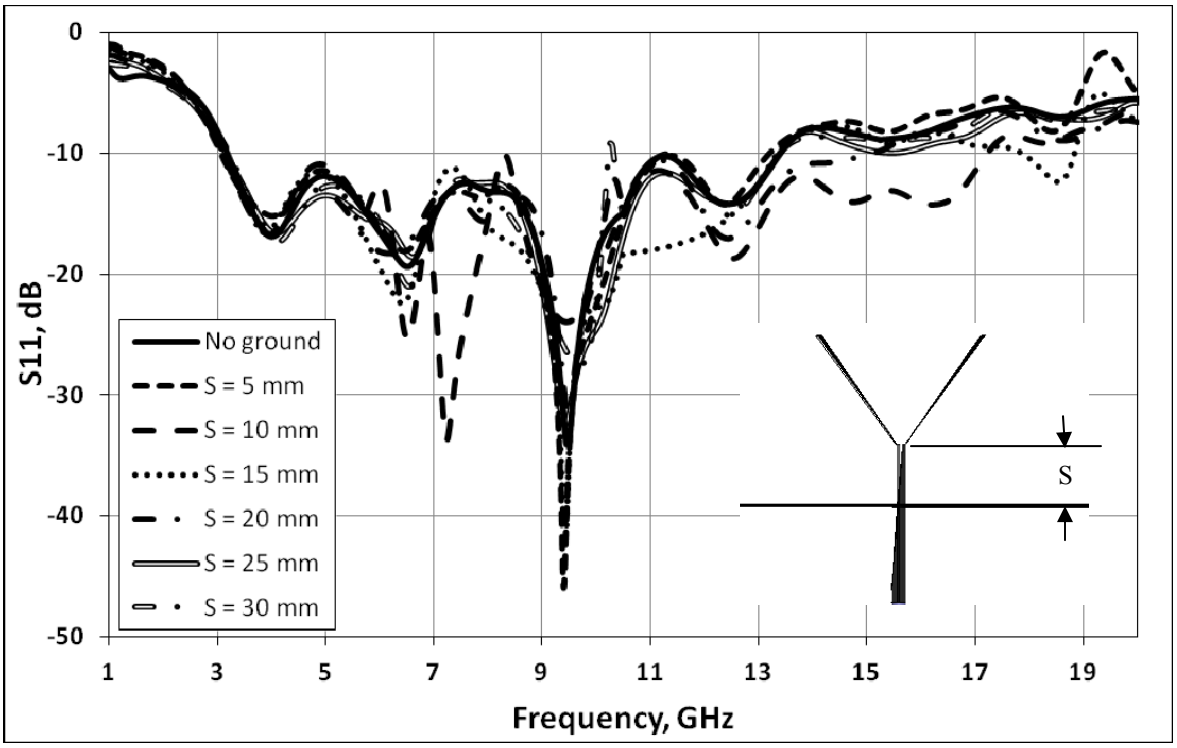

Fig. 6.15 Return loss curves of the Vee dipole antenna of Figure 6.14 with a 120x170mm^2 ground plane at different distance S from the feeding points

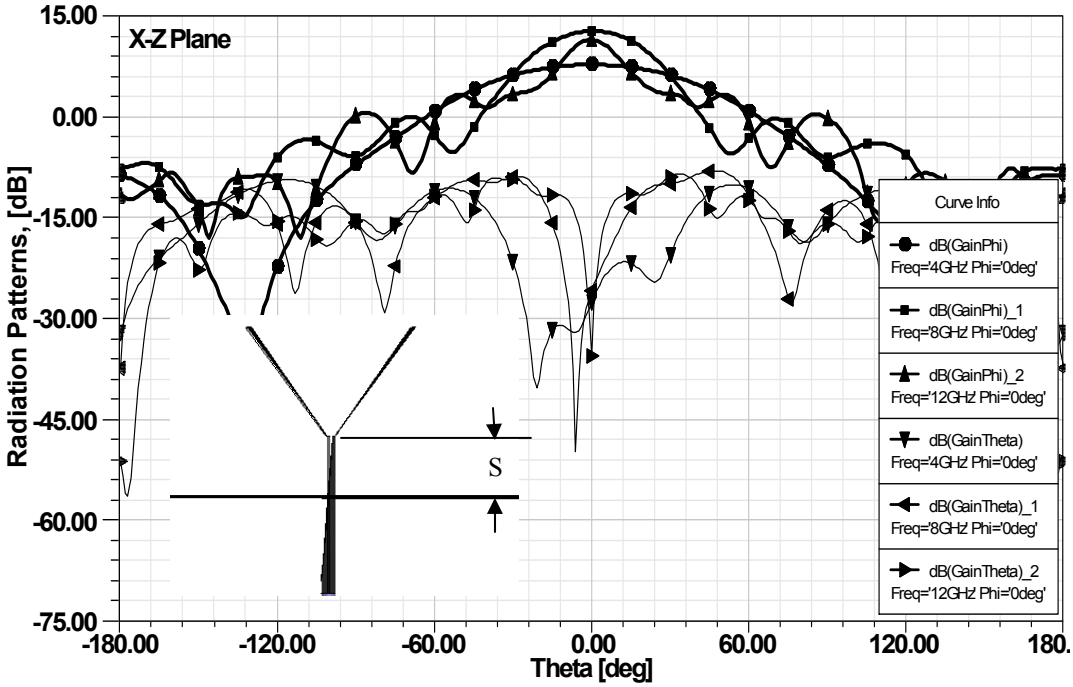

Fig. 6.16 Radiation pattern curves at X-Z plane, for the Vee dipole antenna in Figure 6.14 with a 120x170mm^2 ground plane at S=30mm

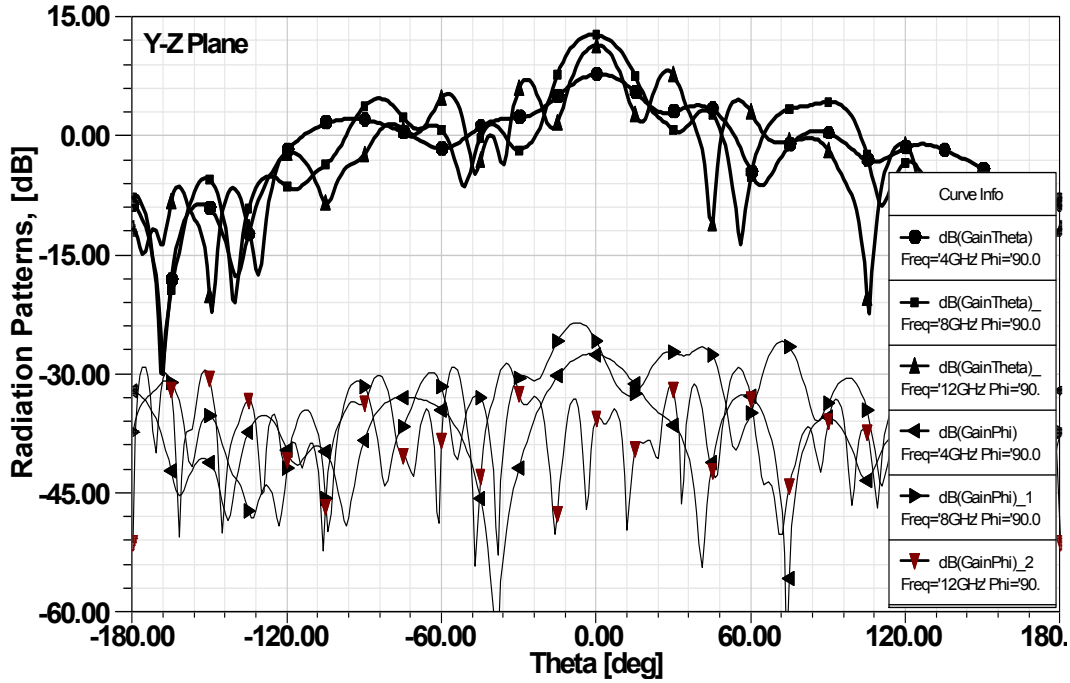

Fig. 6.17 Radiation pattern curves at X-Z plane, for the Vee dipole antenna in Figure 6.14 with a 120x170mm^2 ground plane at S=30mm

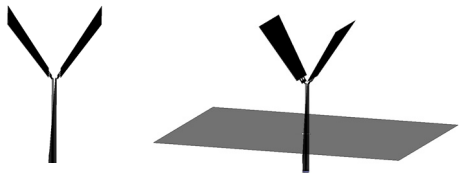			**Vee dipole of Fig. 6.14 without a ground**	**Vee dipole of Fig. 6.14 with a 120x170mm^2 ground at S=30mm**
Boresight Gain, dBi		f =4GHz	5.96 dB_i	8.12 dB_i
		f =8GHz	10.91 dB_i	13.27 dB_i
		f =10GHz	11.55 dB_i	12.54 dB_i
		f =12GHz	9.57 dB_i	11.70 dBi
3-dB Beamwidth, degree	X-Z plane	f =4GHz	96.60^o	80.2^o
		f =8GHz	42.88^o	41.07^o
		f =10GHz	32.20^o	42.00^o
		f =12GHz	26.80^o	20.53^o
	Y-Z plane	f =4GHz	62.00^o	31.38^o
		f =8GHz	24.00^o	23.20^o
		f =10GHz	22.60^o	15.60^o
		f =12GHz	14.60^o	15.54^o
SLL, dB Down from the main beam	X-Z plane	f =4GHz	12.74 dB	16.57 dB
		f =8GHz	10.40 dB	13.23 dB
		f =10GHz	8.83 dB	12.85 dB
		f =12GHz	4.57 dB	8.01 dB
	Y-Z plane	f =4GHz	1.75 dB	4.16 dB
		f =8GHz	4.42 dB	8.39 dB
		f =10GHz	6.42 dB	7.14 dB
		f =12GHz	5.77 dB	5.70 dB
Front-to-Back Ratio, dB		f =4GHz	12.86 dB	16.78 dB
		f =8GHz	8.4 dB	20.69 dB
		f =10GHz	14.66 dB	20.43 dB
		f =12GHz	9.57 dB	23.34 dB

Table 6.2 Radiation Characteristics of the Vee dipole antenna of Fig. 6.14 with and without a ground plane at distance S=30mm at different frequencies. Antenna parameters are given in Figs. 6.2c and 6.6

6.5.3 Antenna Performance Evaluation

Simulation results so far show that this Vee dipole antenna can be a good candidate as a high gain UWB antenna. This antenna can have a linear polarization, with low cross-polarization components. The boresight gain reaches 11.7 dB_i at 10 GHz with a back lobe level of oscillations around 11 dB below the main beam. The 3-dB beamwidth of the antenna is wider in the X-Z plane. The return loss curve of this antenna shows a UWB impedance bandwidth that covers the existing UWB communication applications. To improve the performance of this antenna, a 120x170mm^2 reflector plane is placed behind it at different distances from the feeding point which reduced both the back radiations and the sidelobe levels of the antenna by as much as 8 to 10 dB at different frequencies, which in turn increases the antenna gain in the forward direction to about 13 dB_i. In another solution, different directors were placed in front of the driven arms. These directors were placed as parasitic elements at different distances from the driven elements, with a reduction scale factor of 0.5. It was found that a better performance in gain and back lobe level could be achieved, by placing two parasitic arms of the same shape as the Vee dipole arms, with a 0.5 scale factor and at d=20 mm distance from the Vee antenna feed point. It was also found that the lower frequency of operation was reduced from 3.15 to about 2.6 GHz, with the same antenna height.

6.6 Miniaturization of Vee Dipole Antennas

Nowadays, microwave imaging applications are receiving more attention. One of these applications is the breast cancer detection using microwave frequencies. Due to the

space limitations in such applications and the need for using an array of receiving antennas, it is important to design small directional UWB antennas that can be impedance matched easily to different material matching media. The Vee dipole antennas introduced throughout this chapter can be good candidates for such applications. Fig. 6.18 shows a breast cancer detection application, where an array of small directional UWB antennas are used for microwave signal transmittim and receptim.

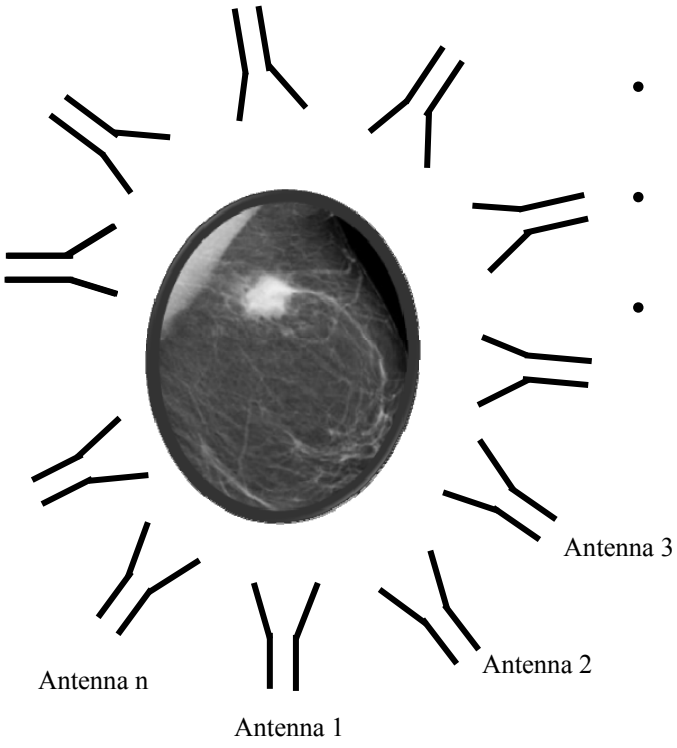

Fig. 6.18 An array of small directional UWB antennas used in microwave imaging applications

6.6.1 Modification to the Arm Shape of Fig. 6.2c

The goal in such a design is to have a small directional UWB antenna with a certain radiation aperture area. To achieve this goal, the Vee dipole antenna studied earlier in this chapter is further modified to achieve a small scale version that can be used in imaging applications. The geometry of the Vee dipole antenna introduced in Fig. 6.2c is modified. The new Vee arm is shown in Fig. 6.14. The same UWB designed before and shown in Fig. 6.6 is used to match this Vee arm.

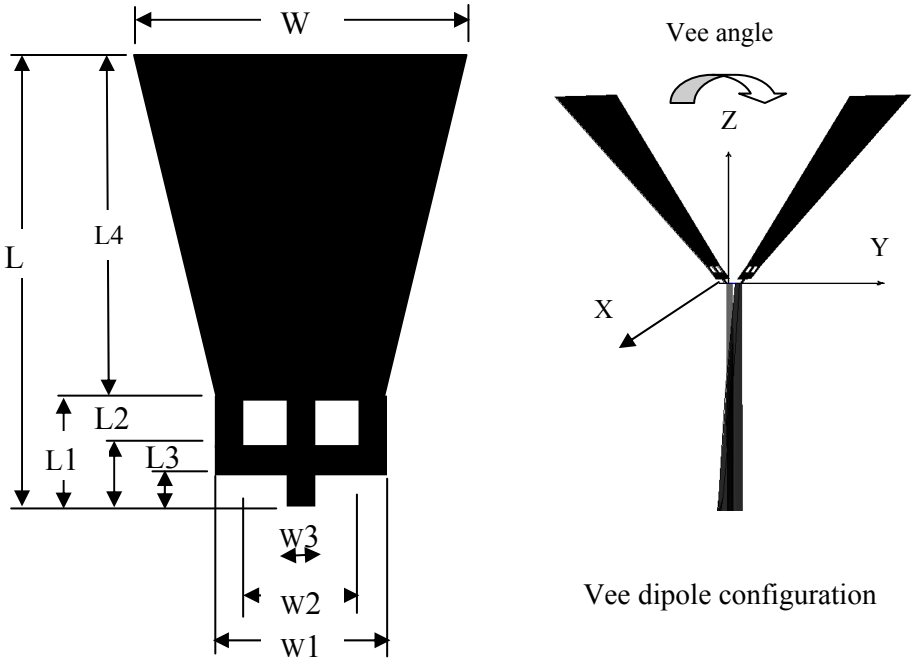

Reduced size arm shape of the Vee dipole antenna,
W=40mm, L 44mm, L1=4mm, L2=2.5mm,
L3=1mm, L4=40mm, W1=9mm, W2=6mm and
W3=1.5mm

Fig. 6.19 Reduced size UWB Vee dipole antenna with new arm geometry

.

6.6.2 Return loss and Radiation Patterns of the Modified Arm Design

Fig. 6.20 shows the return loss curves of the antenna of Fig. 6.19 with different Vee angle. From the return loss curves, the optimum Vee angle is chosen to be 35 degrees. The radiation patterns of this antenna at X-Z and Y-Z planes with a Vee angle of 35 degrees are shown in Fig. 6.21 and Fig. 6.22. Table 6.3 summarizes the important radiation characteristics of this antenna including gains, 3-dB beamwidths, sidelobe levels and front-to-back ratios at different frequencies. This antenna has similar radiation patterns to the antenna of Fig.6.2c, with high sidelobe levels especially in the Y-Z plane. However, it has higher forward gain at all frequencies compared to the same antenna of Fig.6.2c, as can be seen from Table 6.3. The following sections, will investigate the effect of the Vee arm and UWB balun length reductions on the antenna performance along with the effect of dielectric loading on its radiation characteristics.

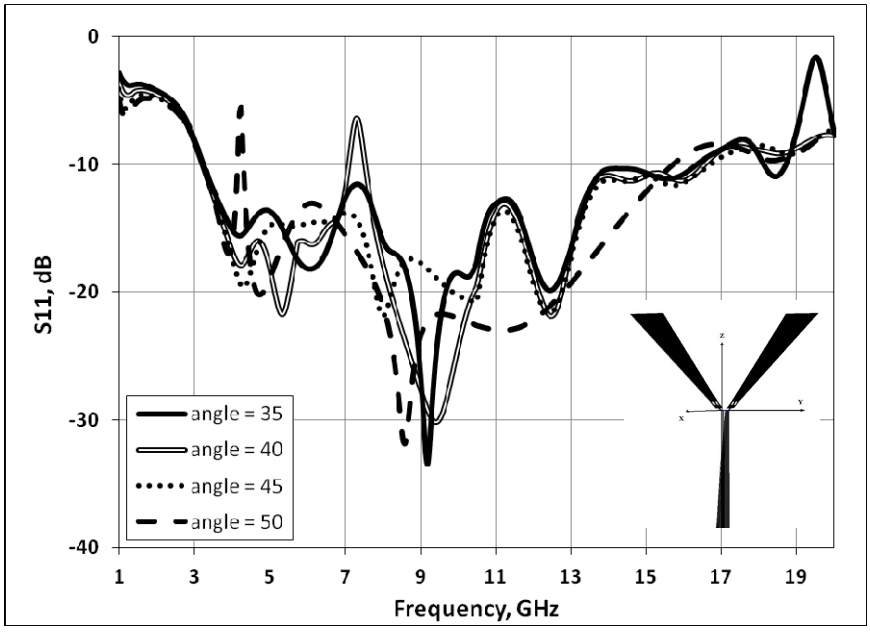

Fig. 6.20 Return losses of the Vee dipole antenna with parameters shown in Fig. 6.19, UWB balun parameters are shown in Fig. 6.6, with different Vee angle

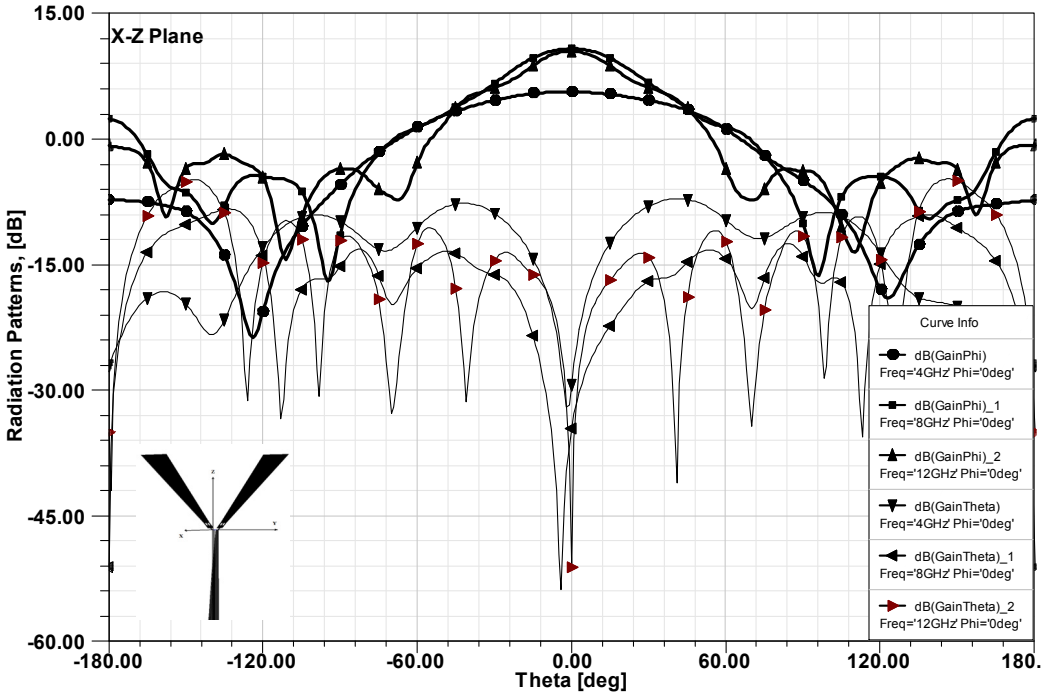

Fig. 6.21 Radiation patterns at X-Z plane, of the reduced size Vee dipole antenna with parameters shown in Fig. 6.19, UWB balun parameters shown in Fig. 6.6, Vee angle= 35^{o}

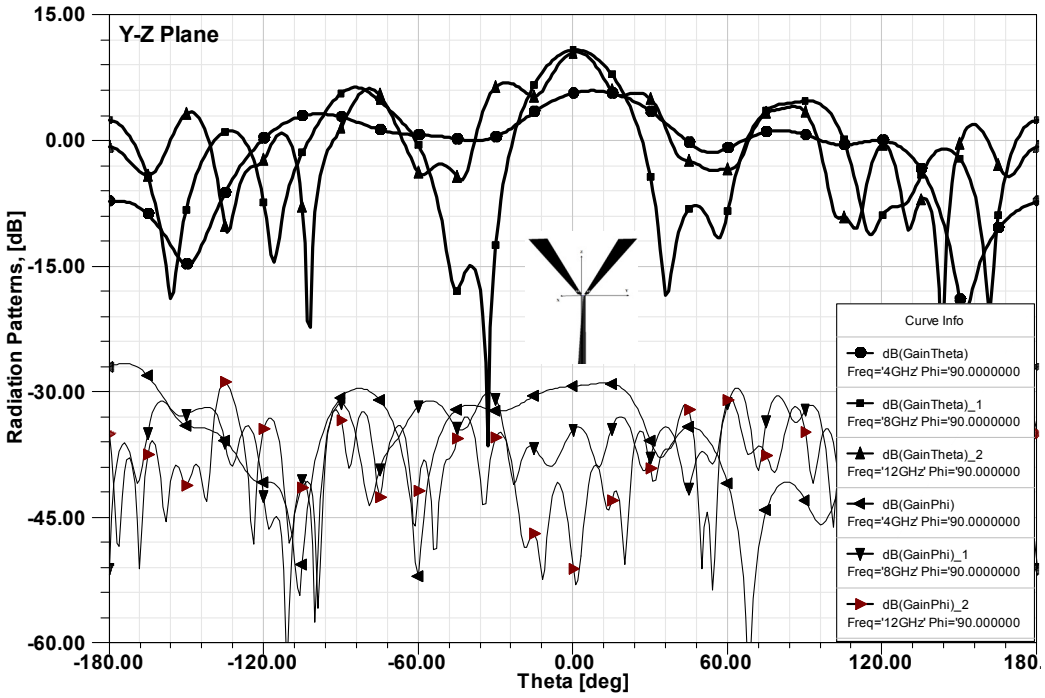

Fig. 6.22 Radiation patterns at Y-Z plane, of the reduced size Vee dipole antenna with parameters shown in Fig. 6.19, UWB balun parameters shown in Fig. 6.6, Vee angle= 35^{o}

Reduced size Vee Dipole Antenna of Fig. 6.19 with the new balun of Fig. 6.6, Vee angle =35^o 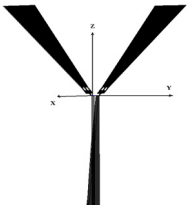			
Boresight Gain, dB$_i$		f =4GHz	6.17 dB$_i$
		f =8GHz	11.09 dB$_i$
		f =10GHz	12.09 dB$_i$
		f =12GHz	10.81 dB$_i$
3-dB Beamwidth, degree	X-Z plane	f =4GHz	100.20^o
		f =8GHz	49.52^o
		f =10GHz	40.40^o
		f =12GHz	40.0^o
	Y-Z plane	f =4GHz	64.0^o
		f =8GHz	24.76^o
		f =10GHz	20.8^o
		f =12GHz	15.8^o
SLL, dB down from the main beam	X-Z plane	f =4GHz	13.23 dB
		f =8GHz	15.35 dB
		f =10GHz	15.45 dB
		f =12GHz	14.36 dB
	Y-Z plane	f =4GHz	3.0 dB
		f =8GHz	4.52 dB
		f =10GHz	6.2 dB
		f =12GHz	3.7 dB
Front-to-Back Ratio, dB		f =4GHz	13.28 dB
		f =8GHz	8.56 dB
		f =10GHz	16.16 dB
		f =12GHz	11.42 dB

Table 6.3 Radiation Characteristics of the reduced size Vee dipole antenna with parameters shown in Fig. 6.19, UWB balun parameters shown in Fig. 6.6, Vee angle= 35^o

6.6.3 Vee Arm Length Reduction

To achieve a small scale version of this Vee dipole antenna, both the arm and balun length reduced in size. In this section, the effect of reducing the arm length on the impedance bandwidth is investigated. As was explained in section 6.3, for each arm length, there is an optimum Vee angle that gives maximum impedance bandwidth and maintains the Vee dipole directional pattern. In this study, the Vee arm length is scaled down, and the angle is optimized for each arm length. As can be seen from Fig.6.23, the reduction in the Vee arm length affects the lower frequency of operation.

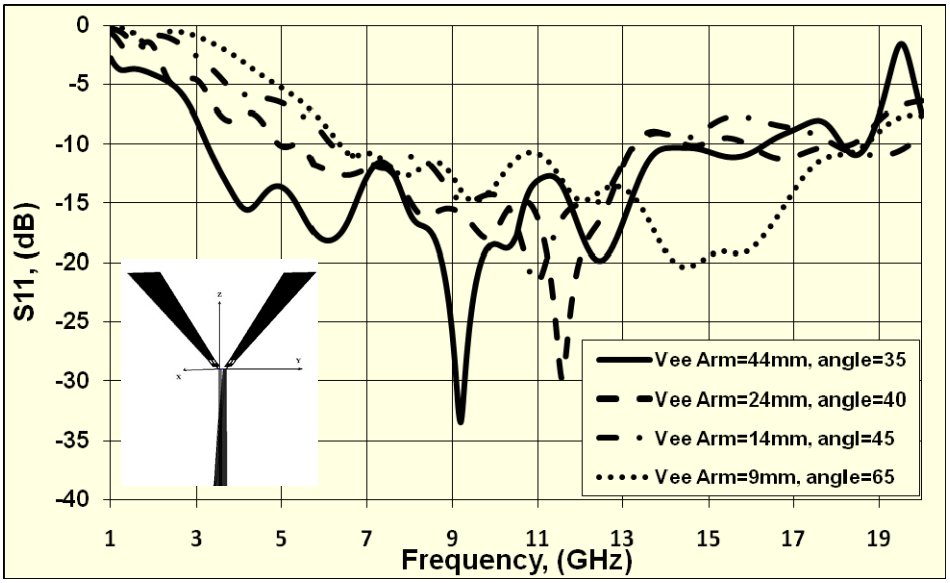

Fig. 6.23 Return loss curves for the Vee dipole antenna with different arm lengths and Vee angles, Vee arm parameters are shown in Fig. 6.19, UWB coaxial balun parameters are shown in Fig. 6.6, each curve represents an arm length with its optimum Vee angle

6.6.4 UWB Balun Size Reduction

To further study the effect of having coaxial cable feed of different sizes, the radii of the coaxial cable used in Fig. 6.6 are doubled, so that the inner radius r_1= 1.6mm and outer radius r_2=4.35mm. This bigger coaxial cable size made it possible to reduce the balun length without affecting the matching of the Vee dipole antenna. It also made it possible to manufacture a rigid and reliable Vee dipole antenna for practical applications. Fig. 6.24 shows the new coaxial cable and balun parameters used in this study, while Fig. 6.25 shows the return loss curves of the Vee dipole antenna of Fig. 6.19 with different lengths L3, of the balun shown here in Fig. 6.24. As can be seen, the UWB balun can have a length L3 as low as 8mm and still have a UWB impedance bandwidth. This will contribute to reducing the overall length of the Vee dipole antenna to fit in imaging applications.

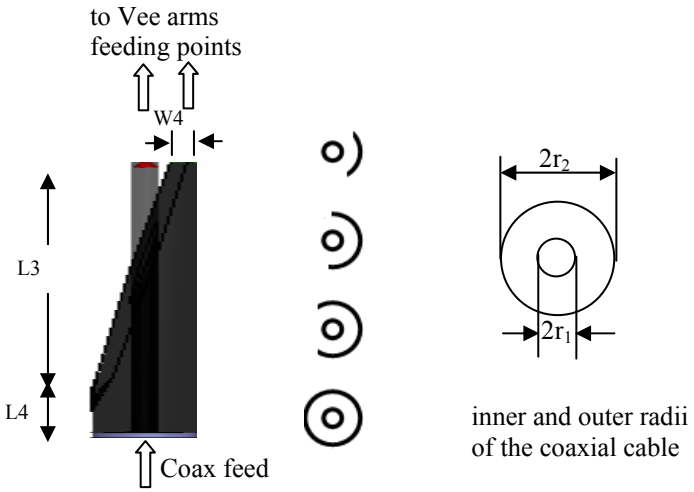

Fig. 6.24 New UWB coaxial Balun design parameters, r_1=1.2mm, r_2= 4.35mm, L3=48mm, L4 = 4mm, W4 = 0.675 mm

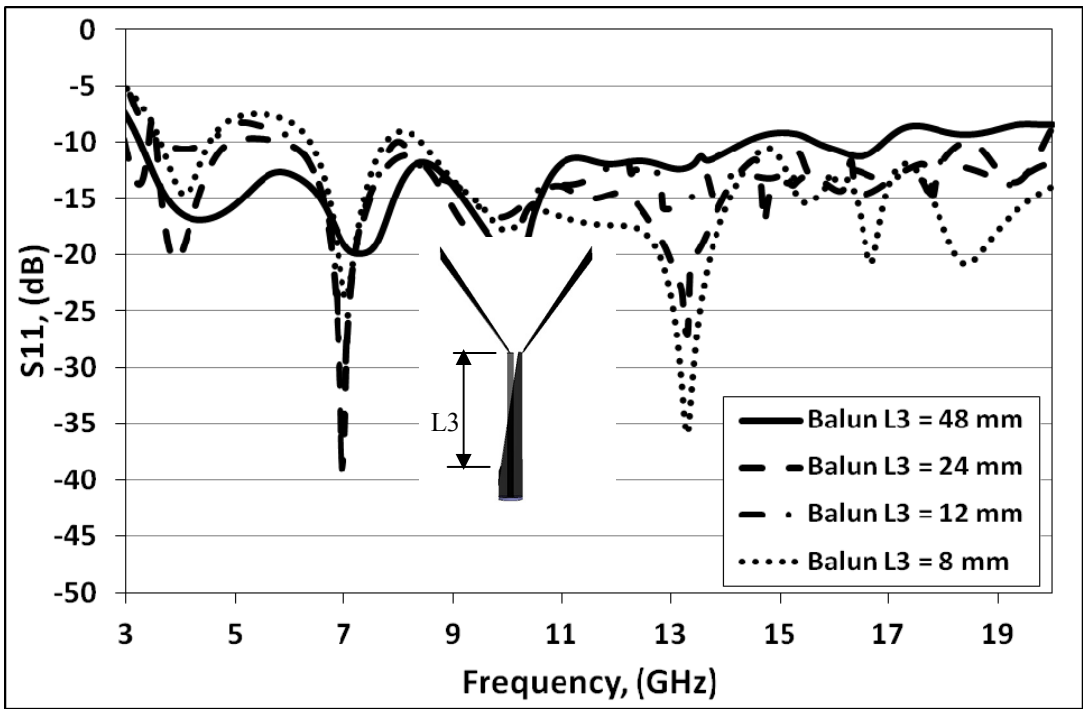

Fig. 6.25 Return loss curves of the Vee dipole antenna of Fig. 6.19 with different coaxial balun lengths, L3. Balun and coaxial cable parameters are shown in Fig.6.24

6.6.5 Dielectric Loading for Further Enhancement of Radiation Characteristics

6.6.5.1 Dielectric Loading of the Balun

In this section, the effect of loading the UWB balun with a dielectric cylinder with different permittivity on the antenna performance is investigated. The antenna with the dielectric cylinder is shown in Fig. 6.26. The antenna is the same as Fig. 6.19, but the balun is loaded with a dielectric cylinder. Dielectric parameters include relative permittivity ε_r, size, shape and location. Antenna parameters studied in this section

include impedance bandwidth, the lower frequency end and upper frequency end. The study also focuses on the size reduction factor that can be achieved. Results show that by adding a hollow dielectric cylinder, with $\varepsilon_r = 6$, the inner radius =2.3 mm and outer radius =7 mm, around the coaxial balun, a considerable improvement in the impedance bandwidth occurs.

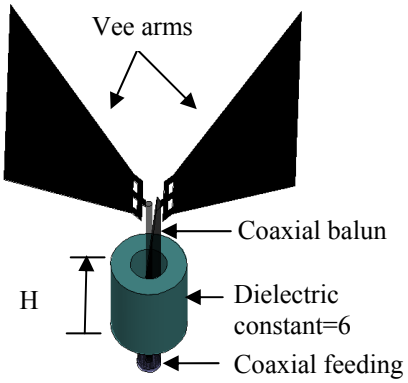

Fig. 6.26 UWB Vee dipole antenna with trapezoidal arm and coaxial balun, loaded with a cylinder of dielectric constant=6, inner radius=2.3mm, outer radius=7mm dielectric material with $\varepsilon_r = 10.2$ and height, H = 32 mm

Fig. 6.27 shows the return losses, with and without the dielectric material, while Figs. 6.28 and 6.29 show the radiation patterns of the antenna loaded with the dielectric cylinder with parameters shown in Fig. 6.26. A summary of the radiation characteristics of the antenna with and without the dielectric loading is given in Table 6.4. Although, the antenna with balun loading gave better impedance matching, its radiation characteristics

are not superior over that without balun loading. Table 6.4 shows that, the antenna with balun loading has better front to back ratios at all frequencies, but the side lobe levels are compared to that of the antenna without balun loading or even higher at some frequencies. The gains of the antenna with balun loading are lower than their corresponding values for the unloaded case, as can be seen from the comparison Table 6.4. In the following section, loading of the Vee arm will be investigated to enhance the radiation characteristics of this Vee dipole antenna.

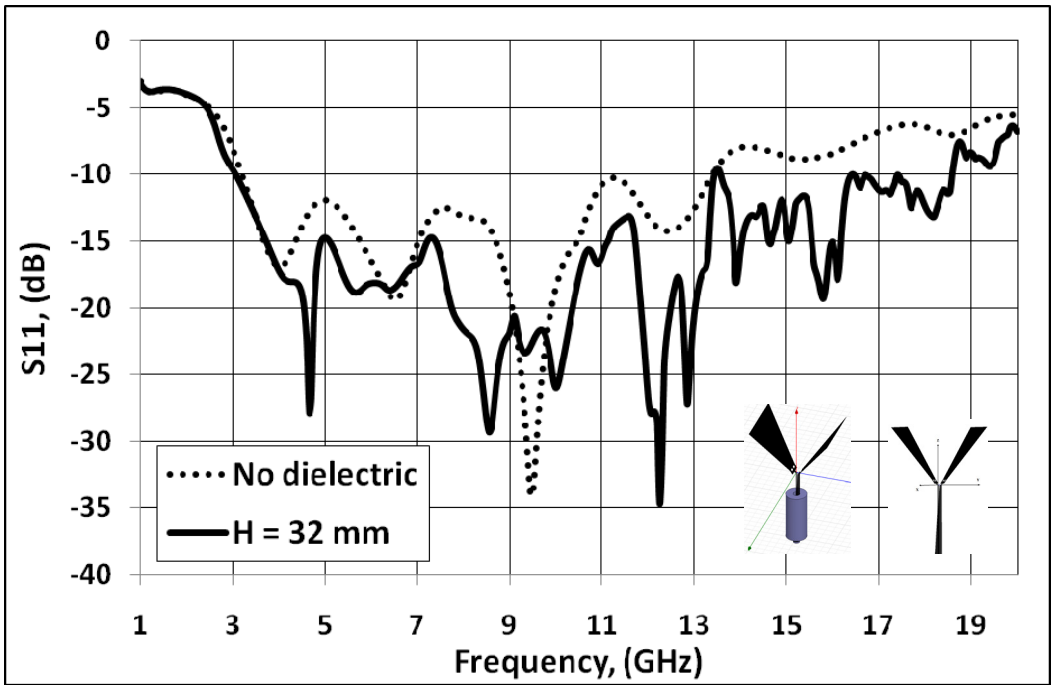

Fig. 6.27 Return losses of the Vee dipole of Fig. 6.26 loaded with dielectric cylinder with inner radius 2.3mm and outer radius of 7 mm and height H=32mm and $\varepsilon_r = 6$

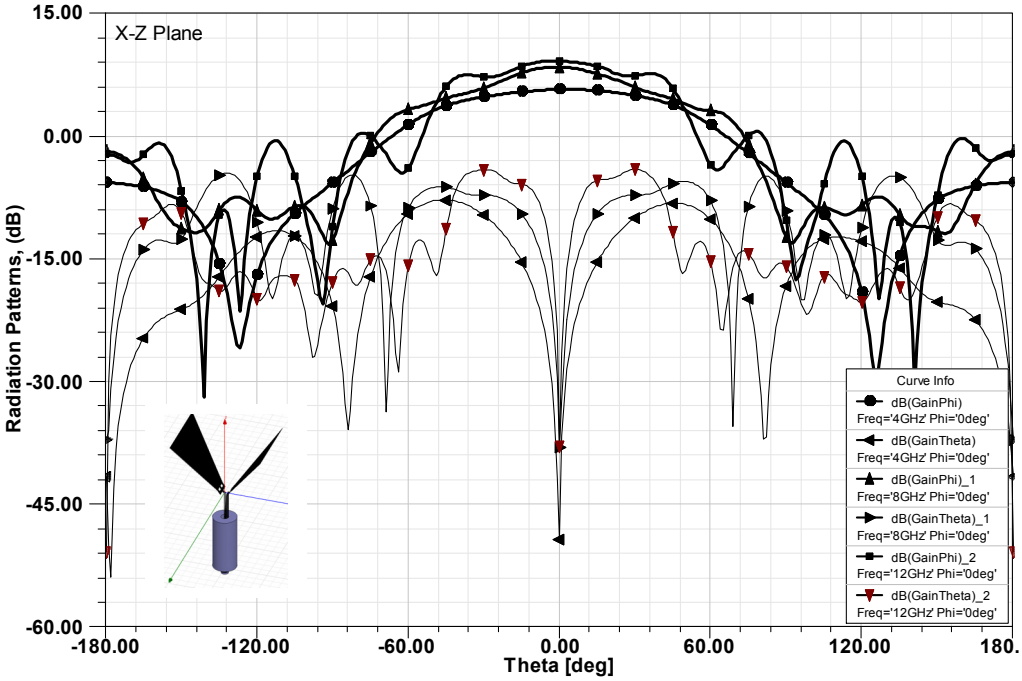

Fig. 6.28 Radiation patterns at X-Z plane, of the Vee dipole loaded with dielectric cylinder with parameters shown in Fig 6.26, antenna parameters are shown in Fig. 6.19, balun parameters are shown in Fig. 6.6, Vee angle= 35^{o}

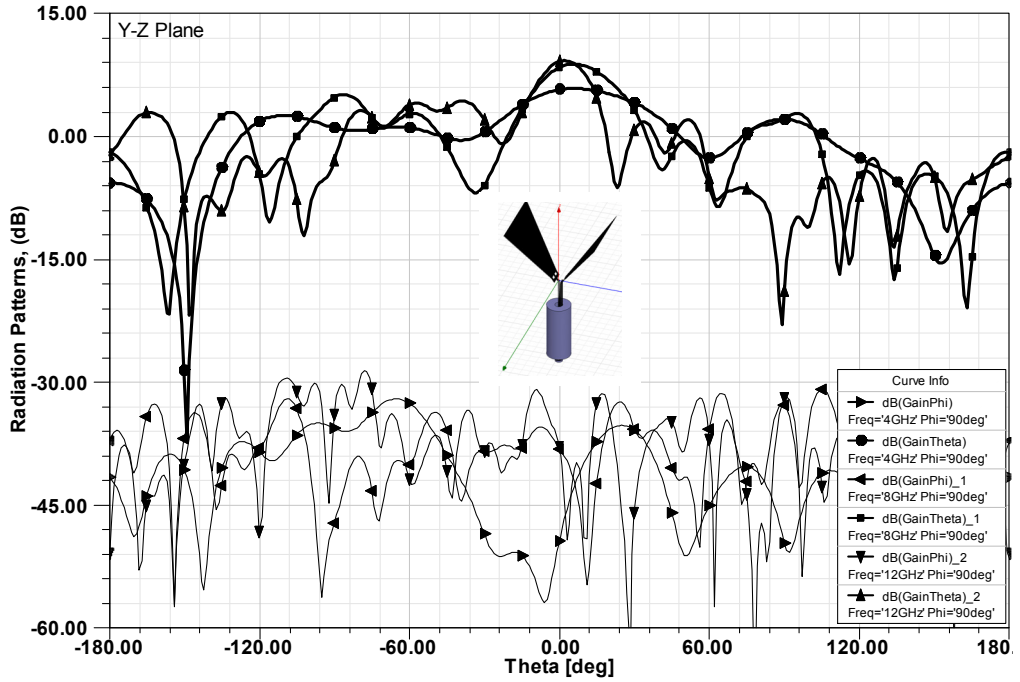

Fig. 6.29 Radiation patterns at Y-Z plane, of the Vee dipole loaded with dielectric cylinder with parameters shown in Fig 6.26, antenna parameters are shown in Fig. 6.19, balun parameters are shown in Fig. 6.6, Vee angle= 35^{o}

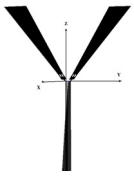 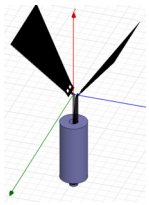			**UWB Vee Dipole Antenna of Fig. 6.19 with the new balun of Fig. 6.6 Without dielectric loading the balun**	**UWB Vee Dipole Antenna of Fig. 6.19 with the new balun of Fig. 6.6 With dielectric cylinder of given parameters**
Boresight Gain, dBi		f =4GHz	6.17 dB_i	6.41 dB_i
		f =8GHz	11.09 dB_i	9.01 dB_i
		f =10GHz	12.09 dB_i	10.61 dB_i
		f =12GHz	10.81 dB_i	9.57 dB_i
3-dB Beamwidth, degree	X-Z plane	f =4GHz	100.20°	105.1°
		f =8GHz	49.52°	64.0°
		f =10GHz	40.40°	40.68°
		f =12GHz	40.0°	90.0°
	Y-Z plane	f =4GHz	64.0°	36.8.0°
		f =8GHz	24.76°	19.0°
		f =10GHz	20.8°	16.0°
		f =12GHz	15.8°	18.0°
SLL, dB Down from the main beam	X-Z plane	f =4GHz	13.23 dB	11.76 dB
		f =8GHz	15.35 dB	15.95 dB
		f =10GHz	15.45 dB	6.7 dB
		f =12GHz	14.36 dB	8.83 dB
	Y-Z plane	f =4GHz	3.0 dB	3.38 dB
		f =8GHz	4.52 dB	5.0 dB
		f =10GHz	6.2 dB	6.5 dB
		f =12GHz	3.7 dB	8.0 dB
Front-to-Back Ratio, dB		f =4GHz	13.28 dB	12.28 dB
		f =8GHz	8.56 dB	10.91 dB
		f =10GHz	16.16 dB	22.17 dB
		f =12GHz	11.42 dB	11.87 dB

Table 6.4 Radiation Characteristics of the reduced size Vee dipole antenna of Fig. 6.19 with and without the dielectric cylinder shown in Fig. 6.26, Cylinder height H=32, inner radius =2.3mm, outer radius =7mm, ε_r=10.2, Vee angle= 35°

6.6.5.2 Dielectric Loading of the Vee Dipole

The next study case is to implement a dielectric cone between the Vee dipole arms. The UWB Vee dipole antenna with the same parameters as Fig. 6.19 is loaded with a dielectric cone with different dielectric constants and 4mm away from the feeding points. The antenna geometry and cone parameters are shown in Fig. 6.30, where the outer radius on the top R_2= 20mm and at the bottom R_1=2 mm. The cone height H=33mm. The return loss curves shown in Fig. 6.31, show that by implementing a solid dielectric cone with a dielectric constant ε_r = 6 between the Vee arms, a small reduction in the lower frequency end from 3.2 to 2.95 GHz is achieved.

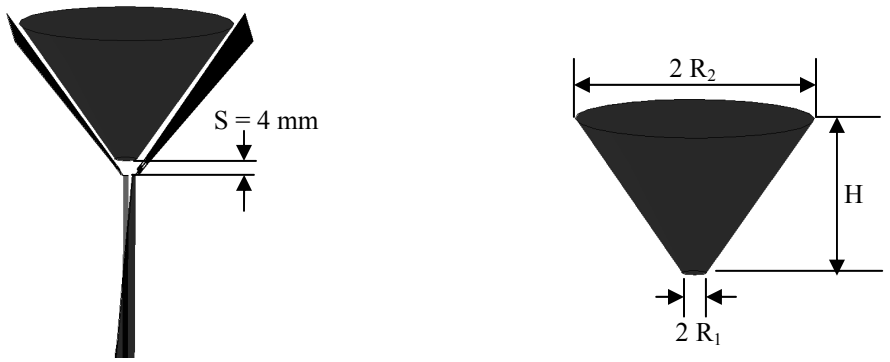

a) Vee antenna with dielectric cone b) Dielectric cone dimensions

Fig. 6.30 Vee dipole antenna of Fig. 6.19, with a solid dielectric cone with different dielectric constants, H=33mm, R_1=2mm, R_2=20mm

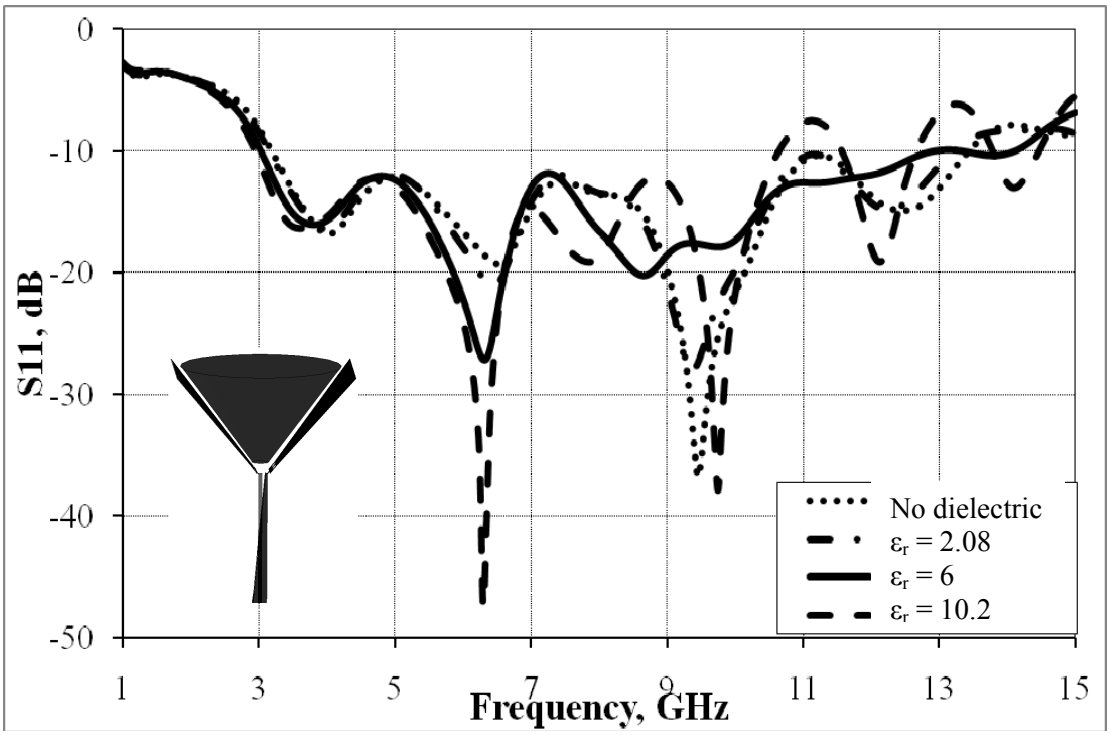

Fig. 6.31Vee dipole antenna with solid dielectric cone of height H=33mm and radii R_1=2 and R_2=20mm with different permittivity ε_r. Antenna parametares are same as of Figs. 6.19, UWB parameters are shown in Fig. 6.6, Vee angle is 35^o

The effect of changing the thickness of the same dielectric cone shown in Fig. 6.30 with ε_r = 6, on the return loss curves is shown in Fig. 6.32. The antenna has an optimum impedance bandwidth with cone thickness of T=1mm. The radiation patterns of this antenna with the dielectric cone of outer and inner radii of R_2=20 and R_1=2 mm, height of H=33mm and thickness T=1mm are shown in Figs. 6.33 and 6.34. Table 6.5 summarizes the radiation characteristics of the Vee dipole antenna with and without the

dielectric cone with parameters shown in Fig.6.30, cone thickness T=1mm. The antenna has a better performance than that without the dielectric cone and that with balun loading. As can be seen from Table 6.5, antenna with the dielectric cone has higher gain at all frequencies, in both X-Z and Y-Z planes. The loaded antenna also, has lower sidelobe levels and lower back radiations.

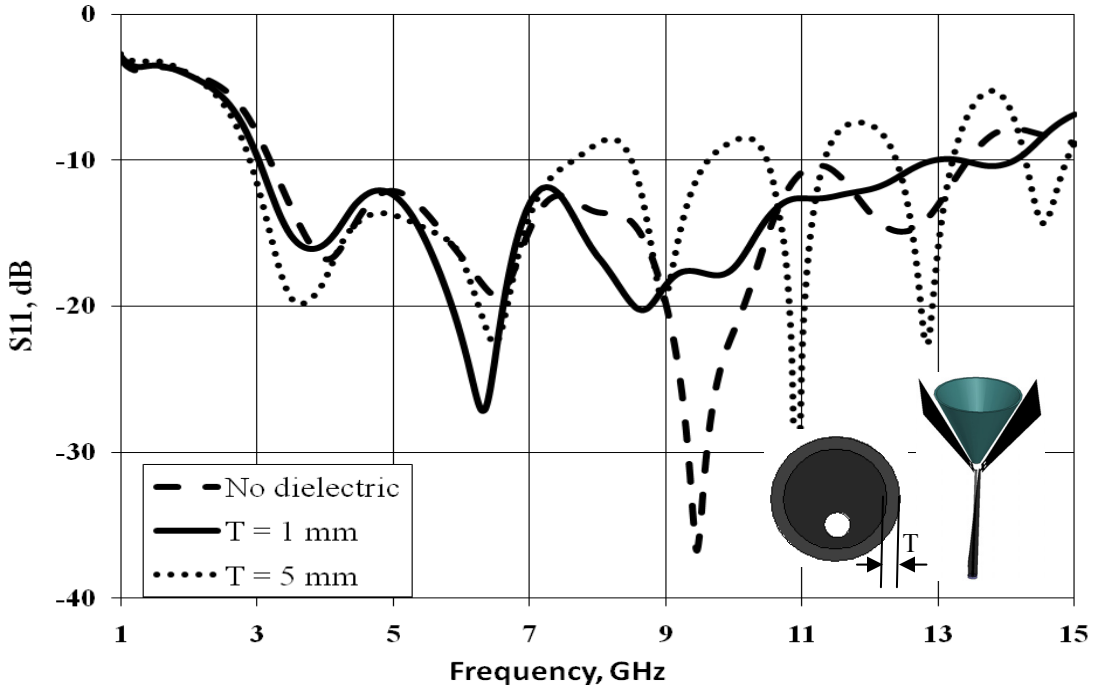

Fig. 6.32 Return losses for the Vee dipole antenna with hollow dielectric cone of height H=33mm and radii R_1 =2 and R_2=20mm, ε_r=6 and with different thicknesses T, antenna parametares are same as of Figs. 6.19, UWB balun parameters are shown in Fig. 6.6, Vee angle is 35^o

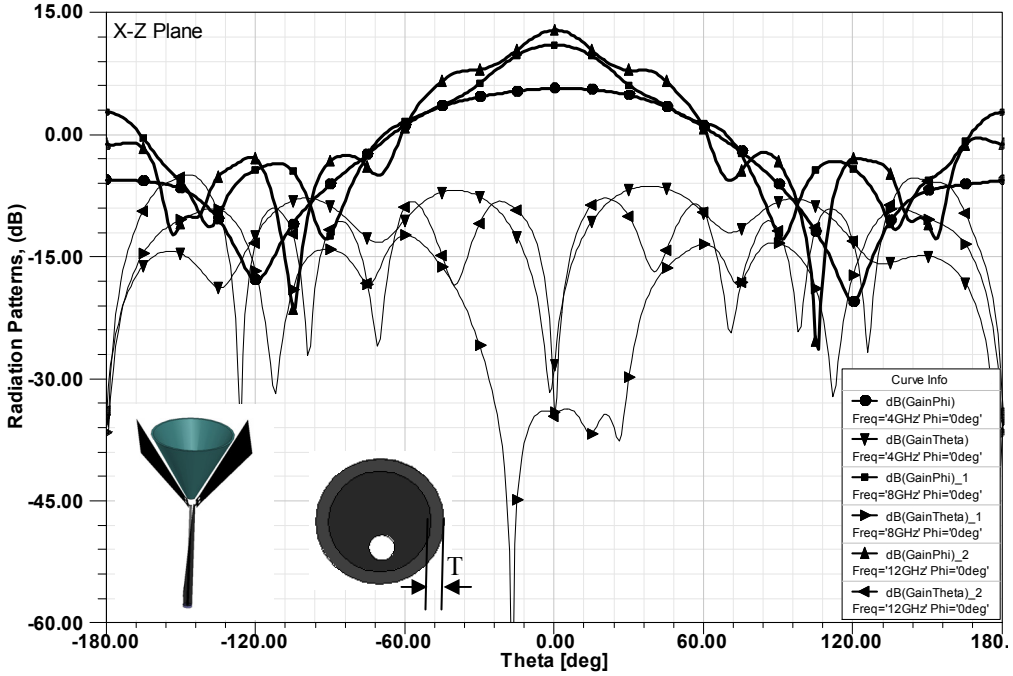

Fig. 6.33 Radiation Patterns at X-Z plane, for the Vee dipole antenna with hollow dielectric cone of height H=33mm and radii R_1=2 and R_2=20mm, ε_r=6 and with thicknesses T=1mm, antenna parametares are same as of Fig. 6.19, balun parameters are shown in Fig. 6.6, Vee angle=35^o

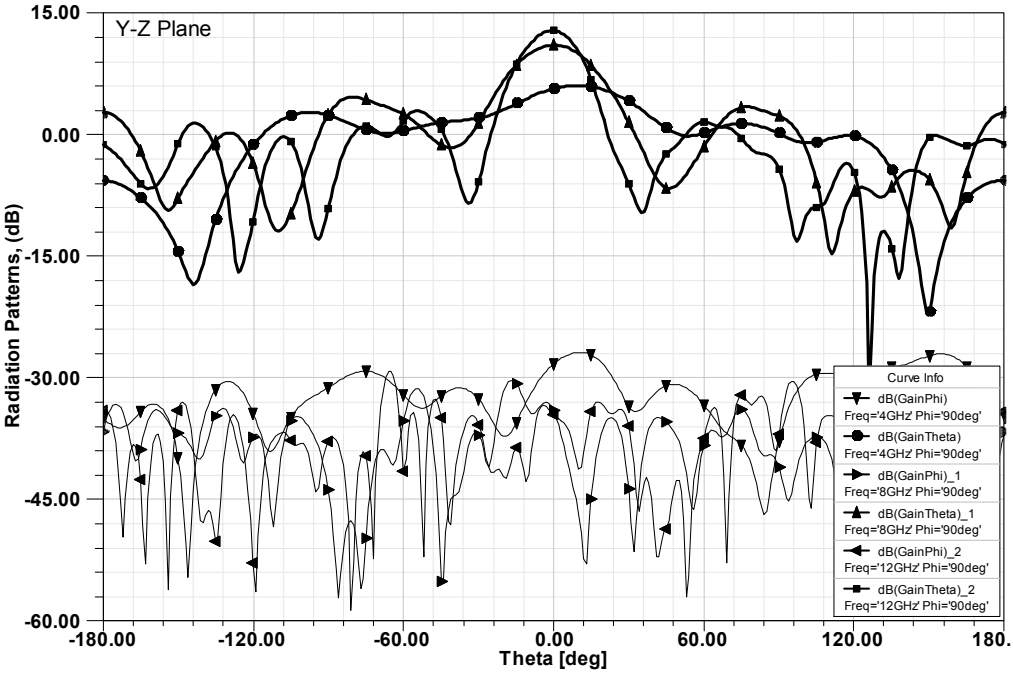

Fig. 6.34 Radiation Patterns at X-Z plane, for the Vee dipole antenna with hollow dielectric cone of height H=33mm and radii R_1=2 and R_2=20mm, ε_r=6 and with thicknesses T=1mm, antenna parametares are same as of Fig. 6.19, balun parameters are shown in Fig. 6.6, Vee angle=35^o

			**UWB Vee Dipole Antenna of Fig. 6.19 with the new balun of Fig. 6.6 without dielectric loading the Vee arm**	**UWB Vee Dipole Antenna of Fig. 6.19 with the new balun of Fig. 6.6 with dielectric cone with T=1mm**
Boresight Gain, dBi		f =4GHz	6.17 dB_i	6.28 dB_i
		f =8GHz	11.09 dB_i	11.47 dB_i
		f =10GHz	12.09 dB_i	13.29 dB_i
		f =12GHz	10.81 dB_i	13.3 dB_i
3-dB Beamwidth, degree	X-Z plane	f =4GHz	100.20^o	100.8^o
		f =8GHz	49.52^o	46.51^o
		f =10GHz	40.40^o	37.74^o
		f =12GHz	40.0^o	34.42^o
	Y-Z plane	f =4GHz	64.0^o	34.6^o
		f =8GHz	24.76^o	32.0^o
		f =10GHz	20.8^o	25.6^o
		f =12GHz	15.8^o	24.0^o
SLL, dB Down from the main beam	X-Z plane	f =4GHz	13.23 dB	13.82 dB
		f =8GHz	15.35 dB	16 dB
		f =10GHz	15.45 dB	15.8 dB
		f =12GHz	14.36 dB	15.9 dB
	Y-Z plane	f =4GHz	3.0 dB	5.0 dB
		f =8GHz	4.52 dB	8.5 dB
		f =10GHz	6.2 dB	9.51 dB
		f =12GHz	3.7 dB	11.53 dB
Front-to-Back Ratio, dB		f =4GHz	13.28 dB	13.96 dB
		f =8GHz	8.56 dB	12.2 dB
		f =10GHz	16.16 dB	22.85 dB
		f =12GHz	11.42 dB	14.97 dB

Table 6.5 Radiation Characteristics of the Vee dipole antenna with and without hollow dielectric cone of height H=33mm and radii R_1=2 and R_2=20mm, ε_r=6, thicknesses T=1mm, antenna parametares are shown in Fig. 6.19, balun of Fig. 6.6, Vee angle=35^o

6.7 Fabrication and Testing a Prototype UWB Vee Dipole Antenna

To verify the simulated results presented in this chapter, one of the Vee dipole antennas studied so far is fabricated and tested at the University of Manitoba Antenna Laboratory. To easily mount the Vee arms over the coaxial cable, each arm is etched on a substrate with ε_r=2.5 and height=0.8mm, which was available at the Antenna Laboratory. To keep the Vee-angle unchanged during the measurements, a foam pyramid was included between the two arms. The Vee dipole antenna tested is etched on a 40x44mm^2 substrate. The antenna to be tested has parameters shown in Fig. 6.19 with a Vee angle of 35^o and balun parameters shown in Fig. 6.6. The effect of etching the Vee arms on a substrate with ε_r=2.5 and thickness of 0.8mm, on the return loss curves of the antenna is shown in Fig. 6.35. The dimensions of the substrate are 40x44mm^2. As shown from the return loss curves, including the arms inside or outside the substrate has minor effect on the return loss curves. Also the optimum Vee angle was not changed as can be seen from Fig. 6.36.

Fig. 6.37 shows the Vee dipole antenna with parameters shown in Fig. 6.19, etched on a substrate with ε_r=2.5 and thickness 0.8mm. A foam pyramid is designed to hold the antenna angle at 70^o. The measured and simulated return loss curves of the antenna are compared in Fig. 6.38. Measured and simulated return loss curves are in good agreement and the antenna has a UWB impedance bandwidth..

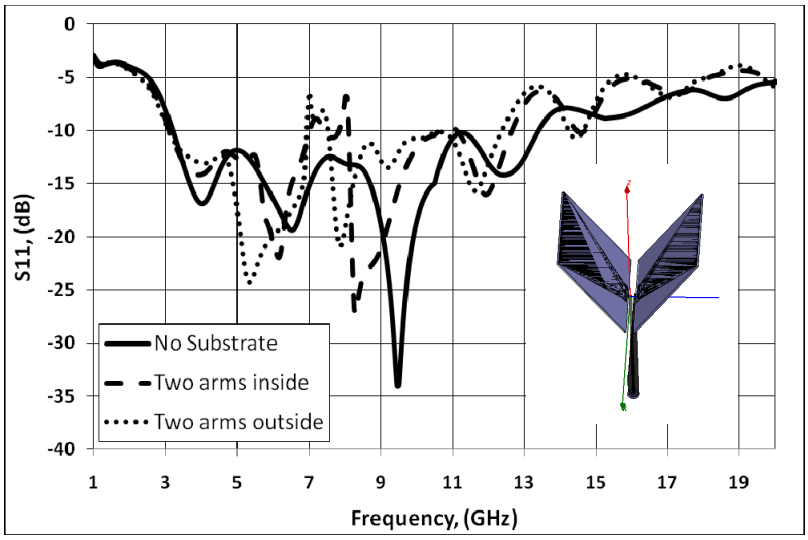

Fig. 6.35 Simulated return losses of the Vee of Fig. 6.19 with and without a 40x44mm^2 substrate supporting the Vee arms with height 0.8mm, UWB balun of Fig. 6.6, the two arms were included inside or outside the supporting substrate

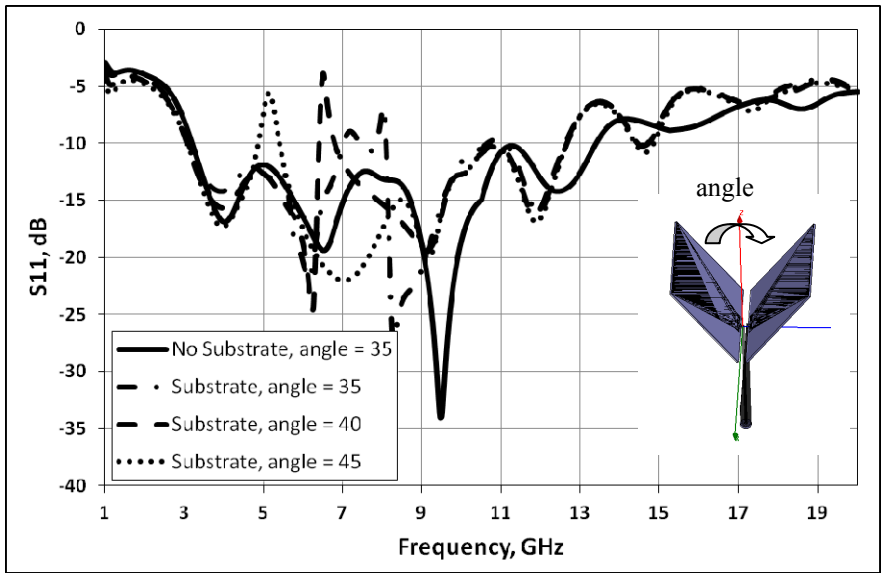

Fig. 6.36 Simulated return losses for the Vee of Fig. 6.19 with and without a 40x44mm^2 substrate supporting the Vee elements with height 0.8mm, UWB balun of Fig. 6.6, the two arms were included inside with different Vee dipole angle

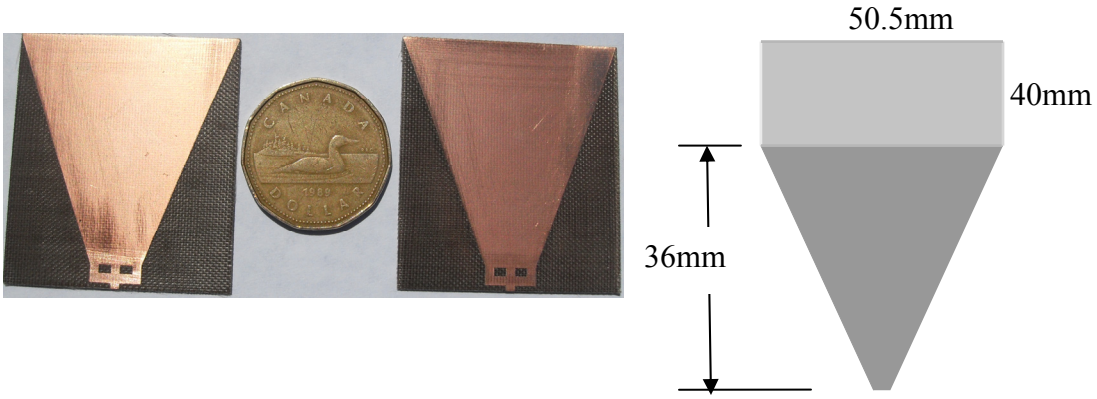

Fig. 6.37 Two-arms of the Vee dipole antenna of Fig. 6.19, with the designed foam to keep their angle

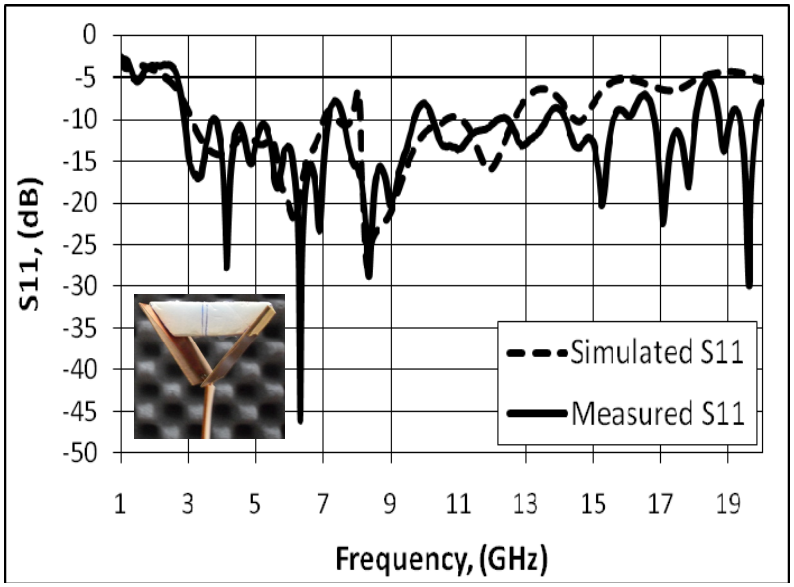

Fig. 6.38 Measured and simulated return losses for the Vee dipole antenna shown in Fig. 6.19, balun parameters are shown in Fig. 6.6, Vee angle=35^{o}

Fig. 6.39 shows the Vee dipole antenna mounted and ready for radiation pattern measurements at the University of Manitoba Antenna Laboratory. Fig. 6.40 and Fig. 6.41 show the measured and simulated radiation patterns at different frequencies at X-Z and Y-Z planes. The measurements were done over theta ranges from -90^{o} to 90^{o} due to the blocking effect of the supporting structure. Figs. 6.40 and 6.41 show the radiation patterns at f=3.5, 7, 10 and 11 GHz. Both the simulated and measured Co-Polarization components are almost identical in the X-Z plane, while measured side lobe levels are higher than expected in the X-Z plane due to fabrication tolerance of Vee angle and arms alignment. The measured and simulated cross-polarization components are in good agreement almost at all frequencies while the measured Cross-Polarization components are higher than expected in the Y-Z plane due to fabrication tolerance and Vee arms misalignment.

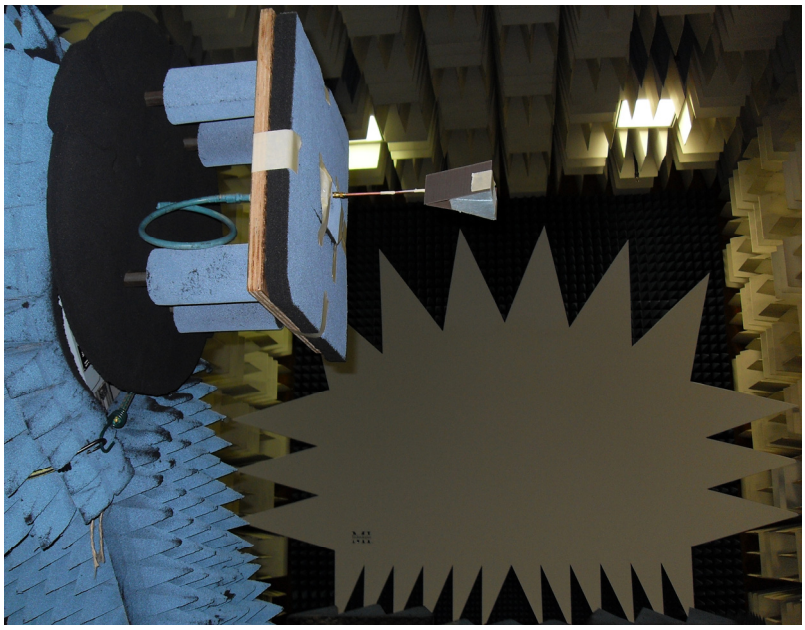

Fig. 6.39 The Vee dipole antenna mounted for radiation pattern measurements

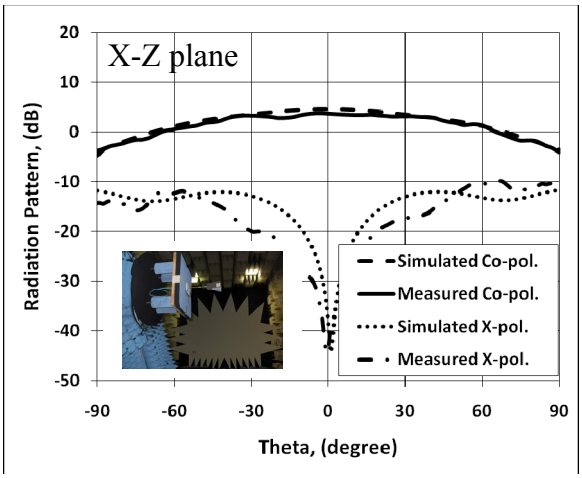

X-Z plane, f=3.5 GHz

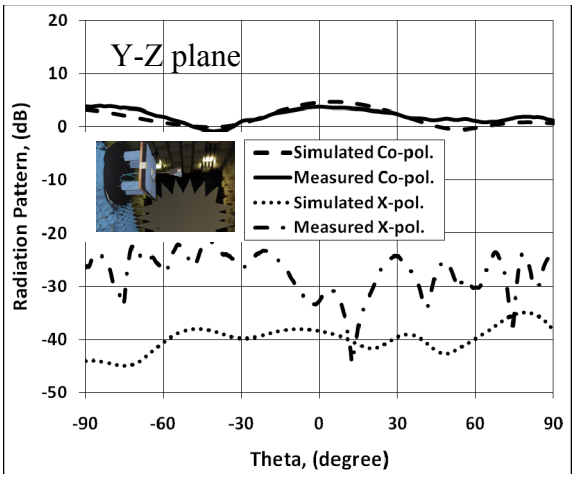

Y-Z plane, f=3.5 GHz

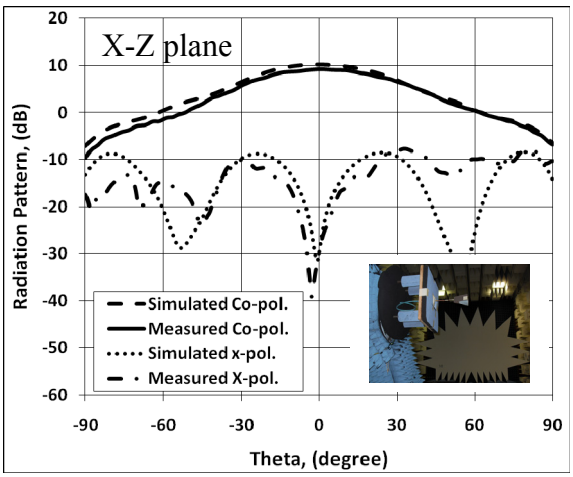

X-Z plane, f=7 GHz

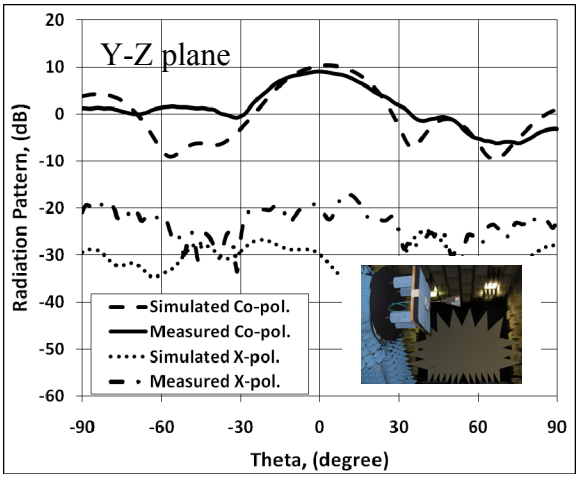

Y-Z plane, f=7 GHz

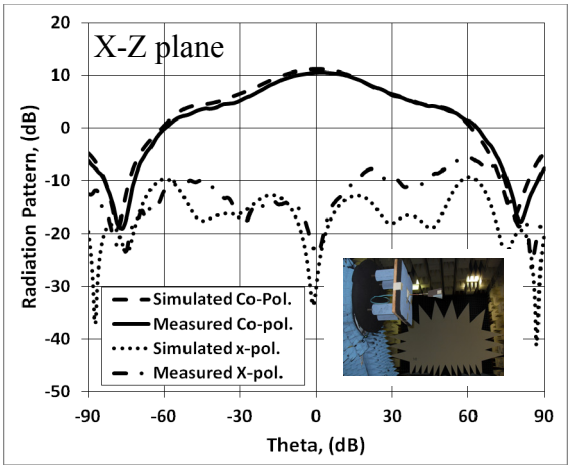

X-Z plane, f=10 GHz

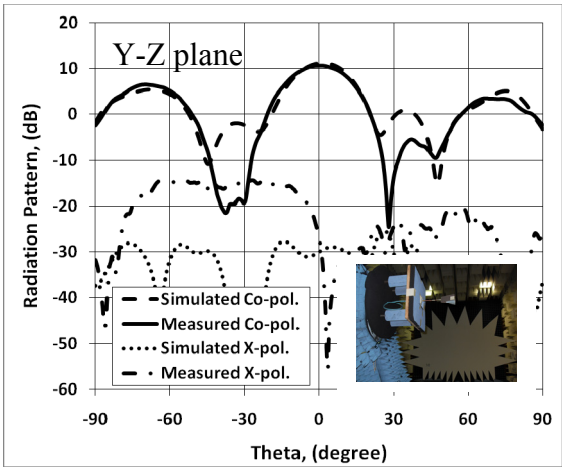

Y-Z plane, f=10 GHz

Fig. 6.40 Measured and simulated radiation patterns of the Vee dipole antenna of Fig. 6.37 and Fig. 6.19, UWB balun parameters are shown in Fig. 6.6, f=3.5, 7, 10 GHz

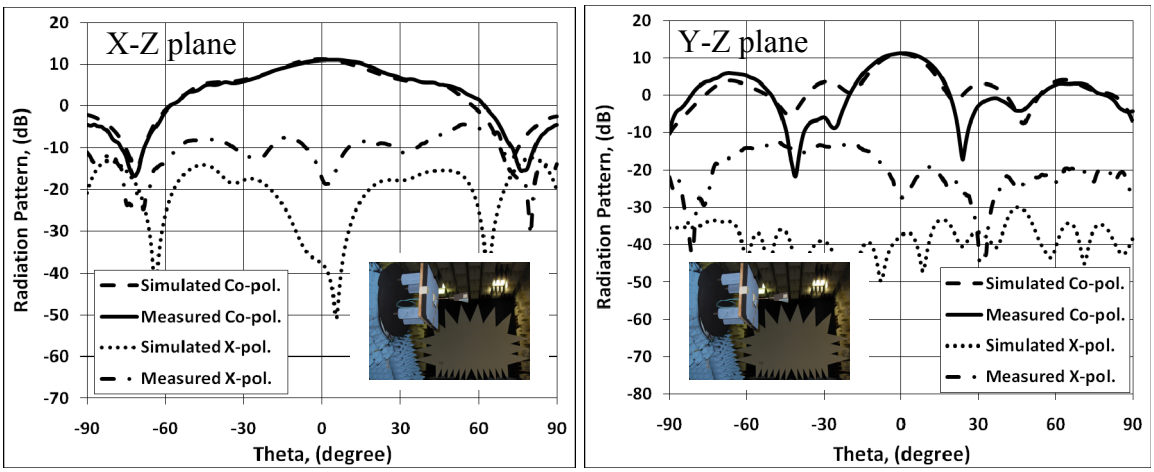

X-Z plane, f=11 GHz Y-Z plane, f=11 GHz

Fig. 6.41 Measured and simulated radiation patterns of the Vee dipole antenna of Fig. 6.37 and Fig. 6.19, UWB balun parameters are shown in Fig. 6.6, f = 11 GHz

6.8 Conclusion

This chapter introduced a new high gain UWB Vee dipole antenna with a coaxial feed and novel arm shape. The antenna was designed with different lengths and compared to a conventional triangular arm one. A Balun was also used to enhance the impedance bandwidth. A bandwidth ratio of 153% was achieved with a center frequency of 10.75 GHz. The boresight gain of the antenna reaches 12 dBi with the cross polarization level of less than 30 dB. However, this antenna suffered from high side lobe levels, especially in the Y-Z plane, along with high back radiation at some frequencies. Directors of the same arm shape were used to increase the antenna gain. It was found that, By using directors of the same shape as the Vee arms and parallel to them, and at a vertical distance of d=20 mm, from the feeding point,

gain was increased at different frequencies. The directors were scaled down with a factor of 0.5 from the Vee arms. The gain was increased by 1, 1.7 and 1.4 dB at 3, 4 and 5 GHz, respectively.

To enhance antenna radiation characteristics, by increasing the forward gain and decreasing the back radiation and sidelobe levels, a 120x170mm^2 rectangular ground plane was introduced at a distance S=30mm from the antenna feeding point. It was found that, the forward gain was increased along with a reduction in the backlobe radiation, at different frequencies. A comparison between the antenna with and without the ground plane was shown in Table 6.2. The antenna gains increased at all frequencies. Sidelobe levels were decreased at all frequencies along with an increase in the front to back ratios. The 3-dB beamwidths were narrower both at X-Z and Y-Z planes.

A reduced size Vee dipole antenna was designed. This antenna had similar radiation patterns to the original antenna of Fig.6.2c, with high sidelobe levels especially at the Y-Z plane. However, it had higher forward gain at all frequencies. Also the effect of the reduction in Vee arm length and coaxial balun length on the antenna matching was investigated. It was found that by doubling the radii dimensions of the coaxial cable, a balun with reduced length could be used without affecting the antenna impedance matching.

The effect of loading the antenna with dielectrics of different permittivities at the coaxial balun and between Vee arms was studied. Although, the antenna with balun loading gave better impedance matching, its radiation characteristics were not superior over that without a balun loading. Table 6.4 showed that, the antenna with a balun

loading had better front to back ratios at all frequencies, but the sidelobe levels were compared to that of the antenna without a balun loading or even higher at some frequencies. The gains of the antenna with balun loading were lower than their corresponding values for the unloaded case.

To further enhance the radiation characteristics of the Vee dipole antenna, a dielectric cone was used to load the Vee dipole arms. It was found that by loading the Vee arms with a hollow dielectric cone of $\varepsilon_r = 6$, with thickness T=1mm, outer radius on the top R_2= 20mm and at the bottom R_1=2 mm and of height H= 33 mm, a better antenna performance than that without the dielectric cone and that with balun loading was achieved. A comparison between the loaded and unloaded antenna performance was given in Table 6.5. The antenna with the dielectric hollow cone had higher gains at all frequencies, in both X-Z and Y-Z planes. The loaded antenna also, had lower sidelobe levels and lower back radiations.

UWB Vee dipole antennas introduced in this chapter, had a compact size with volume of (0.44 λ_L x 0.44 λ_L x 0.44 λ_L), that could be reduced to (0.15 λ_L x 0.15 λ_L x 0.2 λ_L), while still having its radiation characteristics with low frequency edge shifted to a higher frequency. A Vee dipole antenna with an arm length of 44mm was fabricated on a supporting substrate of ε_r=2.5 and thickness of 0.8mm. Then both the return loss and radiation patterns were tested at the University of Manitoba Antenna Laboratory. The return loss curve was in a good agreement with the simulated one. The Co-Polarization patterns in the X-Z plane were almost identical to the simulated ones. While the measured Co-Polarization patterns in the Y-Z plane had higher sidelobe levels than expected due to fabricated tolerances, angle change, and Vee arms misalignments. The

measured Cross-Polarization components were compared to the simulated ones in the X-Z plane, but higher than expected in the Y-Z plane, due to Vee angle errors and arms misalignment. Results of this study show that, this antenna can be a good candidate for medical imaging and as a directional UWB antenna in communication applications.

Chapter 7

Conclusion and Future Work

7.1 Summary

In this thesis, UWB omnidirectional and directional antennas were investigated on the basis of bandwidth improvement, interference mitigation with existing technologies, phase centre stabilization, cross polarization reduction and gain enhancement. When designing UWB antennas either for communications or microwave imaging applications, important parameters need to be carefully considered. These parameters include the impedance bandwidth, radiation patterns, gain, interference with existing technologies and the phase centre profile.

A survey was conducted on the UWB antennas, studied during the last few decades, including the open research problems associated with the UWB technology that still need more investigations. The interference, phase centre, cross-polarization and directive UWB antennas were of importance in this study. Previous work done on UWB monopole antennas with stop-band functions showed the need for maximizing the impedance mismatch loss. The effect of implementing such features on the antenna phase centre needed to be investigated. High gain UWB Vee antennas for communication applications along with small directional ones for certain microwave imaging applications were introduced and investigated.

Square, circular and elliptical monopole antennas with trident strip feeds were investigated to cover the currently defined ultra wideband communication band of 3.1 to 10.6 GHz, and extended it up to 19.5 GHz, for future applications. It was found that implementing notches close to the trident-feeding strip structure did not increase the impedance bandwidth of circular and elliptical antennas. Further, implementing a notch decreased the impedance bandwidth of the square monopole antenna. On the other hand, removing central metal from the interior structure of the square, circular and elliptical monopoles gave the same impedance bandwidth as the original antennas. The circular and elliptical monopole antennas with central metal removed showed better omnidirectional behaviour at higher frequencies.

Different slot configurations, implemented within UWB monopole antennas over ground planes, were studied to have new control parameters over the bandwidth; centre frequency and impedance mismatch level of the stop-band. UWB antennas with novel slots were introduced and simulated. The size of the ground plane was optimized to decrease the lower edge of the impedance bandwidth and slots were implemented to isolate the effect of this small ground plane on the radiation pattern of the antenna. Measurements for different monopole antennas were done at the University of Manitoba Antenna Laboratory to confirm simulation results. Also, measurements were done for one square monopole antenna with single and dual U-slot configurations and the gain curves at different planes were plotted, which confirmed the simulated results. Gain loss in all

principle planes were recorded within the stop-band. The finding of this section can be summarized as follows:

- The effect of using different slot shapes on the bandwidth of the stop-band was studied.
- A UWB antenna with optimized U-shape slot regarding the slot position and length was introduced. This antenna gave an impedance mismatch of 13 dB within the stop-band
- A UWB antenna design with 2-U-shape slots of the same length was also introduced. The impedance mismatch of this antenna was 16 dB, i.e. 3 dB more than that of a single slot
- A novel UWB antenna design with one and two-spiral-slots of the same length was introduced. The impedance mismatch of this antenna in the notch band was 15.5 dB, when using one-spiral slot, 18 dB when using two-spiral slots on top of each other, and 19.5 dB when using two-spiral-slots beside each others.
- The effect of the ground plane size on the performance of the monopole antennas was investigated.

The phase centre behavior of UWB monopole antennas was also investigated. First the locus of the phase centre location of the antenna was determined over the frequency band of operation at the three principle ϕ=0°, 45° and 90° planes, for different θ ranges. It was found that the phase centre moves on the Z-axis with different behavior at the three principle planes ϕ=0°, 45° and 90°. To overcome this problem, a double

interleaved circular monopole antenna was introduced, which stabilized the phase centre behavior. Also the phase centre of the square, circular and elliptical monopole antennas with trident feeding structure was investigated. A detailed phase centre movement locii of these antennas was determined. The phase centre locii were calculated at different principle planes of ϕ=0°, 45° and 90°, and for different θ ranges, over the frequency band of operation.

The phase centre locii of the antennas with different band-stop functions were also investigated. It was found that the current distribution and the active regions of UWB monopole antennas at different frequencies could be affected by inclusion of resonant features in the antenna structure, near or connected to the feed point. However, by carefully selecting the feature shape and position, the phase centre curves of such antennas could be stabilized in all three principal ϕ =0°, 45° and 90° planes, at θ from 60 to 90 degrees. In this study, the E-plane phase centre of a UWB circular monopole antenna with different features for band-stop function was calculated at each frequency and determined for the entire band. It was found that certain feature shapes have small, or even beneficial, effects on the antenna phase centre behavior, while others deteriorated the performance. Examples of phase centre location behaviors, for different θ ranges were illustrated.

Microstrip antennas with UWB impedance and radiation pattern bandwidth and low cross polarization components were investigated to work over the UWB communication frequency band. The antennas were designed over a 30 x30mm^2 substrate

with ε_r=2.5 and different heights. A partial ground plane of width = 30mm and length = 7.95mm, was used to increase the impedance bandwidth. Furthermore, a notch was implemented in the ground plane to enhance the impedance bandwidth. The antenna was fed through a microstrip line of width=2.4mm. Parametric studies were done to determine optimum critical dimensions including the ground plane, notch and distance between radiator and ground plane. A novel trapezoidal shape radiator was used with some modifications including tapering of the rectangle and adding three strips between the radiator and the microstrip line feed. The antenna showed a UWB impedance bandwidth starting at 3 GHz and extending beyond 10.6 GHz, with omnidirectional patterns in the H-plane. However the cross-polarization components were high especially at higher frequencies. To overcome this problem, two modifications were investigated to reduce the cross polarization components of this antenna. First a double layer microstrip antenna was introduced in which the partial ground plane was sandwiched between the two identical radiators, separated by two identical substrates. Second, a double layer microstrip antenna with strip-line feed was investigated. In this design the radiator was sandwiched between the two identical ground planes separated by two identical substrates with the same previous parameters. Both new designs showed a significant reduction in the cross polarization components at all frequencies. More than 20 dB reduction was achieved at $\phi=90^o$ plan, at different frequencies. The effect of misalignment between the two layers on the antenna cross polarization was also investigated. It was found that both horizontal and vertical displacements of one of the two layers increased the maximum cross polarization levels over the frequency band of operation. Two single and double layer antennas were built and tested at the University of

Manitoba Antenna Laboratory. Both return loss and radiation pattern curves were measured for both antennas. They were in good agreement, while the measured cross polarizations curves were higher than the simulated ones.

A novel high gain UWB Vee dipole antenna with coaxial feed and novel arm shape was introduced and investigated. The antenna was designed with different lengths and compared to a conventional triangular arm one. A Balun was also designed to enhance the impedance bandwidth. A bandwidth ratio of 153% was achieved with a center frequency of 10.75 GHz. The boresight gain of the antenna reached 12 dB_i, with the cross polarization level of less than 30 dB and back lobe level of about 12 dB. Directors with the same arm shape were used to increase the gain by more than 1 dB. Different type of loadings such as a reflecting ground below the antenna, a dielectric sleeve over the UWB balun and conical dielectrics between the Vee plates were also used and studied that showed enhanced gains and lower sidelobes. UWB Vee dipole antennas introduced in this thesis, had a compact size with volume of ($0.44\ \lambda_L$ x $0.44\ \lambda_L$ x $0.44\ \lambda_L$), that could be reduced to ($0.15\ \lambda_L$ x $0.15\ \lambda_L$ x $0.2\ \lambda_L$), while still having its radiation characteristics with low frequency edge shifted to a higher frequency. A Vee dipole antenna with arm length of 44mm was fabricated on a supporting substrate of ε_r=2.5 and thickness of 0.8mm. Then both the return loss and radiation patterns were tested at the University of Manitoba Antenna Laboratory. The return loss curve was in a good agreement with the simulated one. The co-polarization patterns in the X-Z plane were almost identical to the simulated ones. While the measured co-polarization patterns at the Y-Z plane had higher sidelobe levels than expected due to fabricated tolerances, angle

change, and Vee arms misalignments. The measured Cross-Polarization components were compared to the simulated ones in the X-Z plane but higher than expected in the Y-Z plane due to Vee angle errors and arms misalignment. Results of this study show that, this antenna can be a good candidate for medical imaging and as a directional UWB antenna in communication applications.

7.2 Future Research

Several scopes are available for conducting future research related to this thesis and extend behind it. They can be divided in to two separate topics.

UWB Monopole Antennas

The measurement results of the double layer microstrip antenna with strip line feeding, showed discrepancies and high unexpected values for the cross polarizations at some frequencies and planes. More research is needed to determine methods for compensating the effect of misalignment on the performance of this antenna. Also, the effect of using substrates with different height and permittivity needs to be investigated. The phase centre of this antenna needs to be characterized at all principle planes, along with ways to miniaturize this antenna.

Directional UWB Antennas

The Vee dipole antenna introduced in this thesis can be applied in a line of sight communication scenario as a high gain directional antenna, a feed to a reflector antenna

or as a small directional antenna in medical microwave imaging applications. Research that can be conducted on this antenna include:

- Equalize the E- and H-plane patterns of this antenna, currently their beamwidths are different.
- Characterize the combined E- and H- plane phase centres of the two- and four-arm Vee dipole antenna.
- Study Ground plane effect on the gain and phase centre stabilization of UWB Vee dipole antennas
- Apply strip or microstrip feeding transitions, instead of using the coaxial cable feeding
- Implement a wire-arm type UWB Vee dipole antenna.
- Investigate and optimize the reflecting ground effects on antenna performance by designing reflecting planes of different shapes and sizes.
- Study the effect of combining the loading of the balun and the Vee antenna on the radiation characteristics.
- Investigate the effect of combining the directors, the reflecting ground plane, the dielectric loading and the UWB size on the antenna performance.
- Design a dual linear orthogonal polarization UWB Vee dipole antenna

References

[1] L. K. Brunson, J. P. Camacho, W. M. Doolan, R. L. Hinkle, G. F. Hurt, M. J. Murray, F. A. Najmy, P. C. Roosa and R. L. Sole, "Assessment of compatibility between ultra wideband devices and selected federal systems," NTIA Special Publications 01-43, January, 2001

[2] D. S. Anderson, E. F. Drocella, S. K. Jones and M A. Settle, "Assessment of compatibility between ultra wideband (UWB) systems and global positioning system (GPS) receivers," NTIA Special Publications 01-45, February, 2001

[3] FCC 1st Report and Order on Ultra-Wideband Technology, Feb. 2002

[4] Hans G. Schantz,“ Art and Science of Ultra Wideband Antennas,” Artech House, Boston, London, 2005, chapter 6.

[5] D. Lamensdorf and L. Susman, "Baseband pulse antenna technologies," IEEE Ant. and Propag. Magazine, vol. 36, no. 1, pp. 20-30, Feb. 1994

[6] M. Z. Win, D. Dardari, A. F. Molisch, W. Wiesbeck and J. Zhang, "History and applications of UWB," Proceedings of IEEE, Vol. 97, no. 2, pp. 198-204, Feb. 2009

[7] H. G. Schantz, "A brief history of UWB antennas," Proceedings of the IEEE conference on ultra wideband systems and technologies, pp. 209-213, 16-19 Nov., 2003

[8] H. G. Schantz, "Introduction to ultra-wideband antennas," Proceedings of the IEEE conference on ultra wideband systems and technologies, pp. 1-9, 16-19 Nov., 2003

[9] A. Akdagli, C. Ozdemir and S. Yamacli, "A review of recent patents on ultra wide band (UWB) antennas," Recent Patents on Electrical Engineering, vol. 1, no. 1, pp. 68-75, 2008

[10] S. Licul, J. A. N. Noronha, W. A. Davis, D. G. Sweeney, C. R. Anderson and T. M. Bielawa, "A parametric study of time-domain characteristics of possible UWB antenna architectures," IEEE 58th conference on VTC, vol. 5, pp. 3110-3114, 6-9 Oct., 2003

[11] T. Yang and W. A. Davis, "Fundamental-limit perspectives on ultra-wideband antennas," EMTS International URSI Commission B Electromagnetic Theory Symposium, Ottawa, On, July 26-28, 2007

[12] A. Saitou, K. Aoki, K. Honjo and K. Watanabe, “Design considerations on the minimum size of broadband antennas for UWB applications,” IEEE Transactions on Microwave Theory and Techniques, vol. 56, No. 1, pp. 15-21, January, 2008

[13] B. A. Kramer, C.-C Chen, M. Lee and J. L. Volakis, “Fundamental limits and design guidelines for miniaturizing ultra-wideband antennas,” IEEE Antennas and Propagation Magazine, vol. 51, No. 4, pp. 57-69, August, 2009

[14] H. A. Wheeler, “The radiansphere around a small antenna,” Proceedings of the IRE, vol. 47, August 1959

[15] R. H. Johnston and J. G. McRory, “An improved small antenna radiation-efficiency measurement method,” IEEE Antennas and Propagation Magazine, vol. 40, No. 5, pp. 40-48, October 1998

[16] H. G. Schantz, "Radiation efficiency of UWB antennas," IEEE UWBST Conference, 2002

[17] G. L. Fur, P. Besnier and A. Sharaiha, “Efficiency measurement of UWB antennas using time reversal in reverberation chambers,” Electronics Letters, vol. 44, No. 17, 14 August, 2008

[18] R. J. Garbacz and R. H. Turpin, “A generalized expansion for radiated and scattered fields,” IEEE Transactions on Antennas and Propagation, vol. AP-19, No. 3, pp. 348-358, May 1971

[19] R. F. Harrington and J. R. Mautz, “Theory of characteristic modes for conducting bodies,” IEEE Transactions on ASntennas and Propagation, vol. AP-19, No. 3, pp. 348-358, May 1971

[20] M. Cabedo-Fabres, E. Antonino-Daviu, A. Valero-Nogueira, and M. Ferrando-Bataller, “Analysis of wide band planar monopole antennas using characteristic modes,” IEEE International Symposium on Antennas and Propagation Society, vol. 3, pp. 733-736, 2003

[21] E. Antonino-Daviu, M. Cabedo-Fabres, M. Ferrando-Bataller and A. Valero-Nogueira, “A discussion on the feed configuration of planar monopole antennas to obtain ultra wide band performance,” IEEE International Symposium on Antennas and Propagation Society, vol. 2, pp. 1867-1870, 2004

[22] M. Ferrando-Bataller, M. Cabedo-Fabres, E. Antonio-Daviu and A. Valero-Nogueira, “Overview of planar monopole antennas for UWB applications,” Proc. EuCAP, Nice, France, 6-10 Nov. 2006

[23] M. Cabedo-Fabres, E. Antonino-Daviu, A. Valero-Nogueira and M. F. Bataller, “The theory of characteristic modes revisited: a contribution to the design of

antennas for modern applications," IEEE Antennas and Propagation Magazine, vol. 49, No. 5, pp. 52-68, October 2007

[24] K. A. Obeidat B. D. Raines and R. G. Rojas, "Application of characteristic modes and non-foster multiport loading to the design of broadband antennas," IEEE Transactions on Antennas and Propagation, vol. 58, No. 1, pp. 203-207, January 2010

[25] W. Wu and Y. P. Zhang, "Analysis of ultra-wideband printed planar quazi-monopole antennas using the theory of characteristic modes," IEEE Antennas and Propagation Magazine, vol. 52, No. 6, pp. 67-77, December 2010

[26] E. Antonino-Daviu, M. Fabres, M. Ferrando-Bataller and V. M. R. Penarrocha, "Modal analysis and design of band-notched UWB planar monopole antennas," IEEE Transactions on Antennas and Propagation, vol. 58, No. 5, pp. 1457-1466, May 2010

[27] S. B. T. Wang A. M. Niknejad and R. W. Brodersen, "Circuit modeling methodology for UWB omnidirectional small antennas," IEEE Journal on Selected Areas in Communications, vol. 24, No. 4, pp. 871-877, April 2006

[28] G. Quintero, J.-F. Zurcher and A. K. Skrivervik, "System Fidelity Factor: a new method for comparing UWB antennas," IEEE Transactions on Antennas and Propagation, vol. 59, No. 7, pp. 2502-2512, July 2011

[29] W. Dullaert and H. Rogier, "Novel compact model for the radiation pattern of UWB antennas using Vector Spherical and Slepian Decomposition," IEEE Transactions on Antennas and Propagation, vol. 58, No. 2, pp. 287-299, February, 2010

[30] B. K. Chung and H. T. Chuah, "Design and construction of a multipurpose wideband anechoic chamber," IEEE Antennas and Propagation Magazine, vol. 45, No. 6, pp. 41-47, December, 2003

[31] A. V. Kalinin, "Wideband antenna measurements in anechoic chamber," 2nd International Workshop on Ultra wideband and Ultrashort Impulse Signals, Sevastopol, Ukraine, pp. 151-153, 19-22 September 2004

[32] S. Licul and W. A. Davis, "Ultra-wideband (UWB) antenna measurements using Vector Network Analyzer," Proceedings of the International Symposium on Antennas and Propagation, vol. 2, pp. 1319-1321, June 20-25, 2004

[33] A. P. Freundorfer, J. Y. Siddiqui, and Y. M. M. Antar, "Characterization of ultrawideband antennas using noise," IEEE Antennas and Wireless Propagation Letters, vol. 9, 2010

[34] Ansoft Corporation, "HFSS v10-13: High Frequency Structure Simulator Based on the Finite Element Method" 2007 [Online]. Available: http://www.ansoft.com/products.cfm.

[35] N. P. Agrawall, G. Kumar, and K. P. Ray, "Wide-band planar monopole antennas," IEEE Transactions on Antennas and Propagation, vol. 46, no. 2, pp. 294-295, Feb. 1998

[36] Girish Kumar and K. P. Ray.; "Broadband microstrip antennas", Artech House, pages 357-363, Boston, London, 2003

[37] J. A. Evans, M. John and M. J. Ammann, "Note on the corrugated plate monopole," Microwave and Optical Technology Letters, vol. 46, no. 2, Jul. 20, 2005

[38] S. Honda, M. Ito, H. Seki and Y. Jinbo, "A disc monopole antenna with 1:8 impedance bandwidth and omni-directional radiation pattern," Proceedings of ISAP, Sapporo, Japan, pp. 1145-1148, September 1992

[39] M. Hammoud, P. Poey and F. Colombel, "Matching the input impedance of a broadband disc monopole," Electronics Letters, vol. 29, No. 4, pp. 406-407, 18 February 1993

[40] R. Chair, A. A. Kishk and K. F. Lee, "Ultrawide-band coplanar waveguide-fed rectangular slot antenna," IEEE Antennas and Wireless Propagation Letters, vol. 3, pp. 227-229, 2004

[41] A. J. Kerkhoff, R. L. Rogers and H. Ling, "Design and analysis of planar monopole antennas using a genetic algorithm approach," IEEE Transactions on Antennas and Propagation, vol. 52, no. 10, pp. 2709-2718, Oct. 2004

[42] Z. N. Chen and X. Qing, "Research and development of planar UWB antennas," Proc. of the Microwave Conference (APMC), vol. 1, 4-7 Dec. 2005

[43] D. Valderas, J. Legarda, I. Gutierrez and J. I. Sancho, "Design of UWB folded-plate monopole antennas based on TLM," IEEE Transactions on Antennas and Propagation, vol. 54, no. 6, pp. 1676-1687, Jun. 2006

[44] X. H. Wu and Z. N. Chen, "Comparison of planar dipoles in UWB applications," IEEE Transaction on Antenna and Propagation, vol. 53, no. 6, pp. 1973-1983, Jun. 2005

[45] K. G. Thomas, N. Lenin and R. Sivaramakrishnan, "Ultrawideband planar disc monopole," IEEE Transaction on Antennas and Propagation, vol. 54, No. 4, pp. 1339-1341, April 2006

[46] L. Guo, J. Liang, C. C. Chiau, X. Chen, C. G. Parini and J. Yu, "Performances of ultra-wideband disc monopoles in time domain," IET Microwaves, Antennas and Propagation, vol. 1, No. 4, pp. 955-959, 2007

[47] P. McEvoy, M. John, S. Curto and M. J. Ammann, "Group delay performance of ultra wideband monopole antennas for communication applications," Loughborough Antennas and Propagation Conference, UK, pp. 377-380, 17-18 March, 2008

[48] A. M. Abbosh and M. E. Bialkowski, "Design of ultrawideband planar monopole antennas of circular and elliptical shape," IEEE Transactions on Antennas and Propagation, vol. 56, No. 1, pp. 17-23, January, 2008

[49] M. N. Srifi, S. K. Podilchak, M. Essaaidi and Y. M. M. Antar, "Planar circular disc monopole antennas using compact impedance matching networks for ultra-wideband (UWB) applications," Asia-Pacific Microwave Conference (APMC), pp. 782-785, 2009

[50] S. Chamaani, S. A. Mirtaheri, K. Paran, A. Abolghasemi and M. Fardis, "Coplanar waveguide-fed ultra wideband planar monopole antenna optimization," IET Microwaves, Antennas and Propagation, vol. 4, No. 9, pp. 1264-1274, 2010

[51] J. Zhao, C. Chen and J. L. Volakis, "Frequency-scaled UWB inverted-hat antenna," IEEE Transactions on Antennas and Propagation, vol. 58, No. 7, pp. 2447-2451, July 2010

[52] J. Martinez-Fernandez, J. M. Gil and J. Zapata, "Profile optimization in planar ultra-wideband monopole antennas for minimum return losses," IET Microwaves, Antennas and Propagation, vol. 4, No. 7, pp. 881-892, 2010

[53] M. Ojaroudi, Sh. Yazdanifard, N. Ojaroudi and M. Naser-Moghaddasi, “Small square monopole antenna with enhanced bandwidth by using inverted T-shaped slot and conductor-backed plane,” IEEE Transactions on Antennas and Propagation, vol. 59, No. 2, pp. 670-674, February 2011

[54] J. Liu, S. Zhong and K. P. Esselle, “A printed elliptical monopole antenna with modified feeding structure for bandwidth enhancement,” IEEE Transactions on Antennas and Propagation, vol. 59, No. 2, pp. 667-670, February 2011

[55] K. Chen, C. Sim, and J. Row, “A compact monopole antenna for super wideband applications,” IEEE Antennas and Wireless Propagation Letters, Vol. 10, pp. 488-491, 2011

[56] Y. Lu, Y. Huang, H. T. Chattha and P. Cao, “Reducing ground-plane effects on UWB monopole antennas,” IEEE Antennas and Wireless Propagation Letters, vol. 10, pp. 147-150, 2011

[57] Q. Wu, R. Jin and J. Geng, “Ultra-wideband quazi-circular monopole antennas with rectangular and trapezoidal grounds,” IET Microwaves, Antennas and Propagation, vol. 3, No. 1, pp. 55-61, 2009

[58] K. Wong, C. Wu, and S. Su, “Ultrawide-band square planar metal-plate monopole antenna with a trident-shaped feeding strip,” IEEE Transactions on Antennas and Propagation, vol. 53, no. 4, pp. 1262-1269, April 2005

[59] K.-H. Kim, Y.—J. Cho, S.-H. Hwang and S.-O. Park, "Band-notched UWB planar monopole antenna with two parasitic patches," Electronics Letters, vol. 41, no. 14, July 2005

[60] Y.-C. Lin and K.-J. Hung, "Compact ultra wideband rectangular aperture antenna and band-notched designs," IEEE Transactions on Antennas and Propagation, vol. 54, no. 11, pp. 3075-3081, Nov. 2006

[61] Y. J. Cho, K. H. Kim, D. H. Choi, S. S. Lee and S.O. Park, "A miniature UWB planar monopole antenna with 5-GHz band-rejection filter and the time-domain characteristics," IEEE Transactions on Antennas and Propagation, vol. 54, no. 5, pp. 1453-1460, May 2006

[62] J. Qiu, Z. Du, J. Lu and K. Gong, "A planar monopole antenna design with band-notched characteristic," IEEE Transactions on Antennas and Propagation, vol. 54, no. 1, pp. 288-292, Jan. 2006

[63] K. H. Kim and S.-O. Park, "Analysis of the small band-rejected antenna with the parasitic strip for UWB," IEEE Transactions on Antennas and Propagation, vol. 54, no. 6, pp. 1688-1692, June 2006

[64] J. Kim, C. S. Cho and J. W. Lee, "5.2 GHz notched ultra-wideband antenna using slot-type SRR," Electronics Letters, vol. 42, no. 6, March 2006

[65] W.-S. Lee, D.-Z. Kim, K.-J. Kim and J.-W. Yu, "Wideband planar monopole antennas with dual band-notched characteristics," IEEE Transactions on Antennas and Propagation, vol. 54, no. 6, pp. 2800-2806, June 2006

[66] A. J. Kerkhoff and H. L. Ling, "Design of a band-notched planar monopole antenna using genetic algorithm optimization," IEEE Transactions on Antennas and Propagation, vol. 55, no. 3, pp. 604-610, March 2007

[67] T. Dissanayake and K. P. Esselle, "Prediction of the notch frequency of slot loaded printed UWB antennas," IEEE Transactions on Antennas and Propagation, vol. 55, no. 11, pp. 3320-3325, Nov. 2007

[68] T.-G. Ma and S.J. Wu, "Ultrawideband band-notched folded strip monopole antenna," IEEE Trans. on Antennas and Propagation, vol. 55, no. 9, pp. 2473-2479, Sep. 2007

[69] T.-P. Vuong, A. Ghiotto, Y. Duroc and S. Tedjini, "Design and characteristics of a small U-slotted planar antenna for IR-UWB," Microwave and Optical Technology Letters, vol. 49, no. 7, pp. 1727-1731, July 2007

[70] Q.-X. Chu and Y.-Y. Yang, "A compact ultra wideband antenna with 3.4/5.5 GHz dual band-notched characteristics," IEEE Transactions on Antennas and Propagation, vol. 56, no. 12, pp. 1688-1692, Dec. 2008

[71] J. Martinez-Fernandez, V. de la Rubia, J. M. Gil and J. Zapata, "Frequency notched UWB planar monopole antenna optimization using a Finite Element Method-based approach," IEEE Trans. on Antennas and Propag., vol. 56, no. 9, pp. 2884-2893, Sep. 2008

[72] F. J. Wang and J.S. Zhang, "Study of a band-notched double printed dipole antenna," Microwave and Optical Technology Letters, vol. 50, no. 11, pp. 2986-2989, Nov. 2008

[73] Y. Zhang, W. Hong, C. Yu, Z.-Q. Kuai, Y. Don and J.-Y. Zhou, “Planar ultrawideband antennas with multiple notched bands based on etched slots on the patch and/or split ring resonators on the feed line,” IEEE Transactions on Antennas and Propagation, vol. 56, No. 9, pp. 3063-3068, September 2008

[74] J.-P. Zhang, Y.-S. Xu and W.-D. Wang, “Microstrip-fed semi-elliptical dipole antennas for ultrawideband communications,” IEEE Transactions on Antennas and Propagation, vol. 56, No. 1, pp. 241-244, January 2008

[75] K. Chang, H. Kim and Y. J. Yoon, “Ultra-wideband antenna with improved gain characteristics,” IET Microwaves, Antennas and Propagation, vol. 2, No. 5, pp. 512-517, 2008

[76] H. Zhou, Y. Yin, J. Deng and Q. Liu, "CPW-Fed ultra-wideband antenna with dual band-notched characteristics," Microwave and Optical Technology Letters, vol. 51, no. 2, pp. 330-332, Feb. 2009

[77] A. A. Alshehri, A. R. Sebak and T. A. Denidni, "Printed ultra-wideband elliptical antenna with a frequency-band notch function," Microwave and Optical Technology Letters, vol. 51, no. 3, pp. 860-864, March 2009

[78] J. Ma, Y.-Z. Yin, J.-Y. Deng and Q. Ma, "Design of an ultra-wideband antenna with a novel dual band-notched structure," Microwave and Optical Technology Letters, vol. 51, no. 3, pp. 814-817, March 2009

[79] S.-H. Choi, H.-J. Lee and J.-K. Kim, "Design of miniaturized ultra-wideband antennas with band notch characteristic," Microwave and Optical Technology Letters, vol. 51, no. 3, pp. 717-720, March 2009

[80] K. S. Ryu and A. Kishk, “UWB antenna with single or dual band-notches for lower band and upper WLAN band,” IEEE Transactions on Antennas and Propagation, vol. 57, No. 12, pp. 3942-3950, December 2009

[81] R. Bourtoutian, C. Delaveaud and s. Toutain, “Novel method for characterizing filtering antennas,” IEEE Antennas and Propagation Magazine, vol. 51, No. 3, June 2009

[82] M. Naser-Moghadisi, R. A. Sadeghadeh, L. Asadpor, S. Soltani and B. S. Virdee, “Improved band-notch technique for ultra-wideband antennas,” IET Microwaves, Antennas and Propagation, vol. 4, No. 11, pp. 1886-1891, 2010

[83] L. Y. Cai, G. Zeng, H. C. Yang and X. W. Zhan, “Compact printed ultra-wideband antennas with band-notched characteristics,” Electronics Letters, vol. 46, No. 12, 10 June, 2010

[84] A. Ghobadi, Ch. Ghobadi and J. Nourinia, “A novel band-notched planar monopole antenna for ultrawideband applications,” IEEE Antennas and Wireless Propagation Letters, vol. 9, pp. 608-611, 2010

[85] Z.-A. Zheng, Q.-X. Chu and Z.-H. Tu, “Compact band-rejected ultrawideband slot antennas inserting with $\lambda/2$ and $\lambda/4$ resonators,” IEEE Transactions on Antennas and Propagation, vol. 59, No. 2, pp. 390-397, February 2011

[86] D. Carter, "Phase centers of microwave antennas," IRE Transactions on Antennas and Propagation, pp. 597-600, October. 1956

[87] L. Mania, "The antenna phase center in Satellite Radio-Doppler Geodetic Systems," IEEE Transactions on Geoscience and Remote Sensing, vol. GE-20, No. 4, pp. 536-543, October 1982

[88] K. Rao and L. Shafai, "Phase center calculations of reflector antenna feeds," IEEE Transactions on Antennas and Propagation, vol. AP-32, No. 7, pp. 740-742, July 1984

[89] J. Svigelj, U. Navsariwala,E. Porrett and N. Buris, "Correction of antenna phase center offsets in outdoor range measurements," IEEE International Symposium on Antennas and Propagation, vol. 3, pp. 808-811, 22-27 June, 2003

[90] K. Rambabu, H. A. Thiart and J. Bornemann, "Ultrawideband printed-circuit antenna," IEEE Transactions on Antennas and Propagation, vol. 54, No. 12, pp. 3908-3911, December 2006

[91] J.-P. Shang, D. Fu, Y. Deng, and S. Jiang, "Measurement of phase center for antenna with the method of moving reference point," 8th International Symposium on Antennas, Propagation and EM Theory, pp. 114-117, 2-5 November 2008

[92] M. R. Mahfouz, C. Zhang, B. C. Merkl, M. J. Kuhn and A. E. Fathy, "Investigation of high-accuracy indoor 3-D positioning using UWB technology," IEEE Transactions on Microwave Theory and Techniques, vol. 56, No. 6, pp. 1316-1330, June 2008

[93] T. P. Montoya and G. S. Smith, “Land mine detection using a ground-penetrating Radar based on resistively loaded Vee dipoles,” IEEE Transactions on Antennas and Propagation, vol. 47, No. 12, pp. 1795-1805, December 1999

[94] R. Aylo, K. Y. Kabalan, A. El-Hajj, M. Al-Husseini and J. Costantine, “An investigation of the wideband properties of resistively loaded conical-cylindrical V-shaped antenna,” IEEE Antennas and Wireless Propagation Letters, vol. 7, pp. 298-301, 2008

[95] A. Abbosh, B. Mohammed and M. Bialkowski, “Planar array antenna for ultra wideband microwave imaging system,” International Conference on Communications and Information Technology (ICCIT), Aqaba, pp. 199-202, 2011

[96] F. Scotto di Clemente, M. Helbig, J. Sachs, U. Schwarz, R. Stephan, and M. A. Hein, “Permittivity-matched compact ceramic ultra-wideband horn antennas for biomedical diagnostics,” Proceedings of the 5th European on Antennas and Propagation (EuCAP), pp. 2386-2390, 2011

[97] N. Kaneda, W. R. Deal, Y. Qian, R. Waterhouse and T. Itoh, "A broad-band planar Quasi-Yagi antenna," IEEE Transactions on Antennas and Propagation, vol. 50, no. 8, pp. 1158-1160, August. 2002

[98] H. K. Kan, R. B. Waterhouse, A. M. Abbosh and M. E. Bialkowski, "Simple broadband planar CPW-Fed Quasi-Yagi antenna," IEEE Antennas and Wireless Propagation Letters, vol. 6, pp. 18-20, 2007

[99] F. Merli, J. F. Zurcher, A. Freni and A. K. Skrivervik, “Analysis, design and realization of a novel directive ultrawideband antenna,” IEEE Transactions on Antennas and Propagation, vol. 57, no. 11, pp. 3458-3466, December 2008

[100] J. Yang, “On conditions for constant radiation characteristics for log-periodic array antennas,” IEEE Transactions on Antennas and Propagation, vol. 58, No. 5, pp. 1521-1526, May 2010

[101] O. Kramer, T. Djerafi and K. Wu, “Vertically multilayer-stacked Yagi antenna with single and dual polarizations,” IEEE Transactions on Antennas and Propagation, vol. 58, No. 4, pp. 1022-1030, April 2010

[102] T. Jiang, W. Hong and Z. Kuai, “Compact ultra-wideband directional printed antenna with notched band,” Proceedings of the Microwave Conference, China-Japan Joint, 2011

[103] R. Olsson, P. Kildal and S. Weinreb, "A novel low-profile log-periodic ultra wideband feed for the dual-reflector antenna of US-SKA," IEEE International Symposium on Antennas and Propagation, vol. 3, pp. 3035-3038, 20-25 June 2004

[104] R. Olsson, P. S. Kildal, and S. Weinreb, "The eleven antenna: a compact low-profile decade bandwidth dual polarized feed for reflector antennas," IEEE Transactions on Antennas and Propagation, vol. 54, No. 2, pp. 368-375, February 2006

[105] P. S. Kildal, R. Olsson and J. Yang, "Development of three models of the eleven antenna: a new decade bandwidth high performance feed for reflectors," 1st European Conference on Antennas and Propagation, EuCAP, pp. 1-6, 6-10 November 2006

[106] J. Yang, M. Pantaleev, P. S. Kildal, B. Klein, Y. Karandikar, L. Helldner, N. Wadefalk and C. Beaudoin, "Cryogenic 2-13 GHz eleven feed for reflector antennas in future wideband radio telescopes," IEEE Transactions on Antennas and Propagation, vol. 59, No. 6, pp. 1918-1934, June 2011

[107] P. S. Kildal, J. Yang and M. Ivashina, "New BORI and decoupling efficiencies for characterizing ultra-wideband reflectors and feeds for future radio telescopes," Proceedings of the 5th European on Antennas and Propagation (EuCAP), pp. 3712-3714, 2011

[108] J. Bourqui, M. Okoniewski and e. C. Fear, "Balanced antipodal Vivaldi antenna with dielectric director for near-field microwave imaging," IEEE Transactions on Antennas and Propagation, vol. 58, No. 7, pp. 2318-2326, July 2010

[109] Y. K. Kwag, A. D. Hassanein and D. J. Edwards, "A high-directive bowtie RADAR antenna with pyramidal reflector for ultra wideband RADAR imaging applications," Microwave and Optical Technology Letters, vol. 51, no. 2, pp. 387-390, February 2009

[110] A. Mohamed and L. Shafai, "Ultra Wideband Loop Monopole Antennas," International URSI Commission B Electromagnetic Theory Symposium "EMTS", Ottawa, ON, Canada, July 26-28, 2007

[111] A. Mohamed and L. Shafai," Performance study on modern ultra wideband monopole antennas," Ultra Wideband Communications: Novel Trends Book, Chapter 2, INTECH OPEN ACCESS PUBLISHER, 2011

[112] A. Mohamed and L. Shafai, "Ultra Wideband Antennas with Efficient Band-Stop Functions", 14th International Symposium on Antenna Technology and Applied Electromagnetics (ANTEM) and American Electromagnetics Conference, (AMEREM), Ottawa, ON, Canada, July 5 – 9, 2010

[113] H. Moheb, A. Sebak and L. Shafai, "Phase centre analysis of array antennas and its significance for microwave landing system", 7th International Conference on Antennas and Propagation (ICAP), pp. 213–216, 15-18 Apr 1991

[114] A. Helaly, A. Sebak and L. Shafai, "Phase centre movement in linear phased array antennas," IEEE AP-S Int. Symposium, vol. 3, pp. 1166-1169, May 7-11, 1990

[115] A. Mohamed and L. Shafai, "Ultra wideband circular monopole antenna with spiral-slots for band-notch function," URSI Meeting, Ottawa, Canada, July 22-26, 2007.

[116] A. Mohamed and L. Shafai, “Investigation on the phase centre of ultra wideband circular monopole antennas”, IEEE AP-S International Symposium, San Diego, CA, USA, July 5-12, 2008

[117] A. Mohamed and L. Shafai," Investigation on the phase centre of ultra wideband monopole antennas with band-stop functions," Ultra-Wideband Short-Pulse Electromagnetics Book “UWBSP_9”, Springer, 2009

[118] A. Mohamed and L. Shafai, “Investigation on the phase centre of ultra wideband circular monopole antennas with band-stop functions”, European Electromagnetics International Symposium (EUROEM), Lausanne, Switzerland, July 21-25, 2008

[119] J. E. Jones, “A parametric study of the center-fed Vee dipole antenna,” International Symposium on Antennas and Propagation society, vol. 10, pp. 69-72, December 1972

[120] G. Thiele and E. Jr. Ekelman, “Design formulas for Vee dipoles,” IEEE Transactions on Antennas and Propagations, vol. 28, issue 4, pp. 588-590, July 1980

[121] G. A. Thiele, “Wire antennas,” in Computer Techniques for Electromagnetics, R. Mittra, Ed., chapter 2, pp. 29-36, New York: Pergamon, 1973

[122] N. Patwari and A. Safaai-Jazi, “High-gain low-sidelobe double-Vee dipoles,” IEEE Transactions on Antennas and Propagations, vol. 48, issue 2, pp. 333-335, February 2000

[123] S. Licul, A. Safaai-Jazi and A. Chatzipetros, “Gain improvement and backlobe reduction in Vee dipoles with director elements,” Proceedings of the IEEE Southeastcon, pp. 182-188, 7-9 April 2000

[124] P. Knott and A. Bell, “Coaxially-fed tapered slot antenna,” Electronics Letters, vol. 37, issue 18, pp. 1103-1104, 30 August 2001

[125] J. W. Duncan and V. P. Minerva, “100:1 Bandwidth balun transformer,” Proceedings of The IRE, vol. 48, pp. 156-164, issue 2, 1960